PhD Program in Mechanical, Manufacturing, Management and Aerospace Innovation

SENSORS FOR REAL-TIME MONITORING OF OXIDATIVE STRESS

PhD Candidate
Maria Giuseppina Bruno

Coordinator
Prof. Giovanna Lo Nigro

Tutor
Prof. Giuseppe Aiello
Prof. Rosalinda Inguanta
Dott. Ing. Bernardo Patella

CYCLE XXXVII
ACADEMIC YEAR 2023-2024

Table of Contents

Introduction

There is a growing concern over the high incidence of fatal accidents and occupational diseases faced by industrial workers, which result in serious social and economic impacts. Research from the National Institute for Occupational Safety and Health points to a primary cause: prolonged exposure to toxic substances, such as dust particles, gases and chemicals commonly found in industrial settings. Although they can help, preventive measures like wearing protective masks and getting annual checkups don't allow for real-time health monitoring [1].

Research indicates that exposure to these agents is associated with severe health impacts on humans including cancer, neurodegenerative disorders such as Parkinson and Alzheimer diseases, respiratory diseases and genetic modification [2]. The third most common occupational disease is respiratory, such as lung cancer, asthma and Chronic Obstructive Pulmonary disease (COPD) [3]. Oxidative stress plays a key role in the development of these diseases. This is a pathological condition where there is production of Reactive Oxygen Species (ROS) over the capacity of antioxidant systems to neutralize their damaging effects. This imbalance has significant consequences to normal cell physiology and tissue function. Therefore, evaluation of oxidative stress is an important part of clinical diagnosis and treatment strategies [4].

The traditional methods for evaluating oxidative stress often lack the temporal resolution needed to capture dynamic changes in ROS levels. Real-time monitoring represents a significant advancement, enhancing prevention and disease progression, treatment efficacy and physiological responses to various factors [5].

Recently, advancements in both academia and industry have occurred in the development of smart wearable devices for health monitoring. The innovative approaches are largely motivated by the advances made in micro and nano technologies, as well as device miniaturization. In this context, these wearable

systems could be incorporated into existing PPE (Personal Protective Equipment) to monitor workers' physiological conditions in real time. These contributions are also gradually changing the concept of healthcare by enabling self-continuous monitoring of a patient's health status that aligns with personalized medicine approaches [6].

Electrochemical sensors have gained attention as a valuable alternative to traditional detection methods, offering high sensitivity, strong selectivity, quick response times, ease of use, lower costs and the ability to provide continuous measurements. They are also attractive due to the potential for miniaturization, enabling the production of low-cost, disposable, flexible, wearable, or even implantable devices [7].

This thesis is structured into six chapters, each of which contributes to developing the main topic of this research. The organization is as follows:

- **Chapter 1 - Electrochemical Sensors: An Overview**

This chapter describes the classification and highlights of electrochemical sensors, with specific consideration given to wearable sensors. It provides an overview of the different types of electrochemical sensors and their applications in various contexts.

- **Chapter 2 - Materials Used in Electrochemical Sensors Fabrication**

This chapter examines the properties, and the performance of materials used to fabricate the electrochemical sensors in this research work.

- **Chapter 3 - Fabrication and Validation of an Electrochemical Sensor for Hydrogen Peroxide Detection in Exhaled Breath**

This chapter is about the fabrication and validation of an electrochemical sensor designed to be integrated into a face mask for detecting hydrogen peroxide, a key biomarker of oxidative stress, in exhaled breath.

- **Chapter 4 - Fabrication and Validation of a Wearable Microfluidic Sensor for Uric Acid, Chlorides and Glucose Detection in Sweat**

This chapter covers the fabrication and validation of a multi-analyte wearable sensor for detecting other three oxidative stress biomarkers - uric acid, chlorides and glucose - in sweat by employing a microfluidic system. This sensor was developed at the Institute of Microelectronics in Barcelona, under the supervision of Dr. César Fernández-Sánchez and Dr. Manuel Gutiérrez-Capitán.

- **Chapter 5 - A Personalized Medicine Supply Chain Model for Respiratory Diseases in the context of Healthcare 4.0**

This chapter examines how electrochemical sensors could be integrated into healthcare systems, focusing on their potential to improve prevention methods and reduce delays in disease diagnosis. It includes a cost-effectiveness evaluation of an innovative personalized self-testing approach for respiratory pathologies, based on the electrochemical sensor discussed in Chapter 3.

- **Chapter 6 - Conclusions and Future Perspectives**

The final chapter summarizes the key findings and contributions of this research, discussing the implications of the work and suggesting potential future research directions.

References

[1] A. Atsumbe, «Occupational Diseases and Illnesses in Manufacturing Industries in Adamawa State: Causes and Effects», *IOSR-JESTFT*, vol. 3, fasc. 4, pp. 7–13, 2013, doi: 10.9790/2402-0340713.

[2] T. M. Edwards e J. P. Myers, «Environmental Exposures and Gene Regulation in Disease Etiology», *Environ Health Perspect*, vol. 115, fasc. 9, pp. 1264–1270, set. 2007, doi: 10.1289/ehp.9951.

[3] T. Sigsgaard *et al.*, «ERS position paper: work-related respiratory diseases in the EU», *European Respiratory Journal*, vol. 35, fasc. 2, pp. 234–238, feb. 2010, doi: 10.1183/09031936.00139409.

[4] G. Pizzino *et al.*, «Oxidative Stress: Harms and Benefits for Human Health», *Oxidative Medicine and Cellular Longevity*, vol. 2017, pp. 1–13, 2017, doi: 10.1155/2017/8416763.

[5] M. Katerji, M. Filippova, e P. Duerksen-Hughes, «Approaches and Methods to Measure Oxidative Stress in Clinical Samples: Research Applications in the Cancer Field», *Oxidative Medicine and Cellular Longevity*, vol. 2019, pp. 1–29, mar. 2019, doi: 10.1155/2019/1279250.

[6] M. Chan, D. Estève, J.-Y. Fourniols, C. Escriba, e E. Campo, «Smart wearable systems: Current status and future challenges», *Artificial Intelligence in Medicine*, vol. 56, fasc. 3, pp. 137–156, nov. 2012, doi: 10.1016/j.artmed.2012.09.003.

[7] O. Simoska e K. J. Stevenson, «Electrochemical sensors for rapid diagnosis of pathogens in real time», *Analyst*, vol. 144, fasc. 22, pp. 6461–6478, 2019, doi: 10.1039/C9AN01747J.

1. Electrochemical Sensors: An Overview

1.1 Introduction to Electrochemical Sensors

Due to their high sensitivity, selectivity and ability in real-time detection of various chemical and biological substances, electrochemical sensors have become essential tools in modern technology. Their applications span across medical diagnostics, environmental monitoring and food safety. As technology advances, further improvements in electrochemical sensors are enhancing their performance and creating new opportunities for on-site detection and analysis.

1.1.1 Definition and Fundamental Principles

According to IUPAC, a chemical sensor is a device that converts chemical information, such as the concentration of a specific component or a whole composition analysis, in an analytically useful signal. Generally, the receptor and transducer are the key components of chemical sensors. The receptor interacts with the target analyte and gives out chemical data which can be measured by the transducer, designed to convert it into an output signal (Fig. 1.1). Sensors have to guarantee high specificity for the target analyte, even in the presence of other potentially interfering substances. When the receptor in a sensor is of biological origin, such as DNA, antibodies, or enzymes, the sensor is known as a biosensor [1].

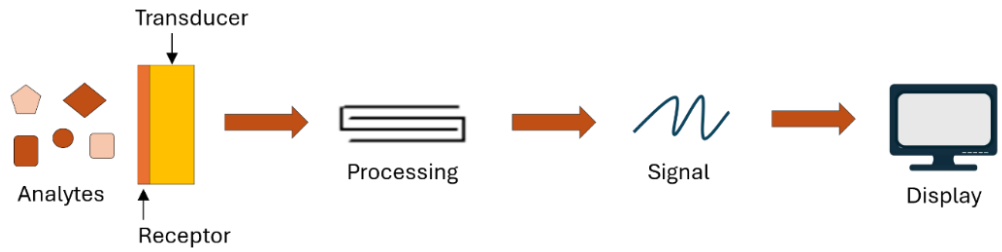

***Figure 1.1**: Schematic diagram illustrating the major components of a sensor.*

An electrochemical sensor is a specific kind of chemical sensor that uses an electrode as its transducer. This electrode is responsible for sensing changes in the environment caused by the presence of an analyte and producing an electrical signal that corresponds to those changes. Due to their capacity to selectively detect specific analytes, they are the most used kind of sensor. However, this selectivity depends on the type of electrode materials and/or bioreceptors that have been attached to it. When the target analyte interacts with these materials or receptors, the response can be converted into a measurable signal that indicates the analyte concentration. Fig. 1.2 shows the three electrodes of an electrochemical sensor: the "working electrode" (WE), the "counter electrode" (CE), and the "reference electrode" (RE). The electrochemical reaction takes place at the WE, the CE completes the circuit (current flows between the WE and the CE), allowing for continuous electron flow, while the RE is used to measure the cell potential relative to the WE [2].

These electrodes are connected to an electrochemical workstation, which can be either a laboratory instrument or a portable field device with an integrated power source. The workstation provides excitation signals and measures the response signals from the electrode setup. The system interfaces with a computer equipped with software specifically designed for data interpretation and analysis [3]. Electrochemical redox reactions involve several processes, such as changes in electrolyte resistance, the adsorption of redox probes, charge transfer at the electrode surface and mass transfer toward the electrode. In this context, WE serves as a site where the analyte and probe are bound, functioning simultaneously as a transducer that produces electrical signals. The counter electrode (CE) establishes a continuum with the electrolyte solution, completing the electrical circuit. The electrolyte facilitates the dissolution of reactants and products, ensuring effective electrochemical contact between the WE, CE and the RE.

When the analyte is detected, the electrochemical sensor generates a current or a voltage proportional to the catalyst concentration, allowing for the measurement of the analyte's presence and concentration [4].

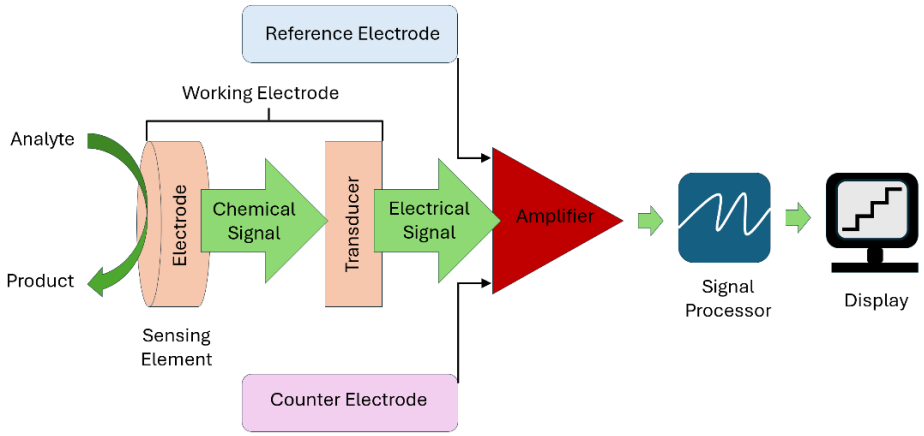

***Figure 1.2**: Schematic diagram of the electrochemical sensor.*

Detection of chemical substances at micro- and nanoscales can be challenging due to interference from other substances that affect signal accuracy. To address these limitations, working electrodes can be modified with materials that improve their sensitivity and selectivity. Nanostructured materials, such as nanoparticles (NPs), nanocomposites, nanocarbons, and conductive polymers are particularly effective in enhancing electrode performance. Notably, metallic NPs are recognized for their exceptional physicochemical and biological properties, making them valuable in a range of applications, including biomedical fields, catalysis, optoelectronics and imaging [5].

1.1.2 Advantages and Disadvantages of Electrochemical Sensors

A range of analytical techniques is utilized for chemical analysis, such as High-Performance Liquid Chromatography (HPLC), Inductively Coupled Plasma Mass Spectrometry (ICP-MS), spectrofluorimetry, Gas Chromatography/Mass

Spectrometry (GC/MS), Gas Chromatography (GC), capillary electrophoresis, chemiluminescence and Atomic Absorption Spectrometry (AAS). Although these methods are highly effective, they tend to be costly, necessitate advanced instrumentation and specialized personnel and often require time-consuming pretreatment steps, which can restrict their practical use.

In contrast, electrochemical sensing offers a promising alternative with advantages such as their potential for miniaturization, cost-effective fabrication, rapid response times, ease to use and the possibility of portable and wearable measurement devices [2].

Ideally, an electrochemical sensor can be brought into contact with a sample and provide results within a few seconds. This efficiency involves several benefits:

- **No Sampling Errors**: the direct contact with the sample eliminates errors associated with sampling.
- **No Sample Pre-Treatment**: the absence of pre-treatment steps, such as dilution, avoids errors associated with these processes.
- **Real-Time Analysis**: the results are available immediately.

Many sensing heads are designed to be cost-effective enough to be disposable after use. Their small size provides high spatial flexibility, making them easily transportable by users or in vehicles.

However, there are notable disadvantages:

- **Matrix Specificity**: most sensors are adapted for specific sample matrices and may fail if the matrix changes.
- **Narrow Analytical Range**: sensors often have limited analytical ranges [6].

1.1.3 Electrochemical sensors feature

Even though sensor requirements are largely determined by its specific use, several standard characteristics are generally relevant for all sensor applications, such as:

- high selectivity;

- signal proportional to the analyte concentration;
- high sensitivity;
- low detection limits;
- fast response times;
- minimal memory effects;
- reusability;
- compact size;
- ease of use.

To calibrate a sensor, standard solutions of the analyte are typically added and the dependence of Steady State Responses on the concentration of analyte is plotted. Each sensor has its characteristic curve (Fig. 1.3), known as the *calibration curve*, which is the relationship of the measured signal (output) and the value of the concentration of the analyte (input).

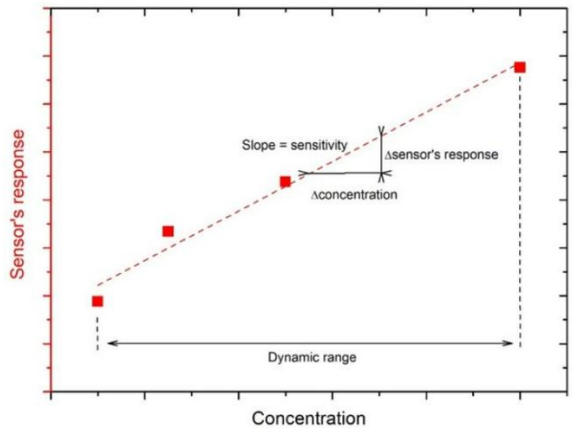

***Figure 1.3**: Calibration curve of a sensor exposed to increasing concentrations of an analyte* [7].

From the calibration curve, two basic characteristics of sensor performance can be derived: the sensitivity and the linear concentration range.

The *sensitivity* is the ratio of the change in the output signal (ΔU) to the change in the input signal (ΔI) in a steady state of sensor. It means that if a sensor is more sensitive, the change in the output voltage for the specified input voltage will be

large as compared to the case of a sensor that is less sensitive. From a mathematical point of view, the sensitivity represents the slope of the calibration curve.

The *linear concentration range* generally refers to the range over which a change in concentration results in a corresponding linear change in the sensor's signal [8].

The *Limit Of Detection* (LOD) is expressed in concentration units and, according to the IUPAC, refers to the concentration from which a device can reliably distinguish an analyte signal from the blank. A signal is considered indicative when, upon injecting a minimal amount of analyte, it results in a signal ($S - S_B$) that is at least three times greater than the background noise (σ_B):

$$|S - S_B| \geq 3\sigma_B, \quad (1.1)$$

From this, the LOD can be calculated using:

$$LOD = 3 * \frac{S_B}{S}, \quad (1.2)$$

,where S represents the sensitivity and S_B denotes the background signal (blank).

The *Limit of Quantification (LOQ)* refers to the lowest concentration of an analyte that can be accurately and precisely measured [9].

The *selectivity* is defined as the sensor's capacity to detect only the concentration of the target analyte while reducing interference from other substances present in the solution. When interfering species are present in the sample matrix, they can produce electrical responses that overlap with the response from the target analyte [10].

The *accuracy* indicates how close the result obtained from the measurement is to the correct result. This parameter is calculated by comparative tests with instruments of known accuracy according to the formula:

$$\varepsilon_a(\%) = 100 \frac{X_m - X_v}{X_v}, \quad (1.3)$$

where X_v represents the true value of the unknown quantity X and X_m is the measured value. A higher ε_a indicates lower accuracy.

The *reproducibility* refers to how consistent the sensor's responses are when the same tests are repeated over a designated time period. The *steady-state response time* is defined as the duration required for the sensor to reach 90% of its final stable output after the analyte is introduced to the electrochemical cell. In contrast, the *response time* indicates how long it takes for the output signal's first derivative (dR/dt) to hit its maximum value after the analyte is added.

The *lifetime* of a sensor is measured by the time it takes for its sensitivity to decrease by a factor of 10 or to be reduced to half of its initial value [6].

1.1.4 Fields of Application

In a fast-paced world, the real-time capabilities of electrochemical sensors have expanded their applications (Fig. 1.4). Clinical tests can now be completed within minutes with high precision and reliability, offering immediate feedback to medical professionals. Increasingly, such tests using sensors and probes are replacing traditional clinical assays that take several hours or even days to yield results.

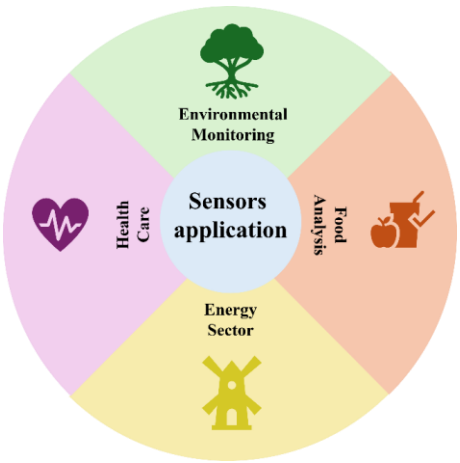

***Figure 1.4**: Application fields of electrochemical sensors.*

The largest field of application for sensors is undoubtedly biomedical sciences. In the last decades, healthcare has moved away from just diagnosing diseases once

they appear. Now, there's a greater focus on preventing diseases before symptoms even show up. Modern sensors can detect key biological markers like DNA, glucose, and cholesterol. They're commonly used in quick tests at the point of care and for spotting infections in patient samples, providing fast and reliable results that make a real difference in patient care and health management. Efforts are underway to develop devices capable of automatically recording these results using computerized data logging and output systems. The integration of electrochemical sensors into healthcare has significantly advanced diagnostics, monitoring, and treatment [6]. Chen et al. [11] fabricated a non-enzymatic electrode strip for rapid detection of uric acid in blood. Uric acid, a significant nitrogenous waste product in urine, results from purine metabolism in the human body and it is associated with various clinical disorders. Elevated UA levels in the blood, known as hyperuricemia or Lesch-Nyhan syndrome, are linked to conditions such as gout, increased alcohol intake, obesity, diabetes, high cholesterol, hypertension, kidney disease, and heart disease. Epidemiological research also indicates that high serum UA may be a risk factor for cardiovascular disease. Consequently, monitoring UA levels in human physiological fluids is crucial for diagnosing patients with disorders related to disrupted purine metabolism.

Electrochemical sensors are extensively employed even in monitoring environmental conditions due to their impressive sensitivity and selectivity, along with low power requirements and real-time data collection capabilities. Unlike traditional techniques that involve transporting samples to labs, these sensors can be installed directly in groundwater to measure various parameters, including pH, chloride, sulfate, uranium, organic contaminants, herbicides and tracer substances. Their use is crucial for enhancing and protecting the quality of air, water, and soil, thereby contributing to ecosystem preservation and public health. Zhao et al. [12] fabricated a bismuth film/carboxylic acid functionalized multi-walled carbon nanotubes-β-cyclodextrin-Nafion nanocomposite modified glassy

carbon electrode (Bi/CMWCNTs-β-CD-Nafion/GCE) for the sensitive detection of cadmium (Cd II) and lead (Pb II) using square wave anodic stripping voltammetry (SWASV). Cadmium (Cd^{2+}) and lead (Pb^{2+}) are well-known for their toxic effects on living organisms due to their persistent toxicity. These heavy metals, which primarily originate from industrial emissions, pose a significant threat to human health and remain prevalent in soil. Heavy metals in soil can enter the food chain and accumulate in the human body, leading to various health issues. Consequently, monitoring trace levels of these heavy metals in soil is of great concern.

In the food industry, electrochemical sensors are employed to detect pollutants such as bacteria, heavy metals, and pesticides in food samples. They are also used for allergen detection to ensure food safety and to monitor the quality and freshness of food products. Additionally, these sensors are valuable for measuring drug concentrations in biological samples, which is essential for understanding drug absorption, distribution, metabolism, and excretion [13]. Mustafa et al. [14] developed a sensor using a carbon-paste electrode modified with multi-walled carbon nanotubes (MWCNTs) to measure sulfite levels in various beverage samples through differential pulse voltammetry (DPV) and amperometry. Sulfite (SO_3^{2-}) is well-known for its strong reducing properties and has been used extensively as a food additive for many years. Its primary function in the food industry is to prevent oxidative degradation and inhibit bacterial growth in foods and beverages, thereby extending their shelf life. Common products containing sulfites include wine, both alcoholic and non-alcoholic beers, cider, as well as bottled juices and concentrates. The Food and Drug Administration (FDA) mandates that any food or beverage containing sulfites at concentrations of 10.0 ppm or higher must carry a caution label. Excessive exposure to sulfites may lead to symptoms such as headaches, nausea, and asthma. Consequently, it is crucial to use electrochemical sensors for accurate and reliable quantification of sulfite

levels in food and beverages to ensure safety and compliance with regulatory standards.

In biotechnology, sensors are increasingly being utilized to meet stringent requirements for sterilization and long-term stability. Sensors designed for monitoring parameters such as oxygen, carbon dioxide, ammonia, hydrogen sulfide, glucose, and penicillin are indicative of a trend toward creating specialized sensors specific to the needs of biotechnologists [6].

In the energy sector, electrochemical sensors monitor the efficiency of batteries and fuel cells. They are also used to detect gas leaks in hydrogen storage and fuel cell systems [13].

1.2 Electrochemical Sensors Classification

According to the type of measurements, electrochemical sensors can be classified into the following categories:

- POTENTIOMETRIC: they measure the potential difference between the working electrode and reference electrode in the absence of current flow [15]. The Ion-Selective Electrode (ISE) for pH measurement is one of the most well-known and widely used sensors. Its popularity arises from its simplicity, affordability, and effectiveness in various practical applications. This sensor consists of a membrane that separates an internal solution with a known and constant concentration of the analyte from the sample solution. The analytical signal is generated based on the charge separation created by ions of the analyte binding to both sides of the membrane through ion exchange, complexation, or other mechanisms [16].
- CONDUCTOMETRIC: these electrochemical sensors measure the ability of the working electrode to conduct an electrical current. In conductometric detection, variations in the concentration of ionic species result in changes in electrical conductivity [15].

- VOLTAMETRIC/AMPEROMETRIC: voltametric sensors measure the current as a function of the applied potential. During measurement, the potential is varied either incrementally or continuously to produce a voltammogram. An example of voltametric sensors are microelectrodes, which are highly versatile due to their small size. This size results in low interfacial capacitance, minimal ohmic drop, and relatively fast mass transport. Consequently, these sensors have a wide range of applications: they are used to determine trace elements (such as As, Cd, Cu, Hg, Pb, Zn) in natural waters and alcoholic beverages, measure substances of biological interest (like dopamine, ascorbic acid, and oxygen) in individual cells or tissues, and monitor chemical or electrochemical processes, including corrosion events [17].

  In a similar way, amperometric sensors measure the current response at a constant potential. Because amperometric sensors operate at specific potentials suited for the analyte of interest, they provide sensitive and selective measurements [15]. In controlled-potential experiments, a supporting electrolyte is crucial. It helps to mitigate electromigration effects by lowering the solution's resistance and keeping the ionic strength constant [1]. Among the most well-known and widely used amperometric sensors are the Clark cell and the blood glucose meter. The Clark cell measures dissolved oxygen in water and can also determine temperature, pH, and conductivity [18].
- IMPEDIMETRIC: they measure resistance, capacitance, and inductance using a small magnitude alternating potential to the cell and observing how the system responds when it reaches a steady state [1].

1.3 Electrochemical techniques

Electrochemical techniques can be classified according to different electrical signals into several types. In most of these techniques, either the current or the potential is controlled while measuring the change in the other parameter [3]. In

the following paragraphs, the main electrochemical techniques used in this research work are explained.

1.3.1 Voltammetry

Voltammetry is an analytical technique that measures the current flowing through an electrode immersed in a solution containing electroactive chemical species (i.e., species that can be oxidized or reduced) when subjected to a change in potential. This technique is highly versatile and plays a crucial role in research, enabling studies on various aspects of electrochemical reactions. The application of different voltametric methods is fundamental for understanding the principles governing electrochemical phenomena. Among its many uses, one of the most significant and widespread applications of voltammetry is the quantitative analysis of chemical species in solution that can be oxidized or reduced, even at low concentration levels (ppb or sub µM). In particular, the peak potential is defined as the maximum point of the peak, which typically does not deviate significantly from the standard potential of the redox pair. This parameter is used to qualitatively characterize a redox pair and to identify its presence in the solution. In contrast, the peak current is the height of the peak, and this current is proportional to the concentration of the electroactive species in the solution. Therefore, the peak current act as the voltammetric parameter for quantitative analysis [19].

The most common voltammetric techniques are the following:

- CYCLIC VOLTAMMETRY: it is a widely employed technique for obtaining detailed information on redox potentials and for investigating the mechanisms and kinetic parameters of reactions involving electroactive analyte solutions. In CV, the voltage is swept from an initial value (E_1) to a predetermined value (E_2) and then returns to its starting point (Fig. 1.5). The scan rate, defined as (E_2 - E_1) / (t_2 - t_1), is a crucial parameter, as varying the scan rate can lead to different results. During the experiment, the current between the working and counter

electrodes is monitored, while changes in the working electrode's potential are controlled by the reference electrode. The resulting voltammograms are generated by plotting the current versus potential.

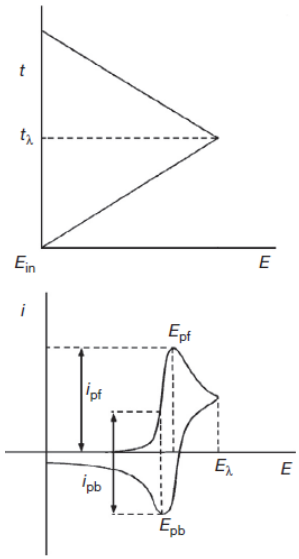

***Figure 1.5**: Potential waveforms and corresponding CV* [20].

As the potential increases towards the analyte's electrochemical reduction potential, the current rises. As the voltage continues to increase towards E_2, the current eventually peaks and then decreases, reflecting a reduction in analyte concentration near the electrode surface due to excessive oxidation potential. When the voltage returns to E_1, the reaction starts to reoxidize the product formed during the initial scan. This causes the current to increase in the opposite direction before decreasing again as the voltage scan proceeds towards E_1. This reverse scan provides valuable information about reaction reversibility at a specific scan rate. The shape of the voltammogram for a known species is significantly influenced by the sweep rate and the changes in the electrode surface after each deposition step. Additionally, the presence of a catalyst and its concentration play a crucial role in determining the voltammogram's profile, with current levels

increasing with higher concentrations of a specific enzyme at a given scan rate compared to conditions without catalysis [21].

- LINEAR SWEEP VOLTAMMETRY: the potential of the working electrode is varied linearly over time. It begins at a potential where no electrode reaction occurs and then shifts to potentials where the analyte undergoes reduction (more negative values) or oxidation (more positive values). Throughout the experiment, the current is recorded, and the resulting current-potential curve (Fig. 1.6).

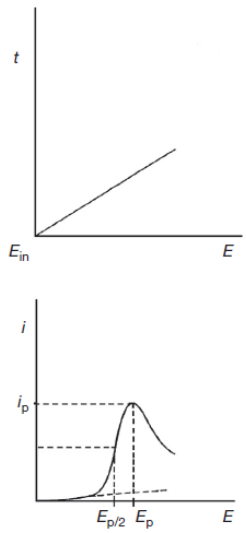

***Figure 1.6**: Potential waveforms and corresponding LSV* [20].

When the electrode potential is within a range where no charge transfer occurs, only a small capacitive current is recorded due to the potential change affecting the orientation of ions and molecules near the electrode surface. Thus, the electrode-solution interface behaves like a capacitor. As the potential reaches the region where the electrochemical reaction takes place, a faradic current is recorded, which increases sharply until it peaks and then decreases steadily. This peak shape results from the competition between the increasing rate of electron transfer as the potential becomes more favourable and the growing thickness of the diffusion layer due to the progressive depletion of the depolarizer at increasing

distances from the electrode surface. The increasing rate of electron transfer dominates in the rising portion of the peak, while depolarizer depletion prevails in the descending branch. Consequently, the peak current is observed at a potential where these opposing effects balance, meaning the analyte concentration at the electrode surface has not yet reached zero [20].

- PULSE VOLTAMMETRIC TECHNIQUES: these techniques involve applying pulses of varying potential and measuring the current response over time. The use of pulses enhances sensitivity because it allows for more effective differentiation between capacitive and faradaic currents. During a pulse, capacitive currents typically decrease more rapidly than faradaic currents. By measuring the current at the end of the pulse, where capacitive effects have reduced, these techniques achieve improved sensitivity compared to continuous potential sweeps [20].

1.3.2 Chronoamperometry

Chronoamperometry is a controlled potential technique where the current is recorded as a function of time (Fig. 1.7). As a result of the electrochemical reaction at the electrode surface, a significant current flows, which is proportional to the concentration gradient of the analyte at the electrode. This approach is used to detect a single component from a mixture of electrochemically reducible species due to the fixed potential of the working electrode [3]. Changes in the current appear in response to rises or decreases in the diffuse layers of the analyte at the surface of the working electrode. By applying an appropriate potential to the system, the local concentration of the analyte at the surface of the electrode drops to zero. Under these conditions, a concentration gradient is generated that provides analyte transfer through diffusion from a higher concentration section (bulk solution) to the electrode surface [21].

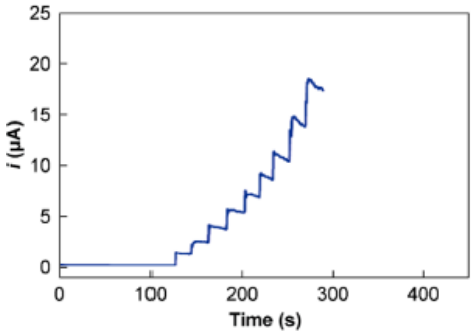

***Figure 1.7**: Current vs Time graph for chronoamperometric signal* [13].

1.4 Wearable electrochemical sensors

1.4.1 Smart Devices: Applications

Digital telemedicine solutions are progressively integrating into our everyday lives via commercial wearable gadgets that facilitate noninvasive remote health monitoring. There has been considerable enthusiasm surrounding the development of telemedicine wearable systems, thanks to their ability to collect data on physiological and biochemical parameters in real time without invasive procedures. The main objective of improving these telemedicine wearables is to support early disease detection and minimize the expenses linked to advanced and invasive treatment options. These wearable technologies are crucial for personalized medicine as they can collect data from the human body in real time and provide meaningful health information for preventive care. Advancements in nanotechnology and multifunctional materials have significantly improved flexible electronics for remote, personalized healthcare. Despite these advancements, several challenges persist, including limitations in monitored biometric data, the reliability, selectivity, and specificity of sensing materials, and issues related to device ergonomics and miniaturization to enhance user-friendliness. Significant efforts are being made to develop miniaturized epidermal

skin sensors capable of detecting important biomarkers, thus advancing personalized healthcare management with real-time clinical feedback [22], [23]. Recently, advanced telemedicine tools have emerged, creating new possibilities in the medical field. The advancement of flexible electronics with substantial data storage capacity has significantly improved telemedicine, positioning it as a valuable technology for remote medical consultations and real-time monitoring of vital signs. Telemedicine, as a decentralized healthcare solution, presents an effective strategy for early intervention in disease progression, helping to prevent chronic conditions and lower mortality rates through enhanced detection of health risks [22]. Fig. 1.8 illustrates a remote health monitoring system based on wearable sensors.

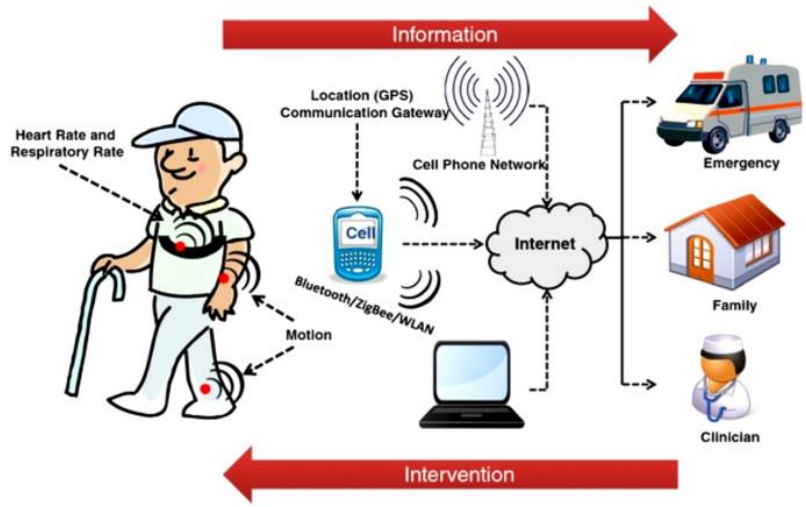

***Figure 1.8**: A schematic diagram illustrating a remote health monitoring system based on wearable sensors* [23].

Research and development of smart devices are increasingly gaining attention in both academic and industrial fields. With the global population aging, the elderly face heightened levels of disability due to increased needs for care and assistance. Many elderly individuals would prefer to stay in their own homes rather than move to expensive care facilities. Currently, only 2 to 5% of elderly people reside in nursing homes. According to data from 30 OECD countries, healthcare

expenditures as a percentage of gross domestic product (GDP) are at unprecedented levels, partly due to increased costs and economic slowdowns. For instance, France spent 11.8% of its GDP on healthcare in 2009, ranking just behind the USA, Germany, Canada, Switzerland, and Austria [24]. Telehealth and telemedicine are emerging models addressing these healthcare challenges, with numerous laboratory prototypes and industrial products already developed. Telehealth equipment serves as a vital tool for managing long-term conditions within the community, enabling the monitoring of patients. This approach for monitoring vital signs aims to reduce the number of hospital admissions by using home-based devices to observe health trends and send alerts if certain predefined limits are exceeded. Patients learn how to operate these devices, which assess daily physiological metrics such as blood pressure, oxygen levels, heart rate, lung function, body temperature, ECG and blood glucose levels from their homes. The data collected by these telehealth tools is relayed through telephone lines to an online portal that can be accessed by healthcare professionals. Alarms can be triggered when abnormalities are detected by the telehealth equipment. For instance, persistent tachycardia or hypoxia might prompt a telephone call or home visit from the hospital staff. The responses to these alarms follow predefined protocols, which should be established in advance in consultation with the patient. Early intervention through such measures could help alleviate the burden on emergency services and potentially prevent hospital admissions [25]. Andreoni et al. [26] designed a T-shirt and belts equipped with embedded textile electrodes for monitoring electrocardiogram (ECG) and heart rate. The T-shirt and belts proved to be comfortable, effectively detecting, recording, and processing signals, which led to the successful generation of alarms when necessary. Yoon et al. [27] developed a skin-attachable piezoelectric pressure sensor and demonstrated its effectiveness in estimating heart rate by sensing pulse waves in the human artery. This flexible piezoelectric generator captures energy from the arterial pulsations at the wrist without the need for invasive methods, providing improved comfort

for users due to its enhanced flexibility. Bachlin et al. [28] introduced a wearable device designed for Parkinson's Disease (PD) patients with the Freezing of Gait (FOG). This system employs acceleration sensors placed on the body to track and analyze the movements of the patient. It automatically detects FOG by analyzing the frequency components of these movements. Upon detecting FOG, the assistant emits a rhythmic auditory signal to prompt the patient to resume walking. Another important application of these systems is the safety at work. The workers face challenges at work like accidents and occupational diseases which directly affect the survival of workers and their families. From the report of the International Labour Organization (ILO), it was found that approximately 2.78 million people have died due to workplace injury or occupational diseases and 374 million people have suffered from non-fatal injuries. Accidents in the workplace have the consequence not only of a damaging company brand to the public; it is also linked to substantial expenditure in human resource, the loss in profit, legal costs, medical insurance premiums and the cost of training new staff to compensate the financial losses. The annual cost of workplace injuries in the United States can be estimated at around one billion dollars per week; these costs are a result of injuries to employees. For example, healthcare workers are at risk of fatigue, overexertion, and hospital-acquired infections; office workers are prone to neck and back pain; chemical factory workers are more likely to suffer from respiratory illnesses; and rubber industry workers have an increased risk of stomach cancer. Hearing loss is commonly associated with workers in the mining, construction, manufacturing, and entertainment industries. Asbestos exposure is linked to mesothelioma and ovarian cancer, plutonium and vinyl chloride exposure is associated with liver cancer, and trichloroethylene (a common industrial solvent) is a risk factor for kidney cancer. For outdoor work activities, employers typically provide standard personal protective equipment (PPE) such as steel-toe boots, safety vests, harnesses, hard hats, earmuffs, and goggles. So, in this context SWS can be integrated into PPE to enhance worker safety, investing

in workplace technologies that offer real-time data collection and predictive analytics can be highly beneficial [29]. Fig. 1.9 provides some examples of wearable devices for safety monitoring at work.

Figure 1.9*: Examples of wearable devices for occupational safety monitoring. a) Smart helmet for monitoring safe working distance and interactions. b) Smart Cap measures brain waves to estimate alertness and fatigue level at work. c) Smart skeleton helps with heavy lifting by transferring the load from the upper body and back to the legs. d) Smart bracelet for the risk management of hand arm vibrations. e) Smart dynamometers to evaluate muscle strength and endurance. f) Smart PPE for safety monitoring of workers by tracking the microclimate, core body temperature, heart rate and exertion. g) Smart system for monitoring the work temperature of frontline workers* [29].

Gatti et al. [30] investigated if a wearable device can effectively monitor a person during work dynamin activities through heart rate and oxygen consumption monitoring. Amrutha et al. [31] proposed a smart helmet for monitoring the physical conditions of the construction workers. This wearable device was designed to enhance the safety and protection of employees by providing real-time data and alerts. Unlike conventional helmets, this high-tech helmet is equipped with a range of sensors and tools that monitor various physical and environmental factors, including temperature, humidity, noise levels, and the presence of hazardous chemicals. It also tracks physiological data such as heart

rate and body temperature to detect signs of exhaustion or stress. Additionally, the helmet is capable of alerting both managers and employees to potential hazards, such as falling objects or adverse weather conditions. Syabila et al. [32] realized a real-time safety monitoring system for workers who are exposed to vibrations for quite a long time, so they can be at risk of Hand Arm Vibration Syndrome (HAVS). Health standards issued by the Ministry of Health specify safe exposure limits for vibrations on the human body. For instance, vibrations with a strength of 20 m/s^2 should not exceed an exposure time of 30 minutes. The system monitors the vibrations experienced by the human arms and will send a notification and activate a buzzer alert if the vibration strength exceeds these health standard limits.

1.4.2 The Role of Smart Devices in Healthcare 4.0

The efficiency and effectiveness of healthcare systems in providing quality services to populations are major concerns for governments and institutions across industrialized nations. Common challenges include the insufficient responsiveness to fast-spreading diseases like the COVID-19 pandemic by the centralized healthcare models, and the rising costs of service provision. With an aging population, these issues are expected to worsen, threatening the ability of healthcare systems to meet the needs of future generations and posing significant risks to their long-term sustainability. Given this scenario, research into more effective and efficient healthcare models has focused on improving critical processes such as screening, early diagnosis, and personalized treatment. The rise of Industry 4.0, with its pervasive computing and biosensing technologies, presents a promising opportunity to shift to more cost-effective and inclusive remote healthcare models. By utilizing advanced information and communication technologies, smart sensors, and wearable devices, vast amounts of health data can be gathered and analyzed in real time, enabling personalized healthcare services and remote diagnostics [33]. These advancements have the potential to

revolutionize healthcare systems by prioritizing prevention and real-time patient monitoring, ultimately reducing costs and improving quality of life [34].

The European Union (EU) has already committed substantial resources to this transformation, with public health spending reaching 16% of the total public expenditure in 2021, 37% of which was allocated to inpatient care. In 2023, the EU launched a €43 billion plan, including nearly €14 billion earmarked for digitalizing health services and transitioning from a hospital-centered to a patient-centered care system [35]. This funding supports the development of point-of-care solutions that enable patients to self-test at home or nearby facilities using smart biosensing devices, reducing the need for physical visits to centralized hospitals. Enhancing proximity medical services offers a valuable opportunity to improve the inclusiveness of healthcare while ensuring affordability and personalization through devices capable of capturing patient data, generating electronic medical records, and supporting clinical decision-making.

While the effectiveness and efficiency of healthcare systems have been widely discussed, the development of digital biosensing technologies is a newer topic within Industry 4.0 and its medical counterpart, Healthcare 4.0. These technologies have the potential to revolutionize the sector by enabling real-time monitoring and personalized treatment [36], [37]. However, the integration of these technologies into existing healthcare systems remains a challenge, particularly with centralized digital infrastructures [23], [38]. A major issue is the vast amount of Internet of Things (IoT) data generated, which can be difficult to transmit in areas with underdeveloped networking infrastructures, especially in remote communities. Additionally, the latency of centralized systems can cause delays in processing healthcare data, which is particularly concerning in critical sectors like healthcare [39].

The Industry 4.0 paradigm, with its cloud computing and IoT capabilities, has made the traditional Automation Pyramid structure, designed in the 1990s, outdated and inadequate for modern industrial digital systems. Edge computing,

introduced by Gelsinger [40], offers a decentralized approach where IoT devices and edge servers process data in real time without relying on a central server [41]. The concept of "fog computing," first proposed by Bonomi et al. [42], further expands on this by placing computing, storage, and networking services closer to the edge of the network, between end-user devices and traditional cloud data centers. Fog computing facilitates the processing of large amounts of data at or near IoT devices, making it well-suited for time-sensitive healthcare applications [43]. Fog computing can serve as a gateway between cloud and IoT layers, reducing latency and improving real-time data processing [44]. This approach has been identified as an effective solution to the challenges of centralized cloud systems, particularly in healthcare where quick data processing is crucial [45], [46].

The digitalization of healthcare systems is considered key to improving organizational performance and responsiveness [47], and is an area of growing interest in academia and industry [48], [49]. A digitized healthcare system facilitates full access to health services from the comfort of home, addressing one of the major drawbacks of traditional models. However, developing daily-use sensors to collect health and activity data for early disease diagnosis remains a challenge for industrial companies [50]. More research is needed to develop fast, portable, miniaturized, and affordable point-of-care devices for long-distance monitoring of disease biomarkers [51]. Over the last decade, significant efforts have been made to develop more efficient healthcare technologies and devices that align with personalized healthcare paradigms. The strategic development of smart devices for personalized medicine has become a key focus for many industrialized countries [52]. Given the importance of timely diagnosis and treatment in telemedicine, further work is required to enhance wearable sensors for effective real-time remote diagnosis, improving patients' health and potentially saving lives [53].

1.4.3 Smart Devices: Classification

Smart devices can be classified as:

- Implantable devices: these devices are integrated to operate within the human body, such as implantable cardioverter defibrillators (ICDs), that are designed to deliver an electrical impulse at the right time when the heart has a different rhythm (Fig. 1.10). These devices are made of compatible materials that do not cause a reaction or have an adverse effect to the body [54]. ICDs are more advanced than traditional pacemakers because they can deliver high-energy electrical shocks to correct life-threatening arrhythmias when lower-energy pulses are insufficient. This reduces the mortality rates due to the sudden cardiac deaths (SCDs), which account for approximately half of all fatalities related to heart disease [55].

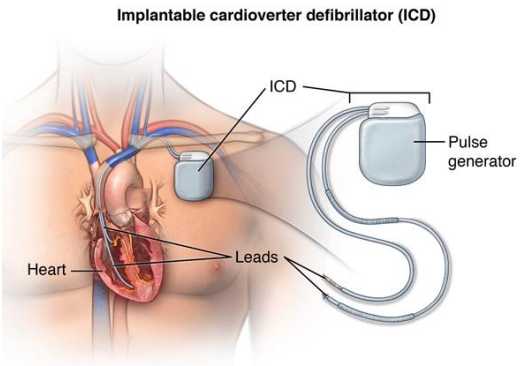

Figure 1.10*: Schematic representation of an ICD* [56].

Jia et al. recently developed a non-invasive system for monitoring glucose, lactate, alcohol, and ammonia levels in the body using a tattoo-based biosensor. These tattoo biosensors can quantify lactate concentrations in human sweat non-invasively by detecting electrochemical signals generated by enzymes. The novel lactic acid oxidase-functionalized skin biosensor shows high linear specificity, accurately measuring lactate concentrations up to 20 mM, which is secreted by the sweat glands. Additionally, the tattoo sensor is designed to be versatile and durable, maintaining functionality even with frequent skin movement. This sensor

has been employed to analyze variations in lactate levels in sweat during long-term, repetitive exercise in real time [57]. Fig. 1.11 shows some wearable skin patches.

***Figure 1.11**: Wearable bioelectronic skin patches* [58].

- Portable devices: one of the most common types of portable wearable devices is the smartwatch. The GlucoWatch® Biographer was the first commercial smartwatch approved by the Food and Drug Administration (FDA), featuring a non-invasive glucose sensor. It uses reverse iontophoresis to electrochemically extract glucose concentrations from skin interstitial fluid [59].
-

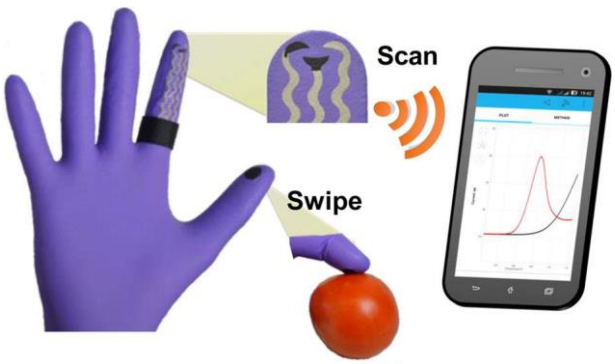

***Figure 1.12**: Flexible Glove-Based Biosensor* [60].

Mishra et al. [60] developed a glove featuring an electrochemical biosensor with a real-time wireless data transmission to a smartphone device (Fig. 1.12). In this system, the thumb acts as a collector/sampling finger, while the index finger, coated with organophosphorus hydrolase, serves as the detecting finger. This "Lab-on-a-glove" serves as a point-of-care (POC) screening device and is also applicable in defense, security, and food safety applications.

1.4.4 Materials for Smart Electrochemical Sensors

For wearable devices, it is crucial to ensure excellent performance even when they are subjected to considerable deformation such as bending, stretching, or twisting. Recent innovations in electrochemical sensors have made it possible to achieve these requirements [22]. The use of rigid and brittle metals in wearable technology that require significant deformation has seen a decline in recent years. To meet the demands of future healthcare applications, sensors that are both stretchable and capable of high performance are highly desirable. Flexible substrates are essential for wearable devices, making materials like polymers, paper, and textiles excellent options. Among various polymers, polyimide (PI), polyethylene terephthalate (PET), silk, parylene, stretchable polydimethylsiloxane (PDMS), acrylic, and Ecoflex are widely used as flexible or stretchable substrates used in wearable technologies. The choice of polymer depends on the specific application. For instance, PI is suitable for high-temperature applications due to its high glass transition temperature, PET is ideal where high transparency is required, and PDMS is well-suited for stretchable sensors. In-clothing sensors often use textiles as they are compatible with human skin and can serve as both sensing material and substrate. Sensors can be fabricated on or integrated into textile fibers, including wool (animal origin), cotton (plant origin), or synthetic textiles like nylon. Paper is another flexible, low-cost, and lightweight substrate commonly used for wearable devices. It is biocompatible and environmentally friendly, as it can naturally degrade in ambient conditions [61].

Beyond synthetic materials, there has been exploration into natural substances for creating substrates for wearable systems. Biomaterials represent one of nature's most abundant resource categories and provide substantial benefits, including biocompatibility, biodegradability, versatility, sustainability and cost-effectiveness. Fibers and textiles are particularly well-suited for wearable sensing technologies due to their natural compatibility with human skin [62]. An example is natural silk, which stands out as a readily available and attractive biomaterial, fulfilling the mechanical criteria necessary for handling irregular deformations. Silk consists of fibrous proteins characterized by highly repetitive amino acid sequences and is produced by various spiders and insects, including wasps, honeybees and silkworms. Of these, silk from the *Bombyx mori* silkworm has received the most attention because of its extensive natural production, remarkable biocompatibility, distinct mechanical properties, controllable degradation and adaptability into various material forms. For thousands of years, silkworm silk has been used in textiles, prized for its shine, flexibility, and lightweight qualities. Recent advancements in biomedicine and nanofabrication have allowed for the functionalization of silk-based materials, thereby expanding their applications. Current uses include scaffolds for tissue engineering, systems for drug delivery and biosensors. Additionally, silk fibroin is garnering increased interest in flexible electronics and photonic devices due to its ability to produce innovative devices that are lightweight, resilient, flexible, biocompatible, non-toxic, sustainable and biodegradable [63]. Chen et al. [64] developed a silk nanofibril (SNF)/reduced graphene oxide(rGO)/glucose oxidase (GOx) sensor for non-invasive detection of glucose in sweat, covering both healthy people and diabetic patients.

So, an ideal material for electrodes should possess excellent electrical conductivity along with strong mechanical properties. The structure and electrical performance of the electrode must remain stable even under significant stress and strain. Furthermore, the physical bond between the substrate and the metallic layer

is crucial, as metal films can detach during stretching. Traditional metals such as gold (Au), silver (Ag), platinum (Pt) and aluminum (Al) have been effectively employed as electrodes for flexible sensors. However, these metals may experience cracking and other defects under high stress, which can negatively affect their electrical performance. To mitigate this problem, researchers have developed porous metal films that exhibit greater resilience to stress and strain [61]. For example, Zhang et al. developed an electrochemical sensor utilizing gold and Prussian blue nanoparticles (AuPBNPs) integrated with carbon ink on PET for detecting hydrogen peroxide. This sensor was fabricated on rubber gloves using screen printing techniques, demonstrating promising results for wearable system applications [65].

In Fig. 1.13 different types of materials used to fabricate wearable sensors are shown.

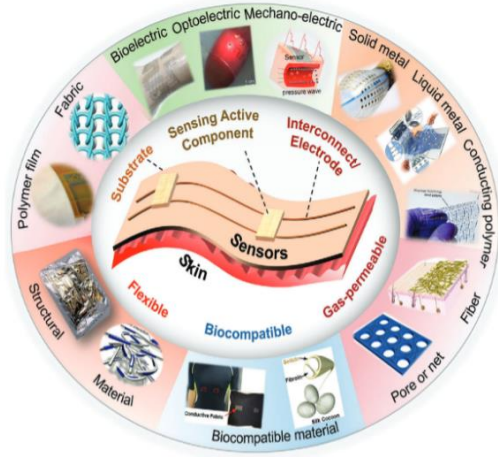

***Figure 1.13**: Materials for wearable sensors* [66].

The next generation of wearable devices is anticipated to achieve higher accuracy and perform a wider range of functions. Advanced materials will be key to driving rapid, continuous, and predictable innovations in wearable technology. The selection of appropriate materials and effective assembly methods will be crucial

in developing wearable sensors with high stability, sensitivity, and a broad strain range. Recent advancements have incorporated various materials, such as nanowires (NWs), metal nanoparticles (MNPs), conductive polymers (CPs), and carbon-based materials, to enhance wearable healthcare devices due to their exceptional mechanical and electrical properties. Among these, advanced carbon-based materials, including carbon black nanoparticles (CBNPs), carbon nanofibers, graphene, and carbon nanotubes (CNTs), provide unique benefits, such as high chemical and thermal stability, excellent electrical conductivity, and ease of functionalization. These properties make them particularly promising for wearable electronic applications. For example, graphene (Gr) has the highest reported electron mobility and is both flexible and mechanically strong, making it ideal as both an electrode material and a sensing element [62]. Pu et al. reported a three-electrode-based electrochemical sensor in which the working electrode was modified with graphene and AuNPs. The highly sensitive sensor integrated with a microfluidic chip formed a wearable sensor for continuous non-enzymatic glucose monitoring [67].

1.5 Conclusions and Future Challenges

Electrochemical sensors are making big improvements in fields like healthcare, environmental monitoring, food safety and biotechnology. They translate chemical data into clear electrical signals, offering a fast, cost-effective and highly sensitive way to analyze samples. They can give real-time results, which is useful for both routine and critical applications. Despite challenges, such as matrix specificity, new materials and technologies keep improving their performance. Using nanomaterials and new designs for electrodes, these sensors are becoming more robust and adaptable to many different needs. As technology moves forward, these sensors support important progress in scientific research, industry, daily safety and health practices. In particular, wearable and smart electrochemical sensors are changing healthcare and safety, as well as

personalized medicine. Made with new materials like nanowires, graphene, and conductive polymers, these sensors are becoming more sensitive, flexible and durable. This allows them to track health and environmental data in real time. As telemedicine and remote health monitoring grow, these devices bring new ways to detect diseases early, customize treatments and improve safety in healthcare and workplaces. However, some challenges remain in improving accuracy, ease of use and selectivity of these systems. Future work might focus on creating new materials, adding wireless features and developing sensors capable of simultaneously monitoring multiple health parameters. In conclusion, while impressive progress has been made in the field of wearable health sensors, further research is still needed. As these devices continue to improve, they could help make healthcare more preventive and workplaces safer.

References

[1] J. Baranwal, B. Barse, G. Gatto, G. Broncova, e A. Kumar, «Electrochemical Sensors and Their Applications: A Review», *Chemosensors*, vol. 10, fasc. 9, p. 363, set. 2022, doi: 10.3390/chemosensors10090363.

[2] R. Singh, R. Gupta, D. Bansal, R. Bhateria, e M. Sharma, «A Review on Recent Trends and Future Developments in Electrochemical Sensing», *ACS Omega*, p. acsomega.3c08060, feb. 2024, doi: 10.1021/acsomega.3c08060.

[3] B. Bansod, T. Kumar, R. Thakur, S. Rana, e I. Singh, «A review on various electrochemical techniques for heavy metal ions detection with different sensing platforms», *Biosensors and Bioelectronics*, vol. 94, pp. 443–455, ago. 2017, doi: 10.1016/j.bios.2017.03.031.

[4] A. Barhoum, S. Hamimed, H. Slimi, A. Othmani, F. M. Abdel-Haleem, e M. Bechelany, «Modern designs of electrochemical sensor platforms for environmental analyses: Principles, nanofabrication opportunities, and challenges», *Trends in Environmental Analytical Chemistry*, vol. 38, p. e00199, giu. 2023, doi: 10.1016/j.teac.2023.e00199.

[5] T. Kant *et al.*, «Design and development of conductive nanomaterials for electrochemical sensors: a modern approach», *Materials Today Chemistry*, vol. 24, p. 100769, giu. 2022, doi: 10.1016/j.mtchem.2021.100769.

[6] O. S. Wolfbeis, «Chemical sensors ? survey and trends», *Fresenius J Anal Chem*, vol. 337, fasc. 5, pp. 522–527, 1990, doi: 10.1007/BF00322857.

[7] J.-M. Tulliani, B. Inserra, e D. Ziegler, «Carbon-Based Materials for Humidity Sensing: A Short Review», *Micromachines*, vol. 10, fasc. 4, p. 232, mar. 2019, doi: 10.3390/mi10040232.

[8] D. R. Thevenot, K. Toth, R. A. Durst, e G. S. Wilson, «Electrochemical biosensors: recommended definitions and classification_», 2001.

[9] Á. Lavín *et al.*, «On the Determination of Uncertainty and Limit of Detection in Label-Free Biosensors», *Sensors*, vol. 18, fasc. 7, p. 2038, giu. 2018, doi: 10.3390/s18072038.

[10] P. Fabry e J. Moutet, «Sensitivity and Selectivity of Electrochemical Sensors», in *Chemical and Biological Microsensors*, 1ª ed., J. Fouletier e P. Fabry, A c. di, Wiley, 2013, pp. 45–80. doi: 10.1002/9781118603871.ch3.
[11] J.-C. Chen, H.-H. Chung, C.-T. Hsu, D.-M. Tsai, A. S. Kumar, e J.-M. Zen, «A disposable single-use electrochemical sensor for the detection of uric acid in human whole blood», *Sensors and Actuators B: Chemical*, vol. 110, fasc. 2, pp. 364–369, ott. 2005, doi: 10.1016/j.snb.2005.02.026.
[12] G. Zhao, H. Wang, G. Liu, e Z. Wang, «Simultaneous Determination of Cd(II) and Pb(II) Based on Bismuth Film/Carboxylic Acid Functionalized Multi-Walled Carbon Nanotubes-β-cyclodextrin-Nafion Nanocomposite Modified Electrode», *International Journal of Electrochemical Science*, vol. 11, fasc. 10, pp. 8109–8122, ott. 2016, doi: 10.20964/2016.10.07.
[13] K. Singh, K. K. Maurya, e M. Malviya, «Review of Electrochemical Sensors and Biosensors Based on First-Row Transition Metals, Their Oxides, and Noble Metals Nanoparticles», *J. Anal. Test.*, vol. 8, fasc. 2, pp. 143–159, giu. 2024, doi: 10.1007/s41664-023-00292-w.
[14] Y. F. Mustafa, G. Chehardoli, S. Habibzadeh, e Z. Arzehgar, «Electrochemical detection of sulfite in food samples: Review paper», *J. Electrochem. Sci. Eng.*, nov. 2022, doi: 10.5599/jese.1555.
[15] H. A. Saputra, «Electrochemical sensors: basic principles, engineering, and state of the art», *Monatsh Chem*, vol. 154, fasc. 10, pp. 1083–1100, ott. 2023, doi: 10.1007/s00706-023-03113-z.
[16] A. Michalska, «All-Solid-State Ion Selective and All-Solid-State Reference Electrodes», *Electroanalysis*, vol. 24, fasc. 6, pp. 1253–1265, giu. 2012, doi: 10.1002/elan.201200059.
[17] O. Ordeig, J. del Campo, F. X. Muñoz, C. E. Banks, e R. G. Compton, «Electroanalysis Utilizing Amperometric Microdisk Electrode Arrays», *Electroanalysis*, vol. 19, fasc. 19–20, pp. 1973–1986, ott. 2007, doi: 10.1002/elan.200703914.
[18] J. R. Stetter e J. Li, «Amperometric Gas SensorsA Review», *Chem. Rev.*, vol. 108, fasc. 2, pp. 352–366, feb. 2008, doi: 10.1021/cr0681039.
[19] P: Protti, « Introduction to Modern Voltammetric and Polarographic Analisys Techniques », *Amel Electrochemistry*, IV edition, 2001.
[20] G. Bontempelli, N. Dossi, e R. Toniolo, «Polarography/Voltammetry», in *Reference Module in Chemistry, Molecular Sciences and Chemical Engineering*, Elsevier, 2018, p. B9780124095472143264. doi: 10.1016/B978-0-12-409547-2.14326-4.
[21] B. Rezaei e N. Irannejad, «Electrochemical detection techniques in biosensor applications», in *Electrochemical Biosensors*, Elsevier, 2019, pp. 11–43. doi: 10.1016/B978-0-12-816491-4.00002-4.
[22] S. Kalasin e W. Surareungchai, «Challenges of Emerging Wearable Sensors for Remote Monitoring toward Telemedicine Healthcare», *Anal. Chem.*, vol. 95, fasc. 3, pp. 1773–1784, gen. 2023, doi: 10.1021/acs.analchem.2c02642.
[23] A. A. Smith, R. Li, e Z. T. H. Tse, «Reshaping healthcare with wearable biosensors», *Sci Rep*, vol. 13, fasc. 1, p. 4998, mar. 2023, doi: 10.1038/s41598-022-26951-z.
[24] M. Chan, D. Estève, J.-Y. Fourniols, C. Escriba, e E. Campo, «Smart wearable systems: Current status and future challenges», *Artificial Intelligence in Medicine*, vol. 56, fasc. 3, pp. 137–156, nov. 2012, doi: 10.1016/j.artmed.2012.09.003.
[25] S. Stowe e S. Harding, «Telecare, telehealth and telemedicine», *European Geriatric Medicine*, vol. 1, fasc. 3, pp. 193–197, giu. 2010, doi: 10.1016/j.eurger.2010.04.002.
[26] P. Perego, C. Standoli, e G. Andreoni, «Wearable monitoring of elderly in an ecologic setting: the SMARTA project», in *Proceedings of 2nd International Electronic Conference on Sensors and Applications*, Sciforum.net: MDPI, nov. 2015, p. S3001. doi: 10.3390/ecsa-2-S3001.

[27] S. Yoon e Y.-H. Cho, «A Skin-attachable Flexible Piezoelectric Pulse Wave Energy Harvester», *J. Phys.: Conf. Ser.*, vol. 557, p. 012026, nov. 2014, doi: 10.1088/1742-6596/557/1/012026.
[28] M. Bachlin *et al.*, «Wearable Assistant for Parkinson's Disease Patients With the Freezing of Gait Symptom», *IEEE Trans. Inform. Technol. Biomed.*, vol. 14, fasc. 2, pp. 436–446, mar. 2010, doi: 10.1109/TITB.2009.2036165.
[29] V. Patel, A. Chesmore, C. M. Legner, e S. Pandey, «Trends in Workplace Wearable Technologies and Connected-Worker Solutions for Next-Generation Occupational Safety, Health, and Productivity», *Advanced Intelligent Systems*, vol. 4, fasc. 1, p. 2100099, gen. 2022, doi: 10.1002/aisy.202100099.
[30] U. C. Gatti, G. C. Migliaccio, e S. Schneider, «Wearable Physiological Status Monitors for Measuring and Evaluating Workers' Physical Strain: Preliminary Validation», in *Computing in Civil Engineering (2011)*, Miami, Florida, United States: American Society of Civil Engineers, giu. 2011, pp. 194–201. doi: 10.1061/41182(416)24.
[31] D. K. Amrutha, M. R. Reddy, e D. R. Vasuki, «SMART HELMET FOR CONSTRUCTION WORKERS», vol. 9, fasc. 4, 2024.
[32] R. Syabila, O. N. Samijayani, N. Parwati, A. Syahriar, D. Astharini, e I. Adhipramana, «IoT based Smart Bracelet for Worker Safety and Health Monitoring», in *2023 International Workshop on Artificial Intelligence and Image Processing (IWAIIP)*, Yogyakarta, Indonesia: IEEE, dic. 2023, pp. 200–203. doi: 10.1109/IWAIIP58158.2023.10462864.
[33] A. Bhattarai, D. Peng, J. Payne, e H. Sharif, «Adaptive Partition of ECG Diagnosis Between Cloud and Wearable Sensor Net Using Open-Loop and Closed-Loop Switch Mode», *IEEE Access*, vol. 10, pp. 63684–63697, 2022, doi: 10.1109/ACCESS.2022.3182704.
[34] G. L. Santos *et al.*, «Analyzing the availability and performance of an e-health system integrated with edge, fog and cloud infrastructures», *J Cloud Comp*, vol. 7, fasc. 1, p. 16, dic. 2018, doi: 10.1186/s13677-018-0118-3.
[35] European Commission. Directorate General for Health and Food Safety., *State of health in the EU: synthesis report 2023*. LU: Publications Office, 2023. Consultato: 9 novembre 2024. [Online]. Disponibile su: https://data.europa.eu/doi/10.2875/458883
[36] A. Gupta e A. Singh, «Healthcare 4.0: recent advancements and futuristic research directions», *Wireless Pers Commun*, vol. 129, fasc. 2, pp. 933–952, mar. 2023, doi: 10.1007/s11277-022-10164-8.
[37] A. Haleem, M. Javaid, R. Pratap Singh, e R. Suman, «Medical 4.0 technologies for healthcare: Features, capabilities, and applications», *Internet of Things and Cyber-Physical Systems*, vol. 2, pp. 12–30, 2022, doi: 10.1016/j.iotcps.2022.04.001.
[38] M. L. Sin, K. E. Mach, P. K. Wong, e J. C. Liao, «Advances and challenges in biosensor-based diagnosis of infectious diseases», *Expert Review of Molecular Diagnostics*, vol. 14, fasc. 2, pp. 225–244, mar. 2014, doi: 10.1586/14737159.2014.888313.
[39] D. Gowda V *et al.*, «Industrial quality healthcare services using Internet of Things and fog computing approach», *Measurement: Sensors*, vol. 24, p. 100517, dic. 2022, doi: 10.1016/j.measen.2022.100517.
[40] P. P. Gelsinger, «Microprocessors for the new millennium: Challenges, opportunities, and new frontiers», in *2001 IEEE International Solid-State Circuits Conference. Digest of Technical Papers. ISSCC (Cat. No.01CH37177)*, San Francisco, CA, USA: IEEE, 2001, pp. 22–25. doi: 10.1109/ISSCC.2001.912412.
[41] M. Iorga, L. Feldman, R. Barton, M. J. Martin, N. Goren, e C. Mahmoudi, «Fog computing conceptual model», National Institute of Standards and Technology, Gaithersburg, MD, NIST SP 500-325, mar. 2018. doi: 10.6028/NIST.SP.500-325.
[42] F. Bonomi, R. Milito, J. Zhu, e S. Addepalli, «Fog computing and its role in the internet of things», in *Proceedings of the first edition of the MCC workshop on Mobile cloud computing*, Helsinki Finland: ACM, ago. 2012, pp. 13–16. doi: 10.1145/2342509.2342513.

[43] Agnivesh Kumar Agnihotri , Shashi Kant Gupta , Basant Tiwari, «Healthcare Technology Evolution And Adoption Of Fog Computing In Healthcare: Review, Issue And Challenges», *Journal of Pharmaceutical Negative Results*, pp. 1419–1428, gen. 2023, doi: 10.47750/pnr.2023.14.S02.172.

[44] I. A. Salah Abusohyon, G. Aiello, R. Inguanta, M. G. Bruno, M. Abu Sahyoun, e S. Quaranta, «A wearable biosensor for non-invasive real-time monitoring of Hydrogen peroxide in exhaled breath for worker's health in the construction industry», in *2023 3rd International Conference on Electrical, Computer, Communications and Mechatronics Engineering (ICECCME)*, Tenerife, Canary Islands, Spain: IEEE, lug. 2023, pp. 1–6. doi: 10.1109/ICECCME57830.2023.10253248.

[45] Y. Cao, P. Hou, D. Brown, J. Wang, e S. Chen, «Distributed Analytics and Edge Intelligence: Pervasive Health Monitoring at the Era of Fog Computing», in *Proceedings of the 2015 Workshop on Mobile Big Data*, Hangzhou China: ACM, giu. 2015, pp. 43–48. doi: 10.1145/2757384.2757398.

[46] G. Aiello, S. Quaranta, M. G. Bruno, G. Marcon, I. A. S. Abusohyon, e M. Venticinque, «A Fog Computing Monitoring System For Fused Visible And Infrared Imagery with an application to building preservation», in *2023 3rd International Conference on Electrical, Computer, Communications and Mechatronics Engineering (ICECCME)*, Tenerife, Canary Islands, Spain: IEEE, lug. 2023, pp. 1–5. doi: 10.1109/ICECCME57830.2023.10253385.

[47] W. Y. C. Wang e Y. Wang, «Analytics in the era of big data: The digital transformations and value creation in industrial marketing», *Industrial Marketing Management*, vol. 86, pp. 12–15, apr. 2020, doi: 10.1016/j.indmarman.2020.01.005.

[48] P. A. Hennelly, J. S. Srai, G. Graham, e S. Fosso Wamba, «Rethinking supply chains in the age of digitalization», *Production Planning & Control*, vol. 31, fasc. 2–3, pp. 93–95, feb. 2020, doi: 10.1080/09537287.2019.1631469.

[49] T. Stank, T. Esper, T. J. Goldsby, W. Zinn, e C. Autry, «Toward a Digitally Dominant Paradigm for twenty-first century supply chain scholarship», *IJPDLM*, vol. 49, fasc. 10, pp. 956–971, dic. 2019, doi: 10.1108/IJPDLM-03-2019-0076.

[50] D. Verma *et al.*, «Internet of things (IoT) in nano-integrated wearable biosensor devices for healthcare applications», *Biosensors and Bioelectronics: X*, vol. 11, p. 100153, set. 2022, doi: 10.1016/j.biosx.2022.100153.

[51] S. Nitin Prabhu, C. P. Gooneratne, K.-A. Hoang, e S. C. Mukhopadhyay, «IoT-Associated Impedimetric Biosensing for Point-of-Care Monitoring of Kidney Health», *IEEE Sensors J.*, vol. 21, fasc. 13, pp. 14320–14329, lug. 2021, doi: 10.1109/JSEN.2020.3011848.

[52] R. P. Aquino, S. Barile, A. Grasso, e M. Saviano, «Envisioning smart and sustainable healthcare: 3D Printing technologies for personalized medication», *Futures*, vol. 103, pp. 35–50, ott. 2018, doi: 10.1016/j.futures.2018.03.002.

[53] A. Bhattarai e D. Peng, «An Integrated Secure Efficient Computing Architecture for Embedded and Remote ECG Diagnosis», *SN COMPUT. SCI.*, vol. 4, fasc. 1, p. 45, nov. 2022, doi: 10.1007/s42979-022-01465-7.

[54] S. Mukherjee, S. Suleman, R. Pilloton, J. Narang, e K. Rani, «State of the Art in Smart Portable, Wearable, Ingestible and Implantable Devices for Health Status Monitoring and Disease Management», *Sensors*, vol. 22, fasc. 11, p. 4228, giu. 2022, doi: 10.3390/s22114228.

[55] K. Guk *et al.*, «Evolution of Wearable Devices with Real-Time Disease Monitoring for Personalized Healthcare», *Nanomaterials*, vol. 9, fasc. 6, p. 813, mag. 2019, doi: 10.3390/nano9060813.

[56] https://centralgaheart.com/implanting-a-difibrillator

[57] W. Jia *et al.*, «Electrochemical Tattoo Biosensors for Real-Time Noninvasive Lactate Monitoring in Human Perspiration», *Anal. Chem.*, vol. 85, fasc. 14, pp. 6553–6560, lug. 2013, doi: 10.1021/ac401573r.

[58] https://www.linkedin.com/pulse/wearable-bioelectronic-skin-patches-booming strong- growth-mrunal-b
[59] S. K. Vashist, «Non-invasive glucose monitoring technology in diabetes management: A review», *Analytica Chimica Acta*, vol. 750, pp. 16–27, ott. 2012, doi: 10.1016/j.aca.2012.03.043.
[60] R. K. Mishra *et al.*, «Wearable Flexible and Stretchable Glove Biosensor for On-Site Detection of Organophosphorus Chemical Threats», *ACS Sens.*, vol. 2, fasc. 4, pp. 553–561, apr. 2017, doi: 10.1021/acssensors.7b00051.
[61] M. Abbas, M. N. Ahmad, T. Hussain, e A. Mujahid, «Materials for Wearable Sensors», *Mater. Innov.*, vol. 2, fasc. 7, lug. 2022, doi: 10.54738/MI.2022.2702.
[62] D. Saber e K. Abd El-Aziz, «Advanced materials used in wearable health care devices and medical textiles in the battle against coronavirus (COVID-19): A review», *Journal of Industrial Textiles*, vol. 51, fasc. 1_suppl, pp. 246S-271S, giu. 2022, doi: 10.1177/15280837211041771.
[63] S. Fan *et al.*, «Silk materials for medical, electronic and optical applications», *Sci. China Technol. Sci.*, vol. 62, fasc. 6, pp. 903–918, giu. 2019, doi: 10.1007/s11431-018-9403-8.
[64] Q. Chen, Y. Liu, K. Gu, J. Yao, Z. Shao, e X. Chen, «Silk-Based Electrochemical Sensor for the Detection of Glucose in Sweat», *Biomacromolecules*, vol. 23, fasc. 9, pp. 3928–3935, set. 2022, doi: 10.1021/acs.biomac.2c00753.
[65] W. Zhang *et al.*, «Wearable biomolecule smart sensor based on Au@PB NPs with high electrochemical activity», *Journal of Alloys and Compounds*, vol. 891, p. 161983, gen. 2022, doi: 10.1016/j.jallcom.2021.161983.
[66] S. Chen, J. Qi, S. Fan, Z. Qiao, J. C. Yeo, e C. T. Lim, «Flexible Wearable Sensors for Cardiovascular Health Monitoring», *Adv Healthcare Materials*, vol. 10, fasc. 17, p. 2100116, set. 2021, doi: 10.1002/adhm.202100116.
[67] Z. Pu *et al.*, «A continuous glucose monitoring device by graphene modified electrochemical sensor in microfluidic system», *Biomicrofluidics*, vol. 10, fasc. 1, p. 011910, gen. 2016, doi: 10.1063/1.4942437.

2. Materials used in Electrochemical Sensors Fabrication

This chapter will discuss the materials used in the fabrication of the two electrochemical sensors developed in this thesis work. The first sensor was designed for integration into a face mask, enabling real-time detection of hydrogen peroxide in exhaled breath. It was fabricated using the silver metallic layer from compact discs, with a thin chitosan coating to improve surface wettability in the humid conditions of exhaled breath. Sensitivity to the low hydrogen peroxide concentrations typically found in exhaled air was enhanced by electrodepositing Prussian Blue Nanoparticles (PBNPs) on the WE.

The second electrochemical sensor presented in this work is a wearable device for monitoring uric acid, chloride, and glucose levels in sweat. It features three distinct gold-based working electrodes, each modified for a specific target analyte. Uric acid detection was achieved by co-depositing reduced Graphene Oxide and Gold Nanoparticles (rGO-AuNPs), chloride detection was enabled by electrodeposition of silver, and glucose detection was made possible through the electrodeposition of Nickel Nanoparticles (NiNPs). This chapter will provide a detailed overview of the materials that contribute to the functionality of these innovative sensors.

2.1 Silver-based Sensor Development from Recycled CDs and DVDs

2.1.1 Electronic Wastes: Challenges, Impacts and Solutions

Electronic waste (e-waste) is a big challenge due to the short life cycles of modern electronics. The issue of inadequate recycling systems plays a role in the problem of e-waste and worsens the pollution which is often produced in landfills. Stephan Sicars, Director of the Department of Environment at the UN Industrial

Development Organization, highlighted e-waste as "a serious threat to the environment and human health worldwide" [1].

According to a report issued by the United Nations in 2019 of the 7.3 kg of e-waste generated per year, only about 1.7 kg of e-waste is recyclable per year. In order to reach the desired recycling target by 2030, the present recycling system would need to increase by approximately tenfold. Although there are significant amounts of valuable materials in e-waste, such as iron, steel, copper, silver, and gold, only about 15-20% of this waste is recycled, with the remaining 80% not being collected due to high costs and poor or absence of adequate infrastructure all over the world. On the other hand, the waste generated from electronics including toxic materials such as mercury and lead which have been found in industrial processes and waste materials from landfills [2]. Fig. 2.1 illustrates global e-waste production from 2014 to 2030.

***Figure 2.1**: Global e-waste generation from 2014 to 2030* [3].

Most e-waste of today consists of outdated technologies, including Compact Discs (CDs), Digital Versatile Discs (DVDs), old televisions and computer monitors. Since 1999, 9.02 billion CDs have been shipped in the United States alone [4]. In 2021, CD sales accounted for 40.6 million music CDs but included 3,500 DVDs and 10.3 million video games [5]. The use of CDs within the

biomedical field is also evident by how medical images are exchanged between patients and providers, which means that the number of available CDs is much greater.

The lifecycle and recycling process of CDs is also a concern as polycarbonate can be decomposed to form the polycarbonate mono-glycerol bisphenol A (BPA), the compound responsible for toxicity. It is possible that over the years, the release of BPA in gradual amounts might have some adverse effects for both humans and nature. This emphasizes the importance of looking for solutions to address recycling and upcycling of the e-waste before they are fully processed, thus requiring them at the recycling level [6].

Biointegrated electronics provides possibilities to monitor pathophysiological alterations, overall state, and athletic performance in real-time, by tracking a wide array of biomarkers. Current microfabrication techniques for creating stretchable, active components typically rely on expensive and time-intensive printing or lithography-based methods. For example, evaporated gold, commonly used in microfabrication and thin-film production, is estimated to cost around $95 per gram for films approximately 125 nm thick. Additionally, the lead time for these processes can range from several hours to days, depending on the device's complexity. Moreover, these processes often require the use of volatile chemicals, such as chemical etchants, photoresists, and developers, which pose environmental risks. Although these advanced techniques have many advantages, they may not be ideal for rapid prototyping, experimental testing, or developing one-time-use sensors, especially in environments with limited resources [7].

There is a growing demand for disposable sensors that provide reliable, accessible, and fast measurements without the need for recalibration or concerns about contamination. This demand is particularly evident in medical diagnostics, where point-of-care sensors are being developed to replace central laboratories in resource-limited or time-sensitive situations. Additionally, there is a pressing need to simplify and reduce the cost of fabricating stretchable electronic prototype

devices, which would broaden manufacturing capabilities and lower the skill level required for fabrication [5].

2.1.2 Cost-Effective and Disposable Electrochemical Sensors from CDs and DVDs

CDs and DVDs are widely available at low cost and can be easily sourced from recycled materials. Although the exact composition varies among manufacturers, they typically consist of several layers (Fig. 2.2): a base polycarbonate layer, a dye layer for data storage, and a metal reflective layer ranging from 40 to 100 nm in thickness. The metal layer is designed to reflect laser light back to the detector during the reading and writing processes. The surface of the discs features concentric tracks approximately 0.4 mm wide and 0.1 mm deep, separated by 1.3 mm, which guide the laser [8]. For most discs, the metal layer is usually composed of aluminum, although silver (Ag) or gold (Au) are also commonly used. This metal layer presents several attractive possibilities for electrochemical analysis. Aluminum, however, has poor electroanalytical properties and is rarely used as an electrode material because it oxidizes quickly, leading to poor conductivity. In contrast, both silver and gold are well-known for their excellent electrochemical properties in various applications. Despite this, their relatively high cost and the extensive cleaning required for their use have limited their widespread adoption [9].

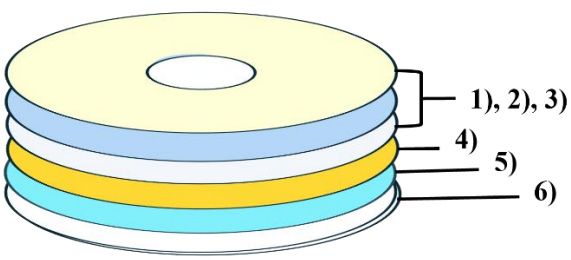

Figure 2.2*: Structure of a CD: 1), 2) and 3) protective polymer layers; 4) reflective gold layer; 5) phtalocyanine layer; 6) polycarbonate support* [10].

Angnes et al. [11] demonstrated the feasibility of fabricating gold electrodes from CDs, offering a simple and cost-effective alternative method for electrode production. The silver or gold layer can be exposed either by mechanically delaminating the disc or by removing the upper polymer layers using a solvent like nitric acid. A single disc can be used to create multiple electrodes at minimal cost, customizable to various geometries and configurations. Due to their low cost, these discs can be used as disposable, single-use devices if needed. Angnes et al. [11] were the first to demonstrate the fabrication of Au electrodes from compact discs, pioneering a technique that has since become the most widely reported method in this field. Their process involved slicing the disc into segments. They then applied concentrated nitric acid to dissolve the upper protective polymer layers, revealing the gold layer beneath. This step reportedly took only a few minutes, and any remaining polymer residue was easily washed away with a water jet. Once exposed, the gold layer could be utilized as the working electrode. Alternative methods have also been reported including the mechanical delamination of the disc. Honeychurch [12] developed an electrochemical sensor based on the Ag layer of a CD for the lead detection on spiked and unspiked roof drainage water. Sections of the CD can be cut out with a suitable pair of scissors, and in this case, the upper Ag layer was then removed by slowly peeling it away from the lower polycarbonate substrate. The use of conventional Ag and Au electrodes has often been limited by their high cost and the tendency for electrode fouling, which necessitates thorough cleaning and lengthy preparation steps. However, fabricating Ag and Au electrodes from CDs and DVDs addresses many of these challenges. Due to their low cost and wide availability, these materials can be treated as disposable, enabling single-use applications that eliminate concerns about fouling and cross-contamination [5].

2.1.3 Electrochemical Detection of Hydrogen Peroxide Using Ag Electrodes from CDs and DVDs

In recent years, several studies have employed electrochemically roughened Ag CD-based electrodes for the electrocatalytic detection of hydrogen peroxide. More recently, Shafei and Honeychurch [13] utilized an unmodified Ag electrode, fabricated from a DVD-R, for determining hydrogen peroxide levels in water. They simply mechanically delaminated a Verbatim DVD-R, using the exposed Ag layer as the working electrode without further modification. Lian et al. [14] roughened Ag layer of a CD by electrochemical oxidation-reduction cycles in a KCl solution for quantitative determination of hydrogen peroxide. Maynard and Honeychurch [15] explored the use of Ag electrodes made from recycled Recordable Compact Discs (CD-R) for the amperometric detection of hydrogen peroxide. The analytical response showed linearity up to at least 30 mM of hydrogen peroxide, with a sensitivity of 21.89 μA/mM in this range. A detection limit of 17.7 μM was achieved, based on a signal-to-noise ratio of three. The sensor design offers a straightforward, cost-effective, and reliable approach for detecting hydrogen peroxide, eliminating the need for lengthy, multi-step fabrication processes by using recycled materials. Wen et al. [16] have successfully developed a highly catalytic H_2O_2 sensor utilizing silver dendritic nanostructures and silver nanoparticles, formed on the surface of a DVD substrate via a simple electrochemical multi-potential step-scan method. The resulting sensor demonstrates a rapid amperometric response to H_2O_2 reduction, with a low detection limit and a broad linear detection range.

2.2 Humidity Sensing: The Role of Biopolymers and Paper-Based Materials

Humidity sensors have a wide range of applications. In the medical field, these sensors play a critical role in respiratory equipment, sterilizers, incubators, and

pharmaceutical processing. In agriculture, they are used in greenhouse climate control, protecting plantations from dew, monitoring soil moisture, and storing cereals. Within the general industry, humidity sensors are employed for controlling humidity in chemical gas purification, dryers, ovens, film drying, paper and textile production, and food processing [17]. The challenges posed by the lack of liquid electrolytes can be addressed by utilizing absorbent materials capable of capturing moisture, such as biopolymers and paper. Natural biopolymers, sourced from renewable materials, are increasingly favored for producing soft materials like membranes, hydrogels, and aerogels, owing to their sustainability, non-toxicity, biocompatibility, and biodegradability. Their solubility in water or water-based solvents further enhances the development of biopolymer-based conductive hydrogels, which are essential for creating non-toxic wearable sensors that offer excellent biocompatibility. These natural biopolymers are extracted from renewable sources, including plants, arthropod shells, and silkworm cocoons, using bioprocessing and chemical modification techniques. Biopolymers, including proteins like silk and gelatin, as well as polysaccharides such as cellulose, sodium alginate, chitin, and chitosan, have drawn considerable scientific interest for their natural advantages: they are low-cost, biodegradable, antimicrobial, and renewable. Beyond these biological benefits, natural biopolymers possess structural characteristics that make them ideal for developing high-performance conductive hydrogels [18]. Their abundant functional groups, such as hydroxyl, carboxyl, amino, and amine, enhance their hydrophilicity, which is essential for effective hydrogel formation. The high reactivity of these groups also enables modifications to tailor the mechanical properties, electron transfer capabilities, solubility, and crystal structure of the biopolymers. For instance, chitosan can be modified with positively charged groups through quaternary ammonium modification, enhancing its solubility and improving the conductivity and mechanical properties of the resulting materials

through electrostatic interactions. These characteristics highlight the potential of natural biopolymers in designing conductive hydrogels for wearable sensors [19]. A hydrogel is a gel consisting of polymer network chains and a substantial amount of water molecules, forming a three-dimensional network structure. These materials are highly hydrophilic, allowing them to swell rapidly in water and retain a large volume of it without dissolving. The water absorption capability of hydrogels is due to the hydrophilic functional groups on the polymer backbone, while the crosslinking between the polymer network chains (Fig. 2.3) prevents them from dissolving. As a result, hydrogels exhibit permeability to chemical and biological molecules and are transparent to light and sound waves, properties associated with their high-water content. Additionally, the crosslinked polymer network provides hydrogels with flexibility and stretchability, making them behave similarly to elastic solids [20].

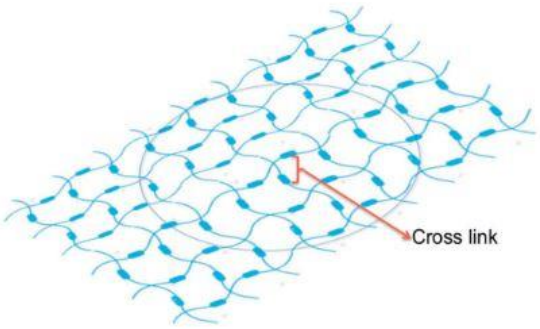

***Figure 2.3**: Structure of hydrogel* [21].

Since Wichterle and Lim first synthesized hydrogel in 1954, these materials have found widespread use across various fields, including food preparation, bioengineering, agriculture, healthcare, and biosensors. Hydrogels can be tailored to meet specific application requirements by functionalizing them to achieve desired properties and structures. This makes them particularly well-suited for the complex demands of flexible and wearable sensors. Their deformability allows them to conform closely to curved surfaces, such as human skin, and

accommodate body movements without sustaining mechanical damage [22]. Practical applications of hydrogel-based vapor sensors have been reported, including smart masks, electronic skin, respiratory analysis, and wireless monitoring, showcasing their potential in environmental monitoring, medical health, and other fields. By attaching hydrogel vapor sensors to human skin or incorporating them into clothing and accessories, it becomes possible to monitor personal health and safety effortlessly, without the need for additional equipment. For example, flexible, stretchable, and wearable vapor sensors made from hydrogel can detect the content and concentration of gases in inhaled and exhaled air by continuously monitoring ambient air or exhaled breath at room temperature, thus enabling real-time personal health and safety monitoring [23]. Gao et al. [24] developed an ultra-thin organohydrogel film (CGGN) with a thickness of just 0.1 mm, designed specifically for humidity sensing applications. This sensor is highly effective in detecting relative humidity levels ranging from 20% to 90%. Thanks to its high sensitivity to humidity changes, the sensor enables rapid, stable, and continuous monitoring of human respiration, with reproducible results. As previously mentioned, in addition to biopolymers, another material used as a flexible substrate for humidity sensors is paper. Paper is a three-dimensional sheet composed of interconnected cellulose fibers, bonded together through hydrogen bonds between hydroxyl groups. It is produced from plant-based raw materials that contain fibers, which undergo processes such as pulping, blending, and finishing. These processes enable the paper to be folded and cut as needed. Cellulose fibers found in paper are exceptionally fine, measuring less than a micron in diameter while extending several millimeters in length. The types of paper most commonly used in humidity sensor development include filter paper and nitrocellulose paper. Filter paper, made entirely of pure cellulose, exhibits several key properties such as wet strength, porosity, particle retention, volume flow, compatibility, efficiency, and capacity. It is available in 13 grades, each categorized by pore size. Nitrocellulose paper, in contrast, is created by treating

standard cellulose with a mixture of sulfuric and nitric acids, which replaces hydroxyl (-OH) groups with nitrate ($-NO_3$) groups in the cellulose structure. This chemical alteration leads to a nitrocellulose surface that is more uniform and smoother, featuring fewer and narrower pores compared to chromatographic cellulose paper [25]. In their research, Fiore et al. [26] developed a filter paper-based screen-printed electrode incorporating a carbon black-Prussian Blue nanocomposite to detect nebulized hydrogen peroxide, which aids in customizing disinfection processes.

2.2.1 Chitosan: Synthesis, Properties and Applications

For the development of the electrochemical sensor for detecting hydrogen peroxide in exhaled breath, chitosan was chosen as the absorbent material. Chitosan is a cationic polysaccharide and is considered one of the most promising natural biopolymers for applications in the biomedical field. The key characteristics of chitosan can be broadly outlined as follows: it is biodegradable, biocompatible, and bio-functional. Additionally, it has the capacity to immobilize proteins, nucleic acids, and virus particles, promotes enhanced cellular attachment, possesses inherent antibacterial properties, accelerates wound healing, offers chemical resistance, provides effective corrosion protection when used as a coating, demonstrates relative thermal stability, forms films easily, exhibits convenient mechanical properties, and is cost-effective. Chitosan is a naturally occurring linear polysaccharide, also referred to as deacetylated chitin $(C_8H_{13}O_{5N})_n$. Chitin was first identified by the French scientist Henri Braconnot in 1811. Later, in 1859, French professor C. Rouget successfully synthesized chitosan by deacetylating chitin through boiling it in a concentrated potassium hydroxide solution [27]. Chitin is the second most abundantly produced polysaccharide in the environment, following cellulose. It is widely distributed among living organisms, both plants and animals, making it a crucial renewable resource. Chitin occurs as structured crystalline microfibrils, forming structural

components in the exoskeletons of arthropods and crustaceans and the cell walls of fungi and yeast. However, despite chitin having a range of beneficial properties that would make it well-suited for different applications, it presents a major drawback: its insolubility in water and in most common solvents, which can limit its applications in certain fields. Chitin derivatives are typically obtained through alkaline deacetylation; among these derivatives, chitosan is the most widely utilized [28]. Chitosan retains the same characteristics as chitin in terms of non-toxicity, biocompatibility, and biodegradability, but it has greater solubility in diluted acids such as acetic acid, formic acid, and lactic acid, making it easier to use. The deacetylation of chitin to produce chitosan occurs in sodium or potassium hydroxide at temperatures of at least 100°C to remove some or all of the acetyl groups from the polymer (Fig. 2.4). The characteristics of the chitosan produced are influenced by the reaction conditions, which need to be as consistent as possible throughout the process. Factors such as temperature, reaction duration, previous treatment of the chitin, and its density all play significant roles. Consequently, the properties of the resulting chitosan can differ based on the original source and the method of preparation; for instance, the molecular weight can range from 300 to over 1000 kDalton, with a degree of deacetylation varying between 30% and 95% [29]. Chitosan is distinguished by its highly reactive amino and hydroxyl groups, which make it an important material for various research applications. The amino groups create a hydrophilic environment for biomolecules and increase solubility in various acids, enabling interaction with polyanions to form complexes and gels through chemical modification. Chitosan's protonatable amino groups enable it to function as a cationic polyelectrolyte. Its eco-friendly characteristics, combined with its capacity for absorption, outstanding film-forming properties, enhanced permeability, mechanical strength, biocompatibility, easy availability and high thermal stability, make chitosan a popular choice for immobilization. Solutions of chitosan are utilized in preparation of a variety of materials, including films, gels, sponges, fibers, and

particles. The presence of hydrogen-bond networks in the solid state is a significant property that enhances fiber and film-forming capabilities, making it suitable for novel applications [30].

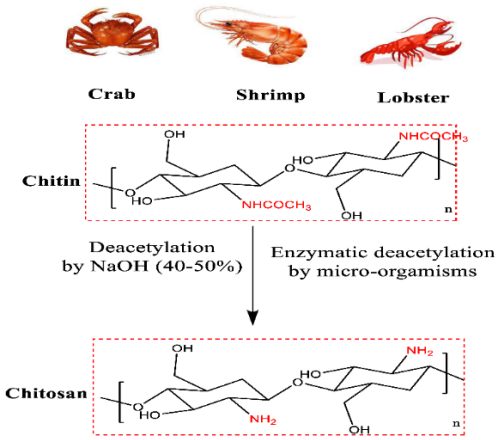

***Figure 2.4**: Chemical structure and some sources of chitin and chitosan* [31].

Therefore, chitosan has numerous properties that make it of particular interest in various fields of application. Kumari et al. [32] have shown that chitosan exhibits excellent humidity-sensing properties, primarily due to its numerous repeating hydrophilic functional groups, such as amines and hydroxyls, which can form hydrogen bonds with water molecules in the environment. Because hydrogen bonds are weak, they facilitate the reversible adsorption and desorption of water molecules on the surface of the chitosan film, depending on the atmospheric relative humidity. A humidity sensor based on a chitosan film was fabricated by depositing it onto a Ti/Au electrode-coated SiO_2 substrate. The sensor demonstrated rapid response and recovery times, low hysteresis, excellent reversibility, a wide detection range (11−95% RH), and high selectivity for water vapor. When it was tested with various human breathing patterns, the sensor effectively distinguished differences in the rate and depth of respiration, including normal, fast, deep, and nasal breathing, as well as detecting apnea-like events. Additionally, the sensor was successfully used for non-contact skin humidity

sensing. Overall, this chitosan film humidity sensor presents a promising solution for the noninvasive detection of respiratory disorders and other health issues through monitoring skin moisture. Teepoo et al. [33] developed an electrochemical sensor based on chitosan-gelatin nanofibers for the detection of hydrogen peroxide. Additionally, there are other advantages, such as simple electrode preparation, long-term stability, and good repeatability compared to previous works. Gao et al. [34] developed an electrochemical sensor for the detection of hydrogen peroxide based on silver nanowires and chitosan films. This sensor exhibited good electrocatalytic activity toward the reduction of H_2O_2. Additionally, this sensor demonstrated acceptable selectivity for the detection of H_2O_2, satisfactory reproducibility, and good long-term stability.

2.3 Electrode modified with Prussian Blue for Hydrogen Peroxide Detection in Exhaled Breath

To enhance the sensitivity of the first electrochemical sensor designed for detecting hydrogen peroxide in exhaled breath, various nanoparticles were applied to the working electrode. The optimal performance was obtained through the electrodeposition of Prussian Blue Nanoparticles (PBNPs), which enabled the detection of the low concentrations of hydrogen peroxide commonly found in exhaled breath.

2.3.1 Prussian Blue: Structure and Properties from Soluble to Insoluble Forms

Prussian Blue (PB) is an inorganic compound frequently employed to modify electrodes in electrochemical sensors due to its remarkable electrocatalytic activity, especially for hydrogen peroxide reduction. The initial synthesis of PB dates back to 1706 in Berlin, which was then the capital of the Kingdom of Prussia. Historically, it served as a pigment for painters and a dye for textiles,

drawing interest for its unique properties; notably, despite containing cyanide groups, the pigment is non-toxic to humans. Since Jöns Jakob Berzelius's work in 1820, two forms of Prussian Blue have been identified: soluble and insoluble. However, it is now understood that both forms are generally insoluble in water and most common solvents. The primary distinction lies in the fact that soluble Prussian Blue forms a stable, blue colloidal suspension in water, resembling a blue solution, while insoluble Prussian Blue tends to settle at the bottom. Further analytical investigations have identified different compositions for the soluble and insoluble varieties of Prussian Blue. Soluble Prussian blue is identified as $AFe^{III}[Fe^{II}(CN)_6]\cdot xH_2O$, where $x = 1–5$ and "A" is a monovalent cation, such as K^+,Na^+ or NH_4^+. In contrast, the composition of insoluble Prussian blue is determined to be $Fe^{III}_4[Fe^{II}(CN)_6]_3\cdot xH_2O$, where x = 14-16. Commonly, if potassium is detected, the compound is considered soluble Prussian blue, while the absence of potassium typically indicates the insoluble form, often without further detailed chemical analysis. Despite their similar names, the distinct characteristics of these two forms justify the continued differentiation between so-called soluble and insoluble Prussian blue [35]. In 1936, James F. Keggin and Frank D. Miles [36] were the first to describe the cubic lattice structure of Prussian blue (Fig. 2.5): "The iron atoms are arranged, ferrous and ferric alternately, at the corners of a cubic lattice with a 5.1 Å edge, and the CN groups lie along the edges of these small cubes. The alkali atoms are situated at the centers of alternate small cubes". They proposed that the additional Fe^{3+} in insoluble Prussian blue occupies the interstitial sites that are otherwise filled by alkali metal cations in soluble Prussian blue.

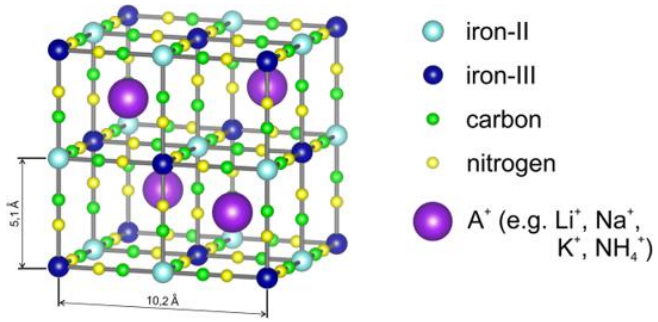

Figure 2.5*: Structure of Prussian blue according to the Keggin and Miles model from 1936 (soluble Prussian blue)* [35].

Today, the precise formulation, composition, and structure of Prussian blue, or ferric ferrocyanide, are typically described using a model developed by Andreas Ludi and his research group at the University of Bern. In the 20th century, Ludi et al. [37] were pioneers in producing larger crystals of insoluble Prussian blue, with edge lengths ranging from 0.05 to 0.1 mm. They achieved this by dissolving $Fe^{2+}(CN)_6^{4-}$ (ferrocyanide or hexacyanoferrate(II)) and Fe^{3+} or Fe^{2+} in concentrated hydrochloric acid (10 mol/L), in which Prussian blue is soluble. Prussian blue was then slowly precipitated from this yellow solution through the gradual diffusion of water, which dilutes the hydrochloric acid. These conditions are extreme, characterized by the absence of potassium or other alkali metal cations and high concentrations of protons and chloride anions. Their structural investigations revealed that the ratio of Fe^{3+} to $Fe^{2+}(CN)_6^{4-}$ in the cubic lattice of Prussian blue is 4:3. This ratio is explained by the presence of vacancies where $Fe^{2+}(CN)_6^{4-}$ is missing, with these vacant sites being randomly distributed. While all Fe^{3+} sites are occupied, only 75% of the $Fe^{2+}(CN)_6^{4-}$ sites are filled. Water molecules are located both in the zeolitic cavities and at the positions of missing ferrocyanide units. In summary, soluble Prussian Blue contains potassium ions (K^+) that can dissociate in aqueous environments, leading to a net negative charge on the crystal surface. This ionization allows for the stable dispersion of the crystals, provided they are sufficiently small. In contrast, insoluble PB (Fig. 2.6) differs from the soluble variant in that excess Fe^{3+} ions replace potassium ions in

the interstitial sites of the lattice. It exhibits defects due to the presence of interstitial water molecules, which can be categorized into two types: those coordinated to Fe(II) sites (coordinative water) and those located within cavities that do not coordinate to metal sites (zeolitic water). In soluble PB, alkali metal ions replace these water molecules within the cavities to balance the overall charge [38].

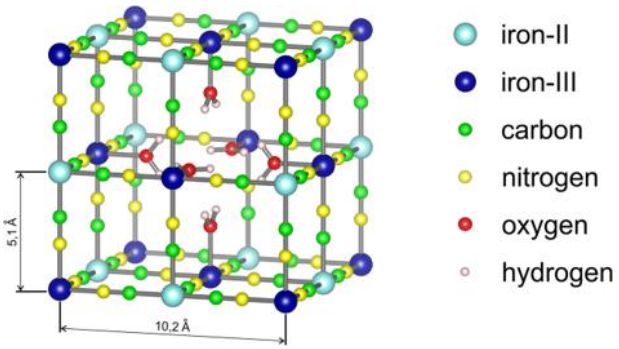

***Figure 2.6**: Structure of (insoluble) Prussian blue according to Ludi and coworkers from 1977 [35].*

While the Ludi formula for Prussian Blue has been widely accepted by most scientists in the field, some experts have always remained skeptical. In 1996, Fritz Scholz and his colleagues [39] suggested that the crystal structure determined for Prussian Blue grown in hydrochloric acid might be just one of several possible structures. They proposed that the defect structure observed in this case could be due to the absence of stabilizing potassium ions. When Prussian Blue is synthesized from solutions containing potassium ions, they hypothesized that it may adopt a structure with fewer missing hexacyanoferrate ions and a more perfect lattice, with potassium ions providing charge compensation. However, due to Prussian Blue's extremely low solubility, the synthesis may never yield a completely perfect structure, and the number of defects is likely dependent on the availability of stabilizing cations.

2.3.2 Prussian Blue Nanoparticles: Synthesis, Activation and Stabilization for Electrochemical Applications

Prussian Blue nanoparticles are increasingly synthesized through various methods for different applications, particularly in biomedical fields, due to their biocompatibility, biodegradability, customizable size and shape, low production costs, and ease of synthesis processes. Prussian Blue is typically synthesized by chemically mixing either Fe^{3+} with $Fe(II)(CN)_6^{4-}$ or Fe^{2+} with $Fe(III)(CN)_6^{3-}$, resulting in the formation of a dark blue colloid. The intense blue color arises from charge transfer between iron (II) at a carbon site and iron (III) at a nitrogen site [40].

As an alternative approach, Neff [41] reported in 1978 the successful deposition of a thin layer of PB onto platinum foil, using electrochemical methods. Electrochemical deposition is now widely used due to its simplicity and effectiveness, particularly in the development of electrochemical sensors and biosensors. Among the various methods available, the potentiostatic approach and potential cycling in a solution of ferricyanide and ferric chloride are the most commonly used techniques for modifying electrochemical sensors with Prussian Blue. It is crucial to ensure that the pH of the growing solution is sufficiently acidic to prevent the hydrolysis of ferric ions. If the pH is too high, hydroxyl ions may replace cyanide bridges by occupying the valence positions of iron atoms. This substitution can severely compromise the regularity and stability of the resulting inorganic film, leading to a less effective or even unstable Prussian Blue structure. Thus, the two precursors are generally mixed in a 0.1M HCl/KCl solution [42]. After deposition, PB-modified electrodes can be cycled in an acidic solution containing potassium ions, a process known as activation. During this stage, a conversion between the insoluble (potassium-free) and soluble (potassium-containing) forms of PB occurs. This activation process disrupts the structure, resulting in the loss of about one-quarter of the high-spin Fe^{3+}, with potassium ions occupying the interstitial sites in the structure of the soluble PB

film. So, the term "solubility" here refers to the ease with which Fe^{3+} ions are exchanged by potassium ions. Clear evidence of these changes is observed when the Prussian White (PW)/Prussian Blue (PB) peak pair becomes slightly narrower and sharper, indicating a successful structural conversion and improved electrochemical properties. After 30–50 cycles, the voltammogram stabilizes, confirming that the film activation has been completed. To further stabilize the PB layer, a heating step at 100 °C for 1 to 1.5 hours can be applied [43].

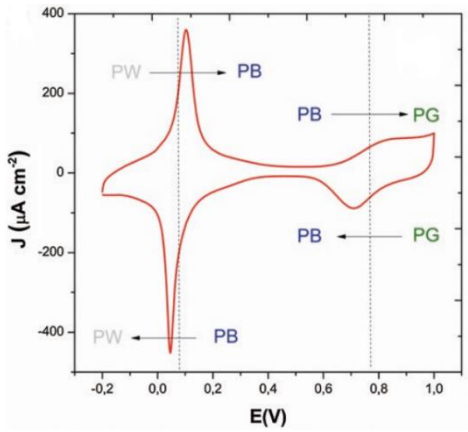

***Figure 2.7**: Cyclic voltammogram recorded at a scan rate of 0.1 V/s in a solution of 3 mM HCl and 0.1 M KCl for a Prussian Blue-modified electrode reveals the interconversion between the various oxidation states of PB* [43].

Fig. 2.7 shows the characteristic peaks associated with the different oxidation and reduction processes of the PB film. The first peak pair in the cyclic voltammogram corresponds to the interconversion between Prussian White (PW) and Prussian Blue (PB), while the second peak pair represents the conversion between PB and Prussian Green (PG).

The reduction and oxidation reactions are facilitated by the free diffusion of cationic and anionic species, which are accompanied by noticeable color changes. The electron-transfer reactions, when potassium chloride is used as the supporting electrolyte, can be represented as follows:

$$Fe(III)_4(Fe(II)(CN)_6)_3 + 4e^- + 4K^+ \rightarrow K_4Fe(II)_4(Fe(II)(CN)_6)_3 \quad (2.1)$$

(PB to PW conversion)

$$Fe(III)_4(Fe(II)(CN)_6)_3 + 3Cl^- \rightarrow Fe(III)_4(Fe(III)(CN)_6)_3Cl_3 + 3e^- \quad (2.2)$$

(PB to PG conversion)

corresponding to peak pairs at 0.1 V and 0.9 V versus SCE, respectively [44].

The only disadvantage of the Prussian blue-based sensing layers is their instability, particularly in neutral and alkaline solutions. The instability arises due to the strong interaction between ferric ions and hydroxide ions at pH levels above 6.4, which leads to the formation of $Fe(OH)_3$. This reaction destroys the Fe–CN–Fe bond, ultimately resulting in the dissolution of PB [45]. To address this issue, several strategies have been developed:

1. *Application of protective polymer films*: coating the PB with external polymer layers such as poly(o-phenylenediamine), poly(o-aminophenol), poly(vinylpyrrolidone), and Nafion to shield it from destabilizing conditions [46].
2. *Use of additives in the working solution*: incorporating substances like tetrabutylammonium toluene 4-sulfonate to enhance the stability of PB in the working environment [47].

2.3.3 Catalytic Performance of Prussian Blue in Electrochemical Sensing of Hydrogen Peroxide

The most traditional application of PB-based electrochemical sensors is for monitoring hydrogen peroxide. In 1984, Itaya et al. [48] demonstrated that the reduced form of Prussian Blue, known as Prussian White, exhibits a catalytic effect in the reduction of oxygen (O_2) and hydrogen peroxide (H_2O_2). They discovered that hydrogen peroxide could diffuse into the zeolite-like structure of Prussian Blue (PB) and undergo electrochemical catalysis by either high-spin Fe^{3+} ions or low-spin Fe^{2+} ions. Based on their findings, they concluded that the Prussian Green (PG) form of PB was responsible for the oxidation of H_2O_2 at higher potentials (around +0.8 V), while the Prussian White (PW) form facilitated

the reduction of H_2O_2 at lower potentials (around +0.1 V). Although this dual catalytic behavior of PB allows for the detection of H_2O_2 at two distinct potentials, for oxidase-based biosensor applications, the reduction of H_2O_2 at lower operational potentials (Fig. 2.8) is generally preferred (Eq. 2.3-2.4). This preference is due to the enhanced selectivity it offers, minimizing interference from endogenous species commonly present in physiological environments [43].

$$(PW)\ K_4Fe_4(II)[Fe(II)(CN)_6]_3 + 2H_2O_2 \rightarrow (PB)\ Fe_4(III)[Fe(II)(CN]_6 + 4OH^- + 4K^+ \quad (2.3)$$

$$H_2O_2 + 2e^- \rightarrow 2OH^- \quad (2.4)$$

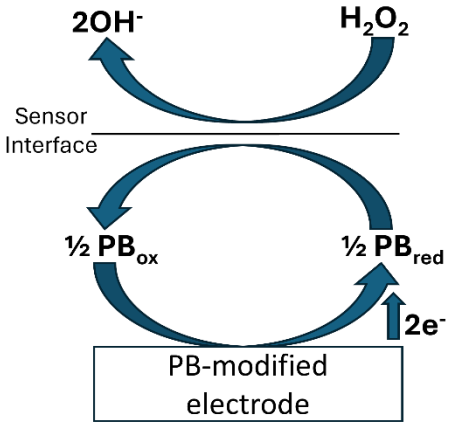

***Figure 2.8**: Mechanism of PB-mediated catalytic reduction of H_2O_2.*

Karyakin [42] conducted a comparison of the catalytic activity of Prussian Blue (PB) in the reduction of hydrogen peroxide with that of platinum, which is conventionally used in commercial first-generation biosensors. The study highlighted PB's superior performance in catalyzing the reduction of H_2O_2: the catalytic activity of Prussian Blue is approximately three orders of magnitude higher than that of platinum. This is demonstrated in Tab. 2.1, where the selectivity is represented by the ratio of cathodic currents for similar concentrations of two oxidants: hydrogen peroxide and oxygen.

***Table 2.1**: Electrocatalytic properties in H_2O_2 reduction in a neutral environment (pH 6-7) – 0.05 M phosphate buffer and 0.1 M KCl* [42].

Electrocatalyst	**Selectivity** $\frac{j_{H_2O_2}}{j_{O_2}}$	**Electrochemical rate constant / cm s^{-1}**
Pt	0.1	4×10^{-6}
Prussian Blue	400-600	1×10^{-2}

As shown, the reduction current of H_2O_2 on platinum electrodes is about 10 times lower than that of oxygen reduction. This significant difference makes it nearly impossible to detect H_2O_2 by reduction in the presence of oxygen when using platinum electrodes. Consequently, the only feasible detection method on platinum is the oxidation of H_2O_2 at relatively high anodic potentials. However, this approach introduces complications due to the generation of parasitic signals, which result from the oxidation of various easily oxidizable compounds. This limitation emphasizes the superiority of Prussian Blue for selective H_2O_2 detection, particularly in environments where oxygen is present. In the potential range optimal for sensor operation (around 0.00 V vs. Ag|AgCl), the reduction current of hydrogen peroxide on Prussian blue-modified electrodes is 400–600 times higher than that of oxygen reduction. The selectivity values obtained, ranging from 400 to 600 (as shown in Tab. 2.1), are also three orders of magnitude greater than those of conventionally used platinum. Because of this high catalytic activity and selectivity, which are comparable to biocatalysis, Prussian blue has been termed an artificial enzyme.

Consequently, PB and PB-based composites have been extensively researched and commonly utilized in the construction of sensors for hydrogen peroxide detection. O'Halloran et al. [46] incorporated PB microparticles into carbon ink, while Mattos et al. [49] modified Au and Pt screen-printed electrodes with electrochemically deposited PB. Ricci et al. [45] enhanced the graphite ink-based

screen-printed electrode surfaces within situ chemically synthesized PB, resulting in improved sensor lifespan and pH stability.

Taking advantage of the recent developments in nanotechnology, PB-based H_2O_2 sensors have been further enhanced with the incorporation of nanomaterials. For example, Li et al. [50] developed an amperometric biosensor by grafting PB nanoparticles onto a polymeric matrix composed of multiwalled carbon nanotubes (MWCNTs) and poly(4-vinylpyridine) (PVP). The MWCNT/PVP/PB composite films were created by casting MWCNTs wrapped with PVP onto gold electrodes, followed by electrochemical deposition of PB. This modified electrode exhibited significantly increased sensitivity of 1.3 $\mu A\ \mu M^{-1}\ cm^{-2}$ and a detection limit of 25 nM, attributed to the synergistic effects of MWCNTs and PB. Further, Du et al. [51] fabricated a porous PB–MWCNT film via electrochemical co-deposition, which demonstrated a higher response current to H_2O_2 reduction, achieving a sensitivity of 856 $\mu A\ mM^{-1}\ cm^{-2}$ and a detection limit of 23 nM.

2.4 Electrode modified with reduced Graphene Oxide and Gold Nanoparticles for Uric Acid Detection in Sweat

As mentioned previously, the second electrochemical sensor developed in this thesis consists of a chip with three gold working electrodes, each modified according to the analyte to be detected. One of these electrodes was modified through the electrodeposition of reduced Graphene Oxide and gold nanoparticles (rGO-AuNPs) to detect uric acid in sweat.

2.4.1 Advances in Graphene and Graphene Oxide: Structural Models, Synthesis Methods and Nanocomposite Applications

Graphene, a two-dimensional carbon sheet with sp^2 hybridization, has gained significant attention recently due to its exceptional electrical, optical, and mechanical properties, along with its potential applications in various fields such

as electronics, supercapacitors, sensors, and composite materials. Graphene oxide (GO) represents the oxidized form of graphene (Fig. 2.9) and is recognized as a crucial precursor for the large-scale production of graphene. This concept has its origins in the early work of Sir Brodie, an English chemist who first described the oxidation of graphite centuries ago [52]. Graphene's structure consists of sp^2 hybridized carbon atoms arranged in a honeycomb lattice, endowing it with a large surface area and exceptional mechanical, electrical, and thermal properties.

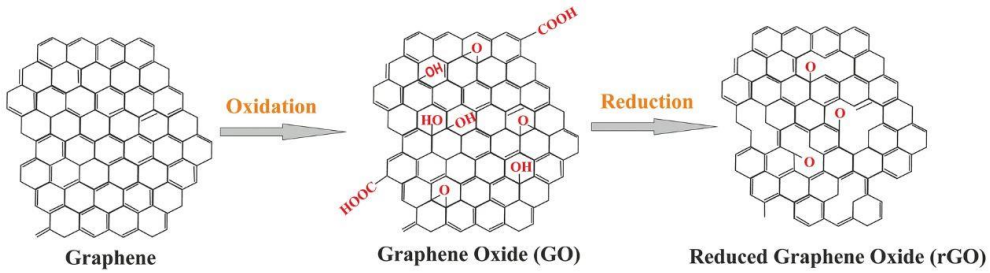

***Figure 2.9**: Conversion of Graphene to Graphene Oxide and Reduced Graphene Oxide* [53].

Despite these impressive characteristics, single-layer graphene faces limitations in practical applications due to challenges in creating well-ordered, large-scale structures. In contrast, GO has seen significant progress in both research and industrial applications over recent decades. GO is a non-stoichiometric compound consisting of carbon, oxygen, and hydrogen in varying proportions, which depend heavily on the specific processing methods employed [54] . The chemical exfoliation process introduces numerous oxygen-containing functional groups into the graphene structure, including epoxides, carbonyls (C=O), hydroxyls (-OH), phenols, and occasionally organosulfate groups. These functional groups disrupt the otherwise stable graphene lattice, leading to various defects such as vacancies and holes. These defects are randomly distributed across GO's hexagonal lattice, resulting in a material with unique properties and a broad range of potential applications. The defect-rich nature of GO enhances its versatility and scalability, enabling its use in a variety of applications, including graphene-like

materials, functionalized polymer composites, sensors, photovoltaic devices, membranes, and purification systems. However, the precise structure of GO remains a subject of ongoing debate, with numerous models proposed in the literature [55] (Fig. 2.10).

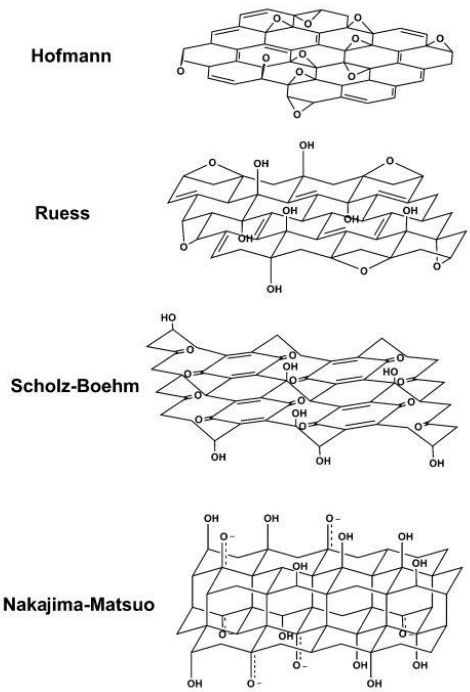

Figure 2.10*: Summary of several older structural models of GO* [56].

The Lerf-Klinowski (L-K) model (Fig. 2.11) is widely accepted, particularly for moderately oxidized GO samples [54]. Lerf and Klinowski have characterized GO using ^{13}C and ^{1}H nuclear magnetic resonance (NMR) spectroscopy. They identified signals corresponding to epoxide groups and aromatic structures and depicted GO with a nearly flat carbon lattice with regions of unoxidized aromatic rings and areas with aliphatic six-membered rings.

In recent years, Liu et al. [57] confirmed aspects of earlier models, particularly the L-K model, by providing experimental evidence of oxygen bonding within GO. From 1939 to 2018, the L-K model has remained the most widely accepted framework due to its broad applicability and ability to incorporate new findings.

Successive models like the Rourke-Wilson and Dimiev-Alemany-Tour have built upon this foundation, advancing the understanding of GO's structure. Despite the evolution of these models, the distinctive two-dimensional structure of GO has consistently been recognized as its key characteristic, laying the groundwork for extensive research.

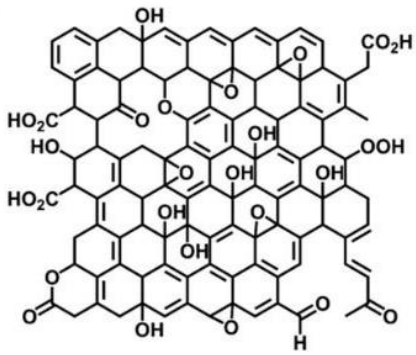

***Figure 2.11**: Structural model of graphene oxide (GO) proposed by Lerf-Klinowski (L-K model)* [58].

However, one of the major challenges in the practical use of graphene is its tendency to irreversibly agglomerate, which significantly diminishes its effectiveness. To address this issue, the introduction of metal nanoparticles was initially suggested to help separate graphene sheets. Incorporating metal nanoparticles onto graphene sheets effectively prevents agglomeration and offers a viable method for creating new catalytic materials. Traditionally, graphene-metal nanocomposites were made through chemical or thermal reduction processes, which required mixing graphene with metallic precursors. These methods often involved toxic chemicals, such as hydrazine hydrate, and required high temperatures, making them complex and time-consuming [59]. Recently, electrochemical reduction of graphene oxide has emerged as a promising method for synthesizing graphene films due to its simplicity, speed, and environmentally friendly process. This process usually involves two primary steps: first, depositing GO onto electrodes through techniques like dip-coating or drop-casting, and second, undergoing electrochemical reduction. A newer technique allows for the

immersion of GO-coated electrodes in a metal precursor solution, facilitating a one-step co-electrochemical reduction that results in graphene–metal nanocomposite films. However, these traditional methods of graphene synthesis have certain limitations, including a lack of control over film thickness and insufficient separation of graphene sheets by metal nanoparticles, as the NPs often remain on the surface of the graphene films [60]. Recently, it was demonstrated that GO in solution can be directly electrochemically reduced on an electrode surface with a one-step co-electrodeposition of graphene–metal composite films. In this process, both the reduction of GO and the metal can occur simultaneously under cathodic conditions. The resulting composites exhibit a layered nanostructure, with alternating layers of metal nanoparticles and graphene sheets. This structure not only prevents graphene agglomeration but also enhances the conductivity of the graphene film [61].

Composites that combine graphene with metal nanostructures demonstrate improved performance due to their synergistic effects, surpassing the capabilities of either nanoparticles or graphene on their own. Noble metal nanoparticles, including silver (Ag) and gold (Au), are known for their distinct chemical and physical properties, which encompass electronic, optical, magnetic, and catalytic features. Their nanoscale size and remarkable sensitivity make them particularly valuable in the development of electrochemical sensors, where they enhance electron transfer processes on electrocatalytic surfaces [62].

2.4.2 Synthesis of Gold Nanoparticles in Graphene-Based Nanocomposites

Gold nanoparticles (AuNPs) are recognized for their strong light absorption, remarkable stability, and excellent conductivity, making them highly effective for biosensing applications, such as enzyme detection and immunosensors. In the synthesis of graphene-metal nanocomposites via co-electrodeposition, ensuring a uniform distribution of exfoliated GO and metallic precursors is essential for optimal performance. Positively charged metal ions such as Cu^{2+}, Ni^{2+}, and Zn^{2+}

were found to cause agglomeration of GO sheets due to crosslinking effects [63]. Conversely, negatively charged metallic precursors coexist well with GO, forming stable colloidal dispersions. In some works [59], $HAuCl_4$ was selected as the model precursor for synthesizing graphene–gold (Au) composite films. The CV for the electrolysis of GO with $HAuCl_4$ exhibited a significantly different pattern compared to that of GO alone, with much larger reduction currents. The progressive increase in current suggested persistent deposition of conductive materials, implying that graphene and Au were simultaneously deposited on the electrode. To confirm this, the resulting electrodes were cycled in 0.5 M H_2SO_4, and the redox behavior was analyzed.

The presence of intercalated AuNPs in the film acted as electron-transfer channels, improving the overall conductivity of the film and preserving the surface area of the graphene sheets by preventing agglomeration. In addition, the AuNPs helped to bridge the graphene sheets, further enhancing electron transfer and stabilizing the layered structure. Liu et al. [59] demonstrated that the AuNPs were confined to the graphene sheets, without scattering, suggesting a strong interaction between the two materials. This can be attributed to the residual oxygen functional groups on the graphene sheets, which acted as anchoring points for immobilizing the Au NPs.

The direct formation of graphene and graphene–metal composite films on the electrode surface makes them highly suitable for electrochemical applications.

2.4.3 Uric Acid Detection Using rGO-AuNPs Nanocomposites: Catalytic Electroactivity and Performance

The simultaneous detection of dopamine (DA), ascorbic acid (AA), and uric acid (UA) is gaining increasing attention due to the need for precise, rapid, and reliable analysis in biological and clinical diagnostics. AA, known for its potent antioxidant properties, is vital in the treatment of conditions like the common cold, scurvy, cancer, and AIDS, and plays a role in various physiological

processes [64]. DA is a critical neurotransmitter involved in the central nervous, renal, and cardiovascular systems, with deficiencies leading to severe disorders such as schizophrenia, Parkinson's disease, and epilepsy [65]. UA, the final product of purine metabolism, is linked to conditions such as hyperuricemia, gout, and kidney stones when found in abnormal levels [66].

In biological systems like human serum and urine, AA, DA, and UA typically coexist, making their simultaneous detection essential for diagnosing diseases and understanding their physiological roles. Various modified electrodes, including those incorporating nanoparticles and functionalized graphene, have emerged as promising solutions for overcoming these limitations. These advanced materials enable the simultaneous and selective detection of AA, DA, and UA by enhancing electron transfer, reducing peak overlap, and improving overall sensitivity, contributing significantly to more accurate diagnostics and monitoring of related health conditions [67].

Wang et al. [68] proposed using AuNPs to modify the surface of rGO for simultaneous detection. In this method, a glassy carbon electrode (GCE) was first electrochemically modified in two steps: the reduction of graphene oxide (GO) to rGO, followed by the deposition of AuNPs from a solution of $HAuCl_4$. This electrode successfully detected DA, AA, and UA simultaneously, with detection limits (LODs) of 1.4 μM for DA, 51 μM for AA, and 18 μM for UA. However, the simultaneous increase of all analytes during testing limited the full evaluation of potential interferences, leaving some questions about selectivity under real-world conditions. To further address these challenges, Tiğ et al. [69] proposed a composite material consisting of AuNPs, GO, and poly(2,6-pyridinedicarboxylic acid) (P(PDA)) for simultaneous detection. They first modified the GCE with AuNPs via electrochemical deposition, followed by electrodeposition of a P(PDA)-GO film onto the AuNP-modified surface. This configuration led to the clear differentiation of DA, AA, and UA peaks with separations of 0.161 V (AA-DA), 0.336 V (AA-UA), and 0.175 V (DA-UA), which indicated that the

modified electrode successfully reduced peak overlap and enhanced the selective detection of each analyte.

These advances in electrode materials illustrate promising approaches toward the simultaneous detection of DA, AA, and UA, with improved selectivity and sensitivity enabled using AuNPs and functionalized graphene composites.

2.5 Electrode modified with Silver for Chlorides Detection in Sweat

The other gold working electrode of the chip was modified through the electrodeposition of silver to detect chlorides in sweat.

2.5.1 Advances in the Synthesis of Silver Based-Electrochemical Sensors

Silver nanoparticles (AgNPs) are among the most widely utilized nanoparticles, primarily because of their remarkable catalytic, electronic, chemical, magnetic, optical, and electrochemical characteristics [70]. These nanoparticles can be synthesized through a variety of methods, including chemical, physical, biological, and mechanical approaches. Chemical and biological methods, in particular, rely on reducing Ag^{+} to Ag^{0} using appropriate reducing agents [71]. Chemical synthesis is the most used approach for producing silver nanoparticles. The foundational work in this area was carried out in 1951 when J. Turhevich introduced a method for synthesizing gold nanoparticles by reducing chloroauric acid with trisodium citrate [72]. This technique was later adapted for the synthesis of silver nanoparticles. To successfully synthesize silver nanoparticles in a batch process, a metal salt as the nanoparticle precursor, a reducing agent, and an encapsulating agent are required. Given that silver has a relatively high electropositive reduction potential ($E° = + 0.799$ V), a broad range of chemicals can act as effective reductants. Silver salts such as acetate or perchlorate can be used as precursors, but silver (I) nitrate is by far the most common due to its

affordability and chemical stability. Additionally, polymers, simple ions, and surfactants are frequently cited in the literature as effective nanoparticle protectants. These compounds attach to the surfaces of silver nanoparticles via covalent (chemisorption) or non-covalent (physisorption) interactions, which assist in dispersing the nanoparticles by means of electrostatic repulsion, steric hindrance, or a combination of both mechanisms. The characteristics of the silver nanoparticles, including their size, shape, and distribution, can be regulated by adjusting factors such as the silver precursor, reducing agent, stabilizing compound, temperature, pH, and the duration the chemical reduction process [73].

Unlike the chemical methods mentioned earlier, electrochemical synthesis (Fig. 2.12b) does not require the introduction of toxic chemicals into the reaction, resulting in nanoparticles of high purity. This makes the electrochemical approach consistent with green chemistry principles [74]. The potential applied, current density, precursor concentration, and deposition time all play crucial roles in determining the size, shape, and uniformity of the particles on the sensing surface [75]. There are significant advantages, including the absence of unwanted by-products, no need for chemical oxidants or reductants, a shorter synthesis time, and the elimination of the need for a binder, which is often necessary in drop-casting (Fig. 2.12a) procedures to secure the particles [76]. Other techniques commonly used for AgNPs synthesis are the spray coating and the sputtering (Fig. 2.12c-d). Although spray coating can be automated and the nozzle properties controlled, this method consumes significant material and is typically a one-sided coating process [77]. The advantages of sputtering include precise control over the deposition rate and film thickness, the ability to use high-purity targets, and its applicability to insulating materials. However, sputtering has a slow deposition rate and requires expensive equipment [78].

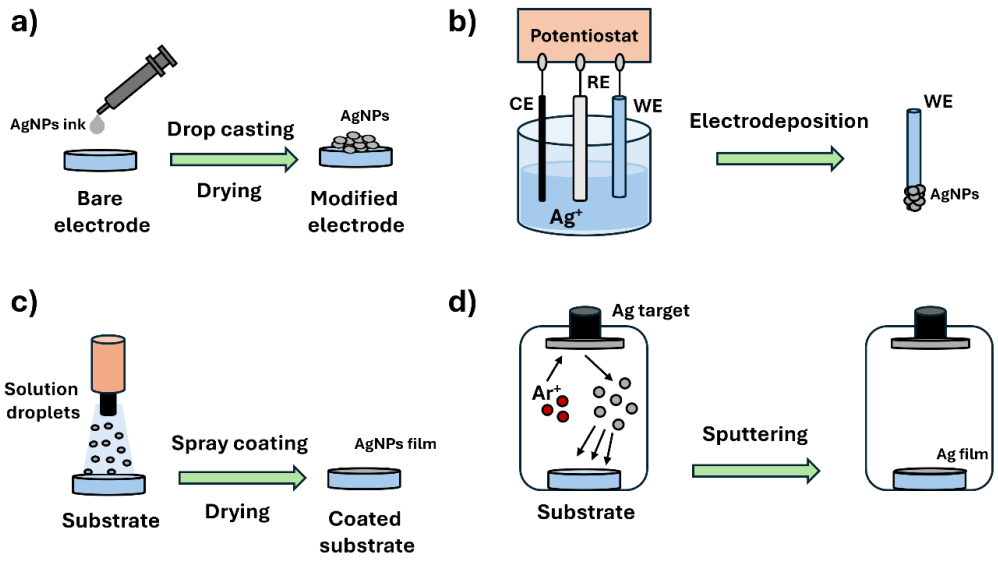

***Figure 2.12**: Schematic illustration of the main Ag deposition methods.a) Drop casting b) Electrodeposition c) Spray coating d) Sputtering.*

2.5.2 Catalytic Performance of Silver-Based Electrochemical Sensors for Chloride Ions Detection

Detecting chloride ions is essential in many areas, including clinical diagnostics, environmental monitoring, and industrial applications. In the field of medical diagnostics, the transport of chloride ions plays a crucial role in various physiological processes, and any disruption in this transport can result in significant health issues. A prominent example is cystic fibrosis (CF), a genetic disorder that affects chloride transport across epithelial membranes, leading to serious complications. In CF diagnosis, the standard method involves measuring chloride concentrations in sweat. Additionally, chloride ion levels in sweat during physical activity can predict the onset of muscle cramps when the concentration decreases significantly. In environmental monitoring, chloride ion detection is important for assessing water quality, as elevated chloride levels can indicate contamination or salinity changes in freshwater systems. Excessive chloride in water can also lead to pipe corrosion and affect disinfection processes in natural

water systems by reducing the efficacy of silver-embedded porous media against bacteria like *Escherichia coli*. Several electrochemical sensors have been developed for selective chloride ion detection in clinical, environmental, and industrial settings [79].

Among electrochemical sensors for chloride ions determination, both amperometric and potentiometric sensors have been developed using electrodes made from silver due to these materials' high affinity for chloride ions. The formation of silver chloride (AgCl) on a silver substrate in a chloride-rich environment has been extensively studied due to its relevance in various applications. For instance, Toh et al. [80] also employed disposable electrodes incorporating AgNPs, achieving a similar LOD of 1 mM, demonstrating their practicality in real-world diagnostics. Furthermore, AgNPs have been integrated into metal-organic frameworks to develop chloride ion sensors with excellent stability, reproducibility, selectivity, and a wide linear detection range with a low LOD. Patella et al. [81] realized an electrochemical sensor for chlorides detection from the silver layer of waste of new CDs. Chloride ions detection was performed using Linear Scan Voltammetry (LSV) with the sensors exhibiting a sensitivity of 0.174 mA mM^{-1} cm^{-2} and a detection limit of 20 μM, along with excellent selectivity against numerous potential interfering substances. This electrochemical sensor was further validated using real samples, including drinking water, seawater, milk, sweat, and physiological solutions, with results comparable to conventional methods.

2.6 Electrode modified with Nickel NanoParticles for Glucose Detection in Sweat

The last gold working electrode of the chip was modified through the electrodeposition of Nickel NanoParticles (NiNPs) to detect glucose in sweat.

2.6.1 Nickel Nanoparticles: Properties and Synthesis

NiNPs have attracted significant attention for its remarkable properties and affordability relative to noble metals, making it suitable for a wide range of applications. With the rapid progress in materials science and nanotechnology, nickel nanoparticles have become a significant research focus, offering new opportunities for custom material design and innovative applications. Compared to other magnetic nanoparticles, NiNPs show considerable potential as catalysts in reactions and as additives in coatings, plastics, and fibers. Due to nickel's relative abundance in the Earth's crust, it is more cost-effective than many metals used as catalysts [82]. The distinctive properties of nickel nanoparticles, influenced by their size, include enhanced reactivity, a larger surface area, elevated surface energy, strong magnetic characteristics, and a lower melting point. These traits promise advancements in fields such as catalysis, medicine, and electronics [83].

For the synthesis of nanoparticles, crucial is the choice of nickel salt and reducing agent. The concentration of the precursor is crucial for controlling nanoparticle size and morphology. By adjusting the concentration, one can promote the formation of complex structures such as nanoflowers, spiky nanospheres, and spiky nanowires, as well as influence the overall size of the nanoparticles [84].

The selection of a reducing agent is pivotal in determining the size, shape, and characteristics of the nanoparticles produced. Reducing agents are classified into three categories based on their reduction potential strength: strong, medium, and weak. Strong reducing agents involve the simultaneous formation of numerous growth species, resulting in the rapid creation of small, uniform nanoparticles typically smaller than 10 nm. Medium-strength reducing agents offer a moderate reduction potential and reaction rate. This results in nanoparticles with sizes around 70 nm and various morphologies. Weak reducing agents have lower reduction potentials and slower reaction rates. These agents are often used for the gradual reduction of metal ions, which leads to a slower nucleation and growth

process. As a result, weak reducing agents require longer reaction times to convert all precursors, which can lead to the formation of larger nanoparticles [83].

2.6.2 Nickel-Based Electrochemical Sensors for Non-Enzymatic Glucose Detection: Mechanisms and Advancements

Nickel-based materials are frequently used in glucose catalysis, as demonstrated by Fleishman et al. [85], who found that nickel can partially electro-oxidize organic substances in alkaline conditions (Fig. 2.13). The oxidation of glucose (Eq. 2.7) takes place on the surface of nickel-based materials, involving electron transfer with the oxidation of Ni^0 to Ni^{2+} (Eq. 2.5), followed by further oxidation to Ni^{3+} in the next step (Eq. 2.6):

$$Ni + 2OH^- \rightarrow Ni(OH)_2 + 2e^- \quad (2.5)$$

$$Ni(OH)_2 + OH^- \rightarrow NiOOH + H_2O + e^- \quad (2.6)$$

So, Ni^{3+} generated on the surface of the electrode, quickly oxidizes glucose to glucolactone:

$$NiOOH + glucose \rightarrow Ni(OH)_2 + glucolactone \quad (2.7)$$

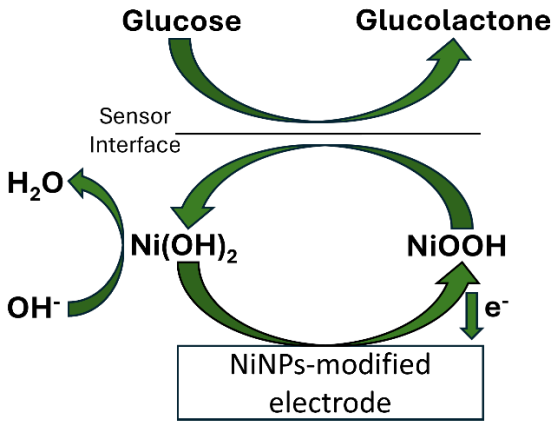

***Figure 2.13**: Sensing mechanism for glucose oxidation by NiNPs.*

Lu et al. [86] used commercially available nickel foam (NF) directly as the working electrode for glucose detection. The sensor exhibited a linear detection range from 0.05 to 7.35 mM, with a detection limit of 2.2 μM, making it one of the simplest electrochemical glucose sensors based on nickel materials. Various nanostructures of Ni-based compounds, including flower-like, sheet-like, needle-like, and spike-like morphologies, have been developed to enhance the analytical performance of non-enzymatic glucose sensors [87]. Başkaya et al. [88] developed a functionalized multi-walled carbon nanotube (MWCNT)-supported, highly monodisperse nickel nanoparticles (Ni@f-MWCNT) were synthesized using a microwave-assisted method and modified on a glassy carbon electrode (GCE) for non-enzymatic glucose sensing. The sensor exhibited a wide linear range of 0.05–12.0 mM and an impressive detection limit of 0.021 μM. Bui et al. [89] created Zn-doped $Ni(OH)_2$ nanosheets attached vertically to a 3D framework (3DF) for non-enzymatic glucose detection. This setup improved charge conductivity, increased sensing stability, and prevented nanosheet exfoliation. The Zn doping introduced structural defects in the $Ni(OH)_2$, which provided more electroactive sites and accelerated the glucose electro-oxidation process.

2.7 Conclusions

This chapter presented a discussion of the materials used in the development of the innovative electrochemical sensors realized in this research work. The first sensor, designed for real-time hydrogen peroxide detection in exhaled breath, was fabricated using silver obtained from compact discs, with additional modification using chitosan and Prussian Blue nanoparticles to enhance its sensitivity and functionality. This approach demonstrates the potential of utilizing recycled electronic materials for biomedical applications, addressing both environmental and economic concerns associated with electronic waste. To address the challenges related to the absence of liquid electrolytes, absorbent materials like biopolymers and paper were employed to retain moisture effectively. Among

these, chitosan, a natural biopolymer derived from chitin found in sources like crustaceans and fungi, stands out due to its solubility in weak acids, unlike the chitin that is generally insoluble. Sensors using chitosan have demonstrated potential in detecting gases like hydrogen peroxide and tracking respiratory patterns, offering promise for non-invasive health monitoring. Additionally, the electrodeposition of Prussian Blue nanoparticles was applied to improve the sensor's sensitivity in detecting hydrogen peroxide from exhaled breath. The excellent electrocatalytic activity of Prussian Blue, especially for reducing hydrogen peroxide, makes it an ideal modifier for electrodes in sensors aimed at detecting trace levels of this compound.

The second electrochemical sensor, a wearable device for the detection of uric acid, chlorides, and glucose in sweat, employed gold electrodes, each modified with specific materials to target different analytes. The co-deposition of reduced graphene oxide and gold nanoparticles enabled efficient uric acid detection, while silver and nickel nanoparticles were used for chloride and glucose sensing, respectively. These modifications provided excellent electrocatalytic properties, leading to high sensitivity and stability across a broad range of conditions.

References

[1] https://news.un.org/en/story/2019/01/1031242

[2] Z. Wang, B. Zhang, e D. Guan, «Take responsibility for electronic-waste disposal», *Nature*, vol. 536, fasc. 7614, pp. 23–25, ago. 2016, doi: 10.1038/536023a.

[3] https://theroundup.org/global-e-waste-statistics/

[4] https://www.statista.com/statistics/186772/album-shipments-in-the-us-music-industry-since-1999/

[5] M. S. Brown, L. Somma, M. Mendoza, Y. Noh, G. J. Mahler, e A. Koh, «Upcycling Compact Discs for Flexible and Stretchable Bioelectronic Applications», *Nat Commun*, vol. 13, fasc. 1, p. 3727, giu. 2022, doi: 10.1038/s41467-022-31338-9.

[6] Z. Pan *et al.*, «A mannosylated PEI–CPP hybrid for TRAIL gene targeting delivery for colorectal cancer therapy», *Polym. Chem.*, vol. 8, fasc. 35, pp. 5275–5285, 2017, doi: 10.1039/C7PY00882A.

[7] M. S. Brown, B. Ashley, e A. Koh, «Wearable Technology for Chronic Wound Monitoring: Current Dressings, Advancements, and Future Prospects», *Front. Bioeng. Biotechnol.*, vol. 6, p. 47, apr. 2018, doi: 10.3389/fbioe.2018.00047.

[8] D. C. Kirkpatrick, C. Antwi, e R. S. Martin, «Use of recordable compact discs to fabricate electrodes for microchip-based analysis systems», *Anal. Methods*, vol. 2, fasc. 7, p. 811, 2010, doi: 10.1039/c0ay00294a.

[9] K. C. Honeychurch, «Cheap and disposable gold and silver electrodes: Trends in the application of compact discs and digital versatile discs for electroanalytical chemistry», *TrAC Trends in Analytical Chemistry*, vol. 93, pp. 51–66, ago. 2017, doi: 10.1016/j.trac.2017.04.013.
[10] M.-C. Radulescu e A. F. Danet, «Mercury Determination in Fish Samples by Chronopotentiometric Stripping Analysis Using Gold Electrodes Prepared from Recordable CDs», *Sensors*, vol. 8, fasc. 11, pp. 7157–7171, nov. 2008, doi: 10.3390/s8117157.
[11] L. Angnes, E. M. Richter, M. A. Augelli, e G. H. Kume, «Gold Electrodes from Recordable CDs», *Anal. Chem.*, vol. 72, fasc. 21, pp. 5503–5506, nov. 2000, doi: 10.1021/ac000437p.
[12] K. C. Honeychurch, «Underpotential Deposition of Lead at Silver Electrodes Manufactured from Compact Discs and its Determination in Environmental Water Samples», *Advances in Analytical Chemistry*, 2013.
[13] M. Shafei e K. C. Honeychurch, «Voltammetric behaviour of hydrogen peroxide at a silver electrode fabricated from a rewritable digital versatile disc (DVD) and its determination in water samples», *Anal. Methods*, vol. 5, fasc. 23, p. 6631, 2013, doi: 10.1039/c3ay41557k.
[14] W. Lian *et al.*, «A hydrogen peroxide sensor based on electrochemically roughened silver electrodes», *Electrochimica Acta*, vol. 54, fasc. 18, pp. 4334–4339, lug. 2009, doi: 10.1016/j.electacta.2009.02.106.
[15] K. Honeychurch e C. Maynard, «Amperometric determination of Hydrogen Peroxide at a Silver Electrode Fabricated from a Recycled Compact disc», 2015, *Unpublished*. doi: 10.13140/RG.2.1.2477.2005.
[16] Y. Wen, A.-J. Lin, H.-F. Chen, Y.-Z. Jiao, e H.-F. Yang, «From DVD to dendritic nanostructure silver electrode for hydrogen peroxide detection», *Biosensors and Bioelectronics*, vol. 41, pp. 857–861, mar. 2013, doi: 10.1016/j.bios.2012.08.032.
[17] Z. Chen e C. Lu, «Humidity Sensors: A Review of Materials and Mechanisms», *Sen Lett*, vol. 3, fasc. 4, pp. 274–295, dic. 2005, doi: 10.1166/sl.2005.045.
[18] C. Cui, Q. Fu, L. Meng, S. Hao, R. Dai, e J. Yang, «Recent Progress in Natural Biopolymers Conductive Hydrogels for Flexible Wearable Sensors and Energy Devices: Materials, Structures, and Performance», *ACS Appl. Bio Mater.*, vol. 4, fasc. 1, pp. 85–121, gen. 2021, doi: 10.1021/acsabm.0c00807.
[19] W. Suginta, P. Khunkaewla, e A. Schulte, «Electrochemical Biosensor Applications of Polysaccharides Chitin and Chitosan», *Chem. Rev.*, vol. 113, fasc. 7, pp. 5458–5479, lug. 2013, doi: 10.1021/cr300325r.
[20] Y. Luo, J. Li, Q. Ding, H. Wang, C. Liu, e J. Wu, «Functionalized Hydrogel-Based Wearable Gas and Humidity Sensors», *Nano-Micro Lett.*, vol. 15, fasc. 1, p. 136, dic. 2023, doi: 10.1007/s40820-023-01109-2.
[21] R. D. Kasai *et al.*, «A review on hydrogels classification and recent developments in biomedical applications», *International Journal of Polymeric Materials and Polymeric Biomaterials*, vol. 72, fasc. 13, pp. 1059–1069, set. 2023, doi: 10.1080/00914037.2022.2075872.
[22] O. Wichterle e D. Lím, «Hydrophilic Gels for Biological Use», *Nature*, vol. 185, fasc. 4706, pp. 117–118, gen. 1960, doi: 10.1038/185117a0.
[23] Y. Luo, J. Li, Q. Ding, H. Wang, C. Liu, e J. Wu, «Functionalized Hydrogel-Based Wearable Gas and Humidity Sensors», *Nano-Micro Lett.*, vol. 15, fasc. 1, p. 136, dic. 2023, doi: 10.1007/s40820-023-01109-2.
[24] Y. Gao, F. Jia, e G. Gao, «Ultra-thin, transparent, anti-freezing organohydrogel film responded to a wide range of humidity and temperature», *Chemical Engineering Journal*, vol. 430, p. 132919, feb. 2022, doi: 10.1016/j.cej.2021.132919.
[25] G. Korotcenkov, «Paper-Based Humidity Sensors as Promising Flexible Devices: State of the Art: Part 1. General Consideration», *Nanomaterials*, vol. 13, fasc. 6, p. 1110, mar. 2023, doi: 10.3390/nano13061110.

[26] L. Fiore *et al.*, «A paper-based electrochemical sensor for H2O2 detection in aerosol phase: Measure of H2O2 nebulized by a reconverted ultrasonic aroma diffuser as a case of study», *Microchemical Journal*, vol. 166, p. 106249, lug. 2021, doi: 10.1016/j.microc.2021.106249.
[27] E. Avcu, F. E. Baştan, H. Z. Abdullah, M. A. U. Rehman, Y. Y. Avcu, e A. R. Boccaccini, «Electrophoretic deposition of chitosan-based composite coatings for biomedical applications: A review», *Progress in Materials Science*, vol. 103, pp. 69–108, giu. 2019, doi: 10.1016/j.pmatsci.2019.01.001.
[28] I. Younes e M. Rinaudo, «Chitin and Chitosan Preparation from Marine Sources. Structure, Properties and Applications», *Marine Drugs*, vol. 13, fasc. 3, pp. 1133–1174, mar. 2015, doi: 10.3390/md13031133.
[29] H. K. No e S. P. Meyers, «Preparation and Characterization of Chitin and Chitosan—A Review», *Journal of Aquatic Food Product Technology*, vol. 4, fasc. 2, pp. 27–52, ott. 1995, doi: 10.1300/J030v04n02_03.
[30] Annu e A. N. Raja, «Recent development in chitosan-based electrochemical sensors and its sensing application», *International Journal of Biological Macromolecules*, vol. 164, pp. 4231–4244, dic. 2020, doi: 10.1016/j.ijbiomac.2020.09.012.
[31] M. A. Ibrahim, M. H. Alhalafi, E.-A. M. Emam, H. Ibrahim, e R. M. Mosaad, «A Review of Chitosan and Chitosan Nanofiber: Preparation, Characterization, and Its Potential Applications», *Polymers*, vol. 15, fasc. 13, p. 2820, giu. 2023, doi: 10.3390/polym15132820.
[32] P. Kumari *et al.*, «Chitosan-Based Highly Sensitive Viable Humidity Sensor for Human Health Monitoring», *ACS Omega*, vol. 8, fasc. 42, pp. 39511–39522, ott. 2023, doi: 10.1021/acsomega.3c05244.
[33] S. Teepoo, P. Dawan, e N. Barnthip, «Electrospun Chitosan-Gelatin Biopolymer Composite Nanofibers for Horseradish Peroxidase Immobilization in a Hydrogen Peroxide Biosensor», *Biosensors*, vol. 7, fasc. 4, p. 47, ott. 2017, doi: 10.3390/bios7040047.
[34] X. Gao, L. Jin, Q. Wu, Z. Chen, e X. Lin, «A Nonenzymatic Hydrogen Peroxide Sensor Based on Silver Nanowires and Chitosan Film», *Electroanalysis*, vol. 24, fasc. 8, pp. 1771–1777, ago. 2012, doi: 10.1002/elan.201200109.
[35] A. Kraft, «Some considerations on the structure, composition, and properties of Prussian blue: a contribution to the current discussion», *Ionics*, vol. 27, fasc. 6, pp. 2289–2305, giu. 2021, doi: 10.1007/s11581-021-04013-0.
[36] J. F. Keggin e F. D. Miles, «Structures and Formulæ of the Prussian Blues and Related Compounds», *Nature*, vol. 137, fasc. 3466, pp. 577–578, apr. 1936, doi: 10.1038/137577a0.
[37] H. J. Buser, D. Schwarzenbach, W. Petter, e A. Ludi, «The crystal structure of Prussian Blue: Fe4[Fe(CN)6]3.xH2O», *Inorg. Chem.*, vol. 16, fasc. 11, pp. 2704–2710, nov. 1977, doi: 10.1021/ic50177a008.
[38] M. A. Busquets e J. Estelrich, «Prussian blue nanoparticles: synthesis, surface modification, and biomedical applications», *Drug Discovery Today*, vol. 25, fasc. 8, pp. 1431–1443, ago. 2020, doi: 10.1016/j.drudis.2020.05.014.
[39] A. Dostal, G. Kauschka, S. J. Reddy, e F. Scholz, «Lattice contractions and expansions accompanying the electrochemical conversions of Prussian blue and the reversible and irreversible insertion of rubidium and thallium ions», *Journal of Electroanalytical Chemistry*, vol. 406, fasc. 1–2, pp. 155–163, apr. 1996, doi: 10.1016/0022-0728(95)04427-2.
[40] A. Abbaspour e M. A. Kamyabi, «Electrochemical formation of Prussian blue films with a single ferricyanide solution on gold electrode», *Journal of Electroanalytical Chemistry*, vol. 584, fasc. 2, pp. 117–123, ott. 2005, doi: 10.1016/j.jelechem.2005.07.008.
[41] V. D. Neff, «Electrochemical Oxidation and Reduction of Thin Films of Prussian Blue», *J. Electrochem. Soc.*, vol. 125, fasc. 6, pp. 886–887, giu. 1978, doi: 10.1149/1.2131575.

[42] A. A. Karyakin, «Advances of Prussian blue and its analogues in (bio)sensors», *Current Opinion in Electrochemistry*, vol. 5, fasc. 1, pp. 92–98, ott. 2017, doi: 10.1016/j.coelec.2017.07.006.
[43] P. Salazar, M. Martín, R. D. O'Neill, e J. L. González-Mora, «In Vivo Biosensor Based on Prussian Blue for Brain Chemistry Monitoring : Methodological Review and Biological Applications», in *In Vivo Neuropharmacology and Neurophysiology*, vol. 121, A. Philippu, A c. di, in Neuromethods, vol. 121. , New York, NY: Springer New York, 2017, pp. 155–179. doi: 10.1007/978-1-4939-6490-1_8.
[44] F. Ricci e G. Palleschi, «Sensor and biosensor preparation, optimisation and applications of Prussian Blue modified electrodes», *Biosensors and Bioelectronics*, vol. 21, fasc. 3, pp. 389–407, set. 2005, doi: 10.1016/j.bios.2004.12.001.
[45] F. Ricci, A. Amine, G. Palleschi, e D. Moscone, «Prussian Blue based screen printed biosensors with improved characteristics of long-term lifetime and pH stability», *Biosensors and Bioelectronics*, vol. 18, fasc. 2–3, pp. 165–174, mar. 2003, doi: 10.1016/S0956-5663(02)00169-0.
[46] P. Salazar, M. Martín, R. Roche, R. D. O'Neill, e J. L. González-Mora, «Prussian Blue-modified microelectrodes for selective transduction in enzyme-based amperometric microbiosensors for in vivo neurochemical monitoring», *Electrochimica Acta*, vol. 55, fasc. 22, pp. 6476–6484, set. 2010, doi: 10.1016/j.electacta.2010.06.036.
[47] M. S. Lin e W. C. Shih, «Chromium hexacyanoferrate based glucose biosensor», *Analytica Chimica Acta*, vol. 381, fasc. 2–3, pp. 183–189, feb. 1999, doi: 10.1016/S0003-2670(98)00745-4.
[48] K. Itaya, N. Shoji, e I. Uchida, «Catalysis of the reduction of molecular oxygen to water at Prussian blue modified electrodes», *J. Am. Chem. Soc.*, vol. 106, fasc. 12, pp. 3423–3429, giu. 1984, doi: 10.1021/ja00324a007.
[49] I. L. De Mattos, L. Gorton, e T. Ruzgas, «Sensor and biosensor based on Prussian Blue modified gold and platinum screen printed electrodes», *Biosensors and Bioelectronics*, vol. 18, fasc. 2–3, pp. 193–200, mar. 2003, doi: 10.1016/S0956-5663(02)00185-9.
[50] J. Li, J. -D. Qiu, J. -J. Xu, H. -Y. Chen, e X. -H. Xia, «The Synergistic Effect of Prussian-Blue-Grafted Carbon Nanotube/Poly(4-vinylpyridine) Composites for Amperometric Sensing», *Adv Funct Materials*, vol. 17, fasc. 9, pp. 1574–1580, giu. 2007, doi: 10.1002/adfm.200600033.
[51] D. Du, M. Wang, Y. Qin, e Y. Lin, «One-step electrochemical deposition of Prussian Blue–multiwalled carbon nanotube nanocomposite thin-film: preparation, characterization and evaluation for H_2O_2 sensing», *J. Mater. Chem.*, vol. 20, fasc. 8, pp. 1532–1537, 2010, doi: 10.1039/B919500A.
[52] «XIII. On the atomic weight of graphite», *Phil. Trans. R. Soc.*, vol. 149, pp. 249–259, dic. 1859, doi: 10.1098/rstl.1859.0013.
[53] S. Priyadarsini, S. Mohanty, S. Mukherjee, S. Basu, e M. Mishra, «Graphene and graphene oxide as nanomaterials for medicine and biology application», *J Nanostruct Chem*, vol. 8, fasc. 2, pp. 123–137, giu. 2018, doi: 10.1007/s40097-018-0265-6.
[54] L. Sun, «Structure and synthesis of graphene oxide», *Chinese Journal of Chemical Engineering*, vol. 27, fasc. 10, pp. 2251–2260, ott. 2019, doi: 10.1016/j.cjche.2019.05.003.
[55] D. R. Dreyer, S. Park, C. W. Bielawski, e R. S. Ruoff, «The chemistry of graphene oxide», *Chem. Soc. Rev.*, vol. 39, fasc. 1, pp. 228–240, 2010, doi: 10.1039/B917103G.
[56] D. R. Dreyer, S. Park, C. W. Bielawski, e R. S. Ruoff, «The chemistry of graphene oxide», *Chem. Soc. Rev.*, vol. 39, fasc. 1, Art. fasc. 1, 2010, doi: 10.1039/B917103G.
[57] Z. Liu *et al.*, «Direct observation of oxygen configuration on individual graphene oxide sheets», *Carbon*, vol. 127, pp. 141–148, feb. 2018, doi: 10.1016/j.carbon.2017.10.100.
[58] D. R. Dreyer, A. D. Todd, e C. W. Bielawski, «Harnessing the chemistry of graphene oxide», *Chem. Soc. Rev.*, vol. 43, fasc. 15, p. 5288, lug. 2014, doi: 10.1039/C4CS00060A.

[59] C. Liu, K. Wang, S. Luo, Y. Tang, e L. Chen, «Direct Electrodeposition of Graphene Enabling the One-Step Synthesis of Graphene–Metal Nanocomposite Films», *Small*, vol. 7, fasc. 9, pp. 1203–1206, mag. 2011, doi: 10.1002/smll.201002340.
[60] C. Jiang, X. Zeng, B. Wu, Q. Zeng, W. Pang, e J. Tang, «Electrochemical co-deposition of reduced graphene oxide-gold nanocomposite on an ITO substrate and its application in the detection of dopamine», *Sci. China Chem.*, vol. 60, fasc. 1, pp. 151–156, gen. 2017, doi: 10.1007/s11426-016-0015-2.
[61] L. Chen, Y. Tang, K. Wang, C. Liu, e S. Luo, «Direct electrodeposition of reduced graphene oxide on glassy carbon electrode and its electrochemical application», *Electrochemistry Communications*, vol. 13, fasc. 2, pp. 133–137, feb. 2011, doi: 10.1016/j.elecom.2010.11.033.
[62] G. Darabdhara, M. R. Das, S. P. Singh, A. K. Rengan, S. Szunerits, e R. Boukherroub, «Ag and Au nanoparticles/reduced graphene oxide composite materials: Synthesis and application in diagnostics and therapeutics», *Advances in Colloid and Interface Science*, vol. 271, p. 101991, set. 2019, doi: 10.1016/j.cis.2019.101991.
[63] S. Park, K.-S. Lee, G. Bozoklu, W. Cai, S. T. Nguyen, e R. S. Ruoff, «Graphene Oxide Papers Modified by Divalent Ions—Enhancing Mechanical Properties *via* Chemical Cross-Linking», *ACS Nano*, vol. 2, fasc. 3, pp. 572–578, mar. 2008, doi: 10.1021/nn700349a.
[64] M. Zhang, K. Liu, L. Xiang, Y. Lin, L. Su, e L. Mao, «Carbon Nanotube-Modified Carbon Fiber Microelectrodes for In Vivo Voltammetric Measurement of Ascorbic Acid in Rat Brain», *Anal. Chem.*, vol. 79, fasc. 17, pp. 6559–6565, set. 2007, doi: 10.1021/ac0705871.
[65] R. M. Wightman, L. J. May, e A. C. Michael, «Detection of dopamine dynamics in the brain», *Anal. Chem.*, vol. 60, fasc. 13, pp. 769A-779A, lug. 1988, doi: 10.1021/ac00164a001.
[66] X. Niu, W. Yang, H. Guo, J. Ren, F. Yang, e J. Gao, «A novel and simple strategy for simultaneous determination of dopamine, uric acid and ascorbic acid based on the stacked graphene platelet nanofibers/ionic liquids/chitosan modified electrode», *Talanta*, vol. 99, pp. 984–988, set. 2012, doi: 10.1016/j.talanta.2012.07.077.
[67] S. I. Kaya, S. Kurbanoglu, e S. A. Ozkan, «Nanomaterials-Based Nanosensors for the Simultaneous Electrochemical Determination of Biologically Important Compounds: Ascorbic Acid, Uric Acid, and Dopamine», *Critical Reviews in Analytical Chemistry*, vol. 49, fasc. 2, pp. 101–125, mar. 2019, doi: 10.1080/10408347.2018.1489217.
[68] C. Wang *et al.*, «A facile electrochemical sensor based on reduced graphene oxide and Au nanoplates modified glassy carbon electrode for simultaneous detection of ascorbic acid, dopamine and uric acid», *Sensors and Actuators B: Chemical*, vol. 204, pp. 302–309, dic. 2014, doi: 10.1016/j.snb.2014.07.077.
[69] G. Aydoğdu Tığ, G. Günendi, e Ş. Pekyardımcı, «A selective sensor based on Au nanoparticles-graphene oxide-poly(2,6-pyridinedicarboxylic acid) composite for simultaneous electrochemical determination of ascorbic acid, dopamine, and uric acid», *J Appl Electrochem*, vol. 47, fasc. 5, pp. 607–618, mag. 2017, doi: 10.1007/s10800-017-1060-7.
[70] M. Zahran, Z. Khalifa, M. A.-H. Zahran, e M. Abdel Azzem, «Recent advances in silver nanoparticle-based electrochemical sensors for determining organic pollutants in water: a review», *Mater. Adv.*, vol. 2, fasc. 22, pp. 7350–7365, 2021, doi: 10.1039/D1MA00769F.
[71] M. Zahran, M. El-Kemary, S. Khalifa, e H. El-Seedi, «Spectral studies of silver nanoparticles biosynthesized by Origanum majorana», *Green Processing and Synthesis*, vol. 7, fasc. 2, pp. 100–105, apr. 2018, doi: 10.1515/gps-2016-0183.
[72] J. Turkevich, P. C. Stevenson, e J. Hillier, «A study of the nucleation and growth processes in the synthesis of colloidal gold», *Discuss. Faraday Soc.*, vol. 11, p. 55, 1951, doi: 10.1039/df9511100055.

[73] I. Ivanišević, «The Role of Silver Nanoparticles in Electrochemical Sensors for Aquatic Environmental Analysis», *Sensors*, vol. 23, fasc. 7, p. 3692, apr. 2023, doi: 10.3390/s23073692.
[74] R. Singaravelan e S. Bangaru Sudarsan Alwar, «Electrochemical synthesis, characterisation and phytogenic properties of silver nanoparticles», *Appl Nanosci*, vol. 5, fasc. 8, pp. 983–991, nov. 2015, doi: 10.1007/s13204-014-0396-0.
[75] M. Hajisafari e N. Nasirizadeh, «An electrochemical nanosensor for simultaneous determination of hydroxylamine and nitrite using oxadiazole self-assembled on silver nanoparticle-modified glassy carbon electrode», *Ionics*, vol. 23, fasc. 6, pp. 1541–1551, giu. 2017, doi: 10.1007/s11581-016-1962-0.
[76] A. Abbas e H. M. A. Amin, «Silver nanoparticles modified electrodes for electroanalysis: An updated review and a perspective», *Microchemical Journal*, vol. 175, p. 107166, apr. 2022, doi: 10.1016/j.microc.2021.107166.
[77] C. Salvo-Comino, F. Martin-Pedrosa, C. Garcia-Cabezon, e M. L. Rodriguez-Mendez, «Silver Nanowires as Electron Transfer Mediators in Electrochemical Catechol Biosensors», *Sensors*, vol. 21, fasc. 3, p. 899, gen. 2021, doi: 10.3390/s21030899.
[78] S. K. Sardana, V. S. N. Chava, e V. K. Komarala, «Morphology and optical properties of sputter deposited silver nanoparticles on plain, textured and antireflection layer coated textured silicon», *Applied Surface Science*, vol. 347, pp. 651–656, ago. 2015, doi: 10.1016/j.apsusc.2015.04.145.
[79] L. Trnkova, V. Adam, J. Hubalek, P. Babula, e R. Kizek, «Amperometric Sensor for Detection of Chloride Ions», *Sensors*, vol. 8, fasc. 9, pp. 5619–5636, set. 2008, doi: 10.3390/s8095619.
[80] H. S. Toh, C. Batchelor-McAuley, K. Tschulik, e R. G. Compton, «Electrochemical detection of chloride levels in sweat using silver nanoparticles: a basis for the preliminary screening for cystic fibrosis», *Analyst*, vol. 138, fasc. 15, p. 4292, 2013, doi: 10.1039/c3an00843f.
[81] B. Patella *et al.*, «Electrochemical detection of chloride ions using Ag-based electrodes obtained from compact disc», *Analytica Chimica Acta*, vol. 1190, p. 339215, gen. 2022, doi: 10.1016/j.aca.2021.339215.
[82] N.-D. Jaji, H. L. Lee, M. H. Hussin, H. M. Akil, M. R. Zakaria, e M. B. H. Othman, «Advanced nickel nanoparticles technology: From synthesis to applications», *Nanotechnology Reviews*, vol. 9, fasc. 1, pp. 1456–1480, dic. 2020, doi: 10.1515/ntrev-2020-0109.
[83] F. E Silva, V. Salim, e T. Rodrigues, «Controlled Nickel Nanoparticles: A Review on How Parameters of Synthesis Can Modulate Their Features and Properties», *AppliedChem*, vol. 4, fasc. 1, pp. 86–106, mar. 2024, doi: 10.3390/appliedchem4010007.
[84] H. Wang, X. Kou, L. Zhang, e J. Li, «Size-controlled synthesis, microstructure and magnetic properties of Ni nanoparticles», *Materials Research Bulletin*, vol. 43, fasc. 12, pp. 3529–3536, dic. 2008, doi: 10.1016/j.materresbull.2008.01.012.
[85] M. Fleischmann, K. Korinek, e D. Pletcher, «The kinetics and mechanism of the oxidation of amines and alcohols at oxide-covered nickel, silver, copper, and cobalt electrodes», *J. Chem. Soc., Perkin Trans. 2*, fasc. 10, p. 1396, 1972, doi: 10.1039/p29720001396.
[86] W. Lu, X. Qin, A. M. Asiri, A. O. Al-Youbi, e X. Sun, «Ni foam: a novel three-dimensional porous sensing platform for sensitive and selective nonenzymatic glucose detection», *Analyst*, vol. 138, fasc. 2, pp. 417–420, 2013, doi: 10.1039/C2AN36138H.
[87] M. Wei *et al.*, «Electrochemical non-enzymatic glucose sensors: recent progress and perspectives», *Chem. Commun.*, vol. 56, fasc. 93, pp. 14553–14569, 2020, doi: 10.1039/D0CC05650B.
[88] G. Başkaya *et al.*, «Rapid, sensitive, and reusable detection of glucose by highly monodisperse nickel nanoparticles decorated functionalized multi-walled carbon

nanotubes», *Biosensors and Bioelectronics*, vol. 91, pp. 728–733, mag. 2017, doi: 10.1016/j.bios.2017.01.045.

[89] D. M. Nguyen, L. G. Bach, e Q. B. Bui, «Hierarchical nanosheets based on zinc-doped nickel hydroxide attached 3D framework as free-standing nonenzymatic sensor for sensitive glucose detection», *Journal of Electroanalytical Chemistry*, vol. 837, pp. 86–94, mar. 2019, doi: 10.1016/j.jelechem.2019.02.019.

3. Fabrication and Validation of an Electrochemical Sensor for Hydrogen Peroxide Detection in Exhaled Breath

Given the significant economic and social impact of respiratory diseases, a monitoring process involving periodic testing is required to enhance service delivery processes. Currently, routine monitoring programs are not recommended for individuals without apparent symptoms, leading to many cases going undiagnosed or being identified at more advanced stages, thereby reducing the potential for effective treatment. In this context, this chapter focuses on developing and validating a novel wearable electrochemical sensor that could be integrated into a face mask to monitor hydrogen peroxide (H_2O_2) in Exhaled Breath (EB). Two different sensors were studied with and without Prussian Blue. These sensors can detect hydrogen peroxide levels in real-time, thus it could help improve diagnostic techniques by offering valuable information on respiratory health and overall physiological conditions.

3.1 Introduction

3.1.1 The Role of Oxidative Stress in Disease Pathogenesis

Oxidative stress is a multicausal process of several negative influences on the body at different levels by different modalities. It is commonly described as an imbalance between pro-oxidants and antioxidants. This is seen when the body produces more Reactive Oxygen Species (ROS) than its natural antioxidant neutralization capability. Several chemicals take part in this oxidative balance that is controlled by redox pathways. It, therefore, causes several intracellular signals due to the oxidative stress causing cell death or uncontrolled cell growth [1] (Fig.3.1). Reactive species (RS) derived from oxygen (ROS) and nitrogen (RNS) have been extensively studied, but recent research has identified new radical

species based on chlorine (RCS), bromine (RBS), and sulfur [2]. All these lead to the development of hypertension, diabetes, aging, and chronic inflammation, causing various diseases like Alzheimer, Parkinson, glaucoma, atherosclerosis, and Chronic Obstructive Pulmonary Disease (COPD). Since oxidizing damage plays a huge role in the development of such conditions, treatments aimed at reducing oxidative stress may protect patients and therefore offer therapeutic benefits to them [3].

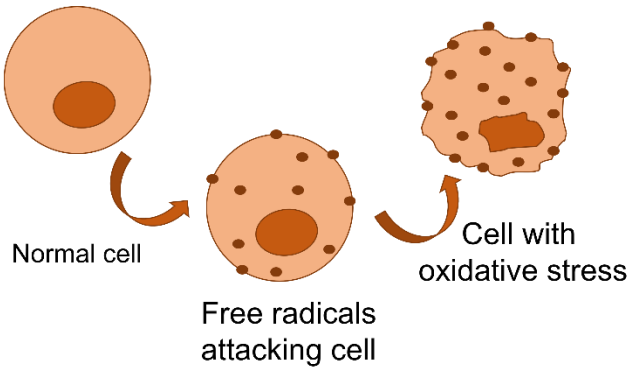

***Figure 3.1**: Schematic process of oxidative stress of cell.*

In normal conditions, ROS act as key second messengers in cell signaling pathways that help cells stay balanced with the external environment. But when ROS levels get too high, they damage biological molecules without discrimination, leading to cell malfunction and death. Biomolecules within living organisms are highly susceptible to oxidative stress, as ROS are generated from molecular oxygen during regular cellular metabolism. ROS can be categorized into two distinct groups: free radicals and non-radicals. Free radicals have one or more unpaired electrons, making them very reactive. While both groups exhibit important chemical differences, they share similar mechanisms in causing damage at the biomolecular level. The free radical group of ROS includes the superoxide anion ($O_2^{\bullet -}$), hydroxyl radical ($OH^{\bullet}$), and hydroperoxyl radical ($H_2O^{\bullet}$). In the non-radical group, hydrogen peroxide (H_2O_2) is the main species.

Despite their typically short half-life, ROS have long been recognized for playing dual roles in biological systems [4].

3.1.2 Exhaled Breath Analysis: A Non-Invasive Approach to Health Monitoring

EB is a human sample of high interest for researchers since it can give insight into several health issues. Among all the biological fluids, breath can offer non-invasive diagnostic data. It provides a window to the internal condition of the organism by containing key indicators concerning physiological and pathological conditions [5], [6]. In this context, the aerosol phase of the breath refers to liquid droplets, usually in the micrometer range, suspended in a gaseous medium comprised mainly of air. The use of EB as a medium for diagnosing diseases is not new [7], [8], [9]. Doctors began using breath as a diagnostic tool as early as 300 A.D., linking certain odors to various diseases [6]. For example, a sweet, fruity breath odor has long been recognized as an indicator of diabetes, while a fishy smell is linked to kidney dysfunction. These early observations laid the groundwork for the modern analysis of EB, though it wasn't until nearly two millennia later that chemical analysis of breath began to take shape. In the late 18th century, the chemical composition of EB was first systematically studied by Antoine Lavoisier and Linus Pauling. Their pioneering work revealed over 200 distinct compounds in human breath [10]. Since then, breath analysis has become a field of intense scientific interest, revealing the presence of various biomarkers, including volatile organic compounds (VOCs), hydrogen peroxide (H_2O_2), ammonia (NH_3), nitric oxide (NO), insulin resistance indicators, and even glucose [11], [12], [13]. These compounds provide rich data about metabolic processes and disease states.

One of the most important components of EB is hydrogen peroxide because it is associated with different conditions. The formation of hydrogen peroxide in healthy subjects is a continuous process within the mitochondrial respiratory

chain, where electron transport results in a reduction of oxygen. The rate of oxygen consumption controls the rate of the production of H_2O_2 [14]. The cellular concentration of steady-state H_2O_2 has been estimated to be 10-30 micromoles per liter under physiological conditions. Hydrogen peroxide is produced through the catalyzing action of a wide variety of enzymes, which include xanthine oxidase, cytochrome P450, and flavoenzymes [5]. One important limitation to the use of H_2O_2, however, as a biomarker of oxidative stress is great variability among healthy individuals. While the normal range of H_2O_2 in EBC ranges from 0.01 to 0.09 μmol/L, the real value is influenced by different factors such as age and smoking status, wherein smokers may reach higher values. Indeed, some studies report values highly superior to this (2.4 ± 1.7 μmol/L) or inferior to this in healthy subjects [15].

Bronchial asthma and COPD are the most common diseases related to EBC H_2O_2 levels. These disorders, featuring airway inflammation, have indeed shown increased levels of H_2O_2, therefore making EBC a useful tool when investigating these conditions. Other respiratory diseases that are explored about EBC H_2O_2 are Acute Respiratory Distress Syndrome (ARDS), cystic fibrosis, idiopathic pulmonary fibrosis, tuberculosis, and community-acquired pneumonia [5]. One of the first investigations into H_2O_2 levels in EBC in COPD patients was conducted by a Dutch research group [16]. Their study showed that COPD patients exhaled significantly higher levels of H_2O_2 compared with healthy subjects. In a rather interesting development, in asymptomatic smokers at risk for COPD, H_2O_2 was present in higher and more frequent levels than in controls, thus pointing out that the marker may be linked to an early risk of disease [17].

Given this range of biological information available from breath, EB analysis represents a rapidly developing non-invasive approach to disease diagnosis and therapeutic monitoring. Conventional methods for EB collection involve cooling breath samples with ice or liquid nitrogen to condense the breath into Exhaled

Breath Condensate (EBC). This EBC can then be analyzed in specialized laboratories, although this method has limitations (Fig. 3.2).

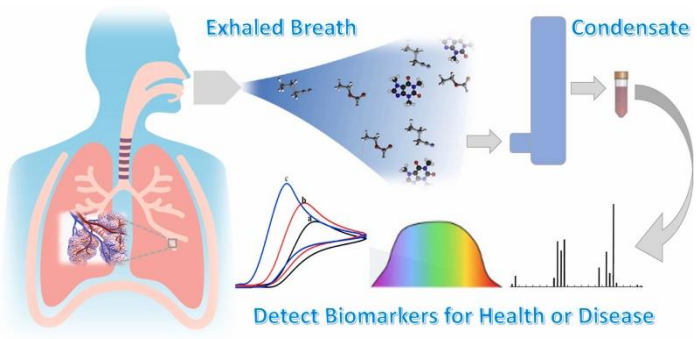

***Figure 3.2**: Exhaled breath analysis for health monitoring and disease detection [18].*

Since EBC collection requires cooling and laboratory equipment, real-time breath analysis in clinical settings remains a challenge [19]. In the last years, nevertheless, various researchers have been working on different technologies that could skip the condensation stage and directly analyze the breath without the use of EBC. Among the main developments in this direction are advanced electrochemical sensor systems enabling real-time in situ monitoring of different biomarkers and indicators in the breath.

For a correct operation, the three electrodes of the electrochemical sensor must maintain electrolytic contact with one another [20]. This requirement poses a challenge for direct breath analysis due to its gaseous nature. As a result, most electrochemical sensors used in breath research still rely on the analysis of EBC rather than the breath aerosol itself [21]. However, progress has been made in addressing this issue. Researchers have explored using absorbent materials, such as paper and biopolymers, to trap the aerosol phase of breath, including its high humidity content [22]. These materials can effectively humidify and bring the electrodes into electrolytic contact, ensuring the analysis of breath components without condensation.

3.2 Materials and Methods

3.2.1 Sensor Fabrication

Sensors were fabricated by mechanically peeling off the silver layer from compact discs (CDs) using double-sided tape [23]. A three-electrode configuration was obtained with a laser cutter (Maitech MT-5030W50), with the spacing between the electrodes optimized to 0.25 mm (Fig. 3.4). Sensors were then fixed on a flexible acetate sheet, and external contacts were made using copper tape. For the reference electrode (RE), an Ag/AgCl paste was applied to produce a pseudo-reference electrode (pseudo-RE), while a graphite layer was added to the counter electrode (CE). The silver working electrode (WE) was not modified. Both the Ag/AgCl and graphite pastes were cured in an oven at 50°C for 30 minutes.

A layer of chitosan, acting as an absorbent material to improve contact between electrodes and electrolyte, was then deposited on the three electrodes. Chitosan was deposited at room temperature using the Electrophoretic Deposition (EPD), a very simple and low-cost method [24]. Chitosan, soluble at pH less than 6.5 [25], was dissolved at 5 g L^{-1} in 0.3 M lactic acid at 50 °C [26]. The sensor (with its three short-circuited electrodes) and a platinum mesh were immersed into the chitosan solution. For the electrodeposition, a potential of 10 V was applied for 30 min. Fig. 3.3 shows the several steps involved in sensor fabrication.

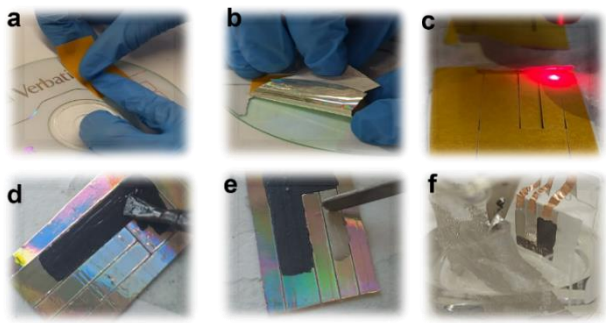

***Figure 3.3**: Sequence of steps for sensor fabrication: a) double-sided is applied to the CD, b) the silver layer is removed from the CD, c) the electrodes are cut by a CO_2 laser, d) the graphite paste is applied on the CE and e) the Ag/AgCl paste on the pseudo-RE. After drying in the oven, f) chitosan film is deposited on the surface sensor by EPD.*

Fig. 3.4 illustrates a sensor after the full manufacturing process has been completed.

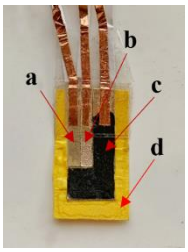

***Figure 3.4**: Photo of the final sensor: a) pseudo-reference electrode coated with Ag/AgCl, b) Ag working electrode, c) graphite counter electrode, and d) acetate support substrate.*

Fig. 3.5 summarizes the main layers that each of the three electrodes is made of.

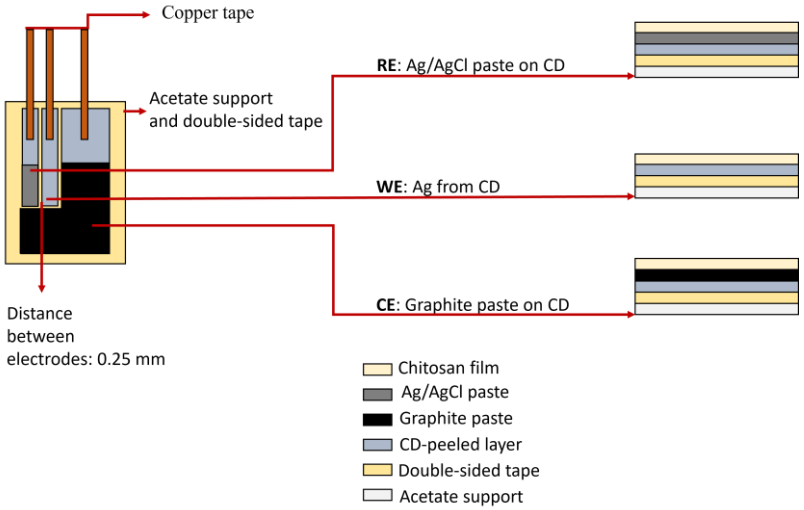

***Figure 3.5**: Representative scheme of the multi-layered electrochemical sensor.*

To increase the ability of the electrochemical sensor to detect hydrogen peroxide in the aerosol phase, further modifications were implemented. Specifically, the working electrode was modified through the electrodeposition of Prussian Blue NanoParticles (PBNPs) before the chitosan deposition. This modification was aimed at detecting the trace concentrations of hydrogen peroxide typically present in exhaled breath. By integrating Prussian Blue, known for its high

electrocatalytic activity toward hydrogen peroxide reduction, the sensor's performance was optimized for more accurate detection of these small concentrations, making it suitable for non-invasive respiratory monitoring applications. To ensure the stability of the WE and prevent the oxidation of silver during subsequent Prussian Blue electrodeposition, the electrode was sputtered with a thin gold layer. As an alternative to gold sputtering, the working electrode can be directly obtained from the gold layer of a CD. The deposition of Prussian Blue nanoparticles was achieved through Pulsed Electrodeposition [27]. It was performed using a platinum wire as CE and an Ag/AgCl electrode as RE, by applying a potential of 0.4 V for 20 s followed by 0.7 V for 10 s over a total time of 300 s (10 cycles). The electrodeposition solution contained 10 mM $FeCl_3$, 10 mM $K_3[Fe(CN)_6]$ [27], and 0.01% chitosan [28] in 0.1 M HCl/KCl. Finally, after the deposition, the Prussian Blue was electrochemically activated by running CVs in a potential window ranging from − 0.05 to 0.35 V vs Ag/AgCl at a scan rate of 50 mV s^{-1} in a solution containing 0.1 M HCl and 0.1 M KCl for 25 cycles. The electrode was finally dried at 100 °C for 30 min and then cooled down to room temperature in the dark [29]. Fig. 3.6 illustrates the sensor after this further modification.

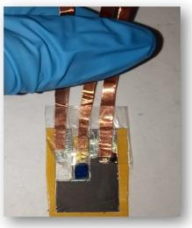

***Figure 3.6**: Photo of electrochemical sensor after PB electrodeposition on WE.*

After the modification of the WE with PBNPs, a layer of chitosan was deposited over the entire sensor surface using the same parameters as previously described. However, in this instance, the electrodeposition process was conducted in the

dark, as Prussian Blue is highly sensitive to light exposure, which could potentially affect its stability and electrochemical properties [30].

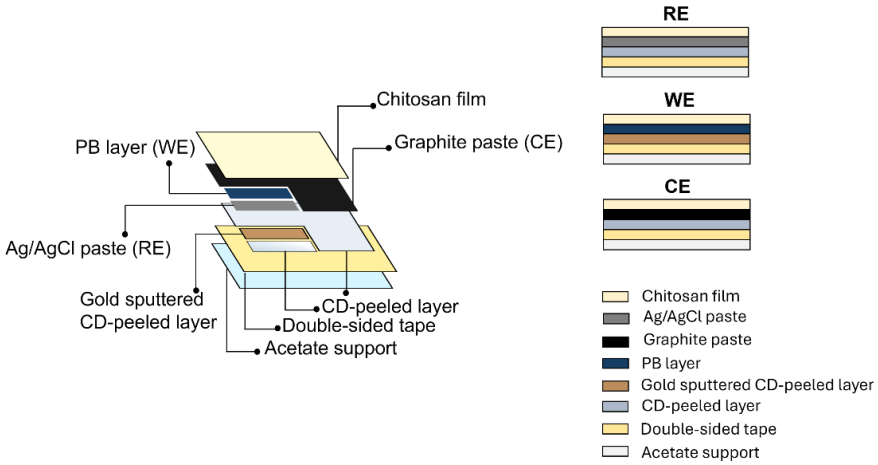

***Figure 3.7**: Representative scheme of the modified electrochemical sensor.*

Fig. 3.7 summarizes the main layers that each of the three electrodes is made of after working electrode modification with Prussian Blue.

3.2.2 Sensor Characterization and Performance

Sensors were characterized using different techniques, including Field Emission Scanning Electron Microscopy (FESEM, FEI, QUANTA 200), Energy Dispersive Spectroscopy (EDS, AMETEK), X-ray Diffraction (XRD, RIGAKU, D-MAX 25600 HK), Raman Spectroscopy (RENISHAW, inVia RAMAN MICROSCOPE) and Fourier Transform Infrared analysis (FT-IR, IRTracer-100, SHIMADZU). All these characterizations were performed at various points on the sensor to study the uniformity of the fabrication process.

Contact angle measurements were conducted to assess the wettability of the sensor surface using a Phosphate Buffer Solution (PBS, pH = 7.4) as the contact fluid. These measurements were performed with an FTA 1000 (First Ten Ångstroms, UK) instrument. Static contact angles were recorded on the WE area

both with and without the chitosan layer, as well as before and after the layer had swelled in PBS. For each measurement, 4 µL droplet of PBS was carefully placed on the sample surface using a micro-syringe, released from a height of 1 cm. The droplet images were captured after 10 seconds, and three droplets were measured for each sample to calculate the mean value of the contact angles.

The electrochemical performance of the sensors was evaluated using a Cell Test System (Solartron, Mod. 1470 E), with data acquisition handled by MultiStat Software.

Regarding the sensor without PB, the effect of the scan rate on H_2O_2 detection was investigated over a range from 10 to 500 mV s^{-1} using a solution containing 5 mM H_2O_2 in PBS. Sensor performance was evaluated through Linear Sweep Voltammetry (LSV) at a scan rate of 10 mV s^{-1}, within a potential range from -0.3 to -1 V versus Ag/AgCl. To evaluate the sensor sensitivity, liquid H_2O_2 solutions with concentrations ranging between 100 µM and 500 µM were prepared by diluting a stock solution of H_2O_2 (30%) in PBS.

A cell fabricated using a Zortrax 3D printer was employed for characterizing the sensor in the liquid phase. To simulate the humid conditions of EB, LSV tests were repeated by nebulizing H_2O_2 solutions of varying concentrations using a commercially available nebulizer (P0111EM F400) at a constant flow rate of 0.15 mL min^{-1}. For aerosol-phase tests, the sensor was first immersed in PBS for 20 minutes to ensure that the chitosan layer swelled. The nebulized H_2O_2 solutions were then exposed to the sensor for approximately 10 seconds, ensuring uniform wetting. Calibration curves were obtained by employing a baseline subtraction method, plotting peak current density against the corresponding H_2O_2 concentration.

This sensor was employed to quantify H_2O_2 released by 16HBE cells in the culture medium. To simulate the EB environment, the culture medium was nebulized, and measurements were carried out in the aerosol phase. In addition, to evaluate the selectivity of the sensor, LSV tests were also performed in the presence of

interfering species. Different substances were selected because they are present in cell culture media or because they are produced by cells during growth. In particular, the interference towards NaCl, glucose, HEPES, $NaNO_3$, and lactic acid was tested. Each interferent was tested at a concentration 10 times higher than that of H_2O_2 to assess any interference.

The performance of the sensor with PB was evaluated through Chronoamperometry (CA) at 0.05 V vs Ag/AgCl pseudo-RE [31]. A solution containing 0.1 M K_2HPO_4/KH_2PO_4 and 0.1 M KCl (pH = 7.4) was used as blank, adding increasing concentrations of hydrogen peroxide [32]. Initially, tests in the liquid phase were carried out on the modified WE before the deposition of chitosan to confirm its capability of detecting hydrogen peroxide concentrations below 10 µM, typical for exhaled breath samples.

All tests were repeated at least three times, using fresh electrodes and solutions for each test.

3.2.3 Cell Culture, Stimulation, and Flow Cytometry Analysis

The tests described in this section were conducted in collaboration with the Institute of Translational Pharmacology (National Research Council) of Palermo and the Ri.MED Foundation.

The immortalized human normal bronchial epithelial cell line, 16HBE, was cultured in Minimum Essential Medium (MEM). The cells were pre-treated with N-acetylcysteine (NAC) at a concentration of 1 mM for 2 h, followed by treatment with Formoterol (FORM) at 10^{-8} M for 30 min. After this pre-treatment, the cells were exposed to Cigarette Smoke Extract (CSE) at 20% for 24 h. CSE was prepared by burning two unfiltered cigarettes (3R4F, Kentucky, The Tobacco Research Institute, University of Kentucky) in 20 mL of PBS using a Watson-Marlow 323 E/D peristaltic pump. The solution was filter-sterilized using a 0.22 µm pore filter and was 100% CSE.

After stimulation, the culture medium was collected for H_2O_2 released using a sensor. Cells were also harvested to evaluate intracellular oxidative stress by flow cytometry using the Mito-SOX™ Red probe.

In addition, Exhaled Breath Condensation (EBC) was collected by the Turbo DECCS System-Medivac, according to the procedure described by Galiniak et al. [33], which allows for the non-invasive collection of exhaled air condensate. The subjects inhaled at a tidal volume using a mouthpiece for 10 minutes without using a nose clip. The condensation temperature was set at -5.5°C. Immediately after collection, the EBC samples were centrifuged for 5 minutes at 1000 g and then frozen at -80°C until analysis.

3.3 Results and Discussion

3.3.1 Fabrication and Characterization of Sensor without PBNPs

One of the main steps involved in the sensor fabrication process is the deposition of the chitosan layer by EPD. The process has been developed to realize a thin, homogeneous, and uniform chitosan film all over the sensor's surface. The main function of this chitosan layer is to absorb the aerosol phase from exhaled breath. Given the high humidity of the aerosol, the chitosan layer swells, creating electrolytic contact between the electrodes. So, hydrogen peroxide diffuses through this layer towards the surface of the working electrode, where it is detected.

The EPD of chitosan occurs through a series of chemical reactions [34], [35]:

$$\text{Chit-NH}_2 + \text{H}_3\text{O}^+ \rightarrow \text{Chit-NH}_3^+ + \text{H}_2\text{O} \qquad (3.1)$$

$$2\text{H}_2\text{O} + 2e^- \rightarrow \text{H}_2 + 2\text{OH}^- \qquad (3.2)$$

$$\text{O}_2 + 2\text{H}_2\text{O} + 4e^- \rightarrow 4\text{OH}^- \qquad (3.3)$$

$$\text{Chit-NH}_3^+ + \text{OH}^- \rightarrow \text{Chit-NH}_2 + \text{H}_2\text{O} \qquad (3.4)$$

In reaction (3.1), the amine groups of the chitosan are protonated in the low pH environment. These positively charged macromolecules are then drawn towards

the cathode under the influence of an electric field. As reactions (3.2) and (3.3) occur [36], the local pH near the cathode rises, and when an interfacial pH value of about 6.5 (corresponding to the pKa of chitosan [37]), due to the electrochemical generation of hydroxide ions, leading to the deposition of insoluble chitosan, as described in reaction (3.4). Fig. 3.8 shows a schematic representation of chitosan EPD on the surface sensor.

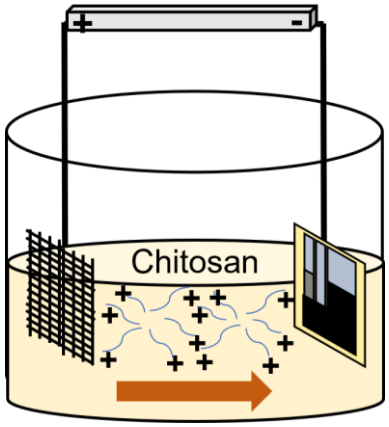

***Figure 3.8**: Schematic representation of the EPD process.*

The deposition process was optimized by varying parameters such as the chitosan solution concentration, deposition time, and applied potential. Tab. 3.1 summarizes the experimental parameters used for optimizing chitosan deposition:

***Table 3.1**: Values of parameters explored for optimizing chitosan deposition.*

Parameter	Value
Solution Concentration / g L^{-1}	1 and 5
Deposition Time / s	1800 and 3600
Deposition Potential / V	5 and 10

The results showed that increasing the concentration of the chitosan solution and the applied potential led to a more compact and uniform film. However, extending the deposition time increased the film thickness, which could reduce the sensor's

sensitivity [38]. The optimized condition for chitosan deposition was identified as a concentration of 5 g/L with an electrodeposition time of 1800 seconds at 10 V. Once fabrication was completed, the sensor was characterized using several physical-chemical techniques. Fig. 3.9a presents SEM images of the Ag-based electrode before the electrochemical deposition of chitosan film. The metallic layer exhibited a series of parallel and uniformly structured silver tracks, measuring approximately 838 ± 17 nm in width [23]. The corresponding EDS spectrum (Fig. 3.9b) confirms the presence of elements such as carbon (C), oxygen (O), titanium (Ti), silicon (Si), sulfur (S), and calcium (Ca), which originate from the substrate (including the acetate substrate).

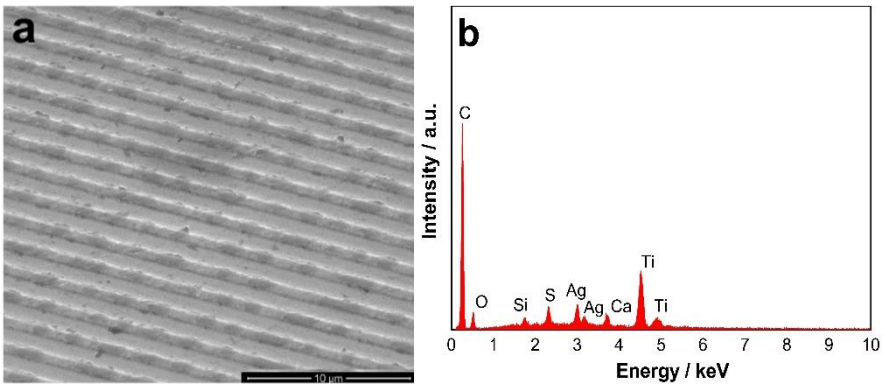

***Figure 3.9**: a) SEM image of CD-peeled layer and corresponding b) EDS spectrum.*

The typical morphology of the chitosan film [39] is shown in Figure 3.10.

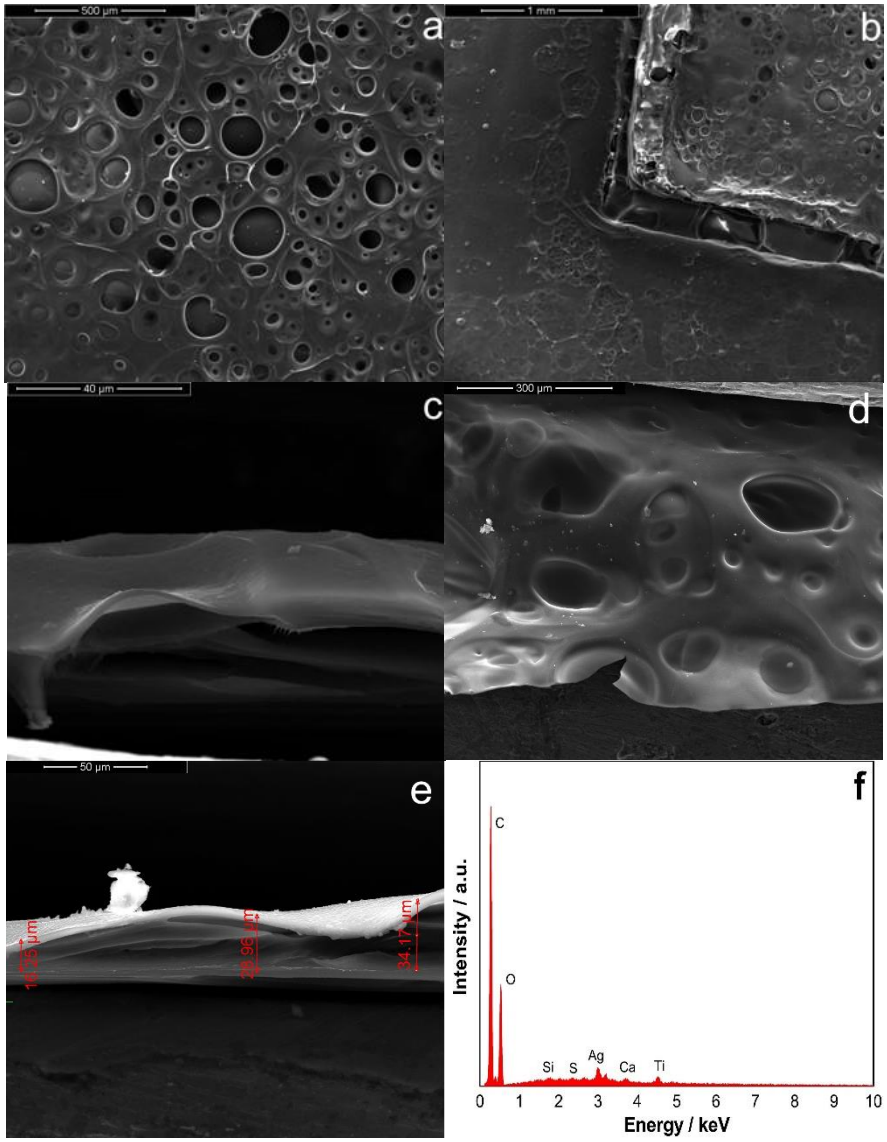

***Figure 3.10**: Chitosan layer before swelling: a) SEM image of WE area b) SEM image of the area between CE and WE c) tilted cross-sectional view of chitosan layer peeled from WE d) another cross-sectional view of chitosan film e) measurements of film thickness f) EDS spectrum of chitosan film on CD-peeled layer.*

In Fig. 3.10a, a highly wrinkled sponge-like morphology is evident, characterized by the presence of pores of varying sizes. This distinctive structure is attributed to the entrapment of hydrogen gas produced during the reaction (3.2) [40], [41]. Furthermore, Figure 3.10b confirms that the chitosan film is uniformly deposited

across the entire sensor surface, including the gap between CE and WE. This uniform coverage is a significant achievement, as it guarantees continuous electrolytic contact between the three electrodes essential for the sensor operation. To better analyze the internal morphology of the chitosan layer, it was peeled off from the working electrode area and the cross-section was prepared for detailed examination. The cross-sectional images (Fig. 3.10c-d) show that the pores that appear on the surface are a thinner area of chitosan. In Figure 3.10e, the SEM image of the cross-sectional view demonstrates a multilayered structure, with the thickness of the chitosan layer ranging from approximately 10 µm to 40 µm. The EDS analysis (Fig. 3.10f), reveals the presence of carbon (C) and oxygen (O), in confirmation of the deposition of chitosan. Other elements detected are attributed to the peeled CD layer used in the sensor fabrication [23].

The deposited chitosan layer was further examined using an optical microscope. Fig. 3.11 shows the surface of each electrode before and after the chitosan layer underwent swelling in PBS. These images highlight changes in surface texture. The swelling process causes the surface roughness to smooth out, resulting in a more homogeneous gel-like layer. The swelling behavior is important for the sensor performance, as it facilitates the diffusion of the target analytes to the working electrode where detection occurs [42].

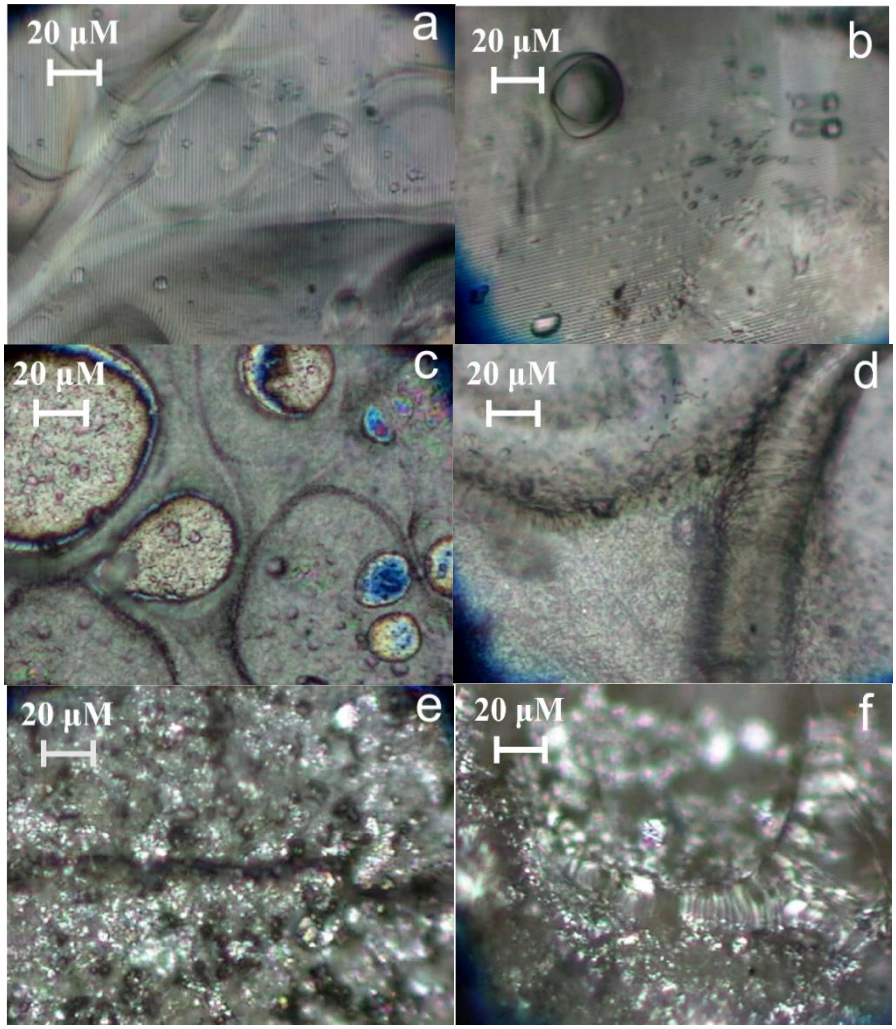

***Figure 3.11**: Optical image of chitosan film on WE (a-b), CE (c-d), and RE (e-f) before and after swelling.*

In Fig. 3.12, the diffraction patterns of the CD-peeled layer before and after the deposition of the chitosan film were reported. By comparing the diffraction peaks with the ICDD database (card number 39-1894 for chitosan and 04-0783 for silver), the materials present on these surfaces were accurately identified [43].

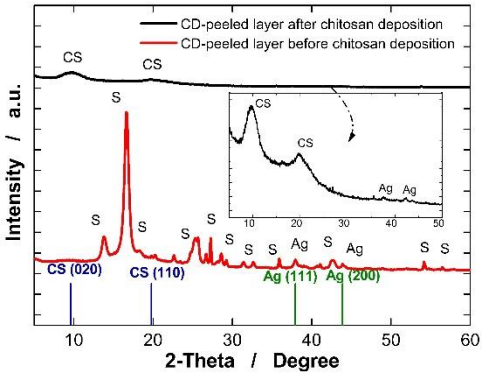

***Figure 3.12**: XRD pattern of CD-peeled layer before and after the deposition of chitosan film (S = substrate).*

The red pattern corresponds to the CD-peeled layer before chitosan deposition. Distinct diffraction peaks at approximately 38.3° and 44.5° were observed, indicating the (111) and (200) planes of the face-centered cubic (FCC) structure of silver. Additional peaks, labeled "S", originate from the substrate of the CD-peeled layer [23]. After the deposition of the chitosan film (black pattern) two broad and low-intensity peaks at approximately 9.6° and 19.8° were noted. These peaks correspond to the (020) and (110) planes of semicrystalline chitosan [34], [44], [45]. The appearance of these peaks highlights the formation of the chitosan layer. Interestingly, the chitosan film reduces the intensity of the peaks coming from the CD-peeled layer. In the inset of Figure 3.11, an enlarged view of the black pattern is provided, where the masked peaks from the CD-peeled layer can be weakly detected, indicating the effective coverage of the silver substrate by the chitosan layer.

The sensor was also characterized by micro-Raman spectroscopy and FT-IR analysis. These analyses were performed on the three electrodes of the sensor to confirm the presence of the different materials.

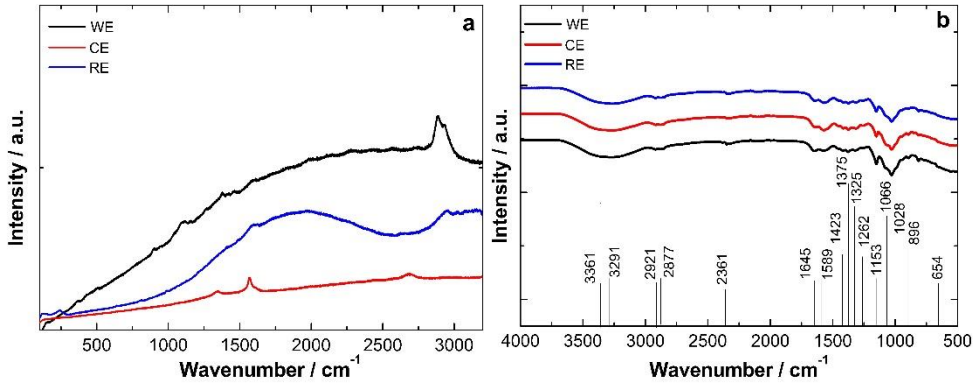

***Figure 3.13**: a) Raman and b) FT-IR spectra collected after the chitosan electrodeposition.*

Fig. 3.13a presents the Raman spectra collected from the CE, WE, and RE. In the spectrum of the CE (CD-peeled layer/ graphite paste/ chitosan layer), all the Raman modes are attributed to graphite [46]. In particular, both the first-order (1328 cm^{-1} (D1 band) and 1577 cm^{-1} (G band)) and the second-order (2685 cm^{-1} (2D band)) Raman bands are present. The weak defect-induced bands at 2437 cm^{-1} (G* band) and 2942 cm^{-1} (D+G band) can be observed with low intensity [47]. Polymer fluorescence emission is also evident. In the working electrode (CD-peeled layer/ chitosan layer), despite strong fluorescence emission [48], several characteristic Raman modes of chitosan were identified (Table 3.2) [45], [49], [50], [51], confirming the presence of the polymer. These Raman bands do not appear in the CE spectrum, as they are hidden by the graphite bands. For the RE (CD-peeled layer/ Ag-AgCl paste/ chitosan layer), several chitosan Raman bands are weakly visible due to interference from the fluorescence signal. The presence of AgCl is confirmed by modes around 145 cm^{-1} and 237 cm^{-1} [52].

***Table 3.2**: Wavenumbers of the bands observed in the Raman spectra for chitosan and their assignment to the respective normal vibrations.*

Wavenumber	Assignment
2932vs	$\nu(CH_3)$
2885vs	$\nu(CH_2)$
2818shm	$\nu(CH_3)$
2743w	$\nu(CH)$
1591m	$\delta(NH_2)$
1458m	$\delta(CH) + \omega(CH_2) + \delta(OH)$
1411m	$\delta_S(CH_3) + \delta(CH)$
1377s	$\delta(CH_2) + \delta(CH) + \delta(OH) + \nu(\phi)$
1263m	$\delta(OH...O) + \nu(C\text{-}C) + \nu(C\text{-}O) + \delta(CH) + \rho(CH_2)$
1146m	$\nu(C\text{-}O\text{-}C) + \nu(\phi) + \nu(C\text{-}OH) + \nu(C\text{-}CH_2) + \delta(CH) + \rho(CH_2) + \rho(CH_3)$
1114s	$\nu(C\text{-}O\text{-}C) + \nu(\phi) + \nu(C\text{-}OH) + \nu(C\text{-}CH_2) + \delta(CH) + \rho(CH_2) + \rho(CH_3)$
1093s	$\nu(C\text{-}O\text{-}C) + \nu(\phi) + \nu(C\text{-}OH) + \nu(C\text{-}CH_2) + \delta(CH) + \rho(CH_2) + \rho(CH_3)$
1044shm	$\rho(CH_3) + \delta(CH) + \delta(OH)$
896m	$\nu(\phi) + \rho(CH_2)$
493m	$\delta(CO\text{-}NH) + \delta(C\text{-}CH_3)$
357m	$\Upsilon(OH) + \Upsilon(\phi)$

In Fig. 3.13b, the FT-IR spectrum shows the characteristic peaks of the chitosan film. A strong band between 3361 and 3291 cm^{-1} corresponds to the stretching of N-H and O-H groups. The bands at 2921 cm^{-1} and 2877 cm^{-1} are attributed to asymmetric and symmetric C-H stretching vibrations, respectively. The peaks around 1645 cm^{-1} and 1325 cm^{-1} are characteristic of the C=O stretching of amide I and the C-N stretching of amide III, respectively. A band at 1589 cm^{-1} is linked to the N-H bending of primary amines. Further confirmation is provided by the bands at 1423 cm^{-1} and 1375 cm^{-1}, which reflect CH_2 bending and CH_3 symmetrical deformations. The band at 1153 cm^{-1} is associated with asymmetric C-O-C bridge stretching, while signals at 1066 cm^{-1} and 1028 cm^{-1} are indicative of C-O stretching. Additional features include bands at 1260 cm^{-1}, 896 cm^{-1}, and 654 cm^{-1}, corresponding to -OH bending, -CH out-of-plane vibration, and -NH twist vibration, respectively [53], [54], [55]. These peaks are observed across the working, counter, and reference electrodes, confirming the successful and uniform deposition of the chitosan film across the entire sensor surface.

The wettability of the sensor surface, both with and without the chitosan film, was evaluated by measuring the contact angle using PBS as the wetting liquid. A decrease in contact angle value is expected with an increase in the surface hydrophilicity. As illustrated in Fig. 3.14, the contact angle for the CD-peeled layer was approximately 89 ± 3.7°, indicating a moderately hydrophobic surface. However, when the CD-peeled layer was coated with chitosan and air-dried, the contact angle was significantly reduced to ~52± 4.5°, demonstrating enhanced hydrophilicity. This hydrophilicity increased even further when the chitosan film was swelled in PBS [56], [57], bringing the contact angle down to an impressively low ~5 ± 2.3°. This decrease in the contact angle highlights the ability of chitosan to facilitate rapid and efficient wetting of the entire sensor surface when hydrated. The high initial contact angle of the Ag layer, which was nearly hydrophobic due to its rough morphology, reinforces the importance of the chitosan layer in modifying the sensor surface properties. The very low value measured in the case of the swelled film indicated the ability of the chitosan to create a highly wettable surface ensures proper electrolytic contact, improving the sensor's effective performance in an aerosol environment [58].

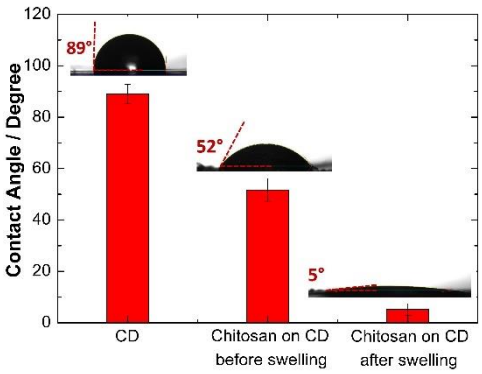

***Figure 3.14**: Mean values of contact angle measured on CD-peeled layer before and after chitosan deposition and before and after chitosan swelling.*

The electrochemical response towards hydrogen peroxide was examined using CV performed at various scan rates, with 5 mM H_2O_2 in PBS. As shown in Fig. 3.15a, an increase in the scan rate resulted in a shift of the reduction peaks toward

more cathodic potentials. There were no corresponding oxidation peaks, suggesting that the redox process of H_2O_2 is irreversible [59].

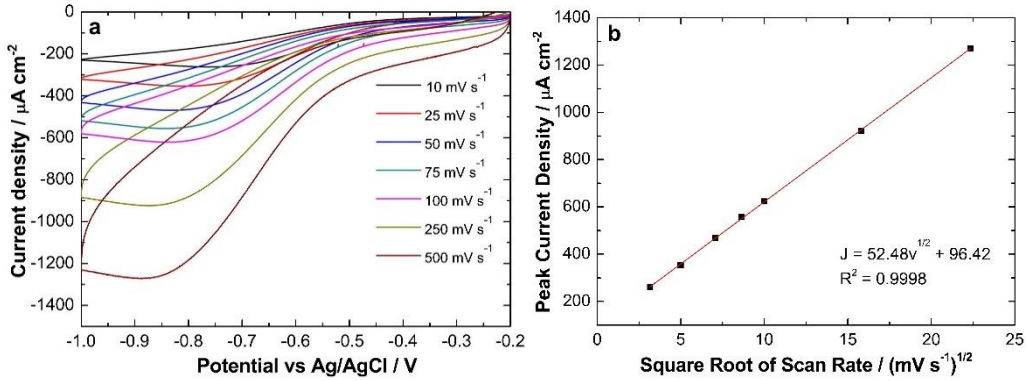

***Figure 3.15**: a) CVs performed in the potential range from - 0.2 V to -1 V vs Ag/AgCl in PBS containing H_2O_2 5 mM. b) Effect of scan rate on peak current density.*

In Fig. 3.15b, a clear linear relationship can be seen between the reduction current density peak and the square root of the scan rate, with a high correlation coefficient ($R^2 = 0.9987$). According to L. Zhang et al. [60] and X. Cai et al. [59], this result indicates that the H_2O_2 reduction is a diffusion-controlled process.

3.3.2 Electrochemical Performance of Sensor without PB

LSV, employed as the detection technique, was carried out in both liquid and aerosol phases to provide a comparative analysis of the sensor behavior across different conditions. In the liquid phase, LSV was performed over a potential range of 0.1 V to -1 V vs Ag/AgCl pseudo-RE, using PBS as blank.

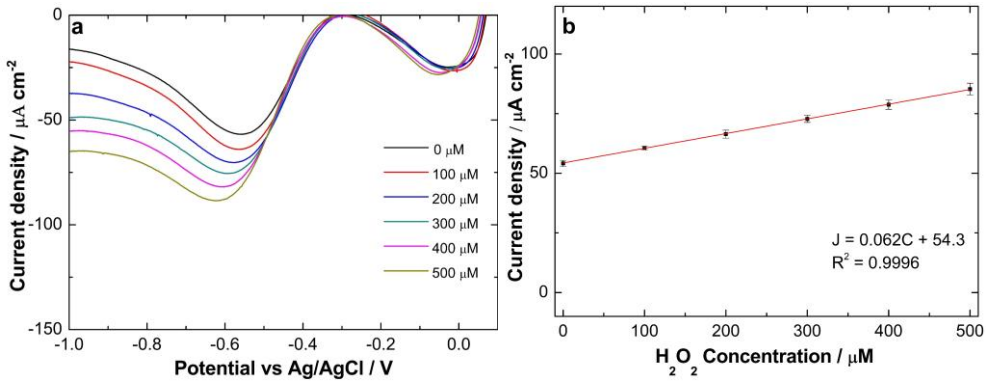

***Figure 3.16**: a) LSV tests in liquid solutions at different concentrations of H_2O_2 and b) corresponding calibration line with SD error bars (N = 3).*

In Fig. 3.16a, LSV curves for varying concentrations of H_2O_2 are presented, with baseline subtraction applied. Two distinct peaks were observed, even in the blank solution voltammogram (represented by the black curve). The first peak, at around 0 V, is independent of the increasing H_2O_2 concentration in the solution, while the second peak, at approximately -0.6 V, shows a direct correlation with the concentration of H_2O_2. The first peak is attributed to the reduction of dissolved oxygen to H_2O_2, following the reaction [61], [62]:

$$O_2 + 2H_2O + 2e^- \rightarrow H_2O_2 + 2OH^- \quad (3.5)$$

The second peak corresponds to the reduction of H_2O_2 to water, described by the reaction [63], [64]:

$$H_2O_2 + 2H^+ + 2e^- \rightarrow 2H_2O \quad (3.6)$$

As shown in Fig. 3.16a, the intensity of this second peak increases linearly with the concentration of H_2O_2 in the range of 100 µM to 500 µM. The shift in the potential peak of the hydrogen peroxide reduction agrees with Nernst's equation [59], [65]. From the calibration line reported in Fig. 3.16b, a sensitivity of 0.062 ± 0.0024 µA μM^{-1} cm^{-2} (R^2 = 0.9996) was obtained. A Limit of Detection (LOD) of 60 µM was calculated using the equation:

$$LOD = 3.3\frac{SD}{S} \quad (3.7)$$

,where SD represents the standard deviation of the blank response (obtained from 10 blank measurements), and S is the sensor's sensitivity.

To simulate a real H_2O_2 detection in exhaled breath, LSV tests were performed by exposing the sensor to nebulized solutions. Before these tests, the sensor was immersed in PBS to allow the chitosan layer to swell, ensuring it was well-prepared for the interaction with nebulized solutions. The LSV curves were recorded after 10 s of nebulization, ensuring the sensor was homogeneously impregnated with the nebulized solutions. Notably, the pre-immersion in PBS to swell the chitosan layer could be avoided in future tests. Through experimental trials, it was observed that even without this initial swelling, the sensor stabilized after approximately 1 minute of exposure to the nebulized solution. This result suggests that while pre-treatment may accelerate sensor activation, it is not strictly necessary for stable and reliable sensor performance.

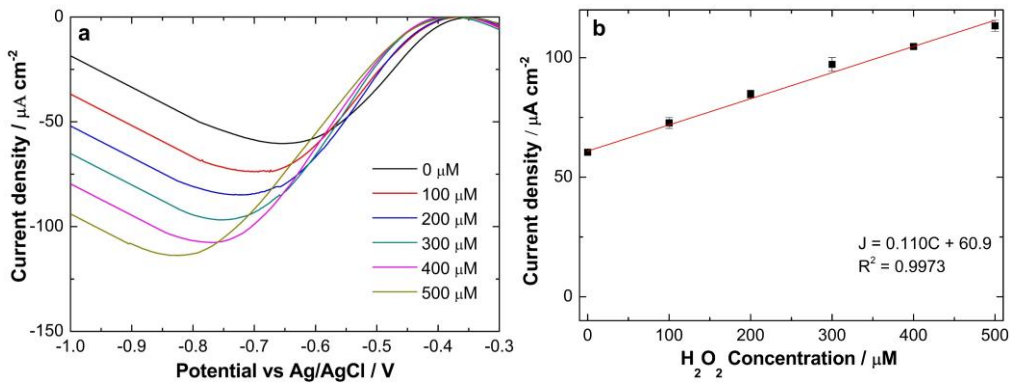

***Figure 3.17**: a) LSV tests in nebulized solutions at different concentrations of H_2O_2 and b) corresponding calibration line with SD error bars (N = 3).*

Fig. 3.17 shows the LSV curves for hydrogen peroxide detection in nebulized solutions (Fig. 3.17a) and the corresponding calibration line (Fig. 3.17b). From these experiments, a sensitivity of 0.110 ± 0.0042 µA μM^{-1} cm^{-2} (R^2 = 0.9973) was obtained and a LOD of 30 µM was calculated. This sensitivity is higher than values reported in previous literature concerning hydrogen peroxide quantification in aerosol phase (Tab. 3.3).

***Table 3.3**: Comparison between electrochemical sensors for H_2O_2 detection in aerosol/gas phase.*

SPE= Screen Printed Electrode CB=Carbon Black PBNPs=Prussian Blue Nanoparticles PB=Prussian Blue CA=Chronoamperometry NS=Not Shown LSV=Linear Sweep Voltammetry

Sensor Type	Detection Method	Sensitivity/ µA μM^{-1} cm^{-2}	Linear Range / mM	LOD / µM	Real Sample	Ref.
Paper-based electrochemical sensor (filter paper and SPE modified with CB/PBNPs)	CA	$1.97*10^{-4}$	324 - 2294	NS	NS	[31]
Paper-based electrochemical sensor (chromatography paper and SPE using PB-modified ink)	CA	0.002	0.04 – 0.32	NS	NS	[66]
Pt-Nafion	CA	0.28	0.003 – 1.18	1.18	NS	[67]
Ag based electrode with chitosan film	**LSV**	**0.110**	**0.1 – 0.5**	**30**	**16HBE cells subjected to different treatments**	**This work**

The sensor demonstrated a linear response to H_2O_2 concentrations ranging from 100 µM to 500 µM with a low mean deviation. The results are promising as they demonstrate the ability of the sensor to operate efficiently within an aerosol phase without any decline in performance when compared to liquid-phase detection. The mean Relative Standard Deviation (RSD) was also evaluated for liquid and aerosol solutions. The mean RSD was approximately 3.8% in the liquid solution, while it was around 4% in the aerosol. These low RSD values indicate that the proposed fabrication method is highly reproducible, resulting in sensors with coherent properties and performance across multiple tests. Furthermore, the higher sensor sensitivity in nebulized solutions aligns with similar findings from Fiore et al. [31]. The increased sensitivity observed in the aerosol phase compared

to the liquid phase can be attributed to the absorbent nature of the chitosan layer, which facilitates the pre-concentration of the analyte. In particular, when the chitosan layer is exposed to the aerosol phase, it dries rapidly due to water evaporation, causing the analyte to become concentrated within the sensor. This led to a higher concentration and, consequently, higher sensitivity. To verify this pre-concentration effect, hydrogen peroxide tests were performed after different times of nebulization. A solution with the same concentration of H_2O_2 was nebulized for 10, 30, 60, and 120 seconds. After LSV measurements were performed. The results, shown in Fig. 3.18, reveal that after 60 seconds of nebulization, the detected H_2O_2 was approximately double the amount measured after 10 seconds. This suggests that prolonged time enhances the concentration of the analyte on the sensor surface. However, it cannot be extended indefinitely without causing the sensor to reach its absorption limit, as indicated by the plateauing trend in the figure. Thus, the sensitivity of the sensor can be increased by adjusting the nebulization time and by further optimizing the thickness of the chitosan film. When the sensor is immersed in a liquid phase, this pre-concentration phenomenon does not occur due to the short analysis times.

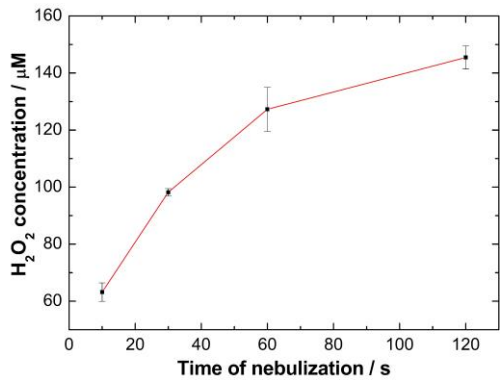

***Figure 3.18**: H_2O_2 detected from the sensor after different times between nebulization and measurement.*

The sensor flexibility was assessed by evaluating its performance after different physical deformation cycles. In particular, the sensor was subjected to bending

and twisting (as shown in Fig. 3.19) for five consecutive cycles. After these deformations, the sensor was tested for hydrogen peroxide detection in the aerosol phase. The bent and twisted electrodes exhibited the same performance as the undeformed sensor (Fig. 3.20). This demonstrates that these mechanical stresses did not compromise sensor functionality. These findings strongly reinforce the sensor reliability, highlighting its potential for integration into face masks without any degradation in performance. This makes it highly suitable for practical applications where flexibility is essential.

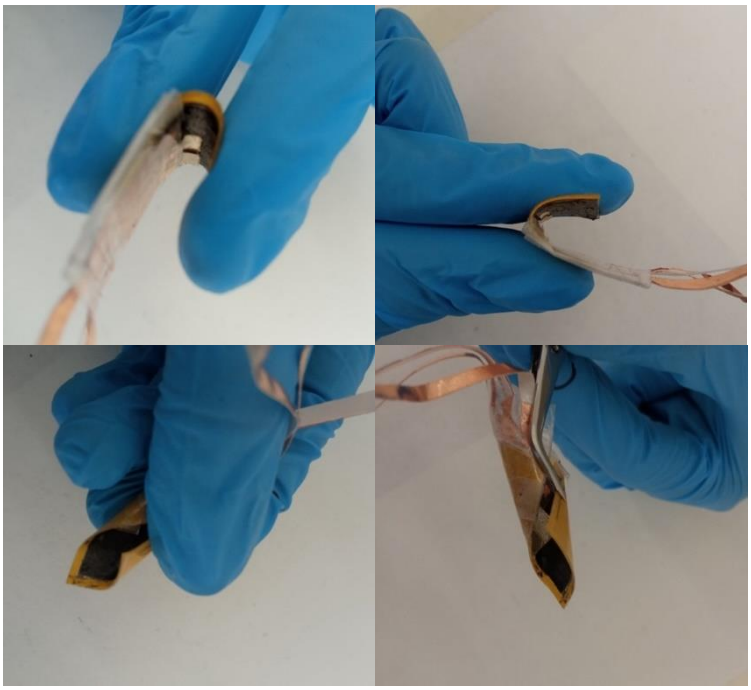

***Figure 3.19**: Images of the sensor after different deformation.*

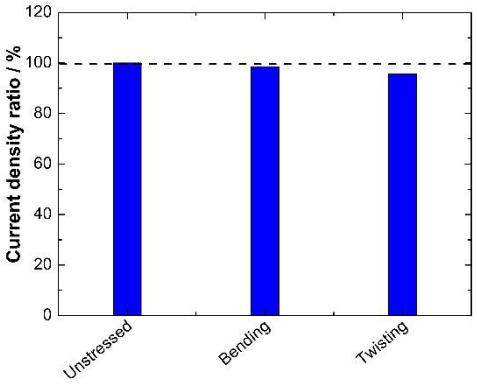

***Figure 3.20**: Effect of deformations on the H_2O_2 detection.*

Sensor performances were evaluated in complex matrices by quantifying hydrogen peroxide in a nebulized conditioned medium of 16HBE cells. Before these measurements, sensor performance was assessed in the presence of potential interfering species, such as glucose, HEPES, lactic acid, sodium chloride, and sodium nitrate, commonly found in culture media or produced by cells [68], [69]. A concentration of 1 mM of each interferent was added to a nebulized solution containing 0.1 mM of H_2O_2 to simulate challenging conditions.

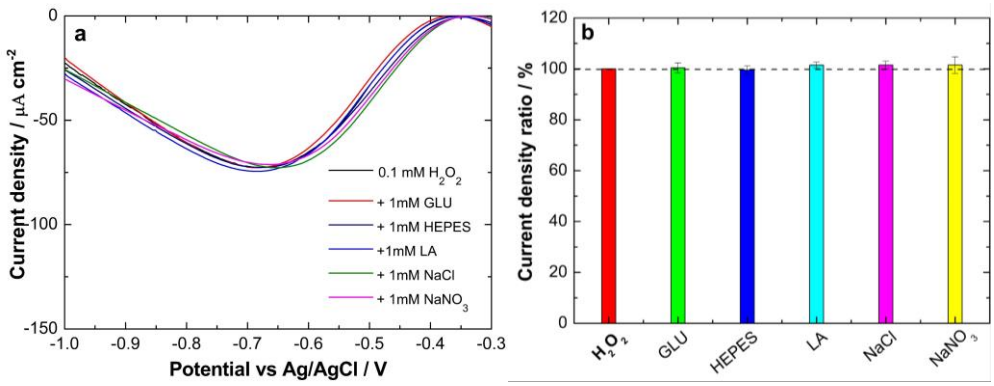

***Figure 3.21**: a) LSV tests in PBS solution containing 0.1 mM of H_2O_2 and 1 mM of interfering species and b) effect of interfering species on the H_2O_2 detection (GLU: glucose; LA: Lactic Acid).*

As shown in Fig. 3.21, even though the concentration of the interfering species was 10 times higher than that of H_2O_2, their effect on the peak current density and

potential was negligible. This result confirms that the sensor has high selectivity to H_2O_2. To accurately quantify H_2O_2 in cell culture media, a calibration curve was created using the 16HBE cell culture medium (MEM) as a blank. This step was important to account for the complex nature of MEM and any potential interference it might introduce [70]. Various concentrations of H_2O_2 were added to the MEM, and LSV measurements were performed (Fig. 3.22a). The resulting calibration line (Fig. 3.22b) indicated a sensitivity of 0.098 ± 0.0022 μA μM^{-1} cm^{-2} ($R^2 = 0.9958$), with a mean RSD of approximately 2% and a LOD of 40 μM.

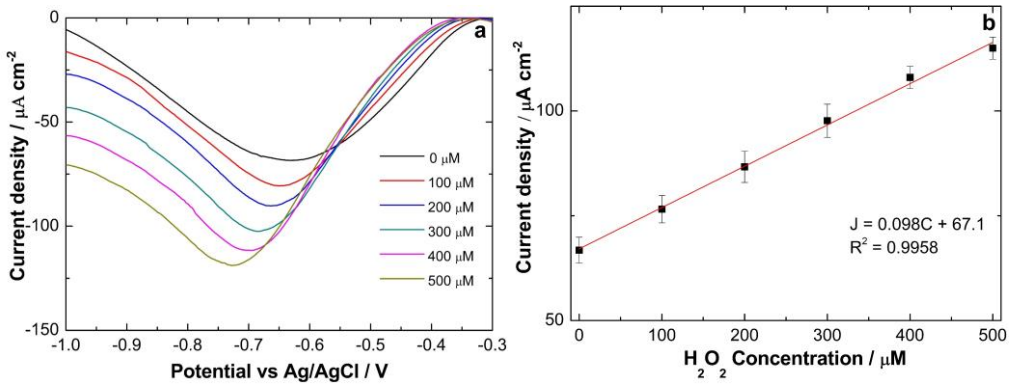

***Figure 3.22**: a) LSV tests in the aerosol phase of MEM with different concentrations of H_2O_2 and b) corresponding calibration line with SD error bars (N = 3).*

These values were very similar to those obtained using nebulized PBS, suggesting that the sensor performance remains stable and reliable even in the MEM. Tab. 3.4 summarizes the key performance characteristics of the sensor in different testing conditions.

***Table 3.4**: Main features of the electrochemical sensor.*

Electrolyte	Sensitivity / μA μM^{-1} cm^{-2}	Mean RSD / %	LOD / μM
Liquid PBS	0.062	3.8	60
Aerosol PBS	0.110	4	30
Aerosol MEM	0.098	2	40

Detection of hydrogen peroxide in the aerosol phase of nebulized culture media obtained from 16HBE cells was performed. Cells were exposed or not to Cigarette

Smoke Extract (CSE) and/or pre-treated with N-acetylcysteine (NAC) and Formoterol (FORM). These two drugs have antioxidant properties and are commonly used in treating chronic respiratory conditions [71], [72]. NAC acts as a mucolytic agent, while FORM is a long-acting beta-2 agonist.

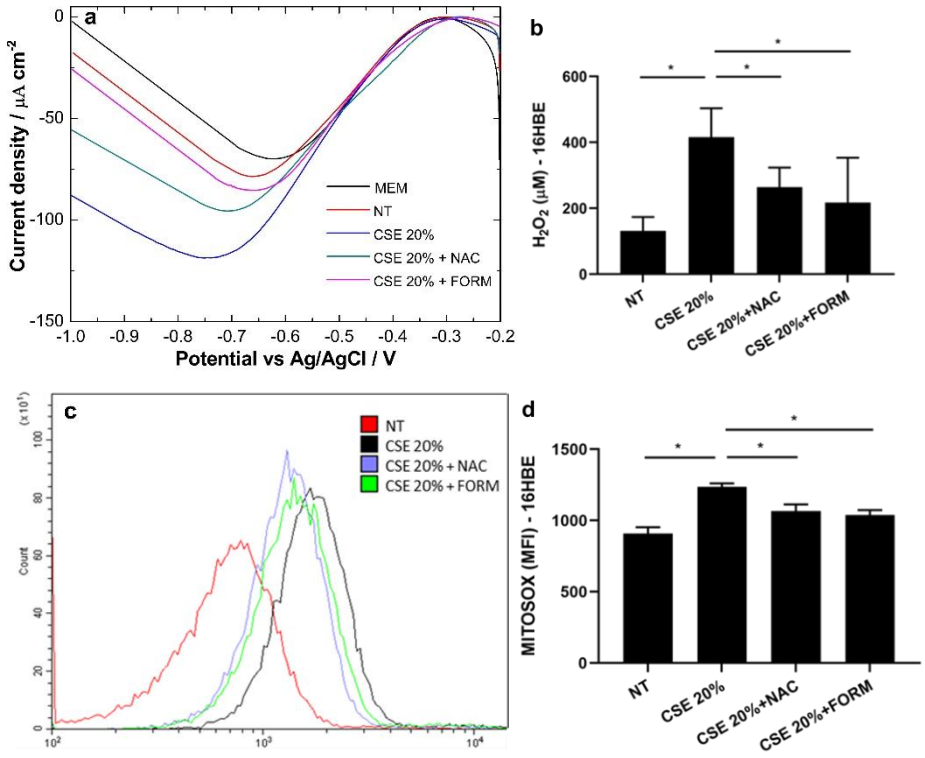

***Figure 3.23**: a) LSV tests in the aerosol phase of nebulized culture media obtained from 16HBE b) mean concentration of H_2O_2 present in the samples (NT: non-treated cells; CSE: cells treated with cigarette smoke extract; CSE + NAC: cells treated with cigarette smoke extract and N-acetylcysteine; CSE + FORM: cells treated with cigarette smoke extract and Formoterol). N = 3 independent experiments c) mitochondrial superoxide detection by flow cytometry using Mitosox Red probe: representative flow cytometric analysis d) mitochondrial superoxide production reported as Mean Fluorescence Intensity (MFI) ± SD (N = 3), *p < 0.05 Paired t-test.*

Fig. 3.23a shows LSV curves for different samples and Fig. 3.23b presents the mean concentrations of H_2O_2 based on the calibration line shown in Fig. 3.22b. CSE treatment significantly increased H_2O_2 production, while treatment with NAC and FORM reduced it.

To confirm these results, intracellular oxidative stress was evaluated by measuring mitochondrial superoxide levels using a ROS-sensitive fluorescent probe and flow cytometry, the gold standard for intracellular ROS quantification. After stimulation, cells were stained with Mitosox Red and analyzed by flow cytometry. The results (Figures 3.23c and 3.23d) confirmed that CSE exposure significantly increased mitochondrial superoxide levels compared to non-treated (NT) cells and the pre-treatment with NAC and FORM effectively reduced this effect. So, these flow cytometry results mirrored those obtained via sensor measurements.

Further tests were conducted to ensure the effectiveness of the sensor under real-world conditions. Exhaled Breath Condensate (EBC) samples from healthy subjects were collected with known concentrations of H_2O_2 and LSV curves were recorded (Fig. 3.24).

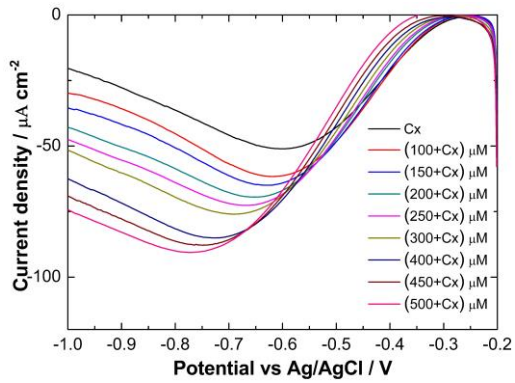

***Figure 3.24**: LSV tests in real EBC (Cx) before and after adding different amounts of hydrogen peroxide.*

This experiment was designed to determine whether the EBC matrix might interfere with the ability of the sensor to detect H_2O_2. The results demonstrated that the sensor accurately detected H_2O_2 in real breath matrices without interference, suggesting that the proposed sensor can be applied to the monitoring of cellular oxidative stress.

3.3.3 Fabrication and Characterization of Sensor with PB

After successfully demonstrating the ability of the sensor to detect hydrogen peroxide concentrations in the aerosol phase, it has undergone further optimization to enhance its sensitivity. The WE was modified through the electrodeposition of PBNPs before the deposition of chitosan. This modification specifically aims to detect the trace concentrations of hydrogen peroxide typically present in exhaled breath [73], making the sensor a valuable tool for non-invasive respiratory monitoring applications. Following the sputtering of the WE with a thin gold layer, Prussian Blue nanoparticles were subsequently deposited using a Pulsed Electrodeposition technique. To optimize the electrodeposition process, key parameters were varied, including the reduction voltage (V_R) and reduction time (T_R), as well as the oxidation voltage (V_O) and oxidation time (T_O). Additionally, the number of cycles used in the pulsed electrodeposition technique was adjusted to optimize the deposition conditions.

The voltage for the electrodeposition of Prussian Blue was set at 0.4 V vs Ag/AgCl, this value was derived from the CVs performed in the electrodeposition solution. For the oxidation, the V_O was established at 0.7 V vs Ag/AgCl [74].

The electrodeposition time significantly influenced the morphology, thickness, and electrochemical properties of the deposited layer. Variations in pulse deposition time can lead to changes in the layer morphology, which is affected by several factors, including the accumulation of species near the interfaces, as well as the nucleation and growth processes of particles and grains [75]. Tab. 3.5 summarizes the experimental parameters chosen for optimized Prussian Blue electrodeposition.

***Table 3.5**: Values of parameters for optimized PB electrodeposition.*

Parameter	**V_R / V**	**T_R / s**	**V_O / V**	**T_O / s**	**Cycles Number**
Value	0.4	20	0.7	10	10

Fig. 3.25 shows the current density vs time recorded during the pulse electrodeposition of PB.

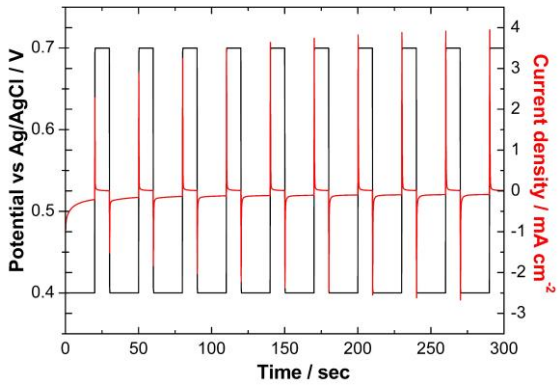

***Figure 3.25**: Current densities and potential vs. time, measured during the Pulse electrodeposition process.*

Upon applying voltage, there is a rapid decline in the current density magnitude, followed by a stabilization phase. It is important to note that the sign of the current density transitions from negative to positive upon shifting the reduction potential to oxidation potential. Thus, during the oxidation step, the PB was partially dissolved [76]. The result of this process is an increase in porosity that not only impacts the structural integrity of the films but also influences their overall electrochemical properties, potentially enhancing their functionality.

Regarding the solution used for the pulse electrodeposition, the addition of chitosan is useful to enhance the operational stability of the PB-based sensor in slightly alkaline conditions. As reported in the literature, a significant improvement in its stability was achieved with PB synthesized in the presence of organic polymers, such as chitosan [29], [77].

PB instability arises due to the thermodynamic instability of the reduced form PW. This behavior is likely due to the strong interaction between ferric ions (Fe^{3+}) and hydroxyl ions (OH^-) produced in H_2O_2 reduction, which leads to the formation of $Fe(OH)_3$ at pH levels higher than 6.4 [78]. This reaction breaks down

the Fe–CN–Fe bond, causing PB to dissolve. As a result, PB leaches from the electrode surface, leading to a reduction in the sensor signal [79], [80].

In the second step of electrode modification, the electrodeposited PB film was activated to enhance the formation of its soluble form on the electrode surface by performing CVs in a solution containing 0.1 M HCl and 0.1 M KCl for 25 cycles.

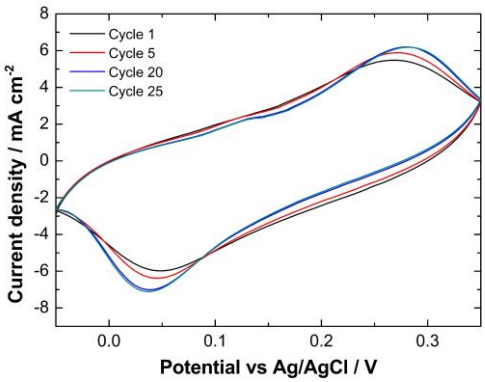

***Figure 3.26**: CVs performed at a scan rate of 50 mV s^{-1} in a solution containing 0.1 M HCl and 0.1 M KCl.*

In particular, the two characteristic peaks in the CVs (Fig. 3.26) correspond to the interconversion between PW and PB. The reduction and oxidation reactions are accompanied by noticeable electrode color changes. The electron-transfer reaction, when KCl is used as the supporting electrolyte, can be represented as follows [81] [82]:

$$Fe(III)_4(Fe(II)(CN)_6)_3 + 4e^- + 4K^+ \leftrightarrows K_4Fe(II)_4(Fe(II)(CN)_6)_3 \quad (2.1)$$

(PB to PW conversion)

A more detailed discussion of these two peaks was provided in Chapter 2. During this activation, potassium ions (K^+) play a crucial role as PB is reduced to PW; they likely replace water molecules within the crystal structure [83]. In addition, CVs reveal that the peak currents of both cathodic and anodic waves gradually increased with each cycle. This increase is due to the accumulation of more PB on the electrode surface [84]. After about 25 cycles, as shown in Fig. 3.26, the current peaks were stable, indicating that the process was complete.

After activation, the electrode was dried at 100°C for 30 min and cooled down to room temperature in the dark [32]. Drying the PB modified in the oven and then at room temperature resulted in a more stable sensor compared to freshly prepared ones. This suggests that the water content within the PB layer plays a significant role in its stability. The presence of water within the polycrystal structure can influence the stability of PB-modified electrodes, likely by affecting the crystal integrity [79]. Furthermore, it was demonstrated that a portion of this water can be irreversibly removed by heating PB at 100°C [85]. This irreversible dehydration could alter the structural properties of PB, potentially impacting its electrochemical performance and stability. In addition, it is important to keep samples in the dark to avoid the degradation of PB under light. As reported in [30], PB can degrade when exposed to light, leading to gradual color shifts, primarily due to the alteration in the iron-cyanide bonds.

After the modification, the surface and characteristics of the samples were examined using FE-SEM.

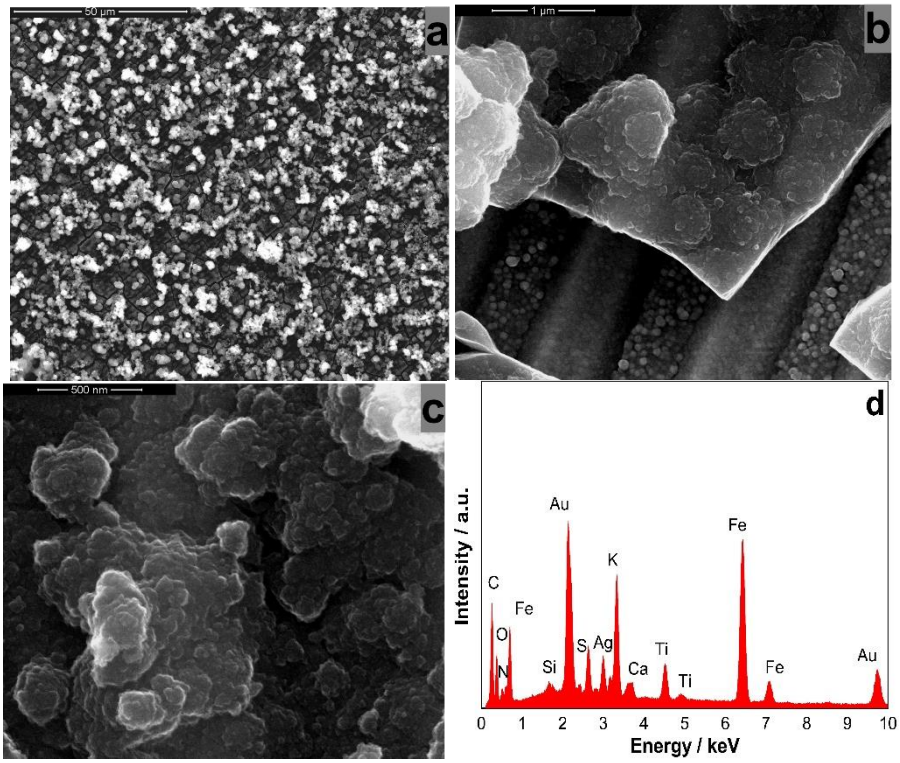

Figure 3.27*: (a-c) SEM images (a) 2000x, b) 60000x, c) 120000x), and d) EDS spectrum of PBNPs electrodeposited on WE.*

Figure 3.27a shows the clusters formed by the agglomeration of nanoparticles, with visible cracks surrounding these clusters. This morphology (clusters of nanoparticles with surrounding cracks) is characteristic of PB films, as reported in [74], [75], [86], [87]. However, variations in electrodeposition parameters, particularly deposition voltage, can lead to different morphologies (Fig. 3.27c). As shown in Fig. 3.27b, through the cracks on the surface, it is possible to observe that PBNPs (with an average diameter of 65 nm) are also present on the silver tracks of the CD. The EDS analysis (Fig. 3.27d) confirms the presence of Fe, C, K, and N in the samples, verifying the successful formation of PB [88]. Other elements, such as Si, S, Ag, Ca, and Ti were also detected, but these stem from the underlying CD substrate. The Au peak is due to the thin layer sputtered on the silver layer of the CD before the PB electrodeposition. As widely discussed in Chapter 2, the presence of potassium cations is the key distinction between PB

insoluble and soluble phases. In the soluble form of PB, K cations occupy vacancies within the water substructures. Therefore, detecting potassium in the samples suggests that both soluble and insoluble phases of PB formed during the electrodeposition process.

FT-IR spectroscopy was used to examine chemical bonds in the electrodeposited PB, with measurements performed in the range 400 - 4600 cm^{-1} (Fig. 3.28).

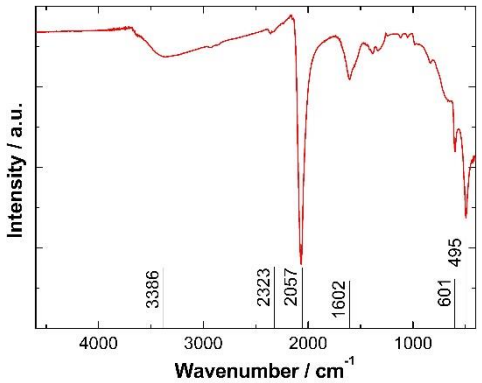

***Figure 3.28**: FT-IR spectrum of electrodeposited PB on WE.*

The FT-IR spectra of PB nanoparticles exhibit several peaks. A prominent peak at 2057 cm^{-1} corresponds to the C≡N stretching vibration in potassium hexaferricyanide, a characteristic feature of PB. The absorption bands around 495 and 601 cm^{-1} are attributed to the Fe^{2+}-CN-Fe^{3+} linkage in PB. Bands at 3386 and 2323 cm^{-1} were attributed to water absorption and O-H stretching, while an absorption band around 1602 cm^{-1} corresponded to H-O-H bending, confirming the presence of interstitial water within the PB structure [76], [88], [89].

Micro-Raman spectroscopy further confirmed the presence of PB on the working electrode (Fig. 3.29).

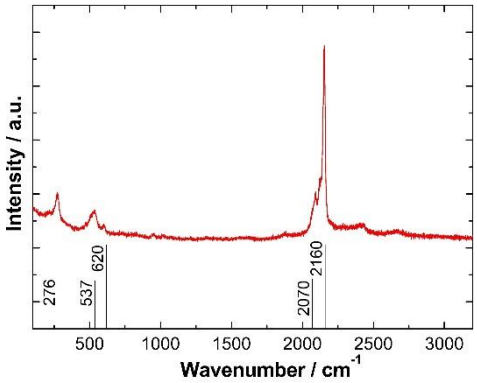

***Figure 3.29**: Raman spectrum of electrodeposited PB on WE.*

The main characteristic peaks at 2070 and 2160 cm^{-1} are representative ν(CN) vibrations. Additionally, characteristic peaks at lower wavenumbers (276, 620, and 537 cm^{-1}) indicate Fe–CN–Fe bond deformations [90], [91], [92].

3.3.4 Electrochemical performance of sensor with PB

As discussed in Chapter 2, the reduced form of Prussian Blue, known as Prussian White, has a catalytic effect in the reduction of hydrogen peroxide (Fig. 3.30) at low potentials (around 0 V), minimizing interference from other species commonly present in physiological environments [82]:

$$K_4Fe_4(II)[Fe(II)(CN)_6]_3 + 2H_2O_2 \rightarrow Fe_4(III)[Fe(II)(CN]_6 + 4OH^- + 4K^+ \quad (3.9)$$

$$H_2O_2 + 2e^- \rightarrow 2OH^- \quad (3.10)$$

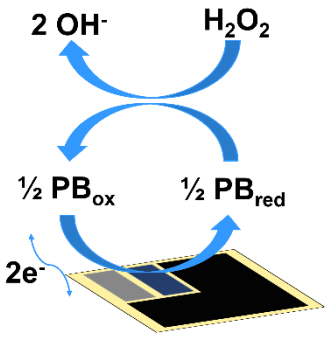

***Figure 3.30**: Mechanism of PB-mediated catalytic reduction of H_2O_2.*

Initial tests in the liquid phase were performed before the deposition of chitosan to verify its ability to detect hydrogen peroxide concentrations below 10 µM, which are typical for exhaled breath samples [15], [73]. CA tests were performed at 0.05 V vs Ag/AgCl pseudo-RE in 0.1 M K_2HPO_4/KH_2PO_4 and 0.1 M KCl (pH=7.4), in which increasing concentrations of hydrogen peroxide were added, as shown in Fig. 3.31a.

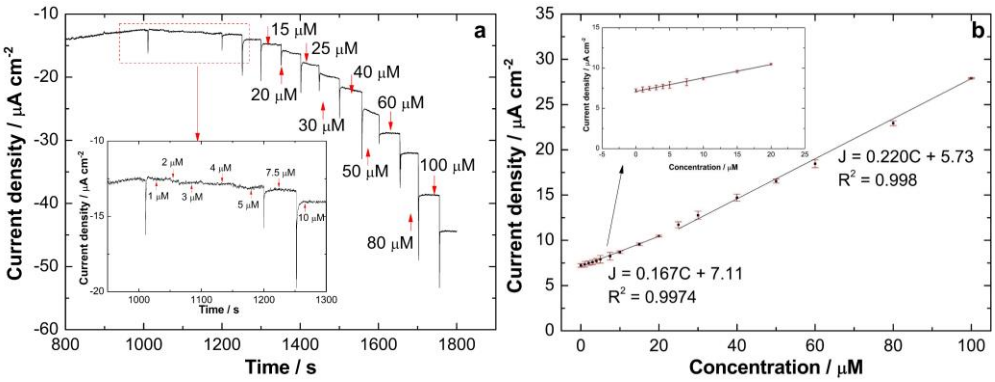

***Figure 3.31**: a) CA test performed at 0.05 V vs Ag/AgCl pseudo-RE and b) corresponding calibration line with SD error bars (N = 3).*

The graph shows the ability of the modified electrochemical sensor to detect hydrogen peroxide concentrations below 10 µM. Sensitivities of 0.167 µA μM^{-1} cm^{-2} (R^2 = 0.9974) and 0.220 µA μM^{-1} cm^{-2} (R^2 = 0.998) were obtained respectively in the range 1-20 µM and 25-100 µM (Fig.3.31b). Tab. 3.6 presents a summary of various PB-based electrochemical sensors from the literature, highlighting its analytical features for hydrogen peroxide detection.

***Table 3.6**: Comparison of developed PB based-electrochemical sensors to detect hydrogen peroxide.*

PB/G/PLA= Prussian Blue Graphite Poly Lactic Acid, PB-SPCE= Prussian Blue-Screen Printed Carbon Electrode, GCE=Glass Carbon Electrode, GE=Graphite Electrode, CILE=Carbon Ionic Liquid Electrode

Sensor Type	Detection Method	Sensitivity/ $\mu A\ \mu M^{-1}\ cm^{-2}$	Linear Range / µM	Sample	Ref.
3D-printed PB/G/PLA sensor	CA	0.057	1-700	0.1 M PBS + 0.1 M KCl (pH=7.4)	[93]
GCE/graphene/PB	CA	0.197	20-200	0.1 M H_3PO_4 and 1.0 M KCl solution	[94]
GE/PBNPs/ Nafion	CA	0.139	2-140	0.05 M PBS + 0.1 M KCl (pH=7.4)	[95]
PB modified Glass Carbon Paste electrode	CA	0.188	0.25-500	0.1 M PBS + 0.1 M KCl (pH= 6)	[96]
PB modified Ag based electrode	**CA**	**0.167** **0.220**	**1-20** **25-100**	**0.1 M PBS + 0.1 M KCl (pH=7.4)**	**This work**

To use this sensor for hydrogen peroxide detection in the aerosol phase, a layer of chitosan must be deposited by EPD on the entire surface sensor. This process was performed in the dark to avoid degrading the Prussian Blue. So, the sensor was characterized to confirm the presence of the polymer on the surface. SEM images reveal the typical morphology of the chitosan layer described previously (Fig. 3.32a-b). They also show the presence of PBNPs under the chitosan layer (Fig. 3.32c). At high magnifications (Fig. 3.32d-e), the characteristic morphology of the Prussian Blue nanoparticles, previously described, becomes clear. The EDS analysis (Fig. 3.32f) further confirms the deposition of PBNPs and chitosan.

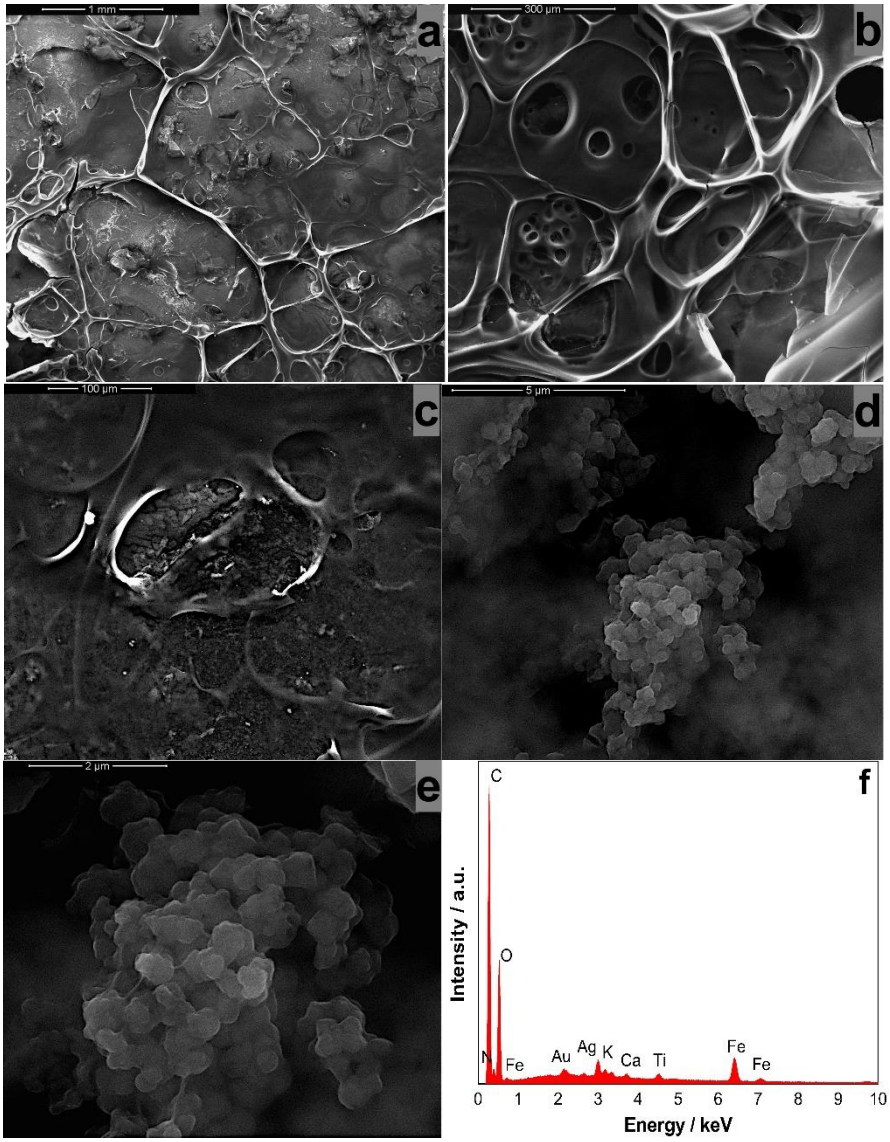

Figure 3.32*: (a-c) SEM images (a) 70x, b) 300x, c) 600x d)20000x e)40000x), and f) EDSspectrum of PBNPs and chitosan electrodeposited.*

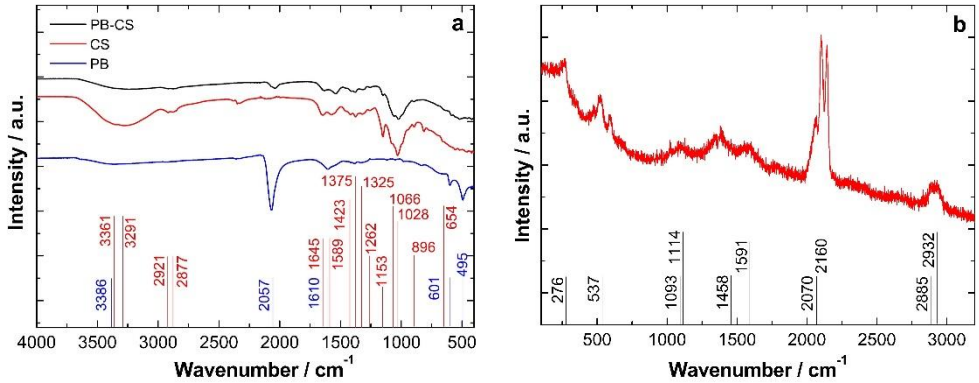

***Figure 3.33**: a) Raman and b) FT-IR spectra collected after the PBNPs and chitosan electrodeposition.*

The WE surface was also characterized by micro-Raman spectroscopy and FT-IR analysis. FT-IR spectra collected after the PBNPs and chitosan electrodeposition (Fig. 3.33a) show the typical peaks of both components. Also, in the Raman spectrum, it is possible to notice the characteristic peaks of Prussian Blue, such as 276 and 537 cm^{-1} (Fe-CN-Fe), 2070 and 2160 cm^{-1} (ν(CN) vibrations). The other peaks that can be observed in Fig. 3.33b, are attributed to the presence of chitosan. The most noticeable ones, such as 1093, 1114, 1591, 1458, 2885, and 2932 cm^{-1}, were reported in Table 3.2.

As mentioned in Chapter 2, the polymer enhances the stability of PB, preventing hydroxide ion diffusion through the PB crystal [97], [98], but can also reduce its ability to detect low concentrations. Therefore, the chitosan deposition is currently being optimized to achieve a thickness that strikes a balance between effectively detecting in the aerosol phase and maintaining sensitivity for small concentrations.

3.4 Conclusions and Future Perspectives

Oxidative stress is a condition resulting from an imbalance between pro-oxidants and antioxidants, which may cause severe cellular damage and could thus play a role in a variety of diseases. With the identification of important biomarkers like

hydrogen peroxide, which can reveal levels of oxidative stress, exhaled breath analysis shows promise as a non-invasive diagnostic technique. Whereas existing approaches depend on EBC collecting, recent developments in electrochemical sensors could enable real-time evaluation of exhaled breath without condensation, thus improving monitoring and early diagnosis. In this research, a low-cost and easy-to-use electrochemical sensor was developed for the quantification of hydrogen peroxide in exhaled air. This eco-friendly sensor is a three-electrode sensor made from the silver layer of compact discs that have accordingly been modified to enhance sensor performance.

A chitosan layer was electrodeposited for effective detection in the aerosol phase. Performance tests LSV showed that the sensor provided a linear response in both liquid and aerosol phases. In liquid PBS, it achieved a sensitivity of 0.062 ± 0.0024 μA μM^{-1} cm^{-2} with a limit of detection (LOD) of 60 μM, while in nebulized PBS, sensitivity increased to 0.110 ± 0.0042 μA μM^{-1} cm^{-2} and a LOD of 30 μM. Calibration in MEM yielded a sensitivity of 0.098 ± 0.0022 μA μM^{-1} cm^{-2} and a LOD of 40 μM. The sensor showed excellent selectivity and successfully measured H_2O_2 levels from human bronchial epithelial cells under different treatments, aligning well with results from traditional cytofluorimetric methods. Following this, the working electrode was further modified to detect the low concentrations of hydrogen peroxide typically found in exhaled breath. It has successfully demonstrated the capability to detect these concentrations in the liquid phase. Future efforts should aim to optimize the chitosan deposition time to achieve an ideal thickness for hydrogen peroxide detection in the aerosol phase with the sensitivity needed for low concentrations.

Overall, these results indicate that the proposed sensor is well-suited for monitoring oxidative stress. In the future, after improving sensor performance even in the aerosol phase, it could be integrated into a face mask for real-time monitoring, eliminating the need for the condensation step required in current clinical practices. This approach offers a wide range of potential applications,

including home care, remote point-of-care healthcare, and workplace diagnostics, all without the need for expensive laboratory equipment or specialized training.

References

[1] D. P. Jones, «Redefining Oxidative Stress», *Antioxidants & Redox Signaling*, vol. 8, fasc. 9–10, pp. 1865–1879, set. 2006, doi: 10.1089/ars.2006.8.1865.

[2] A. Phaniendra, D. B. Jestadi, e L. Periyasamy, «Free Radicals: Properties, Sources, Targets, and Their Implication in Various Diseases», *Ind J Clin Biochem*, vol. 30, fasc. 1, pp. 11–26, gen. 2015, doi: 10.1007/s12291-014-0446-0.

[3] K. Tejchman, K. Kotfis, e J. Sieńko, «Biomarkers and Mechanisms of Oxidative Stress—Last 20 Years of Research with an Emphasis on Kidney Damage and Renal Transplantation», *IJMS*, vol. 22, fasc. 15, Art. fasc. 15, lug. 2021, doi: 10.3390/ijms22158010.

[4] E. Birben, U. M. Sahiner, C. Sackesen, S. Erzurum, e O. Kalayci, «Oxidative Stress and Antioxidant Defense», *World Allergy Organization Journal*, vol. 5, fasc. 1, pp. 9–19, 2012, doi: 10.1097/WOX.0b013e3182439613.

[5] R. Stolarek, P. Bialasiewicz, M. Krol, e D. Nowak, «Breath analysis of hydrogen peroxide as a diagnostic tool», *Clinica Chimica Acta*, vol. 411, fasc. 23–24, pp. 1849–1861, dic. 2010, doi: 10.1016/j.cca.2010.08.031.

[6] S. Das, S. Pal, e M. Mitra, «Significance of Exhaled Breath Test in Clinical Diagnosis: A Special Focus on the Detection of Diabetes Mellitus», *J. Med. Biol. Eng.*, vol. 36, fasc. 5, pp. 605–624, ott. 2016, doi: 10.1007/s40846-016-0164-6.

[7] J. D. Pleil, M. A. G. Wallace, e M. C. Madden, «Exhaled breath aerosol (EBA): the simplest non-invasive medium for public health and occupational exposure biomonitoring», *J. Breath Res.*, vol. 12, fasc. 2, p. 027110, feb. 2018, doi: 10.1088/1752-7163/aa9855.

[8] M. D. Davis, «Exhaled breath condensate and aerosol», in *Breathborne Biomarkers and the Human Volatilome*, Elsevier, 2020, pp. 109–119. doi: 10.1016/B978-0-12-819967-1.00007-4.

[9] M. A. G. Wallace, J. D. Pleil, e M. C. Madden, «Identifying organic compounds in exhaled breath aerosol: Non-invasive sampling from respirator surfaces and disposable hospital masks», *Journal of Aerosol Science*, vol. 137, p. 105444, nov. 2019, doi: 10.1016/j.jaerosci.2019.105444.

[10] S. Das e M. Pal, «Review—Non-Invasive Monitoring of Human Health by Exhaled Breath Analysis: A Comprehensive Review», *J. Electrochem. Soc.*, vol. 167, fasc. 3, p. 037562, gen. 2020, doi: 10.1149/1945-7111/ab67a6.

[11] A. W. Boots, J. J. B. N. Van Berkel, J. W. Dallinga, A. Smolinska, E. F. Wouters, e F. J. Van Schooten, «The versatile use of exhaled volatile organic compounds in human health and disease», *J. Breath Res.*, vol. 6, fasc. 2, p. 027108, giu. 2012, doi: 10.1088/1752-7155/6/2/027108.

[12] D. R. Taylor, M. W. Pijnenburg, A. D. Smith, e J. C. D. Jongste, «Exhaled nitric oxide measurements: clinical application and interpretation», *Thorax*, vol. 61, fasc. 9, pp. 817–827, set. 2006, doi: 10.1136/thx.2005.056093.

[13] M. S. Khan, S. Cuda, G. M. Karere, L. A. Cox, e A. C. Bishop, «Breath biomarkers of insulin resistance in pre-diabetic Hispanic adolescents with obesity», *Sci Rep*, vol. 12, fasc. 1, p. 339, gen. 2022, doi: 10.1038/s41598-021-04072-3.

[14] A. J. Lambert, J. A. Buckingham, H. M. Boysen, e M. D. Brand, «Low complex I content explains the low hydrogen peroxide production rate of heart mitochondria from the long-lived pigeon, *Columba livia*», *Aging Cell*, vol. 9, fasc. 1, pp. 78–91, feb. 2010, doi: 10.1111/j.1474-9726.2009.00538.x.

[15] W. J. C. Van Beurden, P. N. R. Dekhuijzen, G. A. Harff, e F. W. J. M. Smeenk, «Variability of Exhaled Hydrogen Peroxide in Stable COPD Patients and Matched Healthy Controls», *Respiration*, vol. 69, fasc. 3, Art. fasc. 3, 2002, doi: 10.1159/000063622.
[16] P. N. Dekhuijzen *et al.*, «Increased exhalation of hydrogen peroxide in patients with stable and unstable chronic obstructive pulmonary disease.», *Am J Respir Crit Care Med*, vol. 154, fasc. 3, pp. 813–816, set. 1996, doi: 10.1164/ajrccm.154.3.8810624.
[17] W. Möller *et al.*, «Fractionated Exhaled Breath Condensate Collection Shows High Hydrogen Peroxide Release in the Airways», *Journal of Aerosol Medicine and Pulmonary Drug Delivery*, vol. 23, fasc. 3, pp. 129–135, giu. 2010, doi: 10.1089/jamp.2009.0764.
[18] A. Vasilescu, B. Hrinczenko, G. M. Swain, e S. F. Peteu, «Exhaled breath biomarker sensing», *Biosensors and Bioelectronics*, vol. 182, p. 113193, giu. 2021, doi: 10.1016/j.bios.2021.113193.
[19] I. Horváth, J. Hunt, e P. J. Barnes, «Exhaled breath condensate: methodological recommendations and unresolved questions», *Eur Respir J*, vol. 26, fasc. 3, pp. 523–548, set. 2005, doi: 10.1183/09031936.05.00029705.
[20] A. Tiele, A. Wicaksono, S. K. Ayyala, e J. A. Covington, «Development of a Compact, IoT-Enabled Electronic Nose for Breath Analysis», *Electronics*, vol. 9, fasc. 1, p. 84, gen. 2020, doi: 10.3390/electronics9010084.
[21] J. Obermeier, P. Trefz, K. Wex, B. Sabel, J. K. Schubert, e W. Miekisch, «Electrochemical sensor system for breath analysis of aldehydes, CO and NO», *J. Breath Res.*, vol. 9, fasc. 1, p. 016008, mar. 2015, doi: 10.1088/1752-7155/9/1/016008.
[22] F. Lopresti *et al.*, «Green and Integrated Wearable Electrochemical Sensor for Chloride Detection in Sweat», *Sensors*, vol. 22, fasc. 21, p. 8223, ott. 2022, doi: 10.3390/s22218223.
[23] B. Patella *et al.*, «Electrochemical detection of chloride ions using Ag-based electrodes obtained from compact disc», *Analytica Chimica Acta*, vol. 1190, p. 339215, gen. 2022, doi: 10.1016/j.aca.2021.339215.
[24] E. Avcu, F. E. Baştan, H. Z. Abdullah, M. A. U. Rehman, Y. Y. Avcu, e A. R. Boccaccini, «Electrophoretic deposition of chitosan-based composite coatings for biomedical applications: A review», *Progress in Materials Science*, vol. 103, pp. 69–108, giu. 2019, doi: 10.1016/j.pmatsci.2019.01.001.
[25] D. Sikorski, K. Gzyra-Jagieła, e Z. Draczyński, «The Kinetics of Chitosan Degradation in Organic Acid Solutions», *Marine Drugs*, vol. 19, fasc. 5, p. 236, apr. 2021, doi: 10.3390/md19050236.
[26] M. G. Goñi, B. Tomadoni, S. I. Roura, e M. D. R. Moreira, «Lactic acid as potential substitute of acetic acid for dissolution of chitosan: preharvest application to Butterhead lettuce», *J Food Sci Technol*, vol. 54, fasc. 3, pp. 620–626, mar. 2017, doi: 10.1007/s13197-016-2484-5.
[27] P. Najafisayar e M. E. Bahrololoom, «Pulse electrodeposition of Prussian Blue thin films», *Thin Solid Films*, vol. 542, pp. 45–51, set. 2013, doi: 10.1016/j.tsf.2013.06.029.
[28] F. Ricci, A. Amine, G. Palleschi, e D. Moscone, «Prussian Blue based screen printed biosensors with improved characteristics of long-term lifetime and pH stability», *Biosensors and Bioelectronics*, vol. 18, fasc. 2–3, Art. fasc. 2–3, mar. 2003, doi: 10.1016/S0956-5663(02)00169-0.
[29] R. Barber, J. Davis, e P. Papakonstantinou, «Stable Chitosan and Prussian Blue-Coated Laser-Induced Graphene Skin Sensor for the Electrochemical Detection of Hydrogen Peroxide in Sweat», *ACS Appl. Nano Mater.*, vol. 6, fasc. 12, pp. 10290–10302, giu. 2023, doi: 10.1021/acsanm.3c01199.
[30] L. Samain *et al.*, «Fading of modern Prussian blue pigments in linseed oil medium», *J. Anal. At. Spectrom.*, vol. 26, fasc. 5, p. 930, 2011, doi: 10.1039/c0ja00234h.
[31] L. Fiore *et al.*, «A paper-based electrochemical sensor for H2O2 detection in aerosol phase: Measure of H2O2 nebulized by a reconverted ultrasonic aroma diffuser as a case of study», *Microchemical Journal*, vol. 166, p. 106249, lug. 2021, doi: 10.1016/j.microc.2021.106249.

[32] I. L. De Mattos, L. Gorton, T. Ruzgas, e A. A. Karyakin, «Sensor for Hydrogen Peroxide Based on Prussian Blue Modified Electrode: Improvement of the Operational Stability», *ANAL. SCI.*, vol. 16, fasc. 8, pp. 795–798, ago. 2000, doi: 10.2116/analsci.16.795.
[33] S. Galiniak, N. Rohovyk, e M. Rachel, «Biomarkers of nitrosative stress in exhaled breath condensate and serum among patients with cystic fibrosis», *Advances in Medical Sciences*, vol. 68, fasc. 2, pp. 202–207, set. 2023, doi: 10.1016/j.advms.2023.05.002.
[34] X. Pang e I. Zhitomirsky, «Electrodeposition of composite hydroxyapatite–chitosan films», *Materials Chemistry and Physics*, vol. 94, fasc. 2–3, pp. 245–251, dic. 2005, doi: 10.1016/j.matchemphys.2005.04.040.
[35] N. Raddaha, L. Cordero-Arias, S. Cabanas-Polo, S. Virtanen, J. Roether, e A. Boccaccini, «Electrophoretic Deposition of Chitosan/h-BN and Chitosan/h-BN/TiO2 Composite Coatings on Stainless Steel (316L) Substrates», *Materials*, vol. 7, fasc. 3, pp. 1814–1829, mar. 2014, doi: 10.3390/ma7031814.
[36] M. Nobial, O. Devos, O. R. Mattos, e B. Tribollet, «The nitrate reduction process: A way for increasing interfacial pH», *Journal of Electroanalytical Chemistry*, vol. 600, fasc. 1, pp. 87–94, feb. 2007, doi: 10.1016/j.jelechem.2006.03.003.
[37] M. N. Khalid, F. Agnely, N. Yagoubi, J. L. Grossiord, e G. Couarraze, «Water state characterization, swelling behavior, thermal and mechanical properties of chitosan based networks», *European Journal of Pharmaceutical Sciences*, vol. 15, fasc. 5, pp. 425–432, giu. 2002, doi: 10.1016/S0928-0987(02)00029-5.
[38] L. Besra e M. Liu, «A review on fundamentals and applications of electrophoretic deposition (EPD)», *Progress in Materials Science*, vol. 52, fasc. 1, pp. 1–61, gen. 2007, doi: 10.1016/j.pmatsci.2006.07.001.
[39] P. Kowalski, B. Łosiewicz, e T. Goryczka, «Deposition of Chitosan Layers on NiTi Shape Memory Alloy», *Archives of Metallurgy and Materials*, vol. 60, fasc. 1, pp. 171–176, apr. 2015, doi: 10.1515/amm-2015-0027.
[40] J. A. M. Oliveira, R. A. C. De Santana, e A. D. O. Wanderley Neto, «Electrophoretic deposition and characterization of chitosan-molybdenum composite coatings», *Carbohydrate Polymers*, vol. 255, p. 117382, mar. 2021, doi: 10.1016/j.carbpol.2020.117382.
[41] L. Altomare, L. Draghi, R. Chiesa, e L. De Nardo, «Morphology tuning of chitosan films via electrochemical deposition», *Materials Letters*, vol. 78, pp. 18–21, lug. 2012, doi: 10.1016/j.matlet.2012.03.035.
[42] R. D'Amato, A. Polimadei, G. Terranova, e M. A. Caponero, «Humidity Sensing by Chitosan-Coated Fibre Bragg Gratings (FBG)», *Sensors*, vol. 21, fasc. 10, p. 3348, mag. 2021, doi: 10.3390/s21103348.
[43] B. Lafuente, R. T. Downs, H. Yang, e N. Stone, «1. The power of databases: The RRUFF project», in *Highlights in Mineralogical Crystallography*, T. Armbruster e R. M. Danisi, A c. di, DE GRUYTER, 2015, pp. 1–30. doi: 10.1515/9783110417104-003.
[44] M. Jiang, K. Wang, J. F. Kennedy, J. Nie, Q. Yu, e G. Ma, «Preparation and characterization of water-soluble chitosan derivative by Michael addition reaction», *International Journal of Biological Macromolecules*, vol. 47, fasc. 5, pp. 696–699, dic. 2010, doi: 10.1016/j.ijbiomac.2010.09.002.
[45] G. Blanda *et al.*, «Chitosan-Coating Deposition via Galvanic Coupling», *ACS Biomater. Sci. Eng.*, vol. 5, fasc. 4, pp. 1715–1724, apr. 2019, doi: 10.1021/acsbiomaterials.8b01548.
[46] D. Ren, H. Yi, W. Wang, e X. Ma, «The enzymatic degradation and swelling properties of chitosan matrices with different degrees of N-acetylation», *Carbohydrate Research*, vol. 340, fasc. 15, pp. 2403–2410, ott. 2005, doi: 10.1016/j.carres.2005.07.022.
[47] A. Kaniyoor e S. Ramaprabhu, «A Raman spectroscopic investigation of graphite oxide derived graphene», *AIP Advances*, vol. 2, fasc. 3, p. 032183, set. 2012, doi: 10.1063/1.4756995.

[48] Z. Han *et al.*, «Molecular origin of the Raman signal from Aspergillus nidulans conidia and observation of fluorescence vibrational structure at room temperature», *Sci Rep*, vol. 10, fasc. 1, p. 5428, mar. 2020, doi: 10.1038/s41598-020-62112-w.
[49] X. D. Ren, Q. S. Liu, H. Feng, e X. Y. Yin, «The Characterization of Chitosan Nanoparticles by Raman Spectroscopy», *AMM*, vol. 665, pp. 367–370, ott. 2014, doi: 10.4028/www.scientific.net/AMM.665.367.
[50] C. Zanca *et al.*, «Co-Deposition and Characterization of Hydroxyapatite-Chitosan and Hydroxyapatite-Polyvinylacetate Coatings on 304 SS for Biomedical Devices», *KEM*, vol. 813, pp. 153–158, lug. 2019, doi: 10.4028/www.scientific.net/KEM.813.153.
[51] A. Zając, J. Hanuza, M. Wandas, e L. Dymińska, «Determination of N-acetylation degree in chitosan using Raman spectroscopy», *Spectrochimica Acta Part A: Molecular and Biomolecular Spectroscopy*, vol. 134, pp. 114–120, gen. 2015, doi: 10.1016/j.saa.2014.06.071.
[52] T. S. V. Nguyen, T. M. Huynh, T. D. To, T. C. D. Doan, e C. M. Dang, «Ag/AgCl Film Electrodes Coated with Agarose Gel as Planar Reference Electrodes for Potentiometric Sensors», *ujms*, vol. 6, fasc. 5, pp. 148–154, nov. 2018, doi: 10.13189/ujms.2018.060502.
[53] M. Fernandes Queiroz, K. Melo, D. Sabry, G. Sassaki, e H. Rocha, «Does the Use of Chitosan Contribute to Oxalate Kidney Stone Formation?», *Marine Drugs*, vol. 13, fasc. 1, pp. 141–158, dic. 2014, doi: 10.3390/md13010141.
[54] C. Song, H. Yu, M. Zhang, Y. Yang, e G. Zhang, «Physicochemical properties and antioxidant activity of chitosan from the blowfly Chrysomya megacephala larvae», *International Journal of Biological Macromolecules*, vol. 60, pp. 347–354, set. 2013, doi: 10.1016/j.ijbiomac.2013.05.039.
[55] A. B. Vino, P. Ramasamy, V. Shanmugam, e A. Shanmugam, «Extraction, characterization and in vitro antioxidative potential of chitosan and sulfated chitosan from Cuttlebone of Sepia aculeata Orbigny, 1848», *Asian Pacific Journal of Tropical Biomedicine*, vol. 2, fasc. 1, pp. S334–S341, gen. 2012, doi: 10.1016/S2221-1691(12)60184-1.
[56] Research Network Łukasiewicz - Institute of Biopolymers and Chemical Fibres, S. Jagodzińska, B. Pałys, D. Wawro, e Institute of Security Technologies "MORATEX", «EFFECT OF CHITOSAN FILM SURFACE STRUCTURE ON THE CONTACT ANGLE», *PCACD*, vol. 26, pp. 89–100, set. 2021, doi: 10.15259/PCACD.26.008.
[57] M. N. Khalid, F. Agnely, N. Yagoubi, J. L. Grossiord, e G. Couarraze, «Water state characterization, swelling behavior, thermal and mechanical properties of chitosan based networks», *European Journal of Pharmaceutical Sciences*, vol. 15, fasc. 5, pp. 425–432, giu. 2002, doi: 10.1016/S0928-0987(02)00029-5.
[58] Z. Wang, H. Yang, B. Gao, Y. Tong, X. Zhang, e L. Su, «Stability improvement of Prussian blue in nonacidic solutions via an electrochemical post-treatment method and the shape evolution of Prussian blue from nanospheres to nanocubes», *Analyst*, vol. 139, fasc. 5, p. 1127, 2014, doi: 10.1039/c3an02071a.
[59] X. Cai, E. E. L. Tanner, C. Lin, K. Ngamchuea, J. S. Foord, e R. G. Compton, «The mechanism of electrochemical reduction of hydrogen peroxide on silver nanoparticles», *Phys. Chem. Chem. Phys.*, vol. 20, fasc. 3, pp. 1608–1614, 2018, doi: 10.1039/C7CP07492A.
[60] L. Zhang, Y. Ni, X. Wang, e G. Zhao, «Direct electrocatalytic oxidation of nitric oxide and reduction of hydrogen peroxide based on α-Fe2O3 nanoparticles-chitosan composite», *Talanta*, vol. 82, fasc. 1, pp. 196–201, giu. 2010, doi: 10.1016/j.talanta.2010.04.018.
[61] D. Zhang, Y. Fang, Z. Miao, M. Ma, e Q. Chen, «Electrochemical determination of dissolved oxygen based on three dimensional electrosynthesis of silver nanodendrites electrode», *J Appl Electrochem*, vol. 44, fasc. 3, pp. 419–425, mar. 2014, doi: 10.1007/s10800-013-0645-z.
[62] K. Jiang *et al.*, «Highly selective oxygen reduction to hydrogen peroxide on transition metal single atom coordination», *Nat Commun*, vol. 10, fasc. 1, p. 3997, set. 2019, doi: 10.1038/s41467-019-11992-2.

[63] J. Tian *et al.*, «Ultrathin graphitic carbon nitride nanosheets: a low-cost, green, and highly efficient electrocatalyst toward the reduction of hydrogen peroxide and its glucose biosensing application», *Nanoscale*, vol. 5, fasc. 19, p. 8921, 2013, doi: 10.1039/c3nr02031b.
[64] H. V. Tran, C. D. Huynh, H. V. Tran, e B. Piro, «Cyclic voltammetry, square wave voltammetry, electrochemical impedance spectroscopy and colorimetric method for hydrogen peroxide detection based on chitosan/silver nanocomposite», *Arabian Journal of Chemistry*, vol. 11, fasc. 4, pp. 453–459, mag. 2018, doi: 10.1016/j.arabjc.2016.08.007.
[65] I. Katsounaros *et al.*, «Hydrogen peroxide electrochemistry on platinum: towards understanding the oxygen reduction reaction mechanism», *Phys. Chem. Chem. Phys.*, vol. 14, fasc. 20, p. 7384, 2012, doi: 10.1039/c2cp40616k.
[66] D. Maier *et al.*, «Toward Continuous Monitoring of Breath Biochemistry: A Paper-Based Wearable Sensor for Real-Time Hydrogen Peroxide Measurement in Simulated Breath», *ACS Sens.*, vol. 4, fasc. 11, pp. 2945–2951, nov. 2019, doi: 10.1021/acssensors.9b01403.
[67] R. Toniolo, P. Geatti, G. Bontempelli, e G. Schiavon, «Amperometric monitoring of hydrogen peroxide in workplace atmospheres by electrodes supported on ion-exchange membranes», *Journal of Electroanalytical Chemistry*, vol. 514, fasc. 1–2, pp. 123–128, nov. 2001, doi: 10.1016/S0022-0728(01)00612-X.
[68] M. Baker, S. Assis, O. Higa, e I. Costa, «Nanocomposite hydroxyapatite formation on a Ti–13Nb–13Zr alloy exposed in a MEM cell culture medium and the effect of H2O2 addition», *Acta Biomaterialia*, vol. 5, fasc. 1, pp. 63–75, gen. 2009, doi: 10.1016/j.actbio.2008.08.008.
[69] L. Arodin Selenius, M. Wallenberg Lundgren, R. Jawad, O. Danielsson, e M. Björnstedt, «The Cell Culture Medium Affects Growth, Phenotype Expression and the Response to Selenium Cytotoxicity in A549 and HepG2 Cells», *Antioxidants*, vol. 8, fasc. 5, p. 130, mag. 2019, doi: 10.3390/antiox8050130.
[70] B. Patella *et al.*, «Electrochemical Quantification of H2O2 Released by Airway Cells Growing in Different Culture Media», *Micromachines*, vol. 13, fasc. 10, p. 1762, ott. 2022, doi: 10.3390/mi13101762.
[71] P. N. R. Dekhuijzen, «Antioxidant properties of N-acetylcysteine: their relevance in relation to chronic obstructive pulmonary disease», *European Respiratory Journal*, vol. 23, fasc. 4, pp. 629–636, apr. 2004, doi: 10.1183/09031936.04.00016804.
[72] M. Ferraro, M. Gjomarkaj, L. Siena, S. Di Vincenzo, e E. Pace, «Formoterol and fluticasone propionate combination improves histone deacetylation and anti-inflammatory activities in bronchial epithelial cells exposed to cigarette smoke», *Biochimica et Biophysica Acta (BBA) - Molecular Basis of Disease*, vol. 1863, fasc. 7, pp. 1718–1727, lug. 2017, doi: 10.1016/j.bbadis.2017.05.003.
[73] J. I. Sznajder *et al.*, «Increased Hydrogen Peroxide in the Expired Breath of Patients with Acute Hypoxemic Respiratory Failure», *Chest*, vol. 96, fasc. 3, pp. 606–612, set. 1989, doi: 10.1378/chest.96.3.606.
[74] V. Bayzi Isfahani, A. Arab, J. Horta Belo, J. Pedro Araújo, M. Manuela Silva, e B. Gonçalves Almeida, «Comparison of Physical/Chemical Properties of Prussian Blue Thin Films Prepared by Different Pulse and DC Electrodeposition Methods», *Materials*, vol. 15, fasc. 24, p. 8857, dic. 2022, doi: 10.3390/ma15248857.
[75] V. B. Isfahani, H. R. Dizaji, N. Memarian, e A. Arab, «Electrodeposition of prussian blue films: study of deposition time effect on electrochemical properties», *Mater. Res. Express*, vol. 6, fasc. 9, p. 096449, ago. 2019, doi: 10.1088/2053-1591/ab0989.
[76] V. Bayzi Isfahani, A. Arab, J. Horta Belo, J. Pedro Araújo, M. Manuela Silva, e B. Gonçalves Almeida, «Comparison of Physical/Chemical Properties of Prussian Blue Thin Films Prepared by Different Pulse and DC Electrodeposition Methods», *Materials*, vol. 15, fasc. 24, p. 8857, dic. 2022, doi: 10.3390/ma15248857.
[77] A. V. Borisova, E. E. Karyakina, S. Cosnier, e A. A. Karyakin, «Current-Free Deposition of Prussian Blue with Organic Polymers: Towards Improved Stability and Mass Production of

the Advanced Hydrogen Peroxide Transducer», *Electroanalysis*, vol. 21, fasc. 3–5, pp. 409–414, feb. 2009, doi: 10.1002/elan.200804408.
[78] B. J. Feldman e R. W. Murray, «Electron diffusion in wet and dry Prussian blue films on interdigitated array electrodes», *Inorg. Chem.*, vol. 26, fasc. 11, pp. 1702–1708, giu. 1987, doi: 10.1021/ic00258a014.
[79] A. Karyakin, «On the mechanism of H2O2 reduction at Prussian Blue modified electrodes», *Electrochemistry Communications*, vol. 1, fasc. 2, pp. 78–82, feb. 1999, doi: 10.1016/S1388-2481(99)00010-7.
[80] A. A. Karyakin e E. E. Karyakina, «Prussian Blue-based `artificial peroxidase' as a transducer for hydrogen peroxide detection. Application to biosensors», *Sensors and Actuators B: Chemical*, vol. 57, fasc. 1–3, pp. 268–273, set. 1999, doi: 10.1016/S0925-4005(99)00154-9.
[81] F. Ricci e G. Palleschi, «Sensor and biosensor preparation, optimisation and applications of Prussian Blue modified electrodes», *Biosensors and Bioelectronics*, vol. 21, fasc. 3, pp. 389–407, set. 2005, doi: 10.1016/j.bios.2004.12.001.
[82] P. Salazar, M. Martín, R. D. O'Neill, e J. L. González-Mora, «In Vivo Biosensor Based on Prussian Blue for Brain Chemistry Monitoring : Methodological Review and Biological Applications», in *In Vivo Neuropharmacology and Neurophysiology*, vol. 121, A. Philippu, A c. di, in Neuromethods, vol. 121. , New York, NY: Springer New York, 2017, pp. 155–179. doi: 10.1007/978-1-4939-6490-1_8.
[83] S. Esmail Tehrani *et al.*, «Hydrogen Peroxide Detection Using Prussian Blue-modified 3D Pyrolytic Carbon Microelectrodes», *Electroanalysis*, vol. 33, fasc. 12, pp. 2516–2528, dic. 2021, doi: 10.1002/elan.202100387.
[84] Q. Sheng, D. Zhang, Q. Wu, J. Zheng, e H. Tang, «Electrodeposition of Prussian blue nanoparticles on polyaniline coated halloysite nanotubes for nonenzymatic hydrogen peroxide sensing», *Anal. Methods*, vol. 7, fasc. 16, pp. 6896–6903, 2015, doi: 10.1039/C5AY01329A.
[85] S. Ganguli e M. Bhattacharya, «Studies of different hydrated forms of Prussian Blue», *J. Chem. Soc., Faraday Trans. 1*, vol. 79, fasc. 7, p. 1513, 1983, doi: 10.1039/f19837901513.
[86] T.-C. Liao, W.-H. Chen, H.-Y. Liao, e L.-C. Chen, «Multicolor electrochromic thin films and devices based on the Prussian blue family nanoparticles», *Solar Energy Materials and Solar Cells*, vol. 145, pp. 26–34, feb. 2016, doi: 10.1016/j.solmat.2015.08.004.
[87] S.-Y. Lu, Y. Chen, X. Fang, e X. Feng, «Hydrogen peroxide sensor based on electrodeposited Prussian blue film», *J Appl Electrochem*, vol. 47, fasc. 11, pp. 1261–1271, nov. 2017, doi: 10.1007/s10800-017-1113-y.
[88] A. M. Farah *et al.*, «Synthesis of Prussian Blue and Its Electrochemical Detection of Hydrogen Peroxide Based on Cetyltrimethylammonium Bromide (CTAB) Modified Glassy Carbon Electrode», *International Journal of Electrochemical Science*, vol. 8, fasc. 11, pp. 12132–12146, nov. 2013, doi: 10.1016/S1452-3981(23)13250-0.
[89] A. M. Nawar e A. A. Alzharani, «Impedance spectroscopy and conduction mechanism analysis of bulk nanostructure Prussian blue pellets», *Materials Chemistry and Physics*, vol. 306, p. 128000, set. 2023, doi: 10.1016/j.matchemphys.2023.128000.
[90] G. Moretti e C. Gervais, «Raman spectroscopy of the photosensitive pigment Prussian blue», *J Raman Spectroscopy*, vol. 49, fasc. 7, pp. 1198–1204, lug. 2018, doi: 10.1002/jrs.5366.
[91] M. Ricci, F. Sebastiani, M. Becucci, M. Rogozny, e V. Parfenov, «A Spectroscopy-Based Multi-Analytical Approach for Studies in Conservation: Decorations in the Alexander Palace (Tsarskoye Selo)», *Spectroscopy Journal*, vol. 1, fasc. 3, pp. 121–136, ott. 2023, doi: 10.3390/spectroscj1030011.
[92] D. A. Peixoto, S. C. Silva, P. H. S. Borges, R. C. Lima, e E. Nossol, «Hydrothermal synthesis as a versatile tool for the preparation of metal hexacyanoferrates: a review», *J Mater Sci*, vol. 58, fasc. 7, pp. 2993–3024, feb. 2023, doi: 10.1007/s10853-023-08190-3.

[93] R. G. Rocha *et al.*, «Electrochemical synthesis of Prussian blue from iron impurities in 3D-printed graphene electrodes: Amperometric sensing platform for hydrogen peroxide», *Talanta*, vol. 219, p. 121289, nov. 2020, doi: 10.1016/j.talanta.2020.121289.
[94] E. Jin, X. Lu, L. Cui, D. Chao, e C. Wang, «Fabrication of graphene/prussian blue composite nanosheets and their electrocatalytic reduction of H2O2», *Electrochimica Acta*, vol. 55, fasc. 24, pp. 7230–7234, ott. 2010, doi: 10.1016/j.electacta.2010.07.029.
[95] B. Haghighi, H. Hamidi, e L. Gorton, «Electrochemical behavior and application of Prussian blue nanoparticle modified graphite electrode», *Sensors and Actuators B: Chemical*, vol. 147, fasc. 1, pp. 270–276, mag. 2010, doi: 10.1016/j.snb.2010.03.020.
[96] F. Ricci, C. Gonçalves, A. Amine, L. Gorton, G. Palleschi, e D. Moscone, «Electroanalytical Study of Prussian Blue Modified Glassy Carbon Paste Electrodes», *Electroanalysis*, vol. 15, fasc. 14, pp. 1204–1211, ago. 2003, doi: 10.1002/elan.200390148.
[97] P. Salazar, M. Martín, R. Roche, R. D. O'Neill, e J. L. González-Mora, «Prussian Blue-modified microelectrodes for selective transduction in enzyme-based amperometric microbiosensors for in vivo neurochemical monitoring», *Electrochimica Acta*, vol. 55, fasc. 22, pp. 6476–6484, set. 2010, doi: 10.1016/j.electacta.2010.06.036.
[98] L. V. Lukachova *et al.*, «Nonconducting polymers on Prussian Blue modified electrodes: improvement of selectivity and stability of the advanced H/sub 2/O/sub 2/ transducer», *IEEE Sensors J.*, vol. 3, fasc. 3, pp. 326–332, giu. 2003, doi: 10.1109/JSEN.2003.814646.

4. Wearable Microfluidic Sensor for Uric Acid, Chloride and Glucose Detection in Sweat

This chapter will explore the fabrication and validation of a multi-analyte wearable electrochemical sensor for detecting uric acid, chlorides, and glucose in sweat by using a microfluidic system. The sensor was developed in collaboration with the Institute of Microelectronics in Barcelona, under the supervision of Dr. César Fernández-Sánchez and Dr. Manuel Gutiérrez-Capitán.

4.1 Introduction

4.1.1 Wearable Electrochemical Sensors for Sweat Monitoring

An exemplary healthcare system would focus on monitoring health conditions and providing treatments before diseases manifest. Ideally, when patients display signs of declining health, the system should be capable of identifying and addressing these issues early on. In contrast, patients today typically seek medical help only after developing noticeable symptoms, leading to reactive treatment and oversight from specialists. This underscores the critical need for a system that enables individuals to proactively monitor their health, facilitating early detection and timely intervention without expensive equipment or specialized training [1]. With advances in medical diagnostic technologies, wearable biosensors are emerging as a promising solution to healthcare challenges. These devices can continuously and noninvasively track physiological data through real-time measurements of biochemical markers in biofluids, all while maintaining comfort for the user [2].

Biofluids such as sweat, tears, saliva, and tissue are becoming increasingly relevant due to their easy accessibility and potential to offer real-time physiological insights into the body's biochemical state [3]. While several biofluids are potential candidates, many face limitations when they must be used

in wearable sensors. Blood is traditionally defined as the gold standard for analyte monitoring. Taking blood samples might pose challenges for various individuals, especially infants, the elderly, and people with hemophobia. Urine is another commonly used clinical sample, but it is unsuitable for real-time and continuous monitoring. Tears contain salts, enzymes, proteins, and lipids that can signal specific ocular conditions. However, current methods for tear collection may irritate the eyes and lead to reflex tears, potentially affecting test results. Saliva permits the measurement of distinct biomarkers, like hormones or antibodies. However, saliva can be contaminated by food residues that can act as potential interferences, worsening the sensor selectivity [1].

Sweat presents considerable advantages for wearable sensing technologies. It can be collected noninvasively from various areas of the body, making it particularly suitable for continuous monitoring. Sensors designed for sweat analysis can be placed close to sweat glands, enabling rapid detection before analytes degrade. Sweat has great potential for use in wearable electrochemical sensors (Fig. 4.1) that could offer valuable physiological information for health monitoring and disease diagnostics. The concentration of some blood components, including glucose, lactate, and ethanol, is in strong correlation with the value present in sweat, suggesting that its analysis could effectively complement or even replace blood testing [4].

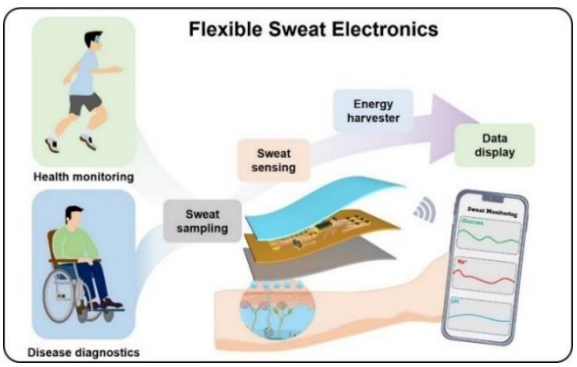

***Figure 4.1**: A schematic representation of flexible sweat-sensing electronics* [5].

4.1.2 Sweat Composition and its Role in Health Monitoring and Disease Detection

Sweat contains hundreds of biomarkers and can be used to continuously monitor various ions, drugs, metabolites, and biomolecules (Tab. 4.1). These include potassium, sodium, calcium, and chloride ions, but also lactic acid, glucose, ammonia, ethanol urea, cortisol as well as several neuropeptides and cytokines [2]. As a rich physiological information, sweat bears great significance in the field of fitness tracking and health monitoring for athletes as well as disease diagnosis. Abnormal health conditions, such as electrolyte imbalances or stress, and diseases are often reflected by changes in the concentrations of sweat components or the appearance of new compounds [2].

***Table 4.1**: Main sweat analytes and associated health conditions [1].*

Analyte category	Analyte	Health condition
Electrolytes	Na^+	Dehydration, hyponatremia, electrolyte imbalance
	Cl^-	Dehydration, cystic fibrosis
	K^+	Hypokalemia, muscle cramps
	Ca^{2+}	Myeloma, cirrhosis, renal failure, acid-base balance disorder
	NH^{4+}	Shift from aerobic to anaerobic metabolic conditions
Metabolites	Glucose	Diabetes
	Lactate	Shift from aerobic to anaerobic metabolic conditions
	Uric acid	Renal dysfunction, gout
Drugs	Caffeine	Coronary syndrome, hypertension, depression
	Levodopa	Parkinson's disease
Trace metals	Zn^{2+}	Stress and immune system-induced muscle damage
	Cu^{2+}	Rheumatoid arthritis, Wilson's disease, cirrhosis of the liver
Other analytes	Interleukin 6	Insulin activity, immune responses in cancer therapy
	Cortisol	Stress

(hormones, cytokines, proteins)	Tyrosine	Metabolic disorders, tyrosinemia
	Neuropeptide Y	Stress

Water makes up about 99% of sweat, with electrolytes contributing to its slightly acidic nature, averaging a pH of 6.3, which is more acidic than blood. The pH of sweat varies with the concentration of electrolytes and thus may serve as a biomarker for metabolic activity, not only under healthy conditions but also during the progression of diseases. Furthermore, pH monitoring is necessary to regulate the pH required for wound recovery, diagnosis of infections, and disease states like metabolic alkalosis [6]. Sodium (Na^+) is an essential biomarker of electrolyte imbalances that are necessities for osmolality and water balance, which indirectly affect pH regulation [8]. Sweat chloride analysis is a widely used diagnostic test for cystic fibrosis (CF), owing to the very high levels of chloride (Cl^-) in CF sweat [7]. Potassium (K^+) in sweat reflects the blood levels of potassium; low levels of potassium in sweat could signal dehydration, a condition that is lethal for cardiovascular patients [8]. Conversely, the monitoring of calcium (Ca^{2+}) in sweat would offer early detection for myeloma, cirrhosis, renal failure, and hyperparathyroidism [9]. Ammonium ion (NH_4^+) is also secreted in sweat in concentrations equivalent to plasma levels, reflecting protein metabolism. The secretion of this ion can indicate the transition between aerobic and anaerobic exercise [1]. Glucose present in sweat, particularly when induced by iontophoresis, is associated with blood glucose and may be a suitable candidate for diabetes screening and monitoring [10].

Lactate concentrations in sweat closely resemble those in blood and serve as markers of tissue viability, providing warnings for ischemic stress. It has been demonstrated that lactate levels are independent of sweat production rate, making them reliable for noninvasive diagnostics [11]. Uric acid (UA) levels in sweat offer insight into kidney function, with elevated UA in gout patients compared to healthy individuals [12]. Toxins and drugs can also be excreted through sweat.

Caffeine concentrations in sweat are related to plasma and urine levels, and chronic caffeine intake can lead to conditions such as coronary syndrome, hypertension, and depression. Levodopa concentrations in sweat have been shown to correlate with plasma levels, enabling optimization of drug dosage for patients [1]. Sweat also has an important role in eliminating heavy metals like zinc and copper. High levels of zinc ions in sweat can indicate stress, immune response, and muscle damage during physical activity. Copper levels in sweat, which are linked to conditions like rheumatoid arthritis, Wilson's disease, and cirrhosis, can also reflect exercise, heat stress, and dietary factors [13]. Besides these, several other components have been identified, including hormones and small proteins such as cortisol, neuropeptides, and cytokines. For example, IL-6 has been regarded as one of the main mediators of inflammation. It can be used as a detectable parameter for the control and treatment of immune responses, especially in tumor therapy [1]. Cortisol is a form of steroid hormone synthesized under stressed conditions. It is an important hormone in metabolism, stress, and immune reactions [14]. The amino acid tyrosine is greatly involved in metabolism. Abnormal concentrations of tyrosine are usually indicative of metabolic disorders such as tyrosinemia. Neuropeptide Y (NPY) acts in response to stress and is present in higher concentrations in the sweats of depressed patients compared with non-depressed individuals [1]. Fig. 4.2 illustrates the most commonly detected analytes in sweat using wearable sensors.

***Figure 4.2**: Wearable sweat sensors for real-time health monitoring [15].*

4.1.3 Microfluidic Devices for Effective Sweat Collection and Monitoring

Sweat sample collection is a critical aspect of sweat sensing, as it directly impacts the accuracy of measurements. Key challenges include the sampling area, evaporation, degradation, and contamination of sweat samples. Water evaporation or cross-contamination from residual components on the skin can lead to overestimated biomarker concentrations. Additionally, some biomarkers in sweat have limited stability, meaning measurements must be taken immediately after sweat is generated to ensure accuracy [16]. Traditionally, sweat collection can be achieved using two primary methods: passive and active. In the passive approach, individuals engage in vigorous physical activities, such as running, cycling, or other exercises, to stimulate sweat production naturally. On the other hand, the active approach involves using external stimuli like electrical stimulation to induce sweat. Iontophoresis is a common non-invasive technique for active sweat induction, allowing sweat samples to be collected without the need for physical exertion. This method involves generating a current beneath the skin by applying a voltage between iontophoretic electrodes. In this process, a current is applied between pilogels (hydrogels infused with the sweat stimulant pilocarpine), creating a potential drop across the test area. This small current drives pilocarpine beneath the skin surface, triggering nearby sweat glands to release sweat for collection by wearable sensors [7].

Compared to blood or other bodily fluids, the concentration of biomarkers in sweat is typically lower, making real-time and accurate monitoring more challenging. In addition, generating enough sweat for analysis often requires vigorous exercise or pharmacological stimulation. Sweat secretion rates at rest are typically low, and evaporation reduces the volume available for collection. For individuals unable to exercise or sensitive to iontophoresis, skin-contact microfluidic systems that capture naturally released sweat offer a viable alternative [17]. The small channel dimensions and low sample volume requirements in microfluidic devices enable multiplexed analysis of various

biomarkers within the same device and at the same time. For instance, Bandodkar et al. [18] (Fig. 4.3A) designed a microfluidic device capable of electrochemical, colorimetric, and volumetric analyses to monitor sweat rate/loss, pH, lactate, glucose, and chloride. Koh et al. [19] (Fig. 4.3B) developed a microfluidic platform with a quantitative assay to measure sweat rate, total sweat loss, pH, chloride, and lactate levels. Another example is Sekine et al. [20] (Fig. 4.3C), whose platform can simultaneously quantify sodium, chloride, and zinc in sweat.

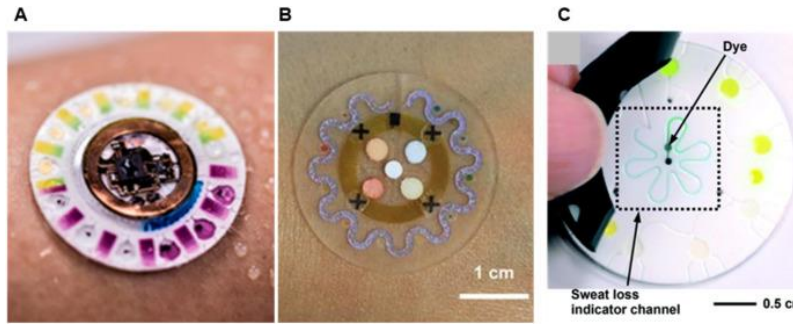

***Figure 4.3**: Multiplexed microfluidic devices for sweat analysis [21]:*
A) A microfluidic system designed for electrochemical, colorimetric, and volumetric assessment of sweat, measuring sweat rate/loss, pH, lactate, glucose, and chloride levels [18].
B) A microfluidic platform for determining sweat rate, total sweat loss, pH, chloride, and lactate concentration [19].
C) A microfluidic device enabling quantitative analysis of sweat biomarkers such as sodium, chloride, and zinc, detected using fluorimetry [20].

Wearable microfluidic devices require lower sample volumes than traditional methods, which is a crucial advantage because sweat glands produce only 5-10 nanoliters of sweat per minute. This limited production results in approximately three microliters of sweat per minute in a one cm^2 area during exercise. The ability to work with such small volumes makes microfluidic devices ideal for continuous and non-invasive sweat analysis, enabling real-time monitoring of various biomarkers without the need for large sweat samples [22]. These microfluidic systems can collect sweat from various small channels and wirelessly connect to external devices for analysis and multi-parametric sensing of clinically relevant markers [23]. These systems improve the reliability of measurements by

minimizing sample loss, evaporation, and contamination while enhancing the temporal resolution of sweat analyte data. Microfluidic devices rely on a driving force to ensure continuous sweat transport. In addition to natural sweat gland pressure, forces such as capillary action, osmotic pressure, and evaporation pumps can drive sweat flow without external equipment [24]. Capillary action can move sweat through microfluidic channels while applying hydrophilic coatings or valve structures to control the flow direction. Hydrogels placed at the chip inlet can create an osmotic pressure gradient, drawing fluid into the channels more efficiently. Additionally, micropores designed into the outlet of a microfluidic chip can use evaporation to generate a continuous flow of sweat, with flow rates modifiable by adjusting the size or shape of the micro-perforations [1].

Microfluidic devices can be applied to different areas of the body without causing chemical or physical discomfort, thanks to biocompatible adhesives and soft mechanical properties such as flexibility, elasticity, and watertight interfaces. Due to their cost-effectiveness, ease of production on an industrial scale, and eco-friendly nature, microfluidic-based health monitoring devices hold vast potential in sweat-sensing applications [25]. Koh et al. [25] developed a microfluidic device for determining sweat rate, total sweat loss, pH, chloride, and lactate. Similarly, Sekine et al. [26] introduced a system capable of simultaneously quantifying sodium, chloride, and zinc in sweat. These advancements highlight the potential of microfluidic technology for comprehensive sweat analysis.

4.1.4 The Role of Uric Acid, Chlorides, and Glucose in Oxidative Stress Monitoring

Uric acid (UA), chloride, and glucose are three key biomarkers that play a crucial role in oxidative stress, a pathological condition discussed in Chapter 3. UA is the final enzymatic product of purine metabolism in the body. It is found inside cells and in all body fluids, although usually in lower amounts than in plasma. It has been suggested that UA may be one of the most significant low-molecular-weight

antioxidants in human biological fluids [27]. Ames et al. [28], in the early 1980s, put forth a proposition that UA had biological significance as an antioxidant and also demonstrated through in vitro experiments that it effectively scavenges peroxyl radicals (RO_2•), hydroxyl radicals (•OH), and singlet oxygen against oxidative damage. Beyond being a radical scavenger, UA also chelates metal ions, especially iron and copper, decreasing their catalytic role in free radical reactions. When UA interacts with ROS or other oxidizing agents, it can be oxidized into allantoin and other byproducts. Therefore, measuring UA or allantoin levels can serve as an indicator of oxidative stress in humans [29]. UA is commonly measured in urine, where the physiological range concentration is 1.5-4.5 mM [30]. However, UA detection in sweat presents a promising approach for real-time health monitoring, allowing a non-invasive analysis [31]. The physiological concentration of UA in human sweat is between 25 μM and 50 μM [32], [33].

Chloride ions (Cl^-) are implicated in many physiological functions, including several interconnected biochemical pathways with oxidative stress. In this respect, the monitoring of Cl^- ions could be proposed as an indirect marker of oxidative stress due to the participation of the ion in physiological reactions that generate Reactive Chlorine Species (RCS), among which hypochlorous acid (HOCl) stands out. In particular, the enzyme myeloperoxidase (MPO), Cl^-, and hydrogen peroxide are involved in HOCl formation. When Cl^- concentrations rise, MPO activity increases, leading to higher HOCl production. Excessive HOCl can then cause tissue damage, contributing to oxidative stress [34]. Commonly, chloride concentration is measured in urine, where the physiological level is between 67 and 131 mM [35]. However, since chloride is the most common electrolyte in human sweat, its concentration has become an excellent representative of estimating the electrolyte balance of the body for the diagnosis and prevention of many diseases. The chloride concentration in sweat is between 10 and 30 mM. In pathological subjects, values higher than 60 mM can be found [36], [37].

The excessive concentration of glucose also contributes to oxidative stress. It is well established that hyperglycemia triggers metabolic issues by activating harmful pathways that elevate oxidative stress in human tissues. It is well known that hyperglycemia might induce metabolic disorders due to the development of destructive pathways which increase oxidative stress in tissues. Indeed, high blood sugar levels, or hyperglycemia, promote the development of metabolic disorders, activating abnormal pathways participating in increasing oxidative stress within human tissues [38]. According to a hypothesis, increased glucose levels increase the availability of electron donors, increasing electron flow through the mitochondrial electron transport chain. This results in hyperpolarization of the mitochondrial membrane potential, leading to an accumulation of electrons in coenzyme Q that facilitates the partial reduction of O_2, generating the free radical anion superoxide (ROS generation) [39].

Sweat serves as a readily accessible source of glucose, featuring numerous sampling sites on the body, consistent availability, and ease of collection. The correlation between sweat glucose and blood glucose has also been demonstrated. However, the monitoring of glucose levels in sweat is rather challenging because of its low concentration-around 100 times lower than glucose levels in blood; hence, highly sensitive devices are required for its detection. The glucose concentration in human sweat varies between 0.06 and 0.2 mM (in pathologic conditions, the concentration increases up to 1 mM), corresponding to 3.9 to 5.6 mM of blood glucose [40] [41]. Tab. 4.2 summarizes the physiological concentration values of the three analytes in sweat and other biofluids where they are commonly measured in clinical practice.

Table 4.2*: UA, chlorides, and glucose physiological concentrations in different biofluids.*

Analyte	Sweat concentration / mM	Other Biofluid concentration / mM
Uric acid	0.025 – 0.05	1.5 – 4.5 (urine)
Chlorides	10 - 30	67 – 131 (urine)
Glucose	0.06 – 0.2	3.9 – 5.6 (blood)

4.2 Materials and Methods

4.2.1 Experimental setup

Chips (0.9 x 1.1 cm) with gold electrodes were fabricated on silicon substrates at the IMB-CNM Clean Room (Barcelona, Spain) by using a standard photolithographic and liftoff process. First, to determine the optimal deposition conditions for each analyte and evaluate the performance of modified working electrodes (WEs), silicon chips with three gold electrodes were utilized (Fig. 4.4). The larger electrode (0.05 cm^2) served as the counter electrode (CE), while the others (0.025 cm^2 each) were the working electrode (WE) and pseudo-reference electrode (pseudo-RE), respectively.

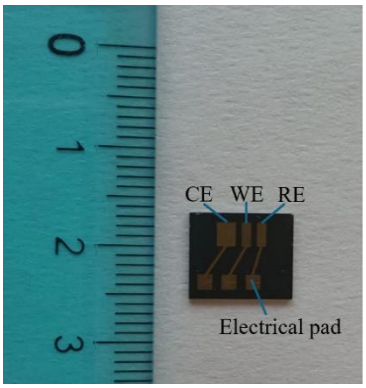

***Figure 4.4**: Gold silicon chip used for the electrochemical tests.*

For the microfluidic system, a gold silicon chip (0.9 × 1.1 cm) with four electrodes was employed (Fig. 4.5). The larger electrode (0.05 cm^2) is the CE, while the others (0.025 cm^2) were used as WE for chloride detection (b), WE for uric acid detection (c), and pseudo-RE (d).

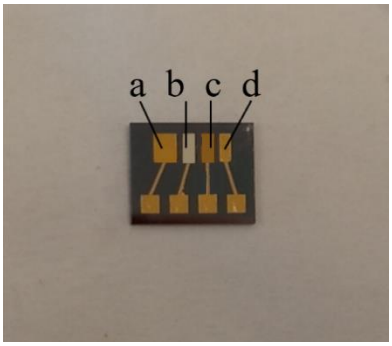

Figure 4.5*: Gold silicon chip with four electrodes: a) CE, b) WE for chloride ions detection, c) WE for uric acid detection, d) RE.*

Before use, each chip was cleaned by immersing it in acetone and ethanol. Other residues were removed by immersing the chip in a cold piranha solution (H_2SO_4:H_2O_2 3:1) and rinsing it with DI water. The electrochemical tests were performed with a MultiPalmSens4 and data was acquired with Multitrace 4.4.

4.2.2 Electrochemical Fabrication and Characterization

To make the gold working electrode selective for the detection of the three analytes, its surface was modified by EPD. Before the EPD, the as-prepared chip was electrochemically characterized. A ferrocene-methanol (Fc-MeOH) redox mediator was used to study the effect of scan rate in the range of 10–150 mV s^{-1} in a solution of KNO_3 0.1 M containing 1 mM of Fc-MeOH.

For the uric acid detection, the surface of the gold WE was modified with rGO-AuNPs electrochemical co-deposition. An external Ag/AgCl reference was used, and a platinum wire served as CE. An Acetate Buffer Solution (ABS, CH_3COONa 0.07 M and CH_3COOH 0.03 M, pH 5), containing 0.5 mg/mL of GO and 0.25 mM of $HAuCl_4$ was used for the potentiostatic co-deposition that was carried out at - 0.8 V vs Ag/AgCl for 200 s [42].

For the detection of chloride ions, the surface of the gold WE was modified with Ag by potentiostatic deposition carried out at - 0.2 V for 600 s. A platinum wire was used as the CE, and the other electrode of the gold chip was used as the

pseudo-RE. An aqueous solution containing 10 mM HNO_3, tartaric acid 15 mM, and 100 mM $AgNO_3$ was used.

For glucose detection, the surface of the gold WE was modified with NiNPs obtained by electrodeposition. A platinum wire was used as the counter electrode (CE), and an external Ag/AgCl reference was used. A solution containing 0.5 M H_3BO_3, KNO_3 0.1 M, and $NiSO_4$ 0.1 M [43] was used. A potentiostatic deposition was carried out at - 0.8 V for 100 s.

After each use, the WE surface can be electrochemically cleaned in a 0.5 M KNO_3 solution by CV in a potential range of + 0.2 to - 2.5 V (vs. Au pseudo-RE) at a scan rate of 100 mV s^{-1}. Afterward, the surface can be re-modified as previously described and reused.

Modified WEs were characterized using Field Emission Scanning Electron Microscopy (FESEM FEI, QUANTA 200) and Energy Dispersive Spectroscopy (EDS, AMETEK).

4.2.3 Electrochemical Performance

For sensor calibration, the potential at which analyte oxidation occurs was selected from LSV tests performed at 50 mV s^{-1} in a 0.1 M PBS containing the analyte. For glucose detection, a solution of NaOH 0.1 M was employed to establish alkaline conditions that are favorable for enhancing the electrocatalytic activity of the catalysts towards glucose [44]. Sensor performance was evaluated using Chronoamperometry (CA) at the selected potential for each analyte. The LOD was calculated for each analyte using the equation 3.7. The electrochemical performance of the sensors was further investigated in artificial sweat to study the effect of the real matrix on the selectivity of the sensor. Artificial sweat was prepared according to the protocol proposed by *Harvey et al* [33] (Tab. 4.3).

***Table 4.3**: Chemical formulation of artificial human sweat* [33].

Components	Concentration [M]
Electrolytes	
Sodium sulfate (Na_2SO_4)	4,10E-04
Sodium bicarbonate ($NaHCO_3$)	3,00E-03
Potassium chloride	6,10E-03
Magnesium chloride hexahydrate ($MgCl_2 \cdot 6H_2O$)	8,20E-05
Sodium phosphate anhydrous monobasic (NaH_2PO_4)	4,00E-04
Sodium chloride (NaCl)	2,70E-02
Organic acids and carbohydrates	
Lactic acid	1,40E-02
Pyruvic acid ($C_3H_4O_3$)	1,80E-04
d(+)-Glucose ($C_6H_{12}O_6$)	1,70E-04
Aminoacids	
dl-Alanine ($C_3H_7NO_2$)	5,70E-04
l-(+)-Arginine ($C_6H_{14}N_4O_2$)	7,80E-04
l-(+)-Aspartic acid ($C_4H_7NO_4$)	3,40E-04
l-(+)-Citrulline ($C_6H_{13}N_3O_3$)	4,00E-04
l-(+)-Glutamic acid ($C_5H_9NO_4$)	3,70E-04
Glycine ($C_2H_5NO_2$)	3,90E-04
l-Histidine ($C_6H_9N_3O_2$)	5,20E-04
l-Isoleucine ($C_6H_{13}NO_2$)	1,70E-04
l-Leucine ($C_6H_{13}NO_2$)	2,10E-04
l-(+)-Lysine Monohydrochloride ($C_6H_{14}N_2O_2 \cdot HCl$)	1,50E-04
l-(+)-Ornithine Monohydrochloride ($C_5H_{12}N_2O_2 \cdot HCl$)	1,50E-04
l-Phenylalanine ($C_9H_{11}NO_2$)	1,30E-04
l-Threonine ($C_4H_9NO_3$)	4,50E-04
l-(–)-Tryptophan ($C_{11}H_{12}N_2O_2$)	5,50E-05
l-Tyrosine ($C_9H_{11}NO_3$)	1,69E-04
l-Valine ($C_5H_{11}NO_2$)	2,50E-04
Nitrogenous substances	
Ammonium hydroxide $(NH_4OH)^-$	5,20E-03
Uric acid	5,90E-05
Urea (CH_4N_2O)	1,00E-02
Creatinine	8,40E-05
Vitamins	
Thiamine hydrochloride ($C_{12}H_{17}ClN_4OS \cdot HCl$)	5,01E-04
Riboflavin ($C_{17}H_{20}N_4O_6$)	2,00E-03

Nicotinic acid ($C_6H_5NO_2$)	4,10E-01
d-Pantothenic acid calcium salt ($(C_9H_{17}NO_5)_2Ca$)	1,04E-02

A solution of tris(hydroxymethyl)aminomethane 1 M was used to adjust the artificial sweat pH to 7.4. This pH value was selected because it is within the typical range of human sweat (between 4 and 8) [45]. In the case of glucose detection, the pH of the artificial sweat solution was increased to 13 to establish the alkaline conditions required for optimal sensor performance [44].

All tests were repeated three times using new electrodes and fresh solutions for each test.

4.2.4 Fabrication of Paper-Microfluidic System

The paper microfluidic system is shown in Fig. 4.6. Chromatographic paper (Whatman type 1) was used. The paper fluidic channels were positioned and sandwiched between two vinyl layers patterned using a cutter plotter. These vinyl layers presented several windows to expose specific areas of the paper and to aid in aligning the paper component with the chip.

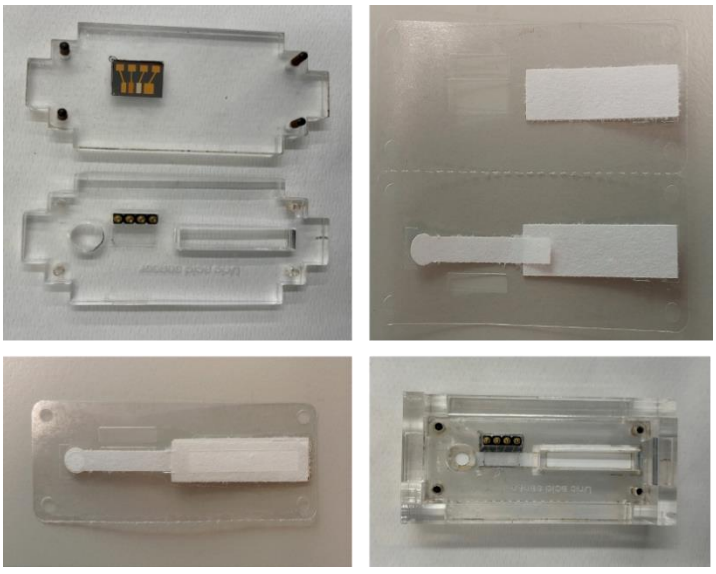

Figure 4.6*: Paper-microfluidic electrochemical system.*

The chip and the paper-based fluidic component were assembled in a PMMA cell, as shown in Fig. 4.6. Four clamping structures were used to press the bottom and top parts of the PMMA cell, maintaining constant pressure. This system was designed for easy assembly and disassembly, allowing the replacement of the paper component after each measurement. Two windows on the top exposed the sample addition and sink areas of the paper component, while a third window accommodated a 4-pin spring-loaded connector to make contact with the transducer array.

4.2.5 Electrochemical Performance in the Paper-Microfluidic System

The gold chip with four electrodes was used to investigate uric acid and chloride detection in the microfluidic paper system described above. Ag electrodeposition was performed on electrode b), and then rGO-AuNps electrodeposition was carried out on electrode c) (Fig.4.5). CA tests were performed. Seven analyte concentrations and a blank were analyzed with a single fluidic paper, with injections each being 7 µL. These tests were conducted with solutions containing a single analyte and with solutions containing both analytes simultaneously.

4.3 Results and Discussion

As mentioned in the previous section, before electrochemically modifying the working electrodes for the detection of the three analytes, the gold bare electrodes were electrochemically characterized. Fig. 4.7a presents the CVs recorded in Fc-MeOH 1 mM at different scan rates. The increase in scan rates resulted in a shift of the peak potential towards higher values [46]. The CV profile corresponds to the redox species in the solution. The oxidation and the reduction current peaks show a linear dependence with the square root of the scan rate, Fig. 4.7b, suggesting a diffusion-controlled process. The similar slope and values of

oxidation and reduction also suggest a reversible reaction. This observation aligns with previous literature [47].

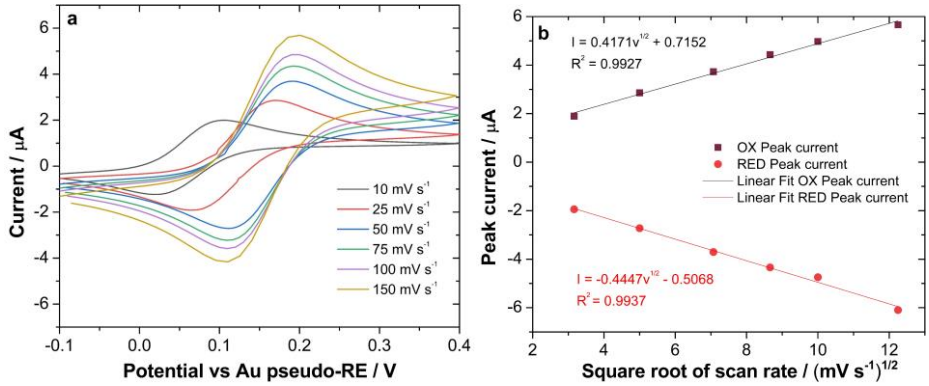

***Figure 4.7**: a) CVs recorded in a 0.1 M KNO_3 solution containing Fc-MeOH 1 mM at different scan rates and b) corresponding linear plots of the recorded anodic and cathodic peak current vs. the square root of the scan rate.*

4.3.1 Uric acid sensor

For the detection of uric acid, the surface of the gold WE was modified with rGO-AuNPs. The potentiostatic co-deposition was carried out at -0.8 V vs Ag/AgCl for 200 s [42]. This process achieved a balanced loading that ensured a high electrochemical surface area and excellent electrocatalytic activity for the oxidation of uric acid (UA). The co-electrodeposition of rGO and Au-NPs followed the reactions [48], [49]:

$$GO + xH^+ + ye^- \rightarrow rGO + zH_2O \quad (4.1)$$

$$AuCl^-_4 + 3e^- \rightarrow Au + 4Cl^- \quad (4.2)$$

These reactions resulted in the deposition of rGO micro-sheets, which were almost uniformly covered with Au nanoparticles. Typical morphology can be observed in the SEM images reported in Fig. 4.8.

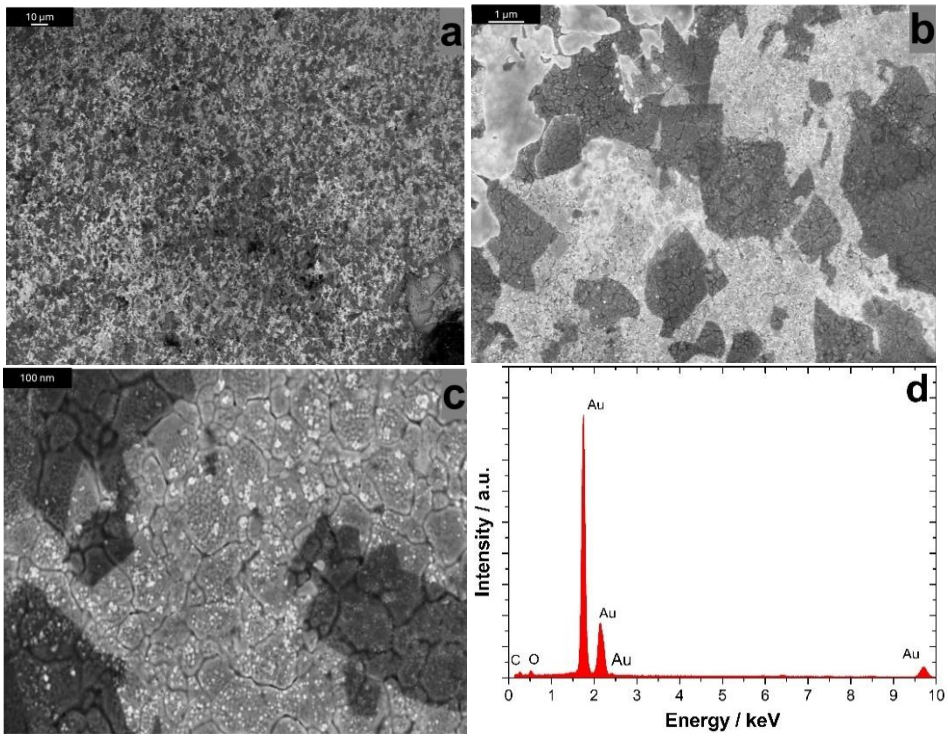

***Figure 4.8**: (a-c) SEM images a) 1000x, b) 20000x, c) 75000x, and d) EDS spectrum.*

The SEM images show the presence of AuNPs between the rGO micro-sheets. EDS spectrum (Fig. 4.8d) shows the Au peaks (from the gold chip and electrodeposited AuNPs) and the C and O peaks (from the electrodeposited rGO). According to the literature [50], the co-electrodeposition of AuNPs and rGO leads to the formation of an electrode with a higher surface area compared to pure rGO film. This is due to AuNPs that space the rGO sheets. In addition, AuNPs act as an electron transfer channel, further improving the rGO conductivity.

The potential for uric acid oxidation was determined from LSV tests, which were conducted over a potential range of - 0.1 to 0.8 V (vs Au pseudo-RE) at a scan rate of 50 mV/s. These tests were carried out in a 0.1 M PBS solution with a pH of 7.4, containing 1 mM of uric acid. Fig.4.9 shows the difference between the gold bare electrode and the modified WE. The gold bare and the modified electrodes were calibrated by CA at 0.5 V vs Au pseudo-RE for 50 s in a range

of 0.01-0.5 mM (Fig. 4.10a). Fig.4.10b shows that the sensitivity of the sensor is about two times higher when the surface of the gold is modified by co-deposition of rGO and Au nanoparticles. A sensitivity of 1.610 μA mM^{-1} (R^2 = 0.9997), with a mean RSD of 3.8 %, and a LOD of 4.3 μM was obtained.

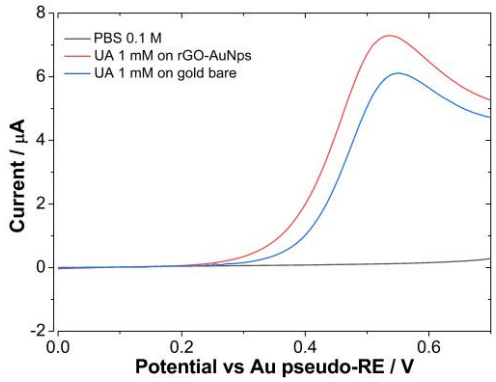

***Figure 4.9**: LSV tests carried out at 50 mV s^{-1} on the gold bare electrode (blue) and modified WE with rGO-AuNps co-deposition (red).*

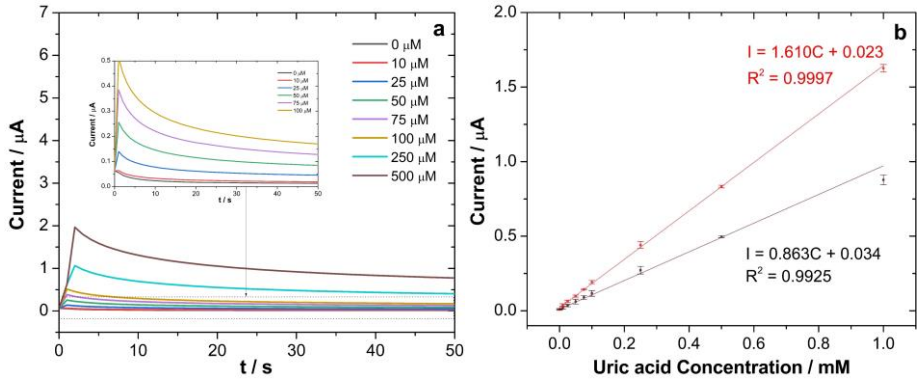

***Figure 4.10**: a) CA at 0.5 V vs Au pseudo-RE in PBS 0.1 M containing different concentrations of uric acid and b) corresponding calibration lines with SD error bars (N=3) for gold bare electrode (black) and WE modified with rGO-AuNps co-deposition (red).*

The performance of the sensors was investigated in artificial sweat to study its behavior in a complex real matrix. From the LSV curve shown in Fig. 4.11a, a value 0.5 V vs Au pseudo-RE was selected to perform the CA tests on the sensor in artificial sweat.

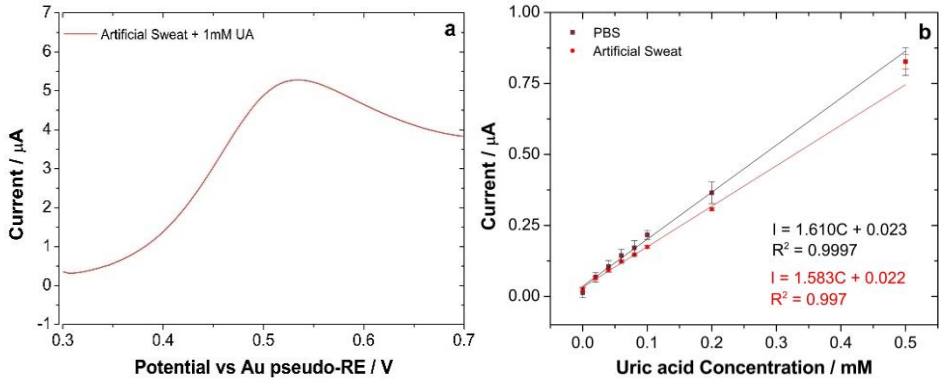

***Figure 4.11**: a) LSV carried out at 50 mV s^{-1} on modified WE with rGO-AuNps co-deposition in artificial sweat and b) calibration lines obtained by CA at 0.5 V vs Au pseudo-RE in PBS (black) and in artificial sweat (red) with SD error bars (N=3).*

For uric acid dissolved in artificial sweat, a sensitivity of 1.610 µA mM^{-1} (R^2 = 0.997) with a mean RSD of approximately 3% was obtained (Fig. 4.11b). Compared to PBS, there was a small reduction in the value of sensitivity, so it can be concluded that there was a negligible effect of the matrix of artificial sweat on the sensor performance. Tab. 4.4 summarizes the key performance characteristics of the sensor in different testing conditions. Tab. 4.5 presents a comparison of various electrochemical sensors for uric acid in sweat.

***Table 4.4**: Main features of the electrochemical sensor.*

Electrolyte	Sensitivity / µA $µM^{-1}$	Sensitivity / µA $µM^{-1}$ cm^{-2}	Mean RSD / %
PBS	1.610	64.4	3.8
Artificial sweat	1.583	63.3	3

***Table 4.5**: Analytical parameters for some existing electrochemical sensors to detect uric acid.*

Sensor Type	Detection Method	Sensitivity/ µA mM^{-1} cm^{-2}	Linear Range / mM	LOD / µM	Sample	Ref.
MWCNT-COOH-modified carbon electrode	CA	23.17	0-0.04	3.58	Undiluted sweat	[51]
CuNi-MOFGO nanomaterials-based sensor	CA	26	0.01-1	9.09	Undiluted sweat	[52]
N-rGO/Au Das-based wearable sensor	CA	7.6	0.005-0.6	3.7	Undiluted artificial sweat	[32]
AgNWs-PrussianBlue composite aerogel-based wearable sensor	CA	50.6	0.01-3	0.05	Undiluted artificial sweat	[53]
rGO-AuNPs-modified gold WE	**CA**	**63.3**	**0.01-0.5**	**4.3**	**Undiluted artificial sweat**	**This work**

4.3.2 Chlorides sensor

Silver (Ag) was selected as the active material for the chloride ion detection. Thus, the surface of the gold WE were modified by silver electrodeposition. LSV test was used to define the deposition potential of Ag on the electrode surface. The potential was varied in the cathodic direction from 0.2 to - 0.4 V at a scan rate of 50 mV s^{-1} in a solution of HNO_3 10 mM containing tartaric acid 15 mM and 10 mM $AgNO_3$ (Fig. 4.12a). Tartaric acid is a capping agent that protects the silver surface, improving its stability [54]. The deposition of silver starts at about - 0.1 V with a deposition potential of - 0.2 V, associated with the reduction process [55]:

$$AgNO_3 + e^- \rightarrow Ag + NO_3^- \quad (4.3)$$

The potentiostatic deposition of Ag was carried out at - 0.2 V vs Au pseudo-RE. Using this potential, deposition time and concentration of $AgNO_3$ were optimized to obtain a silver layer that would allow a complete calibration in the concentration range of 1-100 mM. The optimized conditions are 600 s using a

solution of $AgNO_3$ 100 mM. Fig. 4.12b-c shows the SEM images of the electrode after Ag electrodeposition. The silver particles, having a polygonal shape similar to [56], uniformly covered the electrode surface. From Fig. 4.12c, an average size of about 1 µm was calculated. The EDS spectrum (Fig. 4.12d) shows the formation of a deposit consisting of pure Ag.

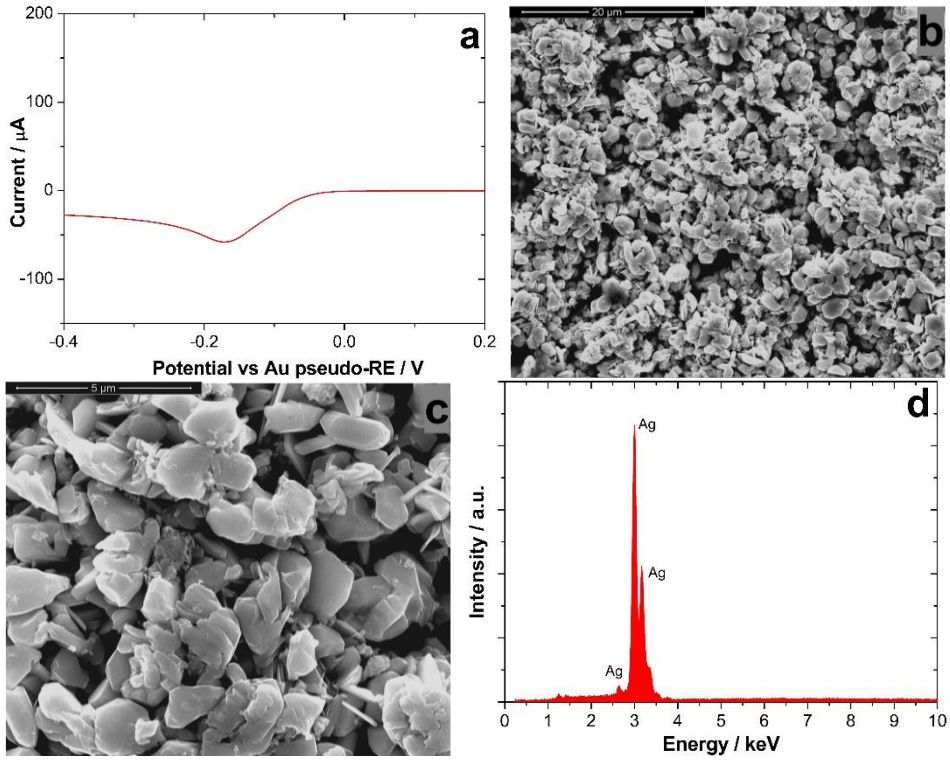

***Figure 4.12**: a) LSV carried out at 50 mV s^{-1} in 10 mM HNO_3 containing tartaric acid 15 mM and 10 mM $AgNO_3$, b) SEM image 5000x, c) SEM image 20000x, and d) EDS spectrum.*

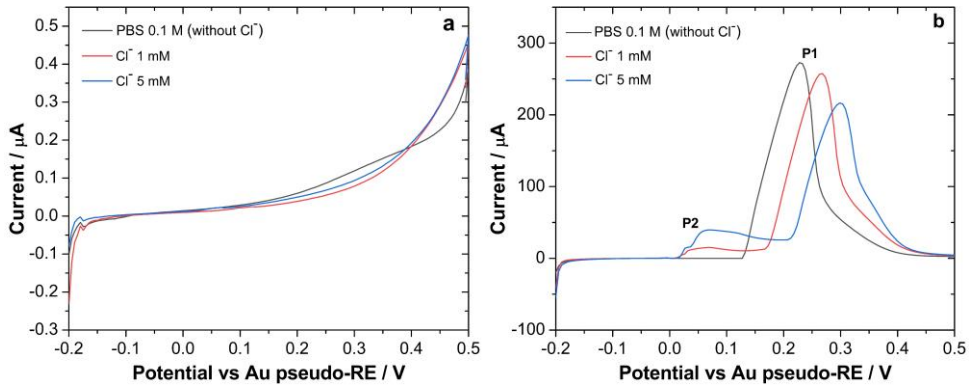

***Figure 4.13**: LSV tests carried out at 50 mV s^{-1} on a) gold bare and b) modified WE.*

The absence of any oxidation peak in Figure 4.13a suggests that gold is inactive for chloride detection. After the surface modification, Figure 4.13b, the presence of two different oxidation peaks can be observed.

In the blank solution (without chloride ions), a peak (P1) at 0.2 V was observed. It is related to the oxidation of Ag to Ag^+. Following the addition of 1 mM NaCl, a second peak (P2) at 0.05 V, attributed to the oxidation of Ag to AgCl, and a decrease of the first peak was observed. Increasing Cl^- concentration, from 1 mM to 5 mM, P2 increases in intensity with a corresponding decrease in the P1 peak intensity [57], [58]. This behavior was further confirmed by the results reported in Fig. 4.14, in which P1 peaks decreased until the complete oxidation of silver.

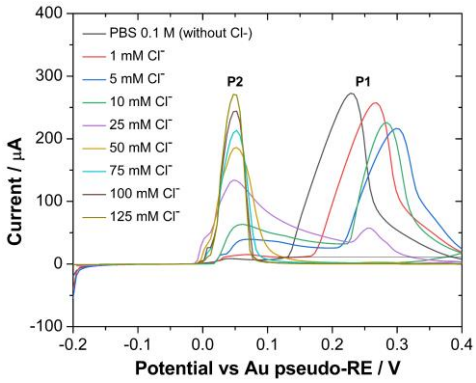

***Figure 4.14**: LSV tests carried out at 50 mV s^{-1} on modified WE in NaCl with different concentrations.*

The sensor was calibrated by CA at 0.05 V vs Au pseudo-RE for 50 s in a range of 1-100 mM (Fig. 4.15a).

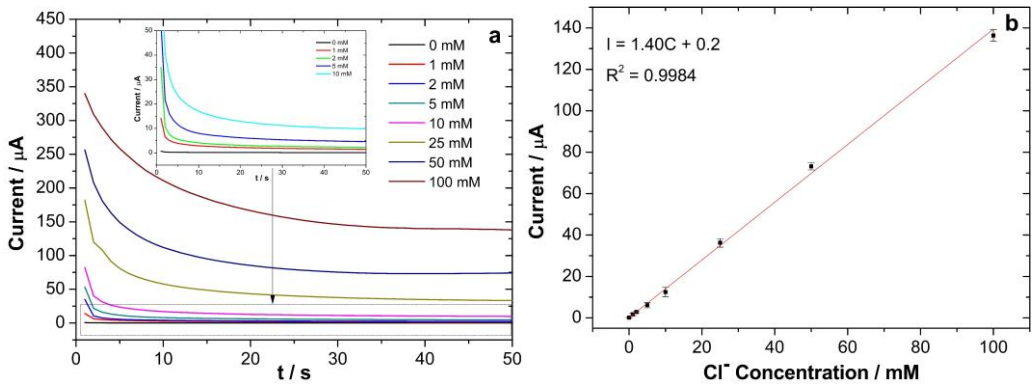

***Figure 4.15**: a) CA at 0.05 V vs Au pseudo-RE in PBS 0.1 M containing different concentrations of NaCl and b) corresponding calibration line with SD error bars (N=3).*

A sensitivity of 1.4 µA mM^{-1} (R^2 = 0.9984) with a mean RSD of 2.5% (Fig. 4.15b) and a LOD of 39 µM were obtained in the linear range of 1-100 mM. From the LSV curve shown in Fig. 4.16a, a value of 0.1 V vs Au pseudo-RE was selected to perform CA tests in artificial sweat.

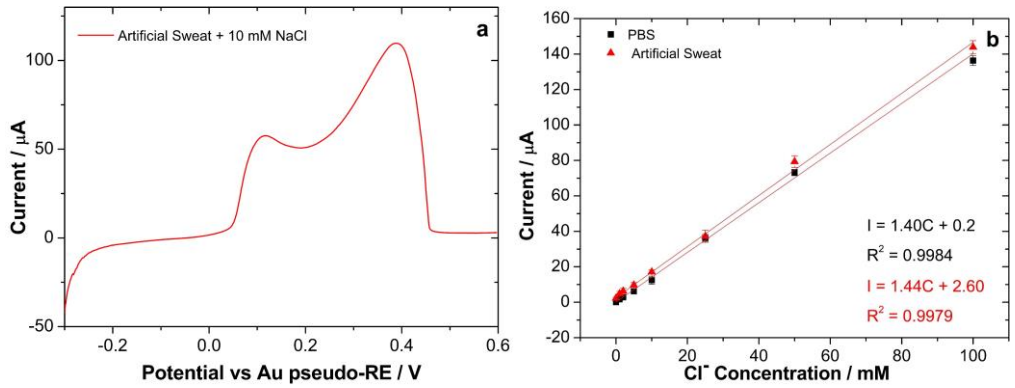

***Figure 4.16**: a) LSV carried out at 50 mV s^{-1} on modified WE with Ag deposition in artificial sweat and b) calibration lines obtained by CA at 0.1 V vs Au pseudo-RE in PBS (black) and in artificial sweat (red) with SD error bars (N=3).*

A sensitivity of 1.44 µA mM^{-1} (R^2=0.9979) with a mean RSD of 1.4% (Fig. 4.16b) was obtained for NaCl dissolved in artificial sweat. This value is

practically the same obtained in PBS, thus the matrix of artificial sweat does not affect the ability of the sensor to detect chloride ions.

Tab. 4.6 summarizes the key performance characteristics of the sensor in different testing conditions.

***Table 4.6**: Main features of the electrochemical sensor.*

Electrolyte	Sensitivity / $\mu A\ \mu M^{-1}$	Sensitivity / $\mu A\ \mu M^{-1}\ cm^{-2}$	Mean RSD / %
PBS	1.40	56	2.5
Artificial sweat	1.44	57.6	1.4

Tab. 4.7 presents a summary of various electrochemical sensors from the literature, highlighting its analytical features for chlorides in sweat.

***Table 4.7**: Analytical parameters for some existing electrochemical sensors to detect chlorides.*

Sensor Type	Detection Method	Sensitivity/ $\mu A\ mM^{-1}\ cm^{-2}$	Linear Range / mM	LOD / µM	Sample	Ref.
Paper-based electrochemical sensor	CV	1.98 µA mM^{-1} (WE are not provided)	10-200	1000	Undiluted sweat	[59]
AgNPs on polyester-SPE	CV	-	2-40	-	1:4 diluted synthetic sweat	[60]
Silver ink on polypropylene film	LSV	-	0.1-20	18.83	1:100 diluted sweat	[61]
AgNPs-modified carbon WE (SPCE)	LSV	2.32	5-60	-	Synthetic sweat	[62]
Ag-modified gold WE	**CA**	**57.6**	**1-100**	**39**	**Undiluted synthetic sweat**	**This work**

4.3.3 Glucose sensor

For the detection of glucose, the surface of the gold WE was modified with NiNPs electrodeposition. To define the deposition potential of Ni, the LSV was carried out in the potential range from 0 to -1 V at a scan rate of 50 mV s^{-1} (Fig. 4.17a). A solution containing 0.5 M H_3BO_3, KNO_3 0.1 M and $NiSO_4$ 0.1 M [43] was used. Ni electrodeposition starts at - 0.6 V with a peak at - 0.8 V. Potential and time deposition values were tuned to obtain optimal conditions (-0.8 V for 100 s).

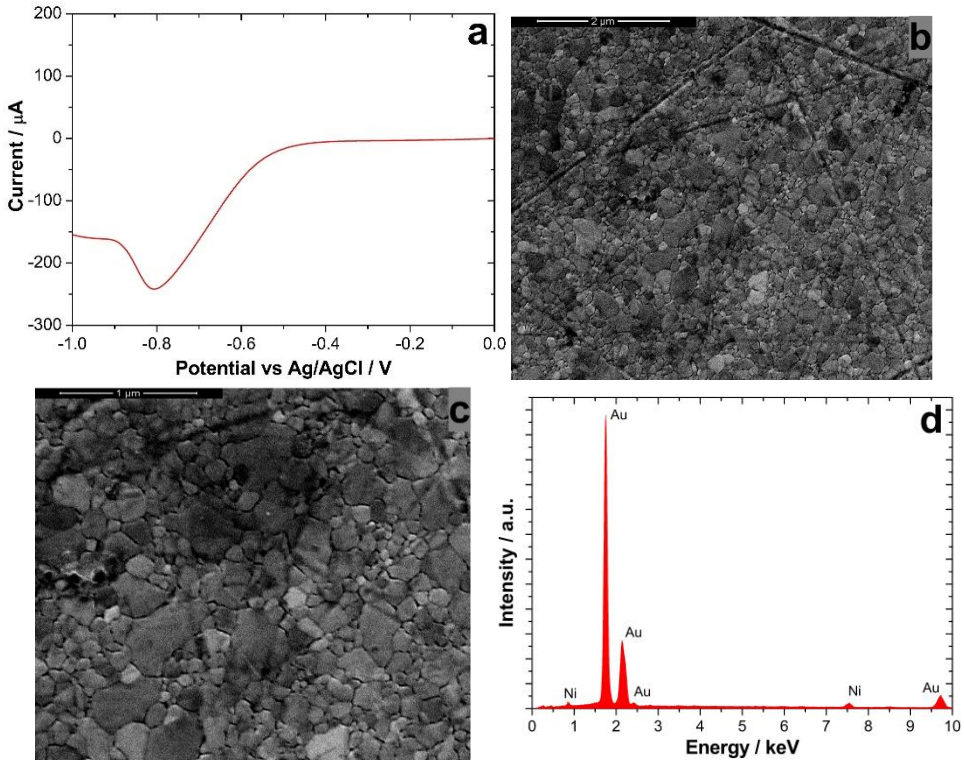

***Figure 4.17**: a) LSV carried out at 50 mV s^{-1} in H_3BO_3 0.5 M containing KNO_3 0.1 M and $NiSO_4$ 0.1 M, b) SEM image 40000x, and c) SEM image 80000x, and d) EDS spectrum.*

Figure 4.17b presents the SEM images of the electrode following the electrodeposition process. The SEM images reveal the formation of a Ni film composed of grains with an average diameter of 80 nm and with a morphology

that closely mirrors patterns reported in the literature [63], [64]. The EDS spectrum (4.17c) further confirms the presence of Ni on gold electrodes.

Fig. 4.18a shows the absence of any oxidation peak, suggesting that the gold bare electrode is not an active material for glucose detection.

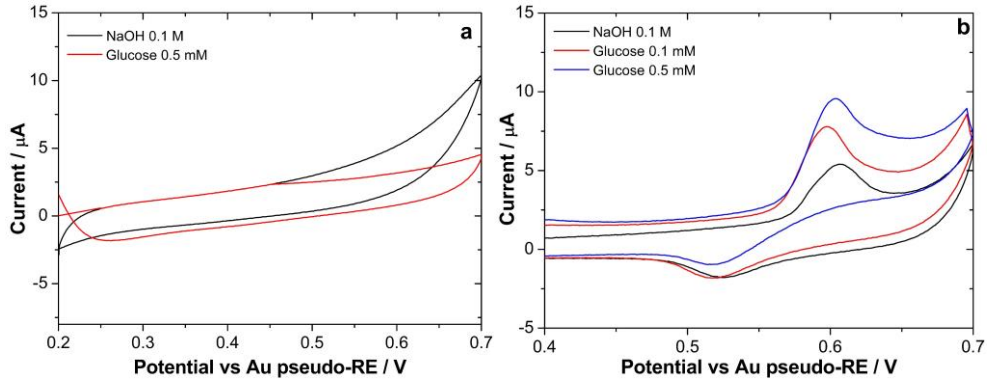

***Figure 4.18**: CVs carried out at 50 mV s^{-1} on a) gold bare and b) modified WE.*

In contrast, using the modified electrode, distinct redox peaks can be observed (Fig. 4.18b). These peaks correspond to the redox reaction of the Ni^{2+}/Ni^{3+} couple occurring on the electrode surface [65]. In alkaline solutions, the following mechanism has been proposed [66], [67]:

$$Ni + 2OH^- \rightarrow Ni(OH)_2 + 2e^- \quad (4.4)$$

$$Ni(OH)_2 + OH^- \rightarrow NiO(OH) + H_2O + e^- \quad (4.5)$$

Upon adding glucose to the NaOH solution, Ni^{3+}, generated on the surface of the electrode, quickly oxidizes glucose to glucolactone:

$$NiO(OH) + \text{glucose} \rightarrow Ni(OH)_2 + \text{glucolactone} \quad (4.6)$$

This process leads to the consumption of Ni^{3+} and the formation of Ni^{2+}, which causes an increase in the oxidation peak current and a decrease in the reduction peak current [65].

From Fig. 4.18a a potential value of 0.6 V vs Au pseudo-RE was selected to calibrate the sensor in the range of 0.05-2 mM (Fig. 4.19a).

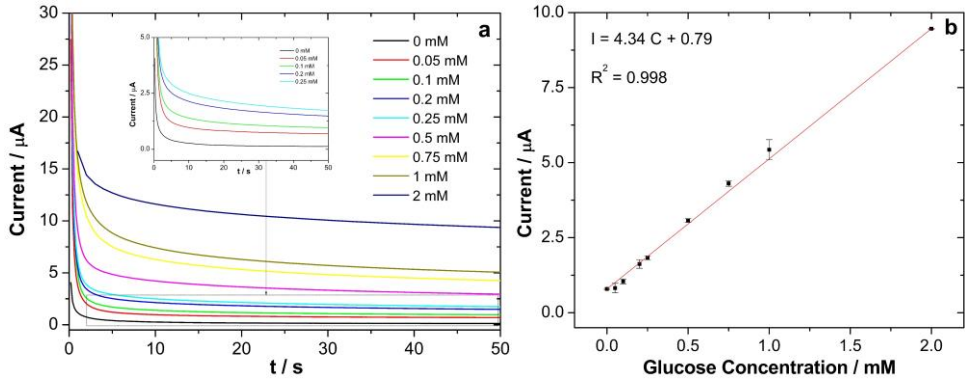

***Figure 4.19**: a) CA at 0.6 V vs Au pseudo-RE in NaOH 0.1 M containing different glucose concentrations and b) corresponding calibration line with SD error bars (N=3).*

A sensitivity of 4.34 µA mM^{-1} (R^2=0.998) with a mean RSD of approximately 0.5% (Fig. 4.19b) and a LOD of 27 µM was obtained in the linear range of 0.05-2 mM. Glucose detection was also studied in artificial sweat. Fig. 4.20 showed that, at increasing glucose concentration, the oxidation peak was less evident.

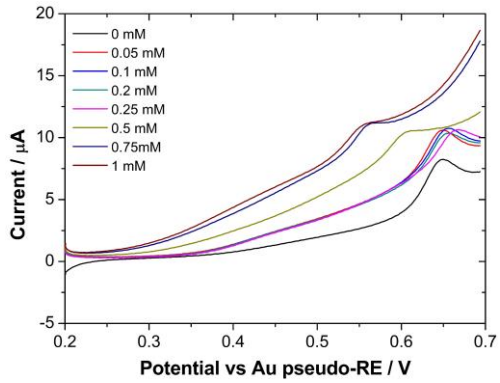

***Figure 4.20**: LSV tests carried out at 50 mV s^{-1} on modified WE with Ag deposition in artificial sweat containing different glucose concentrations.*

The sensor was used for the LSV test in NaOH 0.1 M. As shown in Fig. 4.21a, there were no oxidation peaks anymore. The most likely hypothesis is that some species present in artificial sweat poisoned the nickel on the electrode surface, thereby preventing subsequent glucose detection. For example, chlorides or nitrogen compounds can form complex ions with nickel, blocking its active sites and inhibiting its effectiveness in catalytic application [68], [69].

So, to obtain more stable NiNPs, GO 0.5 mg mL^{-1} was added to the deposition solution [70] and 40 CVs were carried out in NaOH 0.1 M (from 0 to 0.7 V at 100 mVs^{-1}) after the deposition as pretreatment to facilitate the formation of $Ni(OH)_2$ and improve the stability of nanoparticles [71].

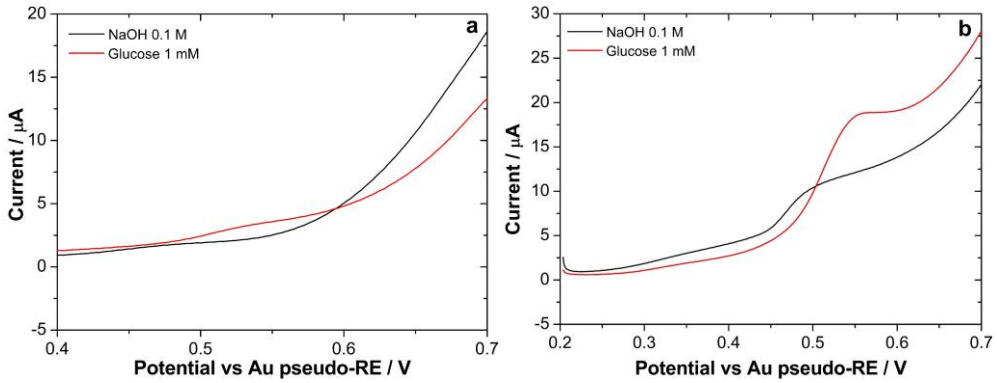

***Figure 4.21**: LSV tests carried out at 50 mV s^{-1} in NaOH 0.1 M and glucose 1 mM after LSV in artificial sweat for WE modified with the a) first method and the b) second one.*

Figure 4.21b shows that, with the new deposition, the oxidation peak is more stable after LSV tests in artificial sweat. Although the stability of NiNPs had been enhanced, the sensor was still unable to detect glucose in artificial sweat. The effect of various components found in artificial sweat that might interfere with glucose detection was investigated. Fig. 4.22 demonstrates that the addition of some species, such as urea, ammonium hydroxide, and lactic acid, which are commonly found in sweat, into the solution leads to a significant shift in the glucose oxidation peak. According to the literature, for non-enzymatic sensors, these species cause interference issues in glucose detection, particularly when

present at typical sweat concentration [72], [73], [74]. As a result, it becomes challenging to reliably detect glucose by CA under these conditions.

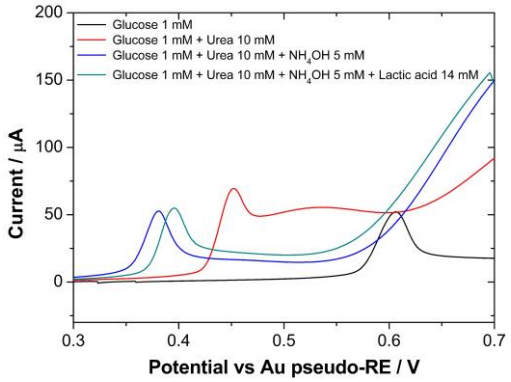

***Figure 4.22**: LSV tests carried out at 50 mVs^{-1} in NaOH 0.1 M also containing some species commonly present in sweat.*

4.3.4 Electrochemical Performance in the Paper-Microfluidic System

The gold chip with four electrodes was employed to detect uric acid and chloride ions in the previously described paper-based microfluidic system. This system was used to demonstrate its potential for real-time, on-site detection with minimal volume required, making it suitable for medical applications. The simplicity and cost-effectiveness of the paper also provided an ideal medium for scalable and point-of-care diagnostics.

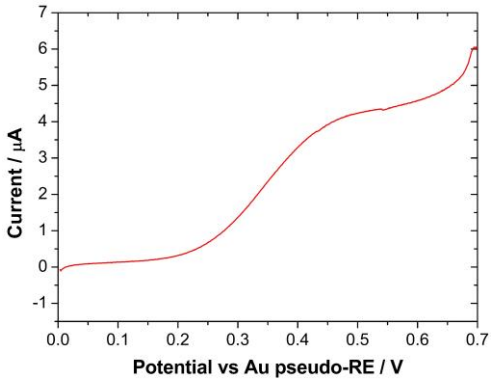

***Figure 4.23**: LSV in a solution containing 0.5 mM of uric acid in a paper-microfluidic system.*

Following the procedure described previously, the two working electrodes were modified with Ag and rGO-AuNps electrodeposition. First, uric acid detection was investigated by LSV, as reported in Fig. 4.23. A potential of 0.5 V was chosen to carry out CA tests (Fig. 4.24a) to detect different concentrations of uric acid.

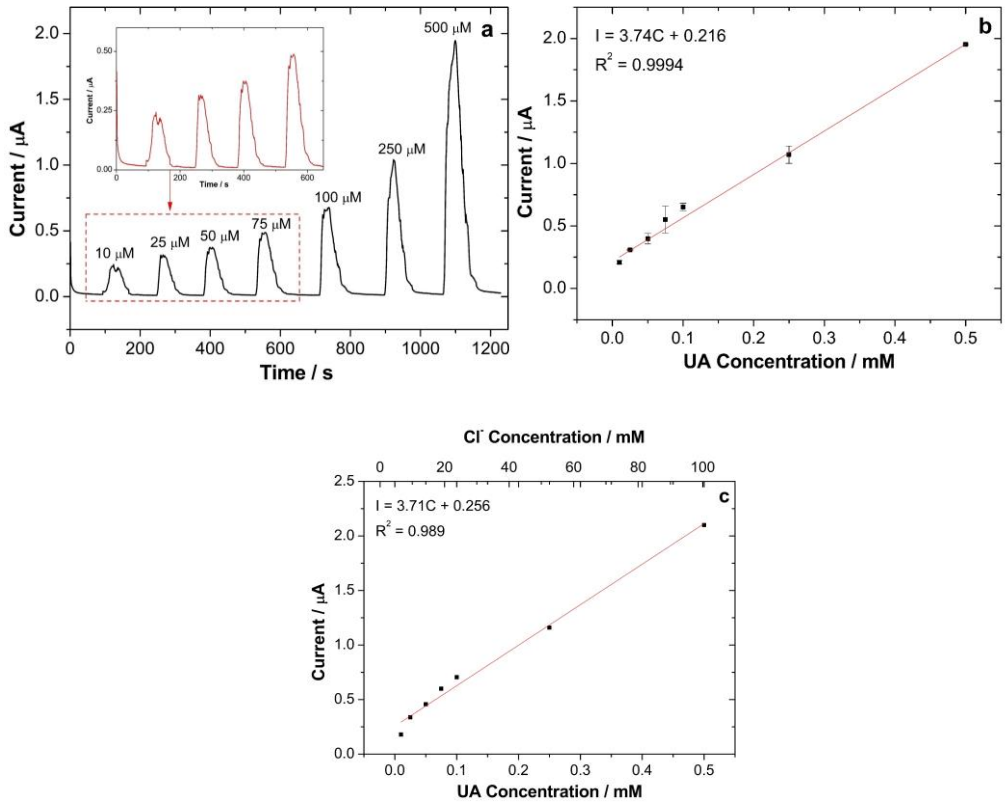

Figure 4.24: a) *CA recorded at 0.5 V and b) corresponding calibration line with SD error bars (N=3), c) calibration line obtained in the presence of increasing* Cl^- *concentration.*

A sensitivity of 3.74 µA mM^{-1} (R^2=0.9994) was obtained in the linear range of 0.01-0.5 mM (Fig. 4.24b). CA tests at 0.5 V vs. Au pseudo-RE were also performed in the presence of increasing chloride concentration and the calibration line obtained under this condition is shown in Fig. 4.24c. The slopes are similar, indicating that the presence of chlorides does not affect uric acid detection.

The detection of chloride ions was subsequently explored within the same paper microfluidic system. From Fig. 4.25, a potential of 0.1 V was chosen to carry out CA tests (Fig. 4.26a) to detect different flowing concentrations of chlorides.

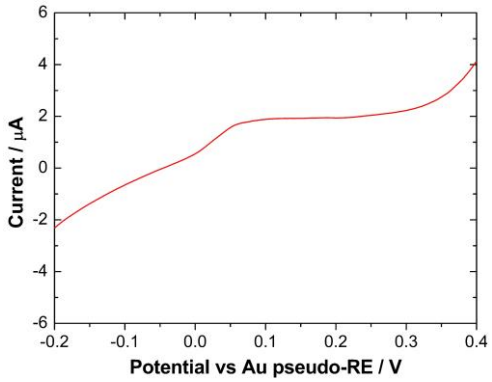

***Figure 4.25**: LSV in a solution containing 1 mM of NaCl in a paper-microfluidic system.*

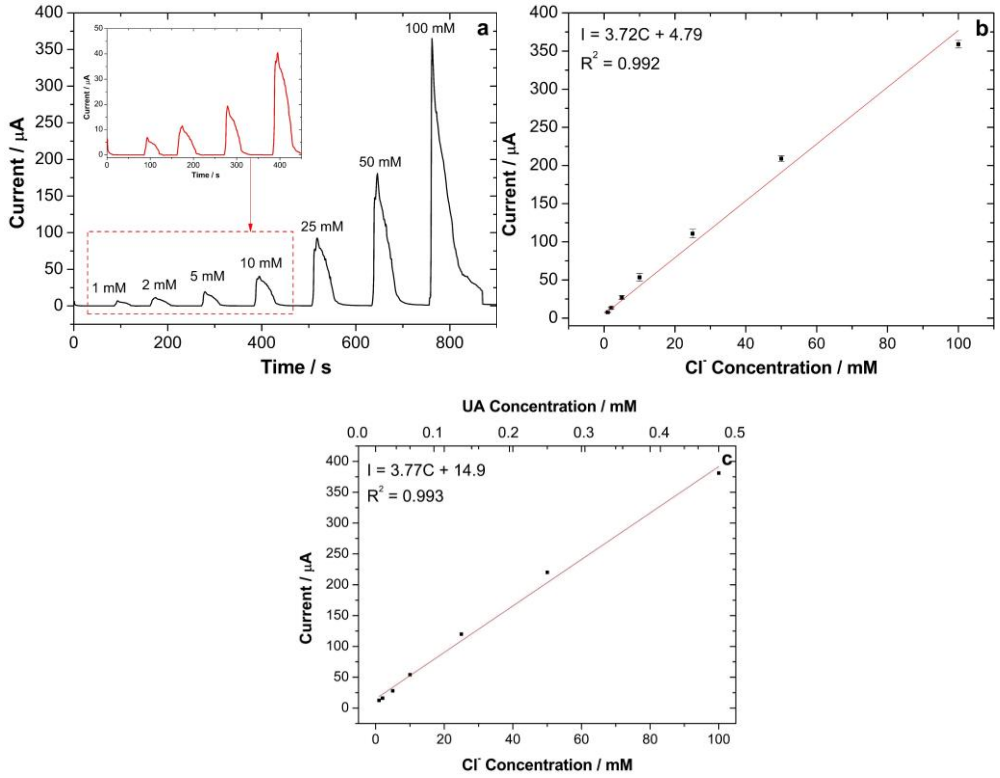

***Figure 4.26**: a) CA recorded at 0.1 V and b) corresponding calibration lines with SD error bars (N=3), c) calibration line obtained in presence of increasing UA concentration.*

A sensitivity of 3.72 µA mM^{-1} (R^2=0.992) was obtained in the linear range of 1-100 mM (Fig. 4.26b). Also in this case, CA tests were performed in the presence

of increasing uric acid concentration, and the resulting calibration line is shown in Fig. 4.26c. The presence of uric acid did not affect the chloride ions detection.

4.4 Conclusions and Future Perspectives

The integration of wearable and noninvasive sensors for real-time sweat analysis represents significant progress in health monitoring and disease prevention. The advantages of using sweat as a diagnostic medium - including its accessibility, ease of collection, and rich biomarker content - establish it as a promising alternative to traditional blood testing methods. While traditional methods rely on vigorous exercise or iontophoretic stimulation to induce sweat, innovations in microfluidic devices present a promising alternative. These devices enable continuous and non-invasive monitoring by requiring minimal sample volumes, which is crucial given the limited sweat production rates. Their ability to connect wirelessly enhances the real-time analysis of biomarker data, paving the way for personalized health monitoring solutions.

In this research work, an electrochemical sensor to detect uric acid, chloride ions, and glucose in sweat was developed. This sensor consists of a silicon chip with gold electrodes, which were modified to optimize the detection performance for each of the three target analytes. Sensitivities of 1.610 μA mM^{-1}, 1.4 μA $mM^{-1,}$ and 4.34 μA mM^{-1} were obtained for uric acid, chloride ions, and glucose, respectively. However, the detection of glucose presented a considerable challenge primarily due to the interference from various species present in the artificial sweat matrix. This complexity limited the ability of the sensor to accurately assess glucose levels. Consequently, the focus of this research analysis shifted to the detection of uric acid and chloride ions within the realized microfluidic system. The system showed a sensitivity of 3.74 μA mM^{-1} for uric acid and 3.72 μA mM^{-1} for chloride ions, with both analytes detection unaffected by the presence of each other. However, to further establish the effectiveness of

the electrochemical sensor, additional tests should be performed in a real sweat sample to assess the levels of these two biomarkers.

This work highlights the promising application of electrochemical sensors in the field of non-invasive health monitoring, paving the way for further advancements in sweat analysis technology.

References

[1] F. Gao *et al.*, «Wearable and flexible electrochemical sensors for sweat analysis: a review», *Microsyst Nanoeng*, vol. 9, fasc. 1, p. 1, gen. 2023, doi: 10.1038/s41378-022-00443-6.

[2] J. Xu, Y. Fang, e J. Chen, «Wearable Biosensors for Non-Invasive Sweat Diagnostics», *Biosensors*, vol. 11, fasc. 8, p. 245, lug. 2021, doi: 10.3390/bios11080245.

[3] J. Kim, A. S. Campbell, B. E.-F. De Ávila, e J. Wang, «Wearable biosensors for healthcare monitoring», *Nat Biotechnol*, vol. 37, fasc. 4, pp. 389–406, apr. 2019, doi: 10.1038/s41587-019-0045-y.

[4] M. Li *et al.*, «A highly integrated sensing paper for wearable electrochemical sweat analysis», *Biosensors and Bioelectronics*, vol. 174, p. 112828, feb. 2021, doi: 10.1016/j.bios.2020.112828.

[5] G. Zhao, Z. Li, X. Huang, Q. Zhang, Y. Liu, e X. Yu, «Recent advances of sweat sampling, sensing, energy-harvesting and data-display toward flexible sweat electronics», *Soft Sci*, vol. 4, fasc. 2, mag. 2024, doi: 10.20517/ss.2024.04.

[6] Annu e A. N. Raja, «Recent development in chitosan-based electrochemical sensors and its sensing application», *International Journal of Biological Macromolecules*, vol. 164, pp. 4231–4244, dic. 2020, doi: 10.1016/j.ijbiomac.2020.09.012.

[7] S. Emaminejad *et al.*, «Autonomous sweat extraction and analysis applied to cystic fibrosis and glucose monitoring using a fully integrated wearable platform», *Proc. Natl. Acad. Sci. U.S.A.*, vol. 114, fasc. 18, pp. 4625–4630, mag. 2017, doi: 10.1073/pnas.1701740114.

[8] J. R. Sempionatto *et al.*, «Eyeglasses based wireless electrolyte and metabolite sensor platform», *Lab Chip*, vol. 17, fasc. 10, Art. fasc. 10, 2017, doi: 10.1039/C7LC00192D.

[9] H. Y. Y. Nyein *et al.*, «A Wearable Electrochemical Platform for Noninvasive Simultaneous Monitoring of Ca^{2+} and pH», *ACS Nano*, vol. 10, fasc. 7, Art. fasc. 7, lug. 2016, doi: 10.1021/acsnano.6b04005.

[10] J. Moyer, D. Wilson, I. Finkelshtein, B. Wong, e R. Potts, «Correlation Between Sweat Glucose and Blood Glucose in Subjects with Diabetes», *Diabetes Technology & Therapeutics*, vol. 14, fasc. 5, Art. fasc. 5, mag. 2012, doi: 10.1089/dia.2011.0262.

[11] W. Jia *et al.*, «Electrochemical Tattoo Biosensors for Real-Time Noninvasive Lactate Monitoring in Human Perspiration», *Anal. Chem.*, vol. 85, fasc. 14, Art. fasc. 14, lug. 2013, doi: 10.1021/ac401573r.

[12] Y. Yang *et al.*, «A laser-engraved wearable sensor for sensitive detection of uric acid and tyrosine in sweat», *Nat Biotechnol*, vol. 38, fasc. 2, Art. fasc. 2, feb. 2020, doi: 10.1038/s41587-019-0321-x.

[13] W. Gao *et al.*, «Wearable Microsensor Array for Multiplexed Heavy Metal Monitoring of Body Fluids», *ACS Sens.*, vol. 1, fasc. 7, Art. fasc. 7, lug. 2016, doi: 10.1021/acssensors.6b00287.

[14] O. Parlak, S. T. Keene, A. Marais, V. F. Curto, e A. Salleo, «Molecularly selective nanoporous membrane-based wearable organic electrochemical device for noninvasive cortisol sensing», *Sci. Adv.*, vol. 4, fasc. 7, Art. fasc. 7, lug. 2018, doi: 10.1126/sciadv.aar2904.

[15] W. Gao *et al.*, «Wearable sweat biosensors», in *2016 IEEE International Electron Devices Meeting (IEDM)*, San Francisco, CA, USA: IEEE, dic. 2016, p. 6.6.1-6.6.4. doi: 10.1109/IEDM.2016.7838363.
[16] N. Davis, J. Heikenfeld, C. Milla, e A. Javey, «The challenges and promise of sweat sensing», *Nat Biotechnol*, vol. 42, fasc. 6, Art. fasc. 6, giu. 2024, doi: 10.1038/s41587-023-02059-1.
[17] Y. Zhang *et al.*, «Passive sweat collection and colorimetric analysis of biomarkers relevant to kidney disorders using a soft microfluidic system», *Lab Chip*, vol. 19, fasc. 9, pp. 1545–1555, 2019, doi: 10.1039/C9LC00103D.
[18] A. J. Bandodkar *et al.*, «Battery-free, skin-interfaced microfluidic/electronic systems for simultaneous electrochemical, colorimetric, and volumetric analysis of sweat», *Sci. Adv.*, vol. 5, fasc. 1, p. eaav3294, gen. 2019, doi: 10.1126/sciadv.aav3294.
[19] A. Koh *et al.*, «A soft, wearable microfluidic device for the capture, storage, and colorimetric sensing of sweat», *Sci. Transl. Med.*, vol. 8, fasc. 366, nov. 2016, doi: 10.1126/scitranslmed.aaf2593.
[20] Y. Sekine *et al.*, «A fluorometric skin-interfaced microfluidic device and smartphone imaging module for *in situ* quantitative analysis of sweat chemistry», *Lab Chip*, vol. 18, fasc. 15, pp. 2178–2186, 2018, doi: 10.1039/C8LC00530C.
[21] S. Cinca-Morros, S. Garcia-Rey, J. Álvarez-Herms, L. Basabe-Desmonts, e F. Benito-Lopez, «A physiological perspective of the relevance of sweat biomarkers and their detection by wearable microfluidic technology: A review», *Analytica Chimica Acta*, vol. 1327, p. 342988, ott. 2024, doi: 10.1016/j.aca.2024.342988.
[22] Z. Sonner *et al.*, «The microfluidics of the eccrine sweat gland, including biomarker partitioning, transport, and biosensing implications», *Biomicrofluidics*, vol. 9, fasc. 3, p. 031301, mag. 2015, doi: 10.1063/1.4921039.
[23] H. Tabasum, N. Gill, R. Mishra, e S. Lone, «Wearable microfluidic-based e-skin sweat sensors», *RSC Adv.*, vol. 12, fasc. 14, pp. 8691–8707, 2022, doi: 10.1039/D1RA07888G.
[24] H. Yu e J. Sun, «Sweat detection theory and fluid driven methods: A review», *Nanotechnology and Precision Engineering*, vol. 3, fasc. 3, pp. 126–140, set. 2020, doi: 10.1016/j.npe.2020.08.003.
[25] A. Koh *et al.*, «A soft, wearable microfluidic device for the capture, storage, and colorimetric sensing of sweat», *Sci. Transl. Med.*, vol. 8, fasc. 366, nov. 2016, doi: 10.1126/scitranslmed.aaf2593.
[26] Y. Sekine *et al.*, «A fluorometric skin-interfaced microfluidic device and smartphone imaging module for *in situ* quantitative analysis of sweat chemistry», *Lab Chip*, vol. 18, fasc. 15, pp. 2178–2186, 2018, doi: 10.1039/C8LC00530C.
[27] G. Glantzounis, E. Tsimoyiannis, A. Kappas, e D. Galaris, «Uric Acid and Oxidative Stress», *CPD*, vol. 11, fasc. 32, Art. fasc. 32, dic. 2005, doi: 10.2174/138161205774913255.
[28] B. N. Ames, R. Cathcart, E. Schwiers, e P. Hochstein, «Uric acid provides an antioxidant defense in humans against oxidant- and radical-caused aging and cancer: a hypothesis.», *Proc. Natl. Acad. Sci. U.S.A.*, vol. 78, fasc. 11, Art. fasc. 11, nov. 1981, doi: 10.1073/pnas.78.11.6858.
[29] H. Kaur e B. Halliwell, «Action of biologically-relevant oxidizing species upon uric acid. Identification of uric acid oxidation products», *Chemico-Biological Interactions*, vol. 73, fasc. 2–3, pp. 235–247, 1990, doi: 10.1016/0009-2797(90)90006-9.
[30] J. Miake *et al.*, «Impact of Hyper- and Hypo-Uricemia on Kidney Function», *Biomedicines*, vol. 11, fasc. 5, p. 1258, apr. 2023, doi: 10.3390/biomedicines11051258.
[31] Z. Xu *et al.*, «A conducting polymer PEDOT:PSS hydrogel based wearable sensor for accurate uric acid detection in human sweat», *Sensors and Actuators B: Chemical*, vol. 348, p. 130674, dic. 2021, doi: 10.1016/j.snb.2021.130674.

[32] Y. Chen *et al.*, «Nonenzymatic Sweat Wearable Uric Acid Sensor Based on N-Doped Reduced Graphene Oxide/Au Dual Aerogels», *Anal. Chem.*, vol. 95, fasc. 7, pp. 3864–3872, feb. 2023, doi: 10.1021/acs.analchem.2c05613.
[33] C. J. Harvey, R. F. LeBouf, e A. B. Stefaniak, «Formulation and stability of a novel artificial human sweat under conditions of storage and use», *Toxicology in Vitro*, vol. 24, fasc. 6, pp. 1790–1796, set. 2010, doi: 10.1016/j.tiv.2010.06.016.
[34] Y. Marunaka, «Physiological roles of chloride ions in bodily and cellular functions», *J Physiol Sci*, vol. 73, fasc. 1, p. 31, nov. 2023, doi: 10.1186/s12576-023-00889-x.
[35] Y. S. Joo *et al.*, «Urinary chloride concentration and progression of chronic kidney disease: results from the KoreaN cohort study for Outcomes in patients With Chronic Kidney Disease», *Nephrology Dialysis Transplantation*, vol. 36, fasc. 4, pp. 673–680, mar. 2021, doi: 10.1093/ndt/gfz247.
[36] A. Mishra *et al.*, «Diagnosis of Cystic Fibrosis by Sweat Testing: Age-Specific Reference Intervals», *The Journal of Pediatrics*, vol. 153, fasc. 6, pp. 758-763.e1, dic. 2008, doi: 10.1016/j.jpeds.2008.04.067.
[37] L. Possanzini *et al.*, «Textile sensors platform for the selective and simultaneous detection of chloride ion and pH in sweat», *Sci Rep*, vol. 10, fasc. 1, p. 17180, ott. 2020, doi: 10.1038/s41598-020-74337-w.
[38] P. González, P. Lozano, G. Ros, e F. Solano, «Hyperglycemia and Oxidative Stress: An Integral, Updated and Critical Overview of Their Metabolic Interconnections», *IJMS*, vol. 24, fasc. 11, Art. fasc. 11, mag. 2023, doi: 10.3390/ijms24119352.
[39] A. P. Rolo e C. M. Palmeira, «Diabetes and mitochondrial function: Role of hyperglycemia and oxidative stress», *Toxicology and Applied Pharmacology*, vol. 212, fasc. 2, pp. 167–178, apr. 2006, doi: 10.1016/j.taap.2006.01.003.
[40] H. Zafar, A. Channa, V. Jeoti, e G. M. Stojanović, «Comprehensive Review on Wearable Sweat-Glucose Sensors for Continuous Glucose Monitoring», *Sensors*, vol. 22, fasc. 2, p. 638, gen. 2022, doi: 10.3390/s22020638.
[41] S. L. Aronoff, K. Berkowitz, B. Shreiner, e L. Want, «Glucose Metabolism and Regulation: Beyond Insulin and Glucagon», *Diabetes Spectrum*, vol. 17, fasc. 3, pp. 183–190, lug. 2004, doi: 10.2337/diaspect.17.3.183.
[42] F. Mazzara *et al.*, «Electrochemical detection of uric acid and ascorbic acid using r-GO/NPs based sensors», *Electrochimica Acta*, vol. 388, p. 138652, ago. 2021, doi: 10.1016/j.electacta.2021.138652.
[43] S. Zafeiratos, F. E. Paloukis, e S. G. Neophytides, «Nickel Electrodeposition on a Gold Polycrystalline Foil: A Combined Voltammetric and Photoelectron Spectroscopy Study», *J. Phys. Chem. B*, vol. 108, fasc. 4, pp. 1371–1379, gen. 2004, doi: 10.1021/jp035804q.
[44] H. Nie, Z. Yao, X. Zhou, Z. Yang, e S. Huang, «Nonenzymatic electrochemical detection of glucose using well-distributed nickel nanoparticles on straight multi-walled carbon nanotubes», *Biosensors and Bioelectronics*, 2011.
[45] Y. Sasaki, X. Lyu, e T. Minami, «A Highly Accurate pH Detection Method for Sweat Analysis using a Printed 96-Microwell Colorimetric Sensor Array», *Analysis & Sensing*, vol. 3, fasc. 5, p. e202200097, set. 2023, doi: 10.1002/anse.202200097.
[46] K. J. Aoki, J. Chen, Y. Liu, e B. Jia, «Peak potential shift of fast cyclic voltammograms owing to capacitance of redox reactions», *Journal of Electroanalytical Chemistry*, vol. 856, p. 113609, gen. 2020, doi: 10.1016/j.jelechem.2019.113609.
[47] B. Zhao e M. M. Collinson, «Hierarchical porous gold electrodes: Preparation, characterization, and electrochemical behavior», *Journal of Electroanalytical Chemistry*, vol. 684, pp. 53–59, set. 2012, doi: 10.1016/j.jelechem.2012.08.025.
[48] M. Zhou *et al.*, «Controlled Synthesis of Large-Area and Patterned Electrochemically Reduced Graphene Oxide Films», *Chemistry A European J*, vol. 15, fasc. 25, pp. 6116–6120, giu. 2009, doi: 10.1002/chem.200900596.

[49] G. Gotti, K. Fajerwerg, D. Evrard, e P. Gros, «Electrodeposited gold nanoparticles on glassy carbon: Correlation between nanoparticles characteristics and oxygen reduction kinetics in neutral media», *Electrochimica Acta*, vol. 128, pp. 412–419, mag. 2014, doi: 10.1016/j.electacta.2013.10.172.
[50] C. Liu, K. Wang, S. Luo, Y. Tang, e L. Chen, «Direct Electrodeposition of Graphene Enabling the One-Step Synthesis of Graphene–Metal Nanocomposite Films», *Small*, vol. 7, fasc. 9, pp. 1203–1206, mag. 2011, doi: 10.1002/smll.201002340.
[51] Z. Li *et al.*, «A Dual-Function Wearable Electrochemical Sensor for Uric Acid and Glucose Sensing in Sweat», *Biosensors*, vol. 13, fasc. 1, p. 105, gen. 2023, doi: 10.3390/bios13010105.
[52] C. Wang *et al.*, «A wearable flexible electrochemical biosensor with CuNi-MOF@rGO modification for simultaneous detection of uric acid and dopamine in sweat», *Analytica Chimica Acta*, vol. 1299, p. 342441, apr. 2024, doi: 10.1016/j.aca.2024.342441.
[53] D. Jiang *et al.*, «A silver nanowires@Prussian blue composite aerogel-based wearable sensor for noninvasive and dynamic monitoring of sweat uric acid», *Chemical Engineering Journal*, vol. 486, p. 150220, apr. 2024, doi: 10.1016/j.cej.2024.150220.
[54] Y. L. Ni'mah, A. Baktir, D. Santosaningsih, e S. Suprapto, «The Influence of Tartaric Acid in the Silver Nanoparticle Synthesis Using Response Surface Methodology», *JRM*, vol. 0, fasc. 0, pp. 1–10, 2023, doi: 10.32604/jrm.2023.045514.
[55] A. Arvinte, I.-A. Crudu, F. Doroftei, D. Timpu, e M. Pinteala, «Electrochemical codeposition of silver-gold nanoparticles on CNT-based electrode and their performance in electrocatalysis of dopamine», *Journal of Electroanalytical Chemistry*, vol. 829, pp. 184–193, nov. 2018, doi: 10.1016/j.jelechem.2018.10.017.
[56] R. Hamdi *et al.*, «Electrodeposition Study of Silver: Nucleation Process and Theoretical Analysis», *J. Electron. Mater.*, vol. 50, fasc. 10, pp. 5507–5513, ott. 2021, doi: 10.1007/s11664-021-09055-8.
[57] B. Patella *et al.*, «Electrochemical detection of chloride ions using Ag-based electrodes obtained from compact disc», *Analytica Chimica Acta*, vol. 1190, p. 339215, gen. 2022, doi: 10.1016/j.aca.2021.339215.
[58] W. Duan, C. Fernández-Sánchez, e M. Gich, «Upcycling Bread Waste into a Ag-Doped Carbon Material Applied to the Detection of Halogenated Compounds in Waters», *ACS Appl. Mater. Interfaces*, vol. 14, fasc. 35, pp. 40182–40190, set. 2022, doi: 10.1021/acsami.2c08332.
[59] S. Cinti *et al.*, «Low-cost and reagent-free paper-based device to detect chloride ions in serum and sweat», *Talanta*, vol. 179, pp. 186–192, mar. 2018, doi: 10.1016/j.talanta.2017.10.030.
[60] H. S. Toh, C. Batchelor-McAuley, K. Tschulik, e R. G. Compton, «Electrochemical detection of chloride levels in sweat using silver nanoparticles: a basis for the preliminary screening for cystic fibrosis», *Analyst*, vol. 138, fasc. 15, p. 4292, 2013, doi: 10.1039/c3an00843f.
[61] M.-H. Chiu, W.-L. Cheng, G. Muthuraman, C.-T. Hsu, H.-H. Chung, e J.-M. Zen, «A disposable screen-printed silver strip sensor for single drop analysis of halide in biological samples», *Biosensors and Bioelectronics*, vol. 24, fasc. 10, pp. 3008–3013, giu. 2009, doi: 10.1016/j.bios.2009.03.004.
[62] J. Bujes-Garrido, D. Izquierdo-Bote, A. Heras, A. Colina, e M. J. Arcos-Martínez, «Determination of halides using Ag nanoparticles-modified disposable electrodes. A first approach to a wearable sensor for quantification of chloride ions», *Analytica Chimica Acta*, vol. 1012, pp. 42–48, lug. 2018, doi: 10.1016/j.aca.2018.01.063.
[63] J. Chen *et al.*, «Glucose Biosensors Based on Pinecone-Shaped Au and Ni Nanoparticle Composite Microelectrodes», *ACS Appl. Nano Mater.*, vol. 5, fasc. 9, pp. 13319–13331, set. 2022, doi: 10.1021/acsanm.2c03001.

[64] N. F. Heinig, N. Kharbanda, M. R. Pynenburg, X. J. Zhou, G. A. Schultz, e K. T. Leung, «The growth of nickel nanoparticles on conductive polymer composite electrodes», *Materials Letters*, vol. 62, fasc. 15, pp. 2285–2288, mag. 2008, doi: 10.1016/j.matlet.2007.11.094.
[65] S. Yu *et al.*, «Ni nanoparticles decorated titania nanotube arrays as efficient nonenzymatic glucose sensor», *Electrochimica Acta*, vol. 76, pp. 512–517, ago. 2012, doi: 10.1016/j.electacta.2012.05.079.
[66] F. Franceschini e I. Taurino, «Nickel-based catalysts for non-enzymatic electrochemical sensing of glucose: A review», *Physics in Medicine*, vol. 14, p. 100054, dic. 2022, doi: 10.1016/j.phmed.2022.100054.
[67] X. Niu, M. Lan, H. Zhao, e C. Chen, «Highly Sensitive and Selective Nonenzymatic Detection of Glucose Using Three-Dimensional Porous Nickel Nanostructures», *Anal. Chem.*, vol. 85, fasc. 7, pp. 3561–3569, apr. 2013, doi: 10.1021/ac3030976.
[68] Y. Du, H. Chen, R. Chen, e N. Xu, «Poisoning effect of some nitrogen compounds on nano-sized nickel catalysts in p-nitrophenol hydrogenation», *Chemical Engineering Journal*, vol. 125, fasc. 1, pp. 9–14, dic. 2006, doi: 10.1016/j.cej.2006.05.019.
[69] X. Dou *et al.*, «Poisoning effects of H2S and HCl on the naphthalene steam reforming and water-gas shift activities of Ni and Fe catalysts», *Fuel*, vol. 241, pp. 1008–1018, apr. 2019, doi: 10.1016/j.fuel.2018.12.119.
[70] B. K. Urhan e Ü. Demir, «Electrochemical fabrication of Ni or Ni(OH)2@Ni nanoparticle-decorated reduced graphene oxide for supercapacitor applications», *Electrochimica Acta*, vol. 302, pp. 109–118, apr. 2019, doi: 10.1016/j.electacta.2019.02.020.
[71] J. Yang, J.-H. Yu, J. Rudi Strickler, W.-J. Chang, e S. Gunasekaran, «Nickel nanoparticle–chitosan-reduced graphene oxide-modified screen-printed electrodes for enzyme-free glucose sensing in portable microfluidic devices», *Biosensors and Bioelectronics*, vol. 47, pp. 530–538, set. 2013, doi: 10.1016/j.bios.2013.03.051.
[72] H. Cao *et al.*, «A non-enzymatic glucose sensing based on hollow cuprous oxide nanospheres in a Nafion matrix», *Sensors and Actuators B: Chemical*, vol. 214, pp. 169–173, lug. 2015, doi: 10.1016/j.snb.2015.03.026.
[73] D.-W. Hwang, S. Lee, M. Seo, e T. D. Chung, «Recent advances in electrochemical non-enzymatic glucose sensors – A review», *Analytica Chimica Acta*, vol. 1033, pp. 1–34, nov. 2018, doi: 10.1016/j.aca.2018.05.051.
[74] A. Olejnik, J. Karczewski, A. Dołęga, K. Siuzdak, e K. Grochowska, «Novel approach to interference analysis of glucose sensing materials coated with Nafion», *Bioelectrochemistry*, vol. 135, p. 107575, ott. 2020, doi: 10.1016/j.bioelechem.2020.107575.

5. A Personalized Medicine Supply Chain Model for Respiratory Diseases in the context of Healthcare 4.0

This chapter will assess how electrochemical sensors can be integrated into the healthcare system, focusing on their capabilities to increase the efficiency of disease prevention and diagnosis. Designed to enable early detection, these sensors should help cut down time spent trying to diagnose a patient's illness, thereby improving treatment and general care. Part of this chapter will assess the economic viability of a novel, personalized self-testing system for patients suffering from respiratory diseases. This innovative method, based on the electrochemical sensor described in Chapter 3, aims to enable individuals to monitor their health, potentially minimizing the need for frequent hospital visits and reducing healthcare costs. This could help address challenges in effective screening and monitoring, reducing the number of undiagnosed or late-diagnosed cases. Despite the surge of research on biosensors for diagnostics, their use in clinical practice is still limited, probably due to the lack of proper patient care models. Drawing on existing literature, this chapter aims to propose a new personalized care model and evaluate its cost-effectiveness compared to traditional methods.

5.1 Introduction

5.1.1 The Evolution of Healthcare Supply Chains

Both the changing demographics of populations in industrialized countries and the consequent increase in healthcare demand are nowadays widely regarded as critical challenges testing the ability of healthcare systems to provide effective patient care in the next future. The COVID-19 pandemic has played the role of a very recent stress test for the supply chains of healthcare, underlining several serious gaps in their resilience against rapid increases in demand [1]. Since SARS-CoV-2 is highly contagious, there was an urgent need for tests capable of

providing rapid turnaround to institute preventive measures such as the isolation of confirmed cases and contact tracing [2]. This situation has heightened the vulnerability of these systems to disruption events, exposing their fragility under pressure. The increasing strain on our current healthcare systems underscores an urgent need for a redesign of the entire Supply Chain (SC). This would mean the approach would focus on enhancing responsiveness, resilience and efficiency in health care delivery [1], hence acting as a means to develop inclusiveness and economic viability for future health care. Fig. 5.1 shows how the pandemic affected different areas in healthcare services and different specialties as a result of the increased risks of transmission with COVID-19.

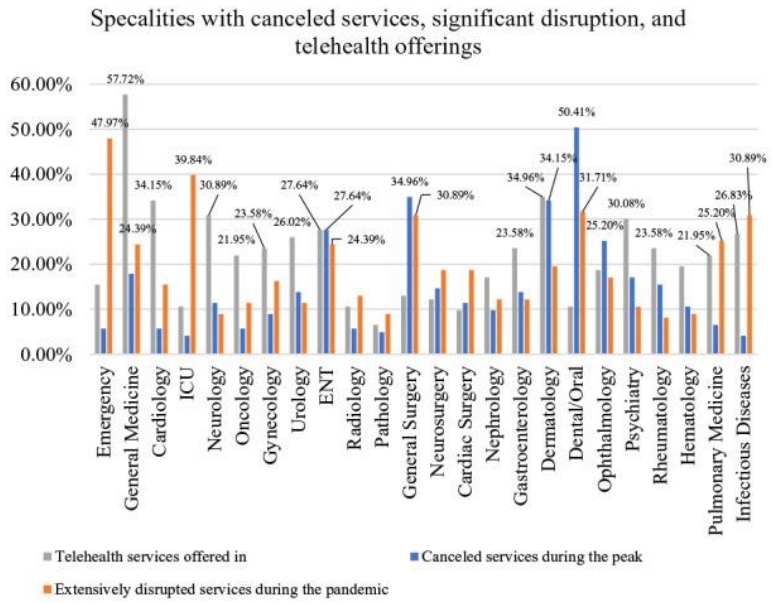

Figure 5.1*: COVID-19 impact on different specialties [1].*

Considering that the aging population trend in most industrialized nations is likely to significantly increase, demand for healthcare, efficiency, and effectiveness of the systems in meeting population needs become a highly debated issue. In this context, decentralized healthcare organizations have the potential to be more responsive and inclusive compared to traditional hospital-centric SC models. This

point of view also reflects a long-standing debate on the decentralization of supply chains in healthcare, a concept born in the second half of the 20th century. During this period, decentralization became a key element, particularly through the evolution of point-of-care (POC) supply chain models. These models prioritize delivering healthcare services closer to or directly at the patient's location rather than relying on centralized structures [3], [4]. POC tests offer numerous advantages, including affordability, ease of use, and the flexibility to be employed both at triage locations and outside traditional healthcare settings, making them essential tools for managing infectious diseases [5], [6]. However, the POC models that developed in different regions were not uniform; they varied significantly in their organizational structures, economic frameworks and regulatory mechanisms [7]. This lack of standardization led to questions regarding the economic efficiency of these models, with several studies highlighting cost-related concerns [8], [9]. Pai et al. [10] have recently offered a comprehensive overview of modern decentralized healthcare supply chain models, outlining the range of remote service provision across five key settings: homes, communities, clinics, peripheral laboratories and hospitals. The growing emphasis on proximity healthcare structures in delivering primary care services has also been underscored by other authors [11], who propose a new, holistic approach to healthcare systems. This approach focuses on territorial medicine, anchored in community homes and community hospitals, representing a shift towards a decentralized healthcare model. Community medicine emerges as a pivotal element of this model, where healthcare professionals engage directly with local populations to address medical needs promptly, emphasizing prevention and early diagnosis. The objective is to harness the potential benefits of decentralization (improved efficiency, greater inclusiveness, reduction of territorial disparities) by establishing proximity healthcare structures that are interconnected through telemedicine technologies. This synergy between decentralization and digital connectivity enhances several healthcare processes, including the collection and

processing of patient data, the generation of electronic medical records and the provision of decision-support tools. These features are now the basis for the recent development of Personalized Medicine (PM), which aims at the improvement of prevention, diagnosis, and treatment, considering the differential needs of individual patients. PM can now be defined as a medical approach concerning the specific characteristics and needs of individual patients or clearly defined groups of patients by which the correct treatment is delivered using new diagnostic and therapeutic techniques. However, the introduction of new approaches and technologies into current health systems presents a range of technical and logistical challenges. It requires a significant redesign of healthcare supply chains, demanding new organizational and operational frameworks to accommodate the complexities of these healthcare models [12].

The shift towards next-generation digitalized SC models in the healthcare sector is fundamentally anchored in modern data management and communication technologies, including the Internet of Things (IoT), big data, augmented reality, and blockchain. This digital transformation is emerging as a crucial driver in the evolution of healthcare organizations [13], [14], steering them towards more efficient, inclusive and adaptable models. Within this framework, digital solutions that enable multidisciplinary and multi-professional diagnosis and treatment are essential for strengthening and standardizing territorial healthcare services. Beyond interconnection technologies, another important technological pillar of PM is the modern bio-sensing system that enables the detection of the concentration of electro-active chemical compounds [15]. Typically, these measurement systems are integrated into miniaturized devices designed as either lab-on-PCB (Printed Circuit Board) (Fig. 5.2) or lab-on-chip platforms. Lab-on-PCB systems are compact, embedded devices that integrate a sensing subsystem, communication module, power supply and human-machine interface into a single PCB enclosed within a small handheld case [16].

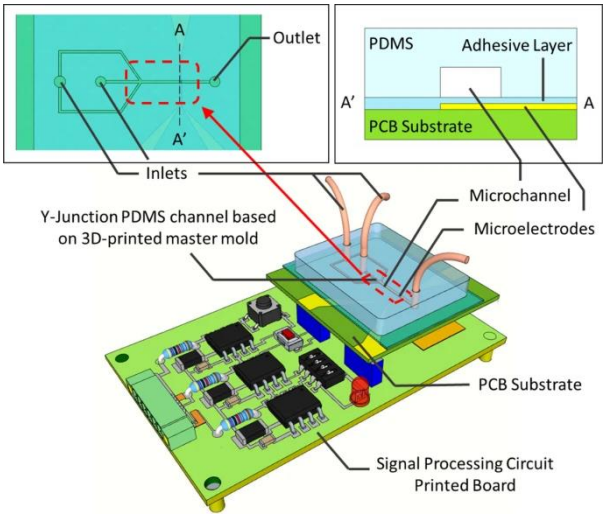

***Figure 5.2**: An example of a lab-on-PCB microfluidic device [17].*

In contrast, lab-on-chip devices elevate this design to a higher level of miniaturization, consolidating these functions onto a single microchip. On top of lowering production costs, several diagnostic or analytic applications transmit data in real time. New techniques, such as deep learning-based Artificial Intelligence (AI), have shown significant contributions in helping medical experts in the development of prevention and treatment strategies. Big data processing technologies can manage huge, multi-dimensional biomedical datasets [18], produced in personalized healthcare applications and constitute the remaining important technological infrastructure necessary for sophisticated PM services.

5.1.2 Global Impact of Chronic Respiratory Diseases

Respiratory diseases affect numerous individuals all over the world, and their numbers are expected to rise in the next few decades [19]. In addition, Chronic Respiratory Diseases (CRDs) include recently focused on airway and lung-related disorders like Chronic Obstructive Pulmonary Disease (COPD), asthma, pneumoconiosis, interstitial lung disease, or pulmonary sarcoidosis. All these diseases, according to the World Health Organization (WHO) data, are encountered by 500 million people taking globally [20]. This is even higher

because there is a great deal of COPD, 45–65% of the cases are not detected due to the lack of systematic screening programs [21]. CRD was ranked the leading cause of death worldwide in 2019, claiming about 4 million lives, thus placing a colossal burden and expense on healthcare systems [22], [23]. These conditions feature in the top ten leading causes of global deaths, accounting for 8% of all deaths in the European Union in 2015. They also impose considerable financial costs, costing about 6% of the EU's annual healthcare budget [24]. Respiratory diseases are among the highest burdens in health expenditure: in the US alone, expenditure due to respiratory diseases accounted for $170.8 billion in 2016 alone, way above that seen in the last decade [25]. Recent global estimates of the burden and health effects of CRDs were based on the Global Burden of Diseases (GBD), Injuries and Risk Factors Study 2017 [26], but updated and more accurate estimates are available from GBD 2019. Major risk factors for CRDs include environmental exposures, as well as smoking, which vary sharply by region, culture, age, and gender. Knowledge of such trends and the identification of high-risk populations can facilitate efforts on the part of policymakers in the development of more effective interventions to minimize disability and premature death [27]. The incidence and prevalence of CRDs in absolute numbers have been increasing over the last three decades worldwide. Fig. 5.3 expresses the Age-Standardized Rate (ASR) of prevalence and incidence of chronic respiratory diseases in 2019 in the world.

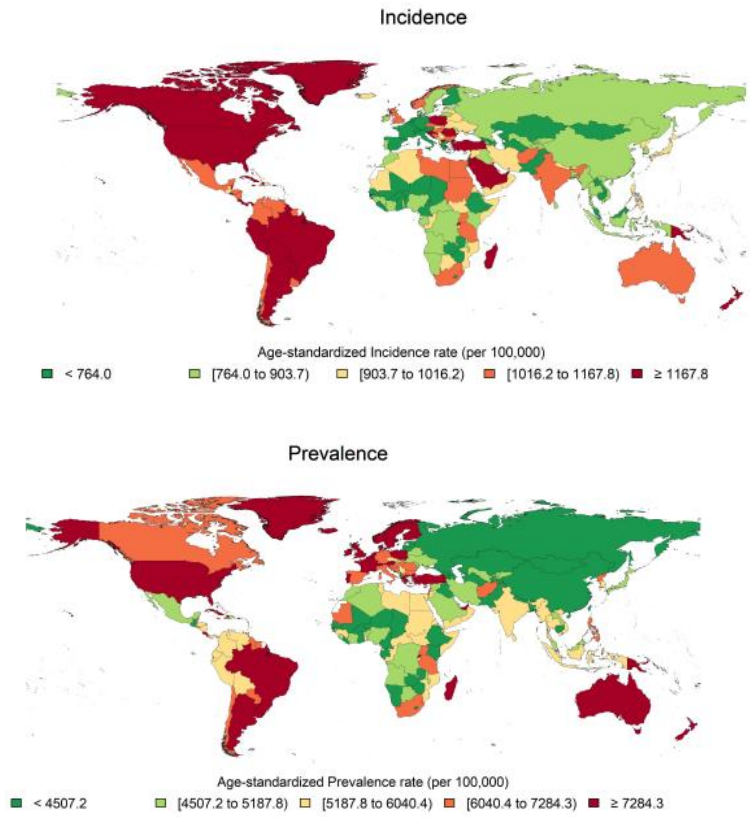

***Figure 5.3**: Age-standardised rate of prevalence and incidence of CRDs in 2019 [28].*

Significant progress has been made globally in reducing the ASRs of deaths, prevalence, and incidence of conditions like COPD, asthma, and pneumoconiosis. However, this progress varies across different regions and demographics [28]. Smoking remains the leading global risk factor for CRDs, followed by ambient PM pollution. New risk factors, like non-optimal temperatures, have highlighted the impact of climate change on CRDs, particularly COPD. Climate change can lead to greater temperature variability, which may exacerbate COPD and extend pollen seasons, increasing asthma cases [29], [30]. Globally, ambient PM pollution is the second-largest risk factor for CRDs, with no major change over the past three decades. While Europe has seen a decline in pollution-related

CRDs, other regions, especially Sub-Saharan Africa, have experienced an increase due to climate change and urbanization [31].

COPD still ranks as one of the main causes of the world's burden of CRDs. In 2019, it contributed to 3.3 million deaths. It has a prevalence of 212.3 million and a new case estimate of 16.2 million reported globally. Geographically, high-income North America has the highest prevalent cases. On the other hand, Oceania reports the highest incidence. COPD is the primary condition associated with occupational risks. The highest rates of occupational risk-related CRDs are seen in South Asia, Oceania, and East Asia, where resource allocation and occupational safety measures are essential to reducing toxic exposures. These findings highlight the critical need for tailored interventions to address COPD and its risk factors, particularly in regions where household air pollution and environmental conditions significantly impact the disease burden [28].

Workplace health is very much affected by respiratory diseases. The situation that has been reached by the increasing of occupational diseases among workers in industry is both dangerous and expensive. There has been a significant change in Europe, particularly in the major sources of occupational exposure to respiratory hazards. In the early 20th century, workers in big industries were generally exposed to mineral dust at higher levels [32]. After World War II, pneumoconiosis, strongly linked to coal mine dust exposure, was the most common occupational lung disease. Minimization of dust levels is one of the incredible progress that has been achieved, along with effective preventive measures through the development of mechanization and automation in mining and foundries [33].

Estimating the share of occupational exposures in the incidence of some respiratory diseases, like COPD, is hard since the affection of smoking is very strong and it often begins late, often after retirement. However, only about 15% of cases of COPD in Western countries can be traced back to exposure to vapors, gases, dust, and chemicals [34]. One sector with a high prevalence of occupational

respiratory diseases is the manufacturing industry. Research has shown that workers in this sector face double the risk of dying from respiratory diseases compared to non-manual workers [35]. While using masks and having regular health checks can help reduce these risks, they don't provide real-time monitoring of workers' health. As industrial processes and materials evolve, new risks emerge for workers in the workplace. This underscores the need for ongoing monitoring of the workers' condition to ensure their well-being [36]. In this context, integrating wearable devices into PPE (Fig. 5.4) that workers already use could allow for real-time monitoring of their physiological conditions, enhancing safety and health management [37].

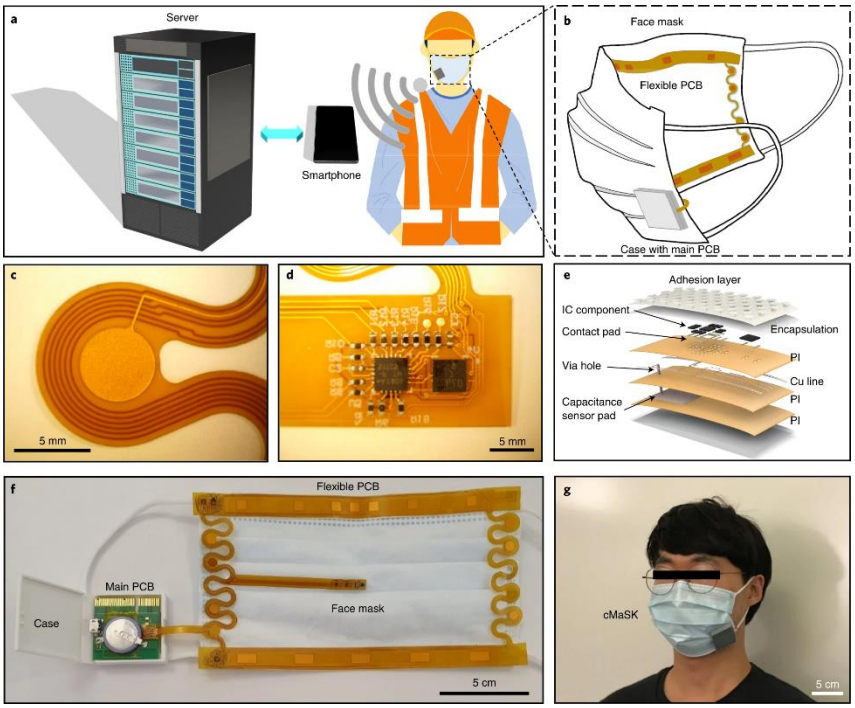

***Figure 5.4**: a) Electronic device integrated into face mask to collect data that are transmitted to smartphone and then to server for data storage, b) scheme of the device attached to face mask attachment of the devices, (c-d) optical microscopy images of c) capacitance sensor pad and d) microprocessor, resistors and accelerometer assembled on the flexible printed circuit board (fPCB), e) scheme of fPCB, f) photo of the face mask integrated with the sensor and g) photo of a person wearing the face mask [38].*

However, a major challenge is the economic and social burden caused by misdiagnoses and delayed diagnoses [39]. The economic impact associated with respiratory diseases is significant with direct healthcare costs amounting to approximately 6% of the EU's total annual healthcare budget [24]. In the United States, spending on respiratory diseases reached $170.8 billion in 2016, reflecting a sharp rise over the preceding decade [25]. These diseases also have a substantial impact on occupational health, with regular medical surveillance tests required in workplaces where exposure to hazardous substances is common. Also, indirect costs associated with respiratory diseases place a significant burden on employers. These costs manifest as productivity losses, absenteeism, reduced work performance, and increased disability claims [40]. Research indicates that indirect costs often surpass direct costs. For instance, in Europe, indirect costs make up 61%, 82%, and 83% of the overall per-patient costs in Italy, the Netherlands, and the UK, respectively. Germany records the highest costs due to work productivity loss, while Greece has the lowest. Similarly, Germany sees the highest costs related to early retirement, while Sweden has the lowest [41], [42], [43]. Additional studies highlight that patients with respiratory diseases are less likely to be employed compared to healthy individuals, with early retirement costs contributing 40–82% of the total economic burden [44], [45]. A specific study on the economic burden of COPD demonstrated that this burden, especially for moderate to severe cases, is expected to rise. The average annual cost per COPD patient was found to be $4,147, with acute exacerbations costing $1,673 per patient, 82% of which was due to hospitalizations. Historical surveys from 2000/2001 and 2001/2002 revealed COPD-related healthcare costs of $3,195 per patient, with costs of $641 for moderate cases and $9,557 for severe cases [46], [47]. This highlights a critical issue with the current diagnostic approaches that have proven inadequate in effectively addressing the needs of the population, indicating a need for more accurate and timely diagnostic tools.

As discussed before, there is an increased concern in identifying new approaches to treat respiratory diseases, particularly over the past three years due to the COVID-19 pandemic. At present, respiratory screening and monitoring are primarily based on analyses of Exhaled Breath Condensate (EBC). Traditional EBC analysis involves collecting and condensing breath samples for lab analysis. However, since this process requires specialized labs, it's not practical for real-time diagnostics [48]. Recently, researchers have been developing systems that skip the condensation step, enabling real-time, on-the-spot monitoring of physiological markers in breath [49], [50]. Advances in nanotechnology have led to a new class of high-performance biosensors [51], [52], [53], [54]. These sensors can be built into respiratory masks, allowing patients to test themselves and representing a reliable alternative to traditional testing.

A key example of this coming revolution is the shift from traditional lab-based EBC analysis to wearable biosensors, like the Lab-on-Mask concept [55], [56], [57], [58], [59]. Recent reviews, such as one by Hussain et al. [60], have explored these cutting-edge approaches. These developments highlight a major challenge in modern PM: integrating decentralized healthcare services into effective patient care models. The goal is to find scenarios where these new methods can outperform current clinical practices.

5.2 Methodology

5.2.1 Respiratory Health Monitoring: from traditional to innovative approaches

The traditional management process of diseases of the respiratory system involves three decisive stages: [61] (Fig.5.5):

- Diagnostics: is concerned with the identification of the pathology affecting the patient, such as Chronic Obstructive Pulmonary Disease (COPD), asthma,

or lung cancer. Proper diagnosis is essential in choosing the right therapy and strength of treatment that needs to be initiated.

- Therapy: once a diagnosis is made, the focus shifts to a specific treatment of the condition that has been diagnosed.
- Follow-Up: when the treatment phase is completed, the next step is to establish an assessment program with the aim of measuring how successful the treatment was and also assessing the patient's condition during the course of time.

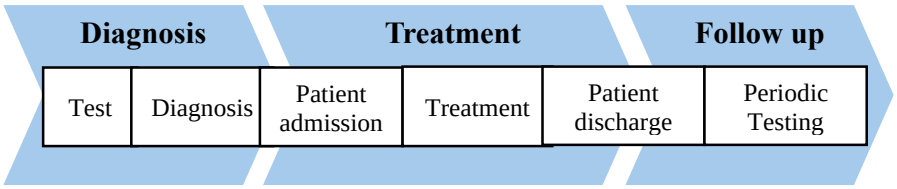

***Figure 5.5**: Workflow of operations for managing respiratory diseases.*

The diagnostic phase focuses on measuring the concentrations of specific biomarkers in EB. Key biomarkers include hydrogen peroxide, lipid mediators, purines, and cytokines [62], [63]. To obtain these samples, a non-invasive collection method is employed, where the patient breathes into a mask connected to the expiratory circuit of a mechanical ventilator [64] (Fig. 5.6).

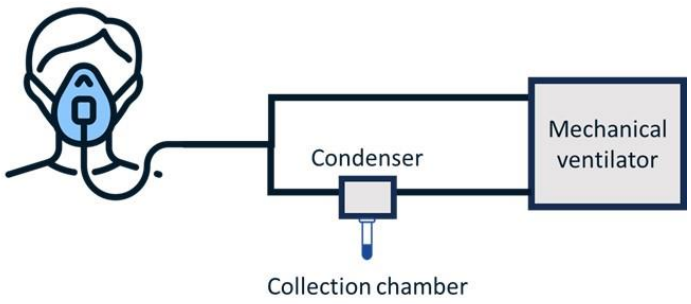

***Figure 5.6**: Representative scheme of the clinical practice for the collection of EBC.*

The process of sample collection involves cooling them within a specialized unit to approximately 4°C, maintaining this temperature until the dew point is achieved. Once condensed, the Exhaled Breath Condensate (EBC) can either be analyzed immediately or preserved for later analysis. To prevent the degradation of key biomarkers during storage, the samples need to be securely sealed and frozen at around −80°C [65]. Various commercial devices are used for this refrigeration process, including the EcoScreen (FILT Lung and Chest Diagnostics Ltd, Germany), TURBO-DECCS (Medivac, Italy), and ANACON (Biostec, Valencia, Spain). These systems use diverse cooling techniques, such as ice, liquid nitrogen, cooling sleeves, and electric refrigeration units. Following the collection and storage of EBC samples, the concentration of essential biomarkers can be determined through a range of analytical techniques, including spectrophotometry, fluorimetric assays, and chemiluminescence. Among these, the gold standard for breath analysis is Gas Chromatography coupled with Mass Spectrometry (GC-MS). This sophisticated technique requires complex laboratory equipment and the expertise of trained personnel, making it suitable only for centralized laboratory settings [66]. GC-MS is hence, unsuitable for POC or homecare applications that demand instrument portability and ease of use. In summary, while the non-invasiveness of EBC analytics represented an important advantage, several other issues significantly limit the practical feasibility and reliability of this diagnostic tool:

- *extended sample collection Time*: collecting a sufficient volume of EBC can be a time-intensive process. For instance, obtaining just a 1-mL sample generally requires the patient to breathe continuously for a minimum of 10 minutes. This extended collection period can be inconvenient for patients and may limit the feasibility of this method for routine or large-scale applications [66].
- *potential alteration of volatile compounds*: one of the critical drawbacks of EBC analysis is the risk of altering the composition of volatile substances

during various stages, such as condensation, freezing, and storage. However, volatile compounds can sublimate into the airspace above the frozen EBC on reopening of the container, such substances may disperse with a potential loss or degradation of key biomarkers. This aspect will compromise the accuracy and reproducibility of the analysis and, thus, the reliability of the results [67].

The most significant issue with EBC sampling lies in the absence of a standardized collection protocol. This lack of uniformity leads to variations in sample quality, as different collection methods can yield inconsistent results. In the context of home care settings, although portable EBC sampling devices exist, such as the R-Tube (Respiratory Research, USA), they are not designed for patient self-operation. Therefore, specialized technicians must visit the patient's location for the collection of the sample and its transportation to a lab for analysis. This process, while being very time-consuming and expensive, is also questionable in terms of its reliability-as pointed out by various studies [68].

The proposed PM approach aims to address these challenges through a self-testing procedure using a smart device designed to measure hydrogen peroxide concentration in exhaled breath. This innovative method eliminates the need for sample condensation, thereby simplifying the testing process and minimizing the risk of sample alteration. This device features a carbon nanocluster mask that complies with the 93/42 EEC bacteriostatic directive and is equipped with the electrochemical sensor widely described in Chapter 3. Fig. 5.7 shows a schematic representation of this proposed smart self-testing device.

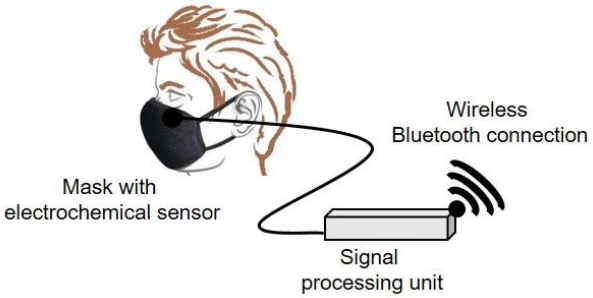

***Figure 5.7**: Representative scheme of smart self-testing device.*

Overall, the smart device's design and functionality offer a promising solution for at-home EBC analysis, streamlining the testing process and ensuring more consistent, reliable results without the need for specialized technicians.

The proposed device is also equipped with a communication system based on fog computing architecture, enabling patients to conduct personalized self-testing at home or in decentralized community healthcare facilities, such as "community hospitals," without needing to visit a traditional hospital setting. The key distinction between conventional methods and the system presented here lies in the testing phase, which is pivotal for the early detection and diagnosis of respiratory diseases. Fig. 5.8 highlights the differences in the workflow of the testing process between the innovative personalized testing method proposed and conventional laboratory-based testing practices.

As previously mentioned, a significant limitation of traditional EBC testing is that it necessitates sample condensation, freezing, and subsequent analysis, procedures that can only be conducted in specialized laboratories equipped with appropriate instruments and skilled personnel. In contrast, the personalized testing method introduced here utilizes a novel sensing device, allowing patients to measure hydrogen peroxide concentrations independently at home, without requiring extensive equipment or expert operators.

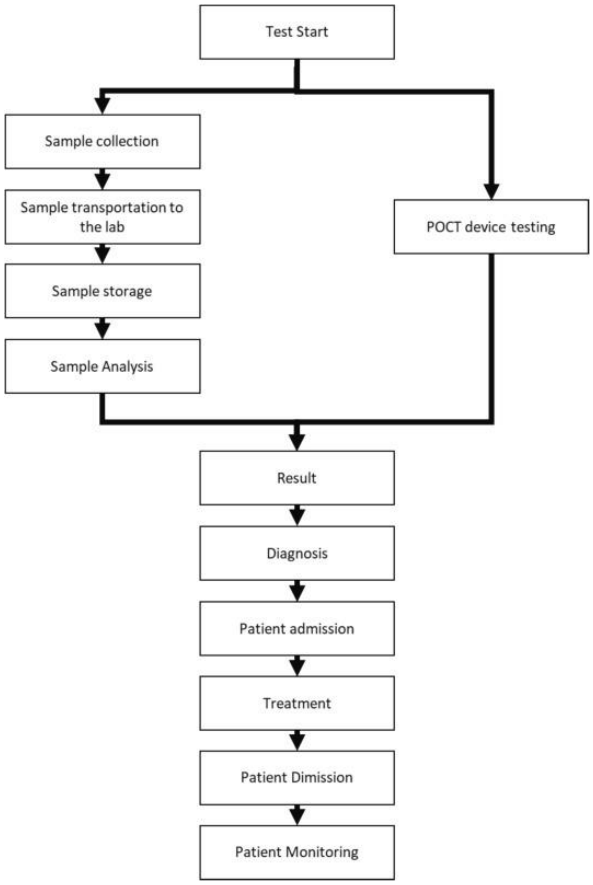

***Figure 5.8**: Traditional testing methods vs. Self-testing methods.*

5.2.2 System architecture of the proposed device

In modern personalized healthcare system, the use of smart sensing devices for the continuous collection of patient clinical data in remote settings is increasingly recognized as a valuable approach for delivering decentralized screening services that enhance prevention while preserving cost efficiency. The real-time sharing of clinical information allows medical staff to engage in a timely, collaborative diagnostic process, which is crucial for reducing treatment costs. This collaborative diagnostic approach involves effective exchange of information and requires a robust and interconnected digital architecture.

The development of a suitable data-sharing infrastructure is therefore essential to modern healthcare systems and serves as a main pillar of the Industry 4.0, which

emphasizes the digitalization and interconnection of supply chains and the creation of intelligent, collaborative networks using cloud, edge, and fog computing architectures. To achieve a scalable, patient-focused infrastructure that enables widespread screening programs for respiratory disease management, this research work proposed a fog-based architectural networking scheme that consists of an edge devices layer, a fog computing layer, and a cloud layer, as illustrated in Fig. 5.9.

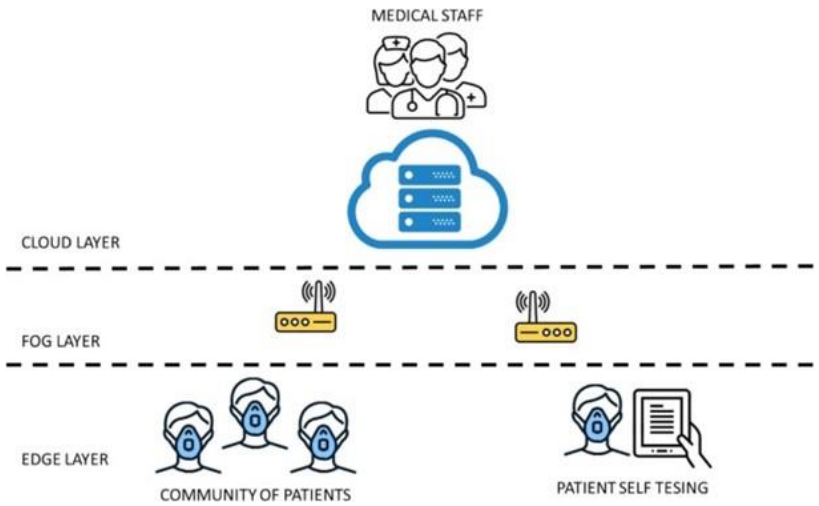

***Figure 5.9**: Fog-based architectural networking scheme for the treatment of respiratory diseases.*

The proposed architecture includes an Edge Computing Layer equipped with smart medical devices designed to measure key clinical parameters and generate anonymized, self-signed timestamped data records. These records are then transmitted to the cloud via edge gateways. Relevant patient data is forwarded to the top layer, where cloud servers facilitate data sharing with medical professionals, thereby aiding the diagnostic decision-making process. A crucial requirement for the effectiveness of fog architecture lies in its ability to allocate services efficiently across fog devices with constrained resources, particularly in real-world scenarios involving hundreds of concurrently connected devices. To ensure efficient processing, scaling the fog infrastructure with optimized service

allocation rules that consider device capabilities and service demands is essential. This necessitates the development and implementation of specialized algorithms that prioritize service allocation based on the severity and urgency of patients' health conditions. Current research is focused on estimating the average computational load and memory usage for standard services, with the goal of assessing how different allocation strategies impact system performance and resource utilization.

Data security is another critical consideration in the design of a data-sharing architecture, especially when handling clinical data within networked healthcare systems. Ensuring patient privacy is paramount; therefore, data cannot be directly transmitted from personalized testing devices to fog nodes and cloud servers without increasing the risk of potential data breaches or security vulnerabilities. Effective management policies are needed to distribute data among fog nodes securely and to support heterogeneous IoT devices, employing encryption and secure transmission protocols to safeguard user privacy. Sensor networks are often seen as the most vulnerable points in data-sharing infrastructures, presenting potential entryways for malicious attacks. The literature on privacy-preserving communication and data security in fog architectures highlights various security solutions, such as access control, cryptography, anonymization, and the use of blockchain technology. Implementing access controls ensures that data requests are made by authorized users, while cryptography maintains data confidentiality. In medical devices, it is equally important to protect both data integrity and firmware, as compromised devices could be exploited for attacks like Denial of Service (DoS) or packet flooding.

The majority of privacy-preserving communication strategies for fog infrastructure incorporate homomorphic encryption from IoT devices or attribute-based encryption between IoT and fog layers. The fog computing model proposed here employs a lightweight attribute-based signcryption scheme, illustrated in Fig. 5.10. This method, an extension of Attribute-Based Encryption and Attribute-

Based Signature, ensures both data confidentiality and authenticity. In this scheme, a private key generator initializes the system and provides private keys to data owners (patients) and data users (medical staff). Patient health data collected by smart biosensing devices is signcrypted by the fog node, forming part of the ciphertext. Patients then complete the final signcryption and upload the ciphertext to the medical cloud. When medical staff request access, the cloud retrieves the ciphertext for preliminary un-signcryption.

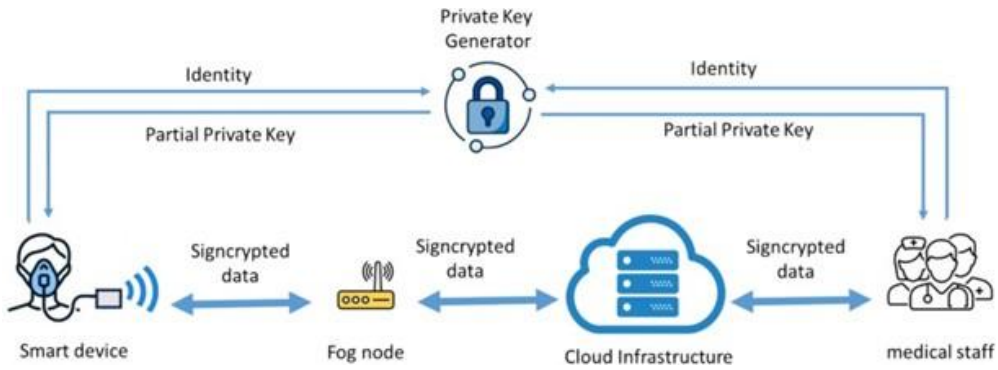

***Figure 5.10**: Fog infrastructure dataflow.*

In conclusion, although the technologies discussed are sufficiently developed for practical application, the security of fog architectures remains a significant concern. Ensuring a high level of reliability and security requires lightweight, efficient, and low-power security functions that can be deployed on resource-constrained devices with limited power, memory, and battery capacity.

The goal of this research work is to create an embedded device that is both cost-effective and user-friendly, enabling homecare and patient self-testing with minimal technical expertise. The device is intended for patients with respiratory diseases to measure the concentration of hydrogen peroxide in their exhaled breath by simply wearing a mask for a brief period. It integrates a sensor, a potentiostat, a data processing microcontroller unit (MCU), a 2.4 GHz transceiver, and a Bluetooth Low Energy (BLE) module, all consolidated on a

single customized Printed Circuit Board (PCB). The modular design of the smart testing device is illustrated in Fig. 5.11.

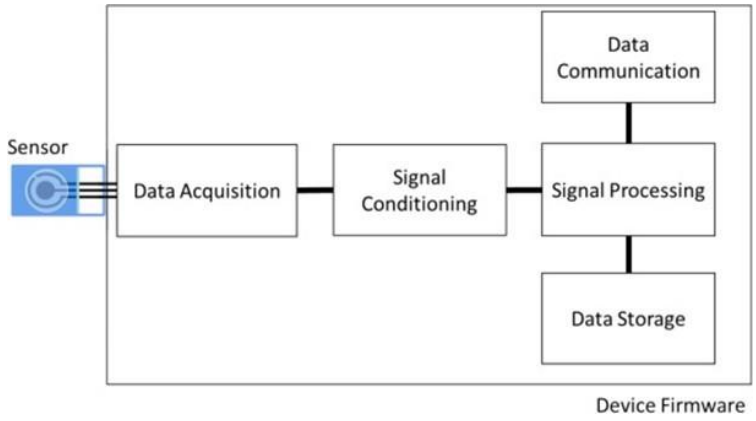

Figure 5.11*: The modular architecture of the proposed device.*

The device operates through an advanced electrochemical sensor designed to detect hydrogen peroxide concentration. The sensor generates a raw electrical signal, which is processed by a microcontroller. This signal is then converted from analog to digital, filtered, and translated into a physical measurement. After processing by the microcontroller, the data is transmitted to the cloud via a fog layer for further analysis and centralized storage. A communication module within the system facilitates TCP/IP communication using the MQTT protocol, which is optimized for edge and fog computing [69]. In addition to employing secure standards like X.509 certificates for TLS/SSL protocols, patient data is pseudonymized to ensure privacy. Consequently, the transmitted MQTT messages contain only numerical data, devoid of any patient identifiers.

The cloud layer processes both real-time and historical data, utilizing advanced computational techniques and machine learning algorithms to assist medical professionals in diagnosis and treatment. This approach supports personalized healthcare services. Additionally, feedback is provided to the user, and emergency alerts can be triggered when necessary. To accommodate elderly or less technically skilled patients, the device features a simplified human-machine

interface with tangible components and clear visual signals. The interface minimizes user interaction to a single button and a multicolor LED (green, yellow, red) to reduce cognitive load. Green indicates normal operation and readiness for use, while yellow signals the test in progress. This minimalistic interface enhances ease of learning, efficiency, and error reduction. The system connects automatically to available networks via Wi-Fi or cellular networks (5G/4G/6G). Maintenance and configuration are managed by technical staff, with the device being remotely monitored for malfunctions. If issues arise, a red light alerts the user, and a message is sent to technical personnel for intervention. Preventive maintenance is scheduled annually, ensuring optimal device performance and calibration. Remote alerting, combined with real-time parameter monitoring, provides a cost-effective solution for healthcare providers.

5.2.3 A systematic methodology for evaluating Healthcare Supply Chains

The approach that was adopted in this research work for evaluating the different SC models is the Cost of Illness (COI) method, which is considered as a useful approach in assessing supply chain management in the healthcare sector. The COI method [70] classifies healthcare expenses into two categories: direct costs and indirect costs. Direct costs are expenses that can be directly attributed to patient care and are essential for delivering healthcare services. These costs include:

- **Labor costs**: cover the salaries of medical and paramedical, calculated based on the median salaries of professionals involved in each cost center. They constitute a significant component of the costs because they include the time healthcare providers spend on patient care ranging from consultations to various diagnostic and treatment procedures.
- **Equipment costs**: account for the selling price of the equipment and devices used in the medical procedures. These consist not only of purchasing costs but also of certain estimated salvage value and costs of periodic calibration, maintenance, and repairs. Proper management of such equipment enhances

the precision and dependability of the diagnostic and therapeutic processes, which are very important for the success of patient outcomes.

- **Consumable costs**: refer to all supplies used during medical testing and procedures like reagents, chemicals, and other disposables.

Indirect costs reflect the economic impact of disease; they account for productivity losses caused by illness, which can arise from morbidity and mortality [71], [72], [73], [74]. Based on the COI method, this research employed two key cost indicators [75], [76] to compare the efficiency of different SC models: the Average Cost per Test (ACt) and the Average Annual Cost per Patient (AACp):

$$AC_t = \frac{(E + S + L)}{N} \quad (5.1)$$

$$AAC_p = AC_t\, n \quad (5.2)$$

,where E is the annual cost of equipment, S is the annual cost of supplies (consumables), L is the labor cost, N is the total test number conducted per year, and n represents the average test number performed on each patient annually. Specifically, labor cost per test is still described in terms of single test costs, which are evaluated through the total time taken to conduct testing processes, which is dictated by the logistics of service delivery in the healthcare sector. The effectiveness of the healthcare supply chain is assessed by looking at three dimensions [28]:

- *Time to Diagnosis*: the time from the start of symptoms to the point a patient is diagnosed. Delays at this stage may adversely affect the health condition of the patient, and hence efficiency improvement in healthcare service needs to focus on this area. A typical example could be a patient delay, which represents the duration between the initial occurrence of the symptom and the time a patient sees a doctor. Some of them, at this point, may attempt to do their assessment about the symptoms they manifest and may even try to treat themselves, thus worsening the state of their health. The delay healthcare

system stands for the period within which the patient goes for the first consultation and the time they get a conclusive diagnosis. It may arise due to scheduling, laboratory processing, and other inter-physician communications. The total of these delays tends to affect the well-being of the patient's condition, as has been widely reported in various diseases [29], [30].

- *Time to Treatment Initiation*: the period between diagnosis and the start of treatment. Reducing this time frame is essential for timely medical intervention, which can significantly impact patient recovery and overall prognosis.
- *Time to Recovery:* the time from the start of treatment until patient recovery, illustrating the effectiveness and efficiency of the therapeutic processes.

Another key performance indicator is the Total Turnaround Time (TAT), defined as the time between ordering a test and receiving the final report [77], [78]. The methodology of this research adopted a comprehensive workflow model, which divides the testing process into three main phases [79]:

- Pre-Analytical Phase: covers activities from the initial test order to the physical transfer of samples to the laboratory. This phase includes sample collection, labeling, and preparation.
- Analytical Phase: begins with sample processing, where samples are identified and analyzed.
- Post-Analytical Phase: involves verification and dissemination of results.

Fig. 5.12 summarizes these different steps in the laboratory test workflow.

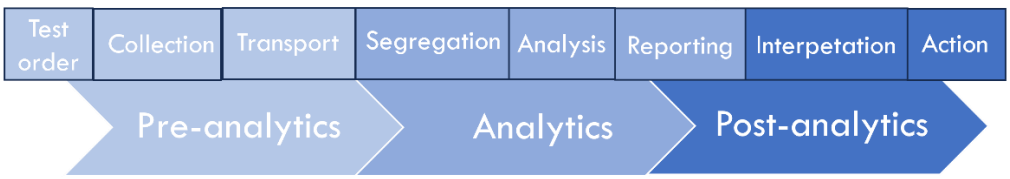

***Figure 5.12**: Workflow of a laboratory test.*

By evaluating these three phases and tracking TAT, this methodology allowed for a detailed assessment of the efficiency of different SC models in healthcare.

5.3 Results and Discussion

This section presents the results on supply chain efficiency for traditional care models (CM and POC) compared to the innovative PM model proposed.

In the CM scenario, a patient travels to a specialized structure for testing, assisted by professional staff. The traditional POC testing model involves medical staff who visit the patient's location with portable equipment, collect the sample and then transport it to the lab for analysis. In contrast, the proposed PM model enables patients to conduct self-testing using a device without the need for professional medical assistance.

Currently, most respiratory medicine testing is conducted in centralized labs, while POC tests using portable devices are primarily reserved for patients who are unable to travel. This method not only incurs higher costs per patient but also introduces delays due to transport and lab queuing. Additionally, the analysis of both CM and POC testing focuses on intra-laboratory activities, overlooking non-analytical delays from extra-laboratory processes [80].

To determine the average testing cost in the CM scenario, several expenses related to equipment, labor and consumables were evaluated. Table 5.1 outlines the market costs for lab devices typically used in EBC sampling, while Table 5.2 lists the costs for suitable commercial GC-MS devices.

***Table 5.1**: Cost of EBC sampling devices.*

Name of Device	Producer	Cooling System	Specific Features	Approx. Unit Cost / €
EcoScreen2	FILT Lungen-& Thorax Diagnostik GmbH, Germany	Electrical cooling System	Fractionated collection possible	20k€
RTube (sample collection only)	Respiratory Research, USA	Pre-cooled sleeve sensitive to higher ambient temperature	May be used at home by unsupervised subjects	50€
TurboDECCS	Medivac, Italy	Electrical cooling System	Fractionated collection possible	15k€

***Table 5.2**: Cost of EBC analysis lab devices.*

Name of Device	Producer	Specific Features	Approx. Unit Cost /€
Agilent 8890 + Agilent 7697A and 5977B	Agilent	Gas Chromatograph With Headspace Sampler and MSD Detector (GC-MS)	125k€
Varian 3800 GC	Varian, Walnut Creek, CA)	VF-5ms 5% phenol/95% PDMS column and a 4000 Ion Trap MS (Varian) equipped with Electron Ionization source (EI)	120k€

The key differences between CM and POC testing lie in the equipment costs and overall TAT. In the POC model, additional costs for the portable sample collection and storage unit are considered, and TAT is longer due to transportation times. In the CM scenario, it is assumed that the patient covers their travel costs to the centralized structure, so transportation is not included.

The fixed annual equipment costs are based on the selling price of an EBC condenser unit and GC-MS equipment in the CM scenario, while the POC scheme includes additional costs for the portable sampling and storage system. In both cases, a non-discounted annual depreciation was applied, assuming a useful life of 5 years for each device with no salvage value. Labor costs are associated with a technician operating the sampling device and analyzer, charged at a rate of €35

per hour. This involves a TAT of 30 minutes for the CM scenario and 60 minutes for the POC scenario. A POC study [80] using a portable GC device reported a total sampling time of 33 minutes, including analysis in homecare settings, which aligns with the assumption of a 1-hour TAT that accounts for transport. In contrast, CM requires patients to visit centralized labs, with a TAT estimated at 30 minutes [81]. Table 5.3 summarizes the testing costs for CM and POC models.

***Table 5.3**: CM and POC testing costs.*

	CM Model	POC Model
Equipment [€/year]	25,000	28,000
Labor [€/test]	17.5	35
Consumables [€/test]	0.5	1
TAT [h]	0.5	1

In the PM scenario, each patient is expected to have a personal testing device, assuming bi-monthly testing for a total of 6 tests annually. This aligns with current clinical practices for managing COPD, which typically involve testing every 6 months for mild cases and every 2 weeks to 1 month for severe exacerbations [82]. The self-testing device, which interacts with a smartphone, consists of several components: a Micro-Controller Unit (MCU), a potentiostat, a battery, a power supply unit, a communication module with an antenna, and minor additional elements. The total variable cost for this device, including the Printed Circuit Board (PCB), is around € 115 per unit. Initial costs also include research and development, patenting, firmware development, compliance with the EU Medical Device Directive 93/42/EEC and CE certification for market entry. Organizations involved in design, production, installation, and servicing must implement an ISO 13485 quality system, subject to annual audits by relevant authorities. The fixed industrial cost is estimated at about € 145 per unit, assuming a minimum production of 1000 units per year. With a reasonable profit margin, the final selling price is estimated at around € 300 per unit. Given a useful life of 3 years, the annual cost per patient comes to € 100. The variable cost, which

includes the mask with the integrated sensor, is roughly € 20, assuming a total of 6 tests annually. The annual costs per patient for the different SC models are illustrated in Fig. 5.13.

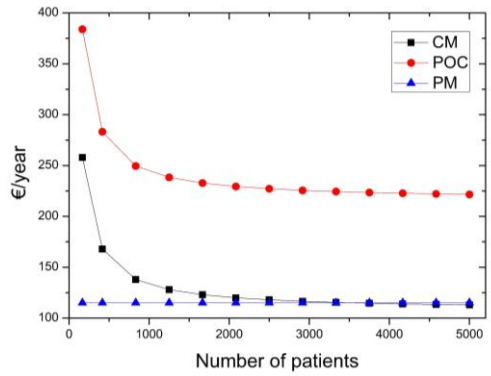

***Figure 5.13**: AACp comparison in CM, POC and PM SC models.*

PM offers cost savings on equipment investment, making it more convenient when only a limited number of patients are involved. However, as the patient number increases, the greater efficiency of the lab-based system becomes evident, leading to a break-even point of approximately 12,500 tests per year (Fig. 5.14).

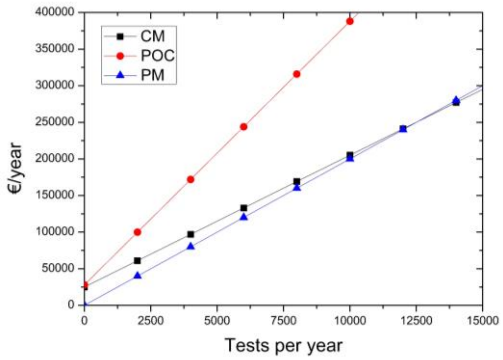

***Figure 5.14**:* Comparison of the cost per year in CM, POC and PM SC models.

The results indicate that the CM scenario offers the lowest cost per patient. However, this cost significantly rises when the number of tests per year is low,

largely due to the high equipment costs. This makes the CM model less viable for small communities and highlights its limited inclusiveness. In contrast, the POC model involves a much higher cost per test, primarily because of the additional sampling equipment and increased labor costs associated with longer turnaround times. As previously mentioned, the PM scenario can only be compared to the others with an average number of tests per patient per year. In the current analysis, where each patient undergoes six tests annually, the PM model has a slightly higher cost per patient than the CM model. However, as the number of patients decreases, the PM model becomes more cost-effective due to the absence of equipment costs. The cost analysis reveals that the TAT significantly hinders the efficiency of the POC model due to increased direct labor costs. In contrast, the high equipment costs make CM less favorable compared to PM when the number of tests per year falls below the breakeven point, which in this case is approximately 12,500 tests annually. With an average testing frequency of six tests per patient per year, this translates to about 2,100 patients. Thus, lab-based testing becomes economically viable only in communities with populations exceeding 21,000, assuming a 10% prevalence rate. This underscores the cost-effectiveness of PM for healthcare delivery in smaller communities.

The cost analysis assumes that all testing methods maintain the same quality, meaning that the diagnosis and treatment processes remain unaffected, and there are no indirect cost implications. However, in the POC scenario, there is a risk of sample degradation during collection or transport, which can compromise results. In the PM scenario, additional scientific validation is needed to confirm that the electrochemical sensing method is equivalent to traditional EBC analysis. To validate the proposed model, a sensitivity analysis was conducted, adjusting the device price in the PM scenario and the number of tests per patient per year. According to the experiment outlined in Tab. 5.4, the device price was varied at three levels (100 ± 5% €/year), while the annual test frequency was assessed at four levels (2, 4, 6, and 8). This analysis reveals how these variables impact the

breakeven points in both the CM/PM and POC/PM scenarios. The breakeven number of tests required each year is also summarized in the same table.

Table 5.4: Sensitivity analysis on device selling price/ number of tests per patient per year.

Device price per year	N° test/year-patient	Breakeven POC/PM (tests per year)	Breakeven CM/PM (tests per year)
95 €	2	1,302	633
95 €	4	-	2,326
95 €	6	-	21,429
95 €	8	-	-
100 €	2	1,167	595
100 €	4	-	-
100 €	6	-	12,500
100 €	8	-	-
105 €	2	1,057	562
105 €	4	-	1,887
105 €	6	-	8,824
105 €	8	-	-

The results indicate that as the test number conducted per patient increases each year, the breakeven point for the CM/PM case also rises when the number of tests is fewer than six. However, when patients undergo more than six tests annually, a breakeven point ceases to exist because the PM strategy becomes more advantageous than CM. This suggests that PM has the potential to replace traditional CM testing, assuming the quality and reliability of results remain consistent. A similar trend is observed when comparing POC and PM. Specifically, if patients have fewer than two tests per year, a breakeven point is present, which decreases as the annual selling price of the device increases. Once the number of tests per patient rises beyond this threshold, the breakeven point disappears, making PM the more favorable option compared to POC.

5.4 Conclusions

Most of the respiratory diseases are among the leading causes of disability and death, having an important impact on healthcare costs in developed countries. As population demographics keep evolving, economic and social burdens due to these diseases are bound to increase even further. It is against this background that the understanding of limitations from conventional healthcare supply chain models can provide a starting point for the development of new approaches to treatments of respiratory diseases, with the aim of promoting more sustainable and inclusive healthcare services. While there have been significant developments in respiratory medicine within the past decade, challenges relating to the reliability and affordability of existing testing methods remain a serious concern. On the other hand, some exciting opportunities are emerging due to recent advances in biosensors, nanotechnology, and smart clinical devices. These innovations promise to enhance POC testing methods, providing timely and accurate diagnostic information directly at the patient's location.

This research proposed a PM supply chain model for monitoring respiratory diseases through hydrogen peroxide detection in EB, simplifying the testing process and enabling self-testing for patients. Additionally, a comparative analysis of different SC models was carried out, demonstrating that current centralized and decentralized supply chain models fall short of delivering accessible and inclusive services for respiratory diseases. Moreover, this research contributes to the existing scientific literature on PM supply chain models, highlighting how these healthcare systems are essential for improving inclusivity and ensuring economic sustainability in healthcare.

However, a key limitation of this study, similar to many others in the field, is that it does not account for the external testing costs that patients may incur, which is important for a more comprehensive analysis. Additionally, the economic analysis should be expanded to include indirect costs to accurately affect the economic efficiency and validate the quality assumptions across different testing

methods. Additionally, future research should assess the reliability of results from PM devices, comparing them with those typically obtained using the gold standard for EBC analysis. This requires expertise from various fields, including nanotechnology, advanced materials, electrochemistry and electronics. The simplicity of operation, achieved by eliminating the condensation step significantly enhances testing efficiency. So, with proper clinical validation, this personalized self-testing device for respiratory diseases represents a significant advancement in the development of next-generation healthcare systems, integrating digital and biosensing technologies. It offers a cost-effective alternative to traditional hospital models and provides valuable insights for creating more sustainable and inclusive healthcare solutions in the future.

References

[1] M. Fatani, A. Shamayleh, e H. Alshraideh, «Assessing the Disruption Impact on Healthcare Delivery», *J Prim Care Community Health*, vol. 15, p. 21501319241260351, gen. 2024, doi: 10.1177/21501319241260351.

[2] J. L. Juul e K. Græsbøll, «Are fast test results preferable to high test sensitivity in contact-tracing strategies?», 19 febbraio 2021. doi: 10.1101/2021.02.17.21251921.

[3] R. W. Peeling *et al.*, «Serology testing in the COVID-19 pandemic response», *The Lancet Infectious Diseases*, vol. 20, fasc. 9, pp. e245–e249, set. 2020, doi: 10.1016/S1473-3099(20)30517-X.

[4] M. P. Cheng *et al.*, «Diagnostic Testing for Severe Acute Respiratory Syndrome–Related Coronavirus 2: A Narrative Review», *Annals of Internal Medicine*, vol. 172, fasc. 11, pp. 726–734, giu. 2020, doi: 10.7326/M20-1301.

[5] D. Kuupiel, V. Bawontuo, e T. Mashamba-Thompson, «Improving the Accessibility and Efficiency of Point-of-Care Diagnostics Services in Low- and Middle-Income Countries: Lean and Agile Supply Chain Management», *Diagnostics*, vol. 7, fasc. 4, p. 58, nov. 2017, doi: 10.3390/diagnostics7040058.

[6] M. Riccò *et al.*, «Point-of-Care Diagnostic Tests for Detecting SARS-CoV-2 Antibodies: A Systematic Review and Meta-Analysis of Real-World Data», *JCM*, vol. 9, fasc. 5, p. 1515, mag. 2020, doi: 10.3390/jcm9051515.

[7] *Home care across Europe: current structure and future challenges*. in Observatory studies series, no. 27. Copenhagen: World health organization, 2012.

[8] D. Jiménez-Rubio, «Health System Decentralization: Creating as Many Problems Than It Solves? Comment on "The Effects of Health Sector Fiscal Decentralisation on Availability, Accessibility, and Utilisation of Healthcare Services: A Panel Data Analysis"», *Int J Health Policy Manag*, p. 1, ott. 2022, doi: 10.34172/ijhpm.2022.7432.

[9] R. Oliveira, G. Santinha, e T. Sá Marques, «The Impacts of Health Decentralization on Equity, Efficiency, and Effectiveness: A Scoping Review», *Sustainability*, vol. 16, fasc. 1, p. 386, dic. 2023, doi: 10.3390/su16010386.

[10] N. P. Pai, C. Vadnais, C. Denkinger, N. Engel, e M. Pai, «Point-of-Care Testing for Infectious Diseases: Diversity, Complexity, and Barriers in Low- And Middle-Income Countries», *PLoS Med*, vol. 9, fasc. 9, p. e1001306, set. 2012, doi: 10.1371/journal.pmed.1001306.
[11] A. Brambilla *et al.*, «Flexibility during the COVID-19 Pandemic Response: Healthcare Facility Assessment Tools for Resilient Evaluation», *IJERPH*, vol. 18, fasc. 21, p. 11478, ott. 2021, doi: 10.3390/ijerph182111478.
[12] M. Beaulieu, O. Bentahar, S. Benzidia, e A. Gunasekaran, «Digitalization Initiatives of Home Care Medical Supply Chain: A Case-Study-Based Approach», *IEEE Trans. Eng. Manage.*, vol. 71, pp. 6481–6494, 2024, doi: 10.1109/TEM.2023.3265624.
[13] W. Y. C. Wang e Y. Wang, «Analytics in the era of big data: The digital transformations and value creation in industrial marketing», *Industrial Marketing Management*, vol. 86, pp. 12–15, apr. 2020, doi: 10.1016/j.indmarman.2020.01.005.
[14] J. Al-Jaroodi, N. Mohamed, e E. Abukhousa, «Health 4.0: On the Way to Realizing the Healthcare of the Future», *IEEE Access*, vol. 8, pp. 211189–211210, 2020, doi: 10.1109/ACCESS.2020.3038858.
[15] R. S. Marks, D. C. Cullen, I. Karube, C. R. Lowe, e H. H. Weetall, A c. di, *Handbook of Biosensors and Biochips*, 1ª ed. Wiley, 2007. doi: 10.1002/9780470061565.
[16] W. Zhao, S. Tian, L. Huang, K. Liu, e L. Dong, «The review of Lab-on-PCB for biomedical application», *Electrophoresis*, vol. 41, fasc. 16–17, pp. 1433–1445, set. 2020, doi: 10.1002/elps.201900444.
[17] H. T. Thanh *et al.*, «A combination of 3D printing and PCB technologies in microfluidic sensing device fabrication», *Microsyst Technol*, vol. 28, fasc. 7, pp. 1607–1619, lug. 2022, doi: 10.1007/s00542-022-05284-x.
[18] B. Ristevski e M. Chen, «Big Data Analytics in Medicine and Healthcare», *Journal of Integrative Bioinformatics*, vol. 15, fasc. 3, p. 20170030, set. 2018, doi: 10.1515/jib-2017-0030.
[19] M. R. Maleki-Yazdi, S. M. Kelly, S. S. Lam, M. Marin, M. Barbeau, e V. Walker, «The Burden of Illness in Patients with Moderate to Severe Chronic Obstructive Pulmonary Disease in Canada», *Canadian Respiratory Journal*, vol. 19, fasc. 5, pp. 319–324, gen. 2012, doi: 10.1155/2012/328460.
[20] J. Bousquet e N. Kaltaev, «Global surveillance, prevention and control of chronic respiratory diseases : a comprehensive approach / edited by Jean Bousquet and Nikolai Khaltaev», *A word where all people breathe freely*, 2007, Consultato: 26 giugno 2024. [Online]. Disponibile su: https://iris.who.int/handle/10665/43776
[21] D. M. G. Halpin, «Chronic Obstructive Pulmonary Disease: The Disease and Its Burden to Society», *Proceedings of the American Thoracic Society*, vol. 3, fasc. 7, pp. 619–623, set. 2006, doi: 10.1513/pats.200603-093SS.
[22] T. Vos *et al.*, «Global burden of 369 diseases and injuries in 204 countries and territories, 1990–2019: a systematic analysis for the Global Burden of Disease Study 2019», *The Lancet*, vol. 396, fasc. 10258, Art. fasc. 10258, ott. 2020, doi: 10.1016/S0140-6736(20)30925-9.
[23] G. Syamlal, A. Bhattacharya, e K. E. Dodd, «Medical Expenditures Attributed to Asthma and Chronic Obstructive Pulmonary Disease Among Workers — United States, 2011–2015», *MMWR Morb. Mortal. Wkly. Rep.*, vol. 69, fasc. 26, Art. fasc. 26, lug. 2020, doi: 10.15585/mmwr.mm6926a1.
[24] OECD e European Union, *Health at a Glance: Europe 2018: State of Health in the EU Cycle*. in Health at a Glance: Europe. OECD, 2018. doi: 10.1787/health_glance_eur-2018-en.
[25] K. I. Duan, M. Birger, D. H. Au, L. J. Spece, L. C. Feemster, e J. L. Dieleman, «Health Care Spending on Respiratory Diseases in the United States, 1996–2016», *Am J Respir Crit Care Med*, vol. 207, fasc. 2, pp. 183–192, gen. 2023, doi: 10.1164/rccm.202202-0294OC.
[26] J. B. Soriano *et al.*, «Prevalence and attributable health burden of chronic respiratory diseases, 1990–2017: a systematic analysis for the Global Burden of Disease Study 2017», *The Lancet*

Respiratory Medicine, vol. 8, fasc. 6, Art. fasc. 6, giu. 2020, doi: 10.1016/S2213-2600(20)30105-3.
[27] S. Momtazmanesh *et al.*, «Global burden of chronic respiratory diseases and risk factors, 1990–2019: an update from the Global Burden of Disease Study 2019», *eClinicalMedicine*, vol. 59, p. 101936, mag. 2023, doi: 10.1016/j.eclinm.2023.101936.
[28] S. Momtazmanesh *et al.*, «Global burden of chronic respiratory diseases and risk factors, 1990–2019: an update from the Global Burden of Disease Study 2019», *eClinicalMedicine*, vol. 59, p. 101936, mag. 2023, doi: 10.1016/j.eclinm.2023.101936.
[29] G. D'Amato, L. Cecchi, M. D'Amato, e I. Annesi-Maesano, «Climate change and respiratory diseases», *Eur Respir Rev*, vol. 23, fasc. 132, pp. 161–169, giu. 2014, doi: 10.1183/09059180.00001714.
[30] G. D'Amato *et al.*, «The effects of climate change on respiratory allergy and asthma induced by pollen and mold allergens», *Allergy*, vol. 75, fasc. 9, pp. 2219–2228, set. 2020, doi: 10.1111/all.14476.
[31] G. Shaddick, M. L. Thomas, P. Mudu, G. Ruggeri, e S. Gumy, «Half the world's population are exposed to increasing air pollution», *npj Clim Atmos Sci*, vol. 3, fasc. 1, p. 23, giu. 2020, doi: 10.1038/s41612-020-0124-2.
[32] A. Siracusa *et al.*, «Asthma and exposure to cleaning products - a European Academy of Allergy and Clinical Immunology task force consensus statement», *Allergy*, vol. 68, fasc. 12, Art. fasc. 12, dic. 2013, doi: 10.1111/all.12279.
[33] S. De Matteis *et al.*, «Current and new challenges in occupational lung diseases», *Eur Respir Rev*, vol. 26, fasc. 146, Art. fasc. 146, dic. 2017, doi: 10.1183/16000617.0080-2017.
[34] P. D. Blanc, «Occupation and COPD: A Brief Review», *Journal of Asthma*, vol. 49, fasc. 1, Art. fasc. 1, feb. 2012, doi: 10.3109/02770903.2011.611957.
[35] T. Sigsgaard *et al.*, «ERS position paper: work-related respiratory diseases in the EU», *Eur Respir J*, vol. 35, fasc. 2, Art. fasc. 2, feb. 2010, doi: 10.1183/09031936.00139409.
[36] F. Longo, L. Nicoletti, e A. Padovano, «Smart operators in industry 4.0: A human-centered approach to enhance operators' capabilities and competencies within the new smart factory context», *Computers & Industrial Engineering*, vol. 113, pp. 144–159, nov. 2017, doi: 10.1016/j.cie.2017.09.016.
[37] T. Kalsoom, N. Ramzan, S. Ahmed, e M. Ur-Rehman, «Advances in Sensor Technologies in the Era of Smart Factory and Industry 4.0», *Sensors*, vol. 20, fasc. 23, p. 6783, nov. 2020, doi: 10.3390/s20236783.
[38] J.-H. Kim *et al.*, «A conformable sensory face mask for decoding biological and environmental signals», *Nat Electron*, vol. 5, fasc. 11, pp. 794–807, ott. 2022, doi: 10.1038/s41928-022-00851-6.
[39] R. Gasparri, G. Sedda, e L. Spaggiari, «The Electronic Nose's Emerging Role in Respiratory Medicine», *Sensors*, vol. 18, fasc. 9, p. 3029, set. 2018, doi: 10.3390/s18093029.
[40] J. Patel, A. Dalal, e S. Nagar, «Indirect costs in chronic obstructive pulmonary disease: A review of the economic burden on employers and individuals in the United States», *COPD*, p. 289, mar. 2014, doi: 10.2147/COPD.S57157.
[41] K. Souliotis, H. Kousoulakou, G. Hillas, N. Tzanakis, M. Toumbis, e T. Vassilakopoulos, «The direct and indirect costs of managing chronic obstructive pulmonary disease in Greece», *COPD*, vol. Volume 12, pp. 1395–1400, mag. 2017, doi: 10.2147/COPD.S132825.
[42] for the COSYCONET Study Group *et al.*, «Costs and health-related quality of life in Alpha-1-Antitrypsin Deficient COPD patients», *Respir Res*, vol. 18, fasc. 1, p. 60, dic. 2017, doi: 10.1186/s12931-017-0543-8.
[43] S.-A. Jansson, H. Backman, A. Stenling, A. Lindberg, E. Rönmark, e B. Lundbäck, «Health economic costs of COPD in Sweden by disease severity – Has it changed during a ten years period?», *Respiratory Medicine*, vol. 107, fasc. 12, pp. 1931–1938, dic. 2013, doi: 10.1016/j.rmed.2013.07.012.

[44] J. Thornton Snider, J. A. Romley, K. S. Wong, J. Zhang, M. Eber, e D. P. Goldman, «The Disability Burden of COPD», *COPD: Journal of Chronic Obstructive Pulmonary Disease*, vol. 9, fasc. 5, pp. 513–521, set. 2012, doi: 10.3109/15412555.2012.696159.
[45] J. Foo *et al.*, «Continuing to Confront COPD International Patient Survey: Economic Impact of COPD in 12 Countries», *PLoS ONE*, vol. 11, fasc. 4, p. e0152618, apr. 2016, doi: 10.1371/journal.pone.0152618.
[46] K. R. Chapman, J. Bourbeau, e L. Rance, «The burden of COPD in Canada: results from the confronting COPD survey», *Respiratory Medicine*, vol. 97, pp. S23–S31, mar. 2003, doi: 10.1016/S0954-6111(03)80022-7.
[47] N. Mittmann, L. Kuramoto, S. J. Seung, J. M. Haddon, C. Bradley-Kennedy, e J. M. FitzGerald, «The cost of moderate and severe COPD exacerbations to the Canadian healthcare system», *Respiratory Medicine*, vol. 102, fasc. 3, pp. 413–421, mar. 2008, doi: 10.1016/j.rmed.2007.10.010.
[48] J. Połomska, K. Bar, e B. Sozańska, «Exhaled Breath Condensate—A Non-Invasive Approach for Diagnostic Methods in Asthma», *JCM*, vol. 10, fasc. 12, p. 2697, giu. 2021, doi: 10.3390/jcm10122697.
[49] A. Tiele, A. Wicaksono, S. K. Ayyala, e J. A. Covington, «Development of a Compact, IoT-Enabled Electronic Nose for Breath Analysis», *Electronics*, vol. 9, fasc. 1, p. 84, gen. 2020, doi: 10.3390/electronics9010084.
[50] G. W. Hunter e R. A. Dweik, «Applied breath analysis: an overview of the challenges and opportunities in developing and testing sensor technology for human health monitoring in aerospace and clinical applications», *J. Breath Res.*, vol. 2, fasc. 3, p. 037020, set. 2008, doi: 10.1088/1752-7155/2/3/037020.
[51] G. A. Naikoo *et al.*, «Nanomaterials-Based Sensors for Respiratory Viral Detection: A Review», *IEEE Sensors J.*, vol. 21, fasc. 16, pp. 17643–17656, ago. 2021, doi: 10.1109/JSEN.2021.3085084.
[52] L. A. Wasiewska, I. Seymour, B. Patella, C. Burgess, e A. O'Riordan, «Reagent free electrochemical-based detection of silver ions at interdigitated micro electrodes using in situ pH control.».
[53] S. M. May e J. T. C. Li, «Burden of chronic obstructive pulmonary disease: Healthcare costs and beyond», *allergy asthma proc*, vol. 36, fasc. 1, Art. fasc. 1, gen. 2015, doi: 10.2500/aap.2015.36.3812.
[54] B. O'Sullivan *et al.*, «A simulation and experimental study of electrochemical pH control at gold interdigitated electrode arrays», *Electrochimica Acta*, vol. 395, p. 139113, nov. 2021, doi: 10.1016/j.electacta.2021.139113.
[55] H. C. Ates e C. Dincer, «Wearable breath analysis», *Nat Rev Bioeng*, vol. 1, fasc. 2, pp. 80–82, gen. 2023, doi: 10.1038/s44222-022-00011-7.
[56] J. Hyysalo *et al.*, «Smart mask – Wearable IoT solution for improved protection and personal health», *Internet of Things*, vol. 18, p. 100511, mag. 2022, doi: 10.1016/j.iot.2022.100511.
[57] J. Li, J. Yin, S. Ramakrishna, e D. Ji, «Smart Mask as Wearable for Post-Pandemic Personal Healthcare», *Biosensors*, vol. 13, fasc. 2, Art. fasc. 2, gen. 2023, doi: 10.3390/bios13020205.
[58] L. Pan *et al.*, «Lab-on-Mask for Remote Respiratory Monitoring», *ACS Materials Lett.*, vol. 2, fasc. 9, Art. fasc. 9, set. 2020, doi: 10.1021/acsmaterialslett.0c00299.
[59] Y. Yu, M. Pan, J. Peng, D. Hu, Y. Hao, e Z. Qian, «A review on recent advances in hydrogen peroxide electrochemical sensors for applications in cell detection», *Chinese Chemical Letters*, vol. 33, fasc. 9, Art. fasc. 9, set. 2022, doi: 10.1016/j.cclet.2022.02.045.
[60] T. Hussain, S. Ullah, R. Fernández-García, e I. Gil, «Wearable Sensors for Respiration Monitoring: A Review», *Sensors*, vol. 23, fasc. 17, p. 7518, ago. 2023, doi: 10.3390/s23177518.
[61] M. MacLeod *et al.*, «Chronic obstructive pulmonary disease exacerbation fundamentals: Diagnosis, treatment, prevention and disease impact», *Respirology*, vol. 26, fasc. 6, pp. 532–551, giu. 2021, doi: 10.1111/resp.14041.

[62] P. Montuschi e P. J. Barnes, «Analysis of exhaled breath condensate for monitoring airway inflammation», *Trends in Pharmacological Sciences*, vol. 23, fasc. 5, pp. 232–237, mag. 2002, doi: 10.1016/S0165-6147(02)02020-5.
[63] D. T. V. Anh, W. Olthuis, e P. Bergveld, «A hydrogen peroxide sensor for exhaled breath measurement», *Sensors and Actuators B: Chemical*, vol. 111–112, pp. 494–499, nov. 2005, doi: 10.1016/j.snb.2005.03.107.
[64] S.-F. Chen e M.-G. C. Danao, «Decomposition and solubility of H_2O_2: implications in exhaled breath condensate», *J. Breath Res.*, vol. 7, fasc. 4, p. 046001, set. 2013, doi: 10.1088/1752-7155/7/4/046001.
[65] E. M. Konstantinidi, A. S. Lappas, A. S. Tzortzi, e P. K. Behrakis, «Exhaled Breath Condensate: Technical and Diagnostic Aspects», *The Scientific World Journal*, vol. 2015, fasc. 1, p. 435160, gen. 2015, doi: 10.1155/2015/435160.
[66] J. Hunt, «Exhaled Breath Condensate: An Overview», *Immunology and Allergy Clinics of North America*, vol. 27, fasc. 4, pp. 587–596, nov. 2007, doi: 10.1016/j.iac.2007.09.001.
[67] J. Vaughan *et al.*, «Exhaled breath condensate pH is a robust and reproducible assay of airway acidity», *European Respiratory Journal*, vol. 22, fasc. 6, pp. 889–894, dic. 2003, doi: 10.1183/09031936.03.00038803.
[68] A. Larsson, R. Greig-Pylypczuk, e A. Huisman, «The state of point-of-care testing: a european perspective», *Upsala Journal of Medical Sciences*, vol. 120, fasc. 1, pp. 1–10, gen. 2015, doi: 10.3109/03009734.2015.1006347.
[69] R. A. Atmoko, R. Riantini, e M. K. Hasin, «IoT real time data acquisition using MQTT protocol», *J. Phys.: Conf. Ser.*, vol. 853, p. 012003, mag. 2017, doi: 10.1088/1742-6596/853/1/012003.
[70] B. Fautrel, A. Boonen, M. De Wit, S. Grimm, M. Joore, e F. Guillemin, «Cost assessment of health interventions and diseases», *RMD Open*, vol. 6, fasc. 3, p. e001287, nov. 2020, doi: 10.1136/rmdopen-2020-001287.
[71] D. M. G. Halpin, «Chronic Obstructive Pulmonary Disease: The Disease and Its Burden to Society», *Proceedings of the American Thoracic Society*, vol. 3, fasc. 7, pp. 619–623, set. 2006, doi: 10.1513/pats.200603-093SS.
[72] R. Ernst, «Indirect Costs and Cost-Effectiveness Analysis», *Value in Health*, vol. 9, fasc. 4, pp. 253–261, lug. 2006, doi: 10.1111/j.1524-4733.2006.00114.x.
[73] K. R. Chapman, «Epidemiology and costs of chronic obstructive pulmonary disease», *European Respiratory Journal*, vol. 27, fasc. 1, pp. 188–207, gen. 2006, doi: 10.1183/09031936.06.00024505.
[74] S. M. May e J. T. C. Li, «Burden of chronic obstructive pulmonary disease: Healthcare costs and beyond», *allergy asthma proc*, vol. 36, fasc. 1, pp. 4–10, gen. 2015, doi: 10.2500/aap.2015.36.3812.
[75] J. H. Howanitz e P. J. Howanitz, «Laboratory Results: Timeliness as a Quality Attribute and Strategy», *Am J Clin Pathol*, vol. 116, fasc. 3, pp. 311–315, set. 2001, doi: 10.1309/H0DY-6VTW-NB36-U3L6.
[76] G. L. Hortin, «Does Point-Of-Care Testing Save Money or Cost More?», *Lab Med*, vol. 36, fasc. 8, pp. 465–467, ago. 2005, doi: 10.1309/AJ9D0GHYYWEDYHPD.
[77] B. Goswami, B. Singh, R. Chawla, V. K. Gupta, e V. Mallika, «Turn Around Time (TAT) as a Benchmark of Laboratory Performance», *Ind J Clin Biochem*, vol. 25, fasc. 4, pp. 376–379, ott. 2010, doi: 10.1007/s12291-010-0056-4.
[78] P. P. Dawande, R. S. Wankhade, F. I. Akhtar, e O. Noman, «Turnaround Time: An Efficacy Measure for Medical Laboratories», *Cureus*, set. 2022, doi: 10.7759/cureus.28824.
[79] G. D. Lundberg, «Acting on Significant Laboratory Results», *JAMA*, vol. 245, fasc. 17, p. 1762, mag. 1981, doi: 10.1001/jama.1981.03310420052033.
[80] R. C. Hawkins, «Laboratory Turnaround Time».

[81] M. Zhou *et al.*, «Rapid breath analysis for acute respiratory distress syndrome diagnostics using a portable two-dimensional gas chromatography device», *Anal Bioanal Chem*, vol. 411, fasc. 24, pp. 6435–6447, set. 2019, doi: 10.1007/s00216-019-02024-5.
[82] P. J. Howanitz e B. A. Jones, «Comparative Analytical Costs of Central Laboratory Glucose and Bedside Glucose Testing: A College of American Pathologists Q-Probes Study», *Archives of Pathology & Laboratory Medicine*, vol. 128, fasc. 7, pp. 739–745, lug. 2004, doi: 10.5858/2004-128-739-CACOCL.

6. Conclusions and Future Perspectives

The research carried out for this doctoral thesis marks significant advances in the development of wearable electrochemical sensors aimed at monitoring oxidative stress in real-time, a pathological condition closely associated with several diseases, particularly respiratory diseases.

The first electrochemical sensor proposed in this work was designed to be integrated in a face mask, enabling real-time quantification of hydrogen peroxide in exhaled breath. This sensor demonstrated remarkable selectivity and successfully detected H_2O_2 levels in the aerosol phase from bronchial epithelial cells under different conditions, aligning closely with results from standard cytofluorimetric methods. The sensor's working electrode was then further modified to detect the trace hydrogen peroxide concentrations typically present in exhaled breath, achieving successful detection in liquid samples. Future efforts should aim to optimize the chitosan deposition time to achieve an ideal thickness for hydrogen peroxide detection in the aerosol phase with the sensitivity needed for low concentrations. Once fully optimized for aerosol-phase detection, this sensor could be integrated into face masks for real-time monitoring without the need for the condensation step currently required in clinical settings. This innovation offers a wide range of potential applications, including home care, remote point-of-care healthcare and workplace diagnostics, all without the need for expensive laboratory equipment or specialized training.

Furthermore, this research included a comparative analysis of existing healthcare supply chain models, revealing that both centralized and decentralized models fall short in providing accessible and inclusive services for respiratory diseases. In contrast, a proposed PM supply chain model, based on a face mask integrated with the developed electrochemical sensor, offers cost-effective and inclusive healthcare, particularly in small communities. However, future research should assess the reliability of results from this PM device, comparing them to those from conventional EBC analysis techniques. With proper clinical validation, this self-

testing approach could substantially improve healthcare delivery, especially within smaller communities.

Additionally, this thesis presents a wearable electrochemical sensor for uric acid, chloride ions and glucose detection in sweat. However, detecting glucose proved challenging due to interference from various components in the artificial sweat. Consequently, the focus of this research analysis shifted to the detection of uric acid and chloride ions in a microfluidic system, used to collect small sweat samples for this purpose. Still, further testing in real sweat samples is necessary to reliably quantify these biomarkers.

So, this research work highlights the promising application of electrochemical sensors in the field of non-invasive health monitoring, paving the way for further advancements in real-time analysis.

Publications

1. Bernardo Patella, Serena Di Vincenzo, Claudio Zanca, Luciano Bollaci, Maria Ferraro, Maria Rita Giuffrè, Chiara Cipollina, **Maria Giuseppina Bruno**, Giuseppe Aiello, Michele Russo, Rosalinda Inguanta, Elisabetta Pace, "Electrochemical Quantification of H_2O_2 Released by Airway Cells Growing in Different Culture Media", Micromachines, 2022

2. **Maria Giuseppina Bruno**, Bernardo Patella, Giuseppe Aiello, Claudia Torino, Antonio Vilasi, Chiara Cipollina, Serena Di Vincenzo, Elisabetta Pace, Alan O'Riordan, Rosalinda Inguanta, "Wearable sensor for real-time monitoring of hydrogen peroxide in simulated exhaled air", CET (Chemical Engineering Transaction), 2023

3. **M. G. Bruno**, B. Patella, M. Ferraro, S. Di Vincenzo, C. Torino, A. Vilasi, M.R. Giuffrè, V. B. Juska, A. O'Riordan, R. Inguanta, C. Cipollina, E. Pace, G. Aiello "Wearable sensor for real-time monitoring of oxidative stress in simulated exhaled breath", Biosensors and Bioelectronics, 2024

4. Islam Asem Salah Abusohyon, Giuseppe Aiello, Cinzia Muriana, **Maria Giuseppina Bruno**, Bernardo Patella, Maria Ferraro, Serena Di Vincenzo, Chiara Cipollina, Elisabetta Pace, Rosalinda Inguanta, Mo'men Abu Sahyoun, "A Novel Healthcare 4.0 System for Testing Respiratory Diseases Based on Nanostructured Biosensors and Fog Networking", Computers & Industrial Engineering, 2024

5. **Maria Giuseppina Bruno**, Giuseppe Aiello, Bernardo Patella, Rosalinda Inguanta, Cinzia Muriana, Alessio Ishizaka, Michele Russo, Islam Asem Salah Abusohyon, "Cost analysis of a personalized medicine supply chain model for respiratory diseases based on a novel nanostructured biosensing system", Paper in preparation

6. **Maria Giuseppina Bruno**, Bernardo Patella, Maria Ferraro, Serena Di Vincenzo, Giuseppe Aiello, Claudia Torino, Antonio Vilasi, Chiara Cipollina, Elisabetta Pace, Alan O'Riordan, Rosalinda Inguanta, "Electrochemical Sensor based on Prussian Blue for Hydrogen Peroxide Detection in Exhaled Breath Condensate", Paper in preparation

7. **Maria Giuseppina Bruno**, Manuel Gutiérrez-Capitán, César Fernández-Sánchez, Bernardo Patella, Rosalinda Inguanta, Giuseppe Aiello, "Wearable Microfluidic Sensor for Uric acid and Chlorides Detection in Sweat", Paper in preparation

Conferences

1. **Maria Giuseppina Bruno**, Bernardo Patella, Giuseppe Aiello, Francesco Lopresti, Vincenzo La Carrubba, Claudia Torino, Antonio Vilasi, Chiara Cipollina, Serena Di Vincenzo, Elisabetta Pace, Alan O'Riordan, Rosalinda Inguanta, "Wearable sensor for real-time monitoring of oxidative stress", *GRICU 2022*, Ischia, 3-6/07/2022

2. ***Summer School*** *GRICU 2022*, "Fundamentals of Electrochemical Processes and their Application Heterogeneous Catalysis", Ischia, 6-9/07/2022

3. **Maria Giuseppina Bruno**, Bernardo Patella, Francesco Lopresti, Giuseppe Aiello, Claudia Torino, Antonio Vilasi, Chiara Cipollina, Elisabetta Pace, Alan O'Riordan, Rosalinda Inguanta, "Wearable sensor for real-time monitoring of hydrogen peroxide in simulated breath", *73rd of Annual Meeting of ISE 2022*, Online conference, 12-16/09/2022

4. **Maria Giuseppina Bruno**, Bernardo Patella, Giuseppe Aiello, Claudia Torino, Antonio Vilasi, Chiara Cipollina, Serena Di Vincenzo, Elisabetta Pace, Alan O'Riordan, Rosalinda Inguanta, "Wearable sensor for real-time monitoring of hydrogen peroxide in simulated exhaled air", *ICHEAP16*, Napoli, 21- 24/05/2023

5. **Maria Giuseppina Bruno**, Bernardo Patella, Giuseppe Aiello, Claudia Torino, Antonio Vilasi, Chiara Cipollina, Serena Di Vincenzo, Elisabetta Pace, Alan O'Riordan, Rosalinda Inguanta, "Electrochemical detection of H_2O_2 for real-time monitoring of oxidative stress", *74th of Annual Meeting of ISE 2023*, Lyon (France), 3-8/09/2023

6. **Maria Giuseppina Bruno**, Bernardo Patella, Claudia Torino, Antonio Vilasi, Chiara Cipollina, Serena Di Vincenzo, Elisabetta Pace, Alan O'Riordan, Rosalinda Inguanta, Giuseppe Aiello, "Electrochemical sensor for worker safety in manufacturing industries", *GEI2023*, Cefalù, 17-22/09/2023

7. **Maria Giuseppina Bruno**, Bernardo Patella, Giuseppe Aiello, Claudia Torino, Antonio Vilasi, Chiara Cipollina, Serena Di Vincenzo, Maria Ferraro, Elisabetta Pace, Alan O'Riordan, Rosalinda Inguanta, "Electrochemical Sensor based on Prussian Blue for Hydrogen Peroxide Detection in Exhaled Breath", ***Summer School*** "Catalysis: from understanding to applications", Albi (France), 17-21/06/2024

8. **Maria Giuseppina Bruno**, Bernardo Patella, Cinzia Muriana, Maria Ferraro, Serena Di Vincenzo, Chiara Cipollina, Elisabetta Pace, Rosalinda Inguanta, Giuseppe Aiello, Article "*An Inclusive supply chain model for the treatment of respiratory diseases based on Personalized medicine through modern biosensing devices*", XXIX AIDI ***Summer School*** "Francesco Turco" - Sustainability and resilience in industrial systems across the era of digitalization, Otranto (Lecce), 11-13/09/2024